Berichte des Instituts für Mechanik

Bericht 1/2008

Wolfgang Bier

A Constitutive Model for Metal Powder and its Numerical Treatment using Finite Elements

kassel university press

This work has been accepted by the faculty of mechanical engineering of the University of Kassel as a thesis for acquiring the academic degree of Doktor der Ingenieurwissenschaften (Dr.-Ing.).

Supervisor: PD Dr.-Ing S. Hartmann
Co-Supervisor: Prof. Dr.-Ing. C. Tsakmakis

Defense day: 16th November 2007

Bibliographic information published by Deutsche Nationalbibliothek
The Deutsche Nationalbibliothek lists this publication in the Deutsche Nationalbibliografie; detailed bibliographic data is available in the Internet at http://dnb.d-nb.de.

Zugl.: Kassel, Univ., Diss. 2007
ISBN: 978-3-89958-396-0

Printed by: Unidruckerei, University of Kassel
Printed in Germany

Vorwort und Danksagung

Die vorliegende Arbeit entstand während meiner Zeit am Institut für Mechanik der Universität Kassel. Als Stipendiat der GIF (German Israeli Foundation) habe ich als wissenschaftlicher Mitarbeiter von PD Dr.-Ing. habil S. Hartmann an einem binationalen Forschungsprojekt mit dem Titel "p-FEM for a class of pressure dependent plasticity models with application to cold isostatic pressing" gearbeitet. Bei der GIF möchte ich mich für die gewährte finanzielle Unterstützung bedanken. Für die freundschaftliche und sehr fruchtbare Zusammenarbeit möchte ich mich bei allen weiteren Kollegen des GIF-Projekts, namentlich Prof. M. P. Dariel, Prof. N. Frage, Prof. S. Holzer, Prof. E. Rank, Prof. Z. Yosibash sowie I. Bronfenbrenner, I. Cohen, S. Cohen, Dr. A. Düster, U. Heisserer, M. Martins-Wagner, Dr. O. Mihailov, Dr. M. Szanto sowie allen weiteren studentischen Hilfskräften bedanken, die in allen Arbeitsgruppen wesentlich zum Erfolg des Projektes beigetragen haben. Ganz besonders möchte ich mich bei meinen israelischen Kollegen für ihre herzliche Gastfreundschaft und die hervorragende Betreuung während unserer Besuche in Beer-Sheva bedanken. Ich werde diese Zeit nie vergessen.

Mein größter Dank gilt Herrn PD Dr.-Ing. S. Hartmann. Bei ihm bedanke ich mich für das interessante Promotionsthema, sowie die Übernahme des Hauptreferrats. Zudem möchte ich mich für seine hervorragende Betreuung und seine stete Diskussions- und Lehrbereitschaft mir gegenüber bedanken, sowie für das durch ihn geschaffene familiäre Arbeitsklima. Ich bin ihm als Schüler, Kollege und Mensch von Herzen dankbar für die Zeit am IfM.

Bei Herrn Prof. Tsakmakis, dem zweiten Gutachter, möchte ich mich für die Übernahme des Korreferates sowie die gewährte Hilfe und Diskussionsbereitschaft bei der Materialmodellierung bedanken. Für die Bereitschaft zur Mitwirkung an der Prüfungskommission bedanke ich mich bei Herrn Prof. B. Scholtes und Herrn Prof. K. Steinhoff.

Ich möchte mich bei den aktuellen und ehemaligen Professoren, Prof. T. Böhlke, Prof. H. Irretier, Prof. A. Matzenmiller, Prof. B. Schulz-Jander, Prof. O. Wünsch und den aktuellen und ehemaligen Mitarbeitern des IfM für die angenehme Atmosphäre und die stets freigiebig gewährte Hilfestellung, sowie für interessante fachliche und nichtfachliche Gespräche während meiner Zeit am IfM bedanken. Bei Fragen der Kontinuumsmechanik und der Materialtheorie habe ich neben der Unterstützung durch meinen Betreuer PD Dr.-Ing. habil S. Hartmann insbesondere durch Prof. P. Haupt und Dr.-Ing. D. Helm einige wertvolle Hinweise erhalten, wofür ich mich herzlich bedanke. Für Ihre Hilfe bei organisatorischen Dingen und verwaltungstechnischen Problemen bedanke ich mich herzlich bei den Sekretärinnen des IfM, Frau L. Klünder, Frau S. Schiminski und besonders bei Frau C. Ellrich, die mir diesbezüglich viel Arbeit abgenommen hat. Für seine Unterstützung bei EDV-Problemen aller Art möchte ich mich bei Herrn K. Farr herzlich bedanken. Für seine Diskussionsbereitschaft bei Fragen der Mechanik und darüber hinaus bedanke ich mich bei Herrn Dr.-Ing. L. Schreiber. Ebenso danke ich den ehemaligen Kollegen F. Burbulla, S. Bröcker, G. Bondár, C. Conzen, I. Danladi, F. Endeshewa, Dr.-Ing. S. Gerlach, A. Hamkar, C. Justine, Dr.-Ing. Ch. Kardelky, Dr.-Ing. T. Kersten, B. Köster, M. Krebs, S. Lindemann, G. Linek, Prof. A. Lion, K. Quint, M. Schäfers, G. Schneider, M. Streng, H. Wahl, W. Zugreif für die eine oder andere kleinere oder größere Hilfe. Besonders sei den Kollegen M. Conic, M. Fiolka und D. Strohschein gedankt, die mir über das Fachliche hinaus mit Rat und Tat zur Seite standen. Ebenso möchte ich mich bei meinen Freunden ausserhalb des IfM insbesondere bei Marc Fischbach für ihre Unterstützung während der manchmal belastenden Arbeit an der Dissertation bedanken. Für die Hilfe bei der Vorbereitung der Disputation und zum Ende

meiner Zeit in Kassel danke ich Frau B. Röhling und Herrn B. Röhling sowie Frau T. Ayalp. Für die gewährte Flexibilität bei der Gestaltung meiner Arbeitszeit, um entsprechende Freiräume für die letzten Korrekturen an der Dissertationsschrift sowie die Vorbereitung auf die Disputation zu schaffen, danke ich meinen Vorgesetzten Herrn Dr.-Ing. O. Scherf und Herrn Dr.-Ing. R. Maucher.

Für ihre aufopferungsvolle Unterstützung während meiner gesamten Ausbildungszeit danke ich meiner Mutter Frau Margret Bier und meinem leider viel zu früh verstorbenen Vater Wolfhard Bier sowie meinem Bruder Siegfried Bier von ganzem Herzen. Insbesondere in der letzten Phase der Anfertigung meiner Dissertation hat mich meine Frau Anke Böttcher sehr unterstützt, insbesondere hat sie durch ihr sorgfältiges Korrekturlesen maßgeblich zur Reduktion der Fehler in der Dissertation beigetragen, wofür ich ihr aufrichtig danke. Auch meinen Kindern Paul und Bela danke ich für ihre Rücksichtnahme in dieser Zeit.

Darmstadt, Dezember 2007 Wolfgang Bier

Preface and acknowledgments

This thesis is the product of my work at the Institute of Mechanics at the University of Kassel. I received a scholarship from the GIF (German Israeli Foundation) to work as a junior researcher under the guidance of PD Dr.-Ing. habil S. Hartmann on a binationale research project with the title "p-FEM for a class of pressure dependent plasticity models with application to cold isostatic pressing". I would like to thank the GIF for the funding of this project and my scholarship. For the friendly and very fruitful collaboration I would like to thank all colleagues of this GIF-project, namely Prof. M. P. Dariel, Prof. N. Frage, Prof. S. Holzer, Prof. E. Rank, Prof. Z. Yosibash as well as I. Bronfenbrenner, I. Cohen, S. Cohen, Dr. A. Düster, U. Heisserer, M. Martins-Wagner, Dr. O. Mihailov, Dr. M. Szanto and all additional students and people, who have contributed in all working groups to the achievements made within this project significantly. I would like to express my special gratitude towards my colleagues from Israel for their heartly hospitality and the outstanding caretaking during our visits in Beer-Sheva. I will never forget this time of my life.

I want to express my best thanks to my supervisor PD Dr.-Ing. S. Hartmann for providing the interesting research topic and taking over the position of the main referee for the thesis. Beyond that I want to thank him for the excellent guidance and his never ending willingness to discuss and teach. Furthermore, I thank him for creating excellent and friendly working conditions. I owe him my deepest gratitude as a student, colleague and human being for my time at the IfM.

Additionally, I thank Prof. Tsakmakis for being the second reviewer and his help as well as some discussions regarding the formulation of the constitutive model. For their willingness to participate in the jury I would like to thank Prof. B. Scholtes and Prof. K. Steinhoff.

I thank all the current and former professors of the IfM, Prof. T. Böhlke, Prof. H. Irretier, Prof. A. Matzenmiller, Prof. B. Schulz-Jander, Prof. O. Wünsch and all the current and former colleagues of the IfM for the friendly atmosphere and their always kindly granted help as well as for many scientific discussions and social talks during my period at the IfM. With questions about continuum mechanics and the theory of materials I was able to ask, in addition to my supervisor PD Dr.-Ing. S. Hartmann, the former head of the IfM Prof. P. Haupt and Dr.-Ing. D. Helm and received some very helpful answers, for which I am very grateful. For help in organisational aspects I thank the secretaries of the IfM Mrs. L. Klünder, Mrs. S. Schiminski and especially Mrs. C. Ellrich, who did a great deal of organisational work for me. For his support with respect to all EDV questions I want to thank Mr. K. Farr. For some discussions concerning mechanics and beyond that I thank Dr.-Ing. L. Schreiber. In the same manner I want to express my gratitude towards my former colleagues F. Burbulla, S. Bröcker, G. Bondár, C. Conzen, I. Danladi, F. Endeshewa, Dr.-Ing. S. Gerlach, A. Hamkar, C. Justine, Dr.-Ing. Ch. Kardelky, Dr.-Ing. T. Kersten, B. Köster, M. Krebs, S. Lindemann, G. Linek, Prof. A. Lion, K. Quint, M. Schäfers, G. Schneider, M. Streng, H. Wahl, W. Zugreif for all their help. Particularly I want to thank my former colleagues M. Conic, M. Fiolka, and D. Strohschein, who helped me within and beyond the professional level.

I thank all my friends outside the IfM, especially Mr. Marc Fischbach, for their reliable friendship and support during the sometimes strenuous time of writing my thesis. For their help in preparing the disputation and in my final days in Kassel I thank Mrs. B. Röhling and Mr. B. Röhling as well as Mrs. T. Ayalp. For the granted flexibility in organizing my working hours, to

generate time for some final corrections of the thesis and my preparation for the disputation, I would like to thank my superiors Dr.-Ing. O. Scherf and Dr.-Ing. R. Maucher.

For their devoted support during my complete education I thank my mother Mrs. Margret Bier and my deceased father Mr. Wolfhard Bier as well as my brother Siegfried Bier. Especially during the final phase of writing the thesis my wife Mrs. Anke Böttcher provided significant support and helped minimizing the errors in the thesis by reading the proofs. Thank you very much! I also want to thank my children Paul and Bela for their considerateness during that time.

Darmstadt, December 2007 Wolfgang Bier

Deutschsprachige Zusammenfassung der Dissertation „A Constitutive Model for Metal Powder and its Numerical Treatment using Finite Elements“

„Ein Konstitutives Modell für Metallpulver und dessen Numerische Behandlung mittels Finiter Elemente“

Die Zuwachsraten bei der Herstellung mechanischer Werkstücke auf pulvermetallurgischem Weg sind seit Jahren hoch. Darum wird es immer wichtiger in der Designphase neuer Teile kostspielige und zeitraubende ”trial and error”-Experimente zur Auffindung optimaler Bedingungen für das Pressen der Teile, durch numerische Simulation des Pressprozesses zu ersetzen. Die Qualität der Simulationsergebnisse hängt von der Qualität der verwendeten Konstitutivgleichungen (Materialmodell) ab. Es muss in der Lage sein, das mechanische Verhalten des Metallpulvers während des Pressens hinreichend genau zu beschreiben. Von gleicher Bedeutung für die Anwendbarkeit der numerischen Simulation ist die robuste und effiziente Implementation der Modellgleichungen. Darüber hinaus ist der Einsatz effizienter Lösungsverfahren für das Anfangsrandwertproblem (ARWP), welches aus den Gleichgewichtsbedingungen, den Konstitutivgleichungen und den Anfangs- und Randbedingungen eines Pressprozesses gebildet wird, notwendig.

Nach einer Einführung und Abgrenzung des Themas der Arbeit in der Einleitung werden im zweiten Kapitel die benötigten kontinuumsmechanischen Grundlagen für die Beschreibung des Metallpulverpressens bereitgestellt. Hierzu gehört eine für große Deformationen geeignete kinematische Formulierung. Weiterhin werden die Bilanzgleichungen, aus denen sich das Prinzip der virtuellen Verschiebungen ableiten lässt, welches ein möglicher Startpunkt für die numerische Lösung der Anfangsrandwertprobleme der Festkörpermechanik ist, angegeben. Anschließend werden einige der später angewandten Regeln und Konzepte zur Formulierung von Konstitutivgleichungen eingeführt, wie zum Beispiel das von HAUPT und TSAKMAKIS entwickelte Konzept der dualen Variablen, welches auf die multiplikative Zerlegung des Deformationsgradienten angewendet wird.

Auf der Basis dieser fundamentalen Konzepte wird im dritten Kapitel die Entwicklung des Konstitutivmodells beschrieben. Hierbei steht zunächst die neu entwickelte Fließfläche als zentrales Element des entwickelten Elastoplastizitätsmodells im Vordergrund. Sie kann als glatte Verbindung eines in der Literatur vorgeschlagenen Ellipsoids sowie einer ebenfalls etablierten exponentialen Versagenslinie aufgefasst werden. Die beiden Teile werden mit Hilfe einer logarithmischen Interpolation zu einer einzigen Fließfläche verschmolzen. Weiterhin wird für den entwickelten Satz an Konstitutivgleichungen, welche ein Modell der finiten druckabhängigen Elastoplastizität darstellen, explizit gezeigt, dass sie in Einklang mit der Clausius-Duhem Ungleichung stehen und in diesem Sinne thermodynamisch konsistent sind. Die nachfolgend beschriebene Verallgemeinerung des Materialmodells auf ein Modell der Viskoplastizität im Sinne einer Perzyna-Typ Verallgemeinerung wird vorrangig betrieben, um die Auswirkungen dieses Schrittes auf die numerische Lösbarkeit zu studieren. In der Tat werden positive Effekte bei der Stabilität der durchgeführten Testrechnungen durch die eingeführte Viskosität erzielt.

Das vierte Kapitel behandelt die Identifikation der in den Konstitutivgleichungen auftretenden Materialparameter für ein Kupferpulver. Zu diesem Zweck werden zunächst die an der Universität in Beer Sheva (Israel) durchgeführten Experimente und deren Aufbau beschrieben. Anschließend erfolgt die Auswertung der Daten und die Identifikation der Materialparameter.

Das fünfte Kapitel stellt die numerische Behandlung des Kompaktierens von Metallpulver im Rahmen impliziter finiter Elemente Formulierungen dar. Die hierfür benötigten mathematischen Algorithmen werden im ersten Teil des fünften Kapitels erörtert. Zunächst werden diagonal implizite Runge-Kutta Verfahren zur Lösung von Algebro-Differentialgleichungssystemen erläutert und anschließend wird das Multilevel-Newton Verfahren (MLNA) zur Lösung des in jeder Stufe der DIRK-Verfahren auftretenden nichtlinearen Gleichungssystems vorgestellt. Dies stellt eine moderne Betrachtung impliziter Finite-Elemente Verfahren auf der Basis von Materialmodellen vom Evolutionsgleichungstyp dar. Diese Vorgehensweise offeriert zudem die Möglichkeit einer fehlerkontrollierten Zeitintegration der gesamten Problemstellung. Innerhalb des Multilevel-Newton Verfahrens ist die Lösung eines nichtlinearen Gleichungssystems auf Gauss-Punkt Ebene erforderlich, welches üblicherweise mit dem klassischen Newton-Verfahren gelöst wird. Da jedoch dies aufgrund der extremen Nichtlinearitäten des zugrunde liegenden Materialmodells zu einer nicht zufriedenstellenden schlechten Konvergenz führt, werden Globalisierungsstrategien für das Newton-Verfahren auf Gauss-Punkt Ebene eingeführt. Der zweite Teil des fünften Kapitels zeigt, wie die im ersten Teil besprochenen Methoden bei der numerischen Lösung des zu lösenden ARWP eingesetzt werden. Nach der Raumdiskretisierung wird das sich ergebende Algebro-Differentialgleichungssystem mit geeigneten DIRK Verfahren integriert, was in jeder Stufe des DIRK Verfahrens die Lösung eines nichtlinearen Gleichungssystems notwendig macht. Hierbei kommt das genannte Multilevel-Newton Verfahren zum Einsatz, welches die Berechnung der in der Literatur bekannten konsistenten Tangente beinhaltet. Diese kann sowohl numerisch als auch analytisch berechnet werden. In dieser Arbeit werden für das vorgestellte Materialmodell die aufwendigen analytischen Ausdrücke (Ableitungen) hergeleitet und im Anhang zusammengestellt.

Im sechsten Kapitel wird die Anwendbarkeit des entwickelten konstitutiven Modells sowie der dargestellten Verfahren anhand einiger Finite-Elemente Berechnungen für einfache Geometrien dargestellt. Die Berechnungen sind mit Hilfe des FE-Programms TASA-FEM durchgeführt worden, wobei die Konstitutivgleichungen in entsprechende Materialroutinen implementiert sind.

Die im Rahmen der Arbeit gewonnen Erkenntnisse werden im siebten Kapitel zusammengetragen. Hierzu zählt ein Vergleich der Spannungsalgorithmen mit den stabilisierten Newton Verfahren. Hier erweist sich ein Newton-Verfahren mit ”line search”-Algorithmus unter Beachtung von Nebenbedingungen als am robustesten. Beim Vergleich der getesteten DIRK Verfahren mit dem klassischen Backward-Euler Verfahren schneidet das Verfahren zweiter Ordnung allgemein am besten ab, da Verfahren höherer Zeitintegrationsgenauigkeit aufgrund eines Ordnungsreduktionsphänomens keine Vorteile liefern. Hiermit wurden erstmals Zeitintegrationsverfahren höherer Ordnung zur Lösung der auftretenden Algebro-Differentialgleichungssysteme auf ein Modell der finiten kompressiblen Elastoplastizität sowie Viskoplastizität angewendet.

Contents

Chapter 1

Introduction

1.1 Scope of the thesis

The production of mechanical parts through powder metallurgical routes is rapidly increasing. Numerical simulation of the necessary pressing process during the design phase of new parts can reduce or even replace costly trial and error experiments to find suitable pressing conditions, see for example KRAFT [86], KRAFT AND YAZICI [87]. The quality of the numerical simulations strongly depends on the applied constitutive model, which has to be able to capture the mechanical behavior of the metal powder during the pressing process. Of equal importance to the applicability of numerical simulations in the field of powder metallurgy is the robustness and efficiency of the implementation of the constitutive model. For the simulation of realistic compaction processes, defining initial boundary value problems (IBVP), the efficiency of the numerical treatment of these IBVP is of equal importance.

In order to enhance the current treatment of metal powder compaction processes a collaboration between five groups of scientists has been funded by the GIF[1] under the project title "p-FEM for a class of pressure dependent plasticity models with application to cold isostatic pressing (CIP)". Besides the group in Kassel led by Dr. Hartmann, there are two groups at the Ben Gurion University of the Negev in Beer Sheva (Israel) and two groups in Munich. The group in Beer Sheva led by Prof. Frage provides the experimental capabilities to facilitate the development of a constitutive model and the necessary parameter identification. The second group in Beer Sheva led by Prof. Yosibash offers expertise in the field of numerics and explicit finite element simulations. The focus of the group of Prof. Rank at the TU München lies on the application of the p-version finite element method, which is supposed to be beneficial for the numerical treatment of the highly non-linear powder compaction processes. The concern of Prof. Holzers group at the Universität der Bundeswehr München is the shape and process conditions optimization. Further details about the GIF project can be found in the final scientific report FRAGE ET AL. [49] and the publications originating from the project, see Appendix E for a list of references.

As a central part of the GIF project this thesis, stemming from the work done in Kassel, treats the development of a suitable constitutive model describing metal powder compaction processes. This is done within the framework of continuum mechanics and implicit finite element methods. With respect to the constitutive modeling a certain emphasis is placed on the development of a new flexible yield function and a thermo-mechanically consistent formulation of the material model. In order to determine the material parameters contained in the constitutive equations several experiments are analyzed which have been set up and conducted by the part-

[1] German Israeli Foundation for scientific research and development

ner group of Prof. Frage in close cooperation. The second major task examined in this thesis is the efficient numerical treatment of powder compaction processes. To this end the constitutive model (stress algorithm) is implemented in the in-house implicit finite elements code TASA-FEM, HARTMANN [62]. The system of equations, originating from the space discretization of the principle of virtual displacements, can be interpreted as a coupled system of differential algebraic equations (DAE) in the case of the developed constitutive model. This interpretation gives rise to the application of, for example, diagonally implicit Runge-Kutta methods (DIRK) methods. Furthermore, TASA-FEM features the application of efficient time adaptive integration by embedded error estimation also based on DIRK methods. The application of these higher order time integration methods is compared to the usual Backward-Euler method in scientific examples of compaction processes. The systems of nonlinear equations are solved with the Multilevel-Newton algorithm at each stage of the applied DIRK methods, see HARTMANN [61], HARTMANN [60] for a clarification of the notion Multilevel-Newton method. At each spatial integration (Gauss) point, i.e. on the local level of the Multilevel-Newton algorithm, a system of nonlinear equations, containing only the internal variables of the same integration point as unknowns, has to be solved. Often this local nonlinear system can be efficiently solved with the Newton algorithm. Due to convergence problems of the classical Newton method several globalization strategies for the Newton algorithm are studied in order to obtain an efficient and robust stress algorithm. Although the application of numerical derivatives on the local as well as on the global level (consistent tangent operator) of the Multilevel-Newton method is possible, analytical tangents have been derived reducing the computational cost significantly.

1.2 Review of related research

The constitutive modeling and numerical treatment of powder metallurgical production processes is much too vast a field to be treated exhaustively within a single thesis. The main focus of the GIF project is placed on the cold isostatic pressing but due to the major importance of (uniaxial) die compaction at ambient temperature and in view of the necessary material parameter identification this process is considered as well. Other powder metallurgical production routes like powder rolling, metal injection molding or hot isostatic pressing are not discussed. Detailed information on powder metallurgy can, for example, be found in ASM [13]. Furthermore, the attention of this work is restricted to the pressing process. The necessary sintering process, which is subsequently applied, has been treated by, for example, LIPPMANN AND IANKOV [98], SVOBODA ET AL. [130]. An overview over the usual modeling of the compaction and sintering process can be found in COCKS [31]. For warm compaction or hot isostatic pressing the constitutive models have to include temperature, this has been addressed among others by LARSSON ET AL. [92], MÄHLER ET AL. [101], WIKMAN ET AL. [140], SVOBODA ET AL. [129] and ARIFFIN ET AL. [8]. For the processes at ambient temperature like cold isostatic pressing and die compaction, the influence of temperature can be ignored. The development of constitutive models for metal powder compaction started about thirty years ago, extensions of the famous von Mises yield criterion have been suggested by GREEN [52], KUHN AND DOWNEY [89], SHIMA AND OYANE [122] to include a dependence of the yield strength on the hydrostatic component of stress. These models have initially been developed to describe the constitutive behavior of already sintered parts with different relative densities. Based on the works of ARZT [11] and HELLE ET AL. [72] Fleck and coworkers proposed a micro-mechanically motivated constitutive model to describe the compaction behavior of metal powders, FLECK ET AL. [48]. This model has been extended afterwards among others by FLECK [47] and OGBONNA AND FLECK [104].

Furthermore, it has been studied experimentally, for example by AKISANYA ET AL. [4]. The micro-mechanically motivated models assume an assembly of spherical powder particles which deform plastically. From this assumption macroscopic yield functions are derived. In STORAKERS ET AL. [127] further extensions to include the effect of two different populations of spheres with different properties are discussed and the spheres are assumed to behave viscoplastic. Since the micro-mechanically motivated model proposed by FLECK ET AL. [48] can be considered to be valid only at low relative densities, it has been combined with the famous Gurson model for voided metals, see GURSON [55], for simulating compaction processes up to high relative densities, see for details REDANZ [114], REDANZ [115], REDANZ [116] and REDANZ AND FLECK [117]. Beside the micro-mechanically motivated models a large number of authors have proposed and applied phenomenological plasticity models to describe the compaction behavior of metal powders. Constitutive models originating from the field of geomechanics have been adopted, taking into account the initially granular behavior of the metal powder and leading to so-called cap models. These models combine a Drucker-Prager failure cone, or exponential failure line (DIMAGGIO AND SANDLER [39]) or a Mohr-Coulomb surface with an usually ellipsoidal cap, which closes the surface in the direction of hydrostatic pressure, see for example CORAPCIOGLU AND UZ [32], WATSON AND WERT [139] or COUBE [33]. The experimental works of ABOU-CHEDID [3] and CARNAVAS [23] support the use of two part yield surfaces, which incorporate an asymmetry of the yield envelope with respect to the first invariant of the stress tensor. Yield function free, endo-chronic plasticity models, have been proposed and applied by BAKHSHIANI ET AL. [15], KHOEI ET AL. [81] and KHOEI ET AL. [78]. In addition to the differences in the constitutive approaches found in the literature on metal powder compaction, there are also different approaches and focuses with respect to the numerical treatment. While some authors propose and apply explicit time integration schemes, e.g. HÄGGBLAD AND ODENBURG [56], XIN ET AL. [141] or COUBE AND RIEDEL [34], others rely on implicit time integration, e.g. MÄHLER ET AL. [101], PEREZ-FOGUET ET AL. [109]. In order to handle the large deformations undergone by the powder, KHOEI AND LEWIS [80] discuss the application of re-meshing to avoid distorted meshes. Huerta and coworkers utilize an Arbitrary Lagrangian Eulerian (ALE) formulation to cope with the large deformations in powder forming processes, see HUERTA ET AL. [74], PEREZ-FOGUET AND HUERTA [108], RODRIGUEZ-FERRAN ET AL. [118] or PEREZ-FOGUET ET AL. [110] for details.

In this thesis a new yield function is proposed, which can be conceived as a smooth combination of the shifted ellipsoid proposed by ABOU-CHEDID [3] and the failure line introduced by DIMAGGIO AND SANDLER [39]. They are merged into a single surface yield function using a logarithmic interpolation previously applied in different contexts by KREISSELMEIER AND STEINHAUSER [88] and ARNOLD AND FRISCHMUTH [10]. For the developed constitutive model falling into the class of elastoplasticity models it is explicitly demonstrated that the proposed (evolution) equations fulfill the second law of thermodynamics in the form of the Clausius-Duhem inequality, i.e. the model is thermo-mechanically consistent. For the solution of the initial boundary value problem formed by the balance equations together with the constitutive equations and initial and boundary conditions an implicit finite elements approach is chosen. The system of equations resulting from the space discretization is identified as a coupled system of differential algebraic equations (DAE). For the time integration diagonally implicit Runge-Kutta methods are applied. The system of non-linear equations, occurring in each stage of the DIRK method is solved using a Multilevel-Newton algorithm, see HARTMANN [61], HARTMANN [60]. For the treatment of the non-linear system of equations on the local level enhanced versions of the Newton algorithm are applied since the classical Newton method frequently leads to convergence

problems. Such convergence problems have been reported for a similar constitutive model in ARMERO AND PEREZ-FOGUET [9] and PEREZ-FOGUET AND ARMERO [107] together with strategies to improve the convergence behavior.

1.3 Structure of the thesis

Chapter 2 establishes the necessary preliminaries for the continuum mechanical description of metal powder compaction processes. A kinematic description capable of handling the large deformations, which the powder material undergoes during compaction, is introduced. After that the universal balance relations are recapped. Out of these the principle of virtual displacements can be derived, which is one starting point for the numerical calculation of initial boundary value problems in solid mechanics. A few of the "rules" and concepts for the proper formulation of a constitutive model are stated in the third section of Chapter 2. Among these concepts we consider the concept of dual variables, which is due to HAUPT AND TSAKMAKIS [69] as well as the multiplicative decomposition of the deformation gradient, going back to LEE [93] and LEE AND LIU [94]. On the basis of these fundamental ideas a constitutive model to describe the compaction behavior of metal powder is developed in Chapter 3. The attention is focused on the yield function, which is a major part of the constitutive model for the pressure dependent material behavior. After a review of pressure dependent yield functions the formulation of a suitable new yield function on the basis of earlier proposals from the literature is discussed. Afterwards, the entire rate-independent (elastoplastic) version of the model is summarized and its thermo-mechanical consistency is established. The expansion of the model to viscoplasticity is considered mainly to study the influence of the introduced viscosity on the numerical treatment. The numerical treatment is supposed to benefit from this, since the viscoplastic model leads to smoother equations. Chapter 4 deals with the identification of the material parameters of the constitutive model. The experimental setup and the obtained experimental data as well as its treatment are discussed. It is shown that a reasonable set of material parameters can be obtained from the uniaxial die compaction experiments on cylindrical specimens with intermediate unloading and reloading cycles. The subsequent fifth Chapter deals with the numerical treatment of the metal powder compaction within the framework of implicit finite element formulations. To this end, some of the applied mathematical algorithms are introduced in the first section starting with diagonally implicit Runge-Kutta (DIRK) methods applied to solve systems of differential algebraic equations (DAE). A short discussion of efficient embedded time adaptive algorithms is included. The second topic of Chapter 5 is the introduction of the Multilevel-Newton algorithm utilized to solve a coupled system of nonlinear equations. Since a two level Newton algorithm is applied afterwards, the discussion is restricted to two levels. Usually a simple Newton algorithm is applied to solve the system of nonlinear equations on the local level of the Multilevel-Newton algorithm. Since the classical Newton algorithm leads to convergence problems, a number of generalized, i.e. globalized Newton-like iteration algorithms are discussed as well at the end of the first section of Chapter 5. The second section of Chapter 5 discusses the numerical solution of the initial boundary value problem formed by the constitutive equations together with the balance relations and the boundary conditions. The previously introduced mathematical concepts are applied. After the space discretization the resulting DAE is solved with suitable DIRK methods and the resulting nonlinear system of equations is computed with the help of the Multilevel-Newton algorithm. The Multilevel-Newton algorithm demands the computation of the consistent tangent matrix which can be done either numerically or analytically. The analytical expressions for the proposed constitutive model can be found in the Appendix D. Before the thesis closes with a

summary in Chapter 7, addressing also major open questions and possible future directions for further developments and improvements, some numerical examples with rather simple geometries are presented in Chapter 6. The numerical examples in Chapter 6 have been computed using the in house finite element code TASA-FEM featuring the application of several DIRK methods as well as time adaptive computation.

Chapter 2

Continuum mechanical foundations

The scope of continuum mechanics is the mathematical description of the motion and deformation of so called *material bodies* under thermomechanical loads. A material body is a continuous assembly of *material points*. All physical quantities are represented by continuous fields which can be related to either the material points (material representation) or the place in space (spatial representation). These fields can be scalar fields like the spatial density distribution $\rho(\boldsymbol{x}, t)$ or tensor fields of any order like the spatial velocity field $\boldsymbol{v}(\boldsymbol{x}, t)$ (first order) or the field of Cauchy stresses $\mathbf{T}(\boldsymbol{x}, t)$ (second order), where $\boldsymbol{x}$ denotes the place of a material point at time t.

The theory of continuum mechanics rests upon three cornerstones. The first one is the *kinematical* description of the motion and deformation a material body can undergo. The second one is the formulation of kinetical laws in form of *balance relations*. These first two fields state fundamental assumptions on the structure of space and time and the principles of mechanics. They represent a generalization of a great variety of observations and are considered to be valid for all materials. The third field of continuum mechanics, the *theory of materials*, deals with the modeling of individual material behavior by the introduction of so called constitutive equations. These constitutive equations are not valid in general, they are merely meant to represent the specific behavior of a certain material under consideration. Material theory gives certain guidelines for the formulation of constitutive models in order to guarantee that the constitutive equations do not contradict any fundamental physical principles. According to HAUPT [67] the material behavior of solids can be subdivided into four groups namely elasticity, viscoelasticity, plasticity and viscoplasticity. Here, the considered continua are restricted to so called simple materials of first degree, see ALTENBACH AND ALTENBACH [6, P.154], i.e. the constitutive equations relate only quantities which belong to the same material point and its infinitesimal neighborhood.

2.1 Kinematics

The purpose of kinematics is the mathematical description of the motion of material points, i.e. the deformation of material bodies. To this end the term *motion* and the concept of *configuration* will be specified. The deformation will be characterized locally by the *deformation gradient* from which several strain tensors can be derived. The time rates of deformations can be measured by the *spatial velocity gradient*, which will in turn be used to define appropriate strain rates.

2.1.1 Motion and configuration

In continuum mechanics the notion *material body* $\mathcal{B}$ is introduced, see HAUPT [67]. A material body $\mathcal{B}$ is a set of material points $\mathcal{P}$ for which a set $\mathcal{K}$ of one-to-one mappings

$$\begin{aligned} \chi : \mathcal{B} &\longrightarrow \chi[\mathcal{B}] \subset \mathbb{R}^3 \\ \mathcal{P} &\longmapsto \chi(\mathcal{P}) = (x^1, x^2, x^3) \end{aligned} \tag{2.1}$$

exists. Due to the bijectivity of χ, $\mathcal{P} = \chi^{-1}(x^1, x^2, x^3)$ holds. The mapping χ is called a *configuration* (of the material body). Furthermore, it is demanded that any composition of two configurations $\chi_1, \chi_2 \in \mathcal{K}$ given by

$$\chi_2 \circ \chi_1^{-1} : \chi_1[\mathcal{B}] \longrightarrow \chi_2[\mathcal{B}] \tag{2.2}$$

is continuously differentiable.

The motion of the material body is defined as a sequence of configurations parameterized by the time t

$$\begin{aligned} \chi_t : \mathcal{B} &\longrightarrow \chi_t[\mathcal{B}] \subset \mathbb{R}^3 \\ \mathcal{P} &\longmapsto \chi_t(\mathcal{P}) = (x^1(t), x^2(t), x^3(t)). \end{aligned} \tag{2.3}$$

The configuration at time t is named *current configuration*. In order to identify each material point $\mathcal{P}$, a *reference configuration* $\mathcal{R} \in \mathcal{K}$ is introduced

$$\begin{aligned} \mathcal{R} : \mathcal{B} &\longrightarrow \mathcal{R}[\mathcal{B}] \subset \mathbb{R}^3 \\ \mathcal{P} &\longmapsto \mathcal{R}(\mathcal{P}) = (X^1, X^2, X^3). \end{aligned} \tag{2.4}$$

Any configuration of the set $\mathcal{K}$ can be chosen as reference configuration. Often the *initial configuration* χ_{t_0} is chosen as reference configuration

$$\begin{aligned} \mathcal{R} \equiv \chi_{t_0} : \mathcal{B} &\longrightarrow \chi_{t_0}[\mathcal{B}] \subset \mathbb{R}^3 \\ \mathcal{P} &\longmapsto \chi_{t_0}(\mathcal{P}) = (X^1, X^2, X^3). \end{aligned} \tag{2.5}$$

The motion of the material body is accordingly characterized by the mapping

$$\boldsymbol{x} = \boldsymbol{\Phi}_{t_0}(\boldsymbol{X}, t) \quad \text{with} \quad \boldsymbol{\Phi}_{t_0} = \chi_t \circ \chi_{t_0}^{-1}. \tag{2.6}$$

In the reference configuration as well as in the current configuration a frame of reference (coordinate system) is introduced by the three basis vectors $\boldsymbol{G}_1, \boldsymbol{G}_2, \boldsymbol{G}_3$ for the reference configuration and the three basis vectors $\boldsymbol{g}_1, \boldsymbol{g}_2, \boldsymbol{g}_3$ for the current configuration. The three numbers (X^1, X^2, X^3) are called the material coordinates and the three numbers (x^1, x^2, x^3) are the spatial coordinates. By using the same frame of reference in the initial and current configuration the motion can be described alternatively by the displacement vector

$$\boldsymbol{u}(\boldsymbol{X}, t) = \boldsymbol{x} - \boldsymbol{X} = \boldsymbol{\Phi}_{t_0}(\boldsymbol{X}, t) - \boldsymbol{X}. \tag{2.7}$$

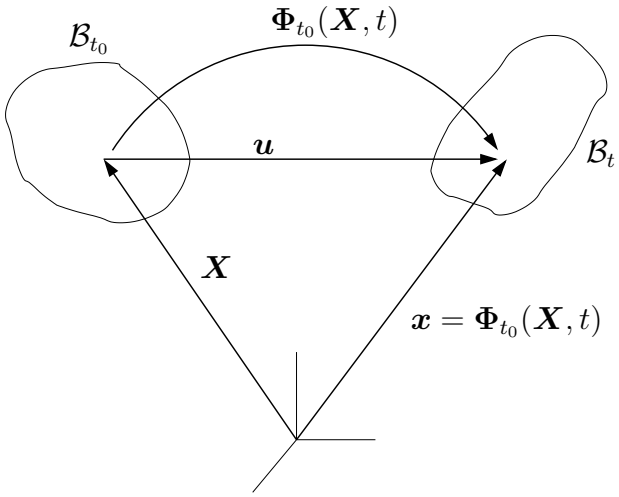

Figure 2.1: Configurations

2.1.2 Deformation gradient

According to Eq. (2.6) the motion of a material body is defined by the family of vector functions $\boldsymbol{\Phi}_{t_0}(\boldsymbol{X},t)$ with the family parameter t representing the time. The difference in motion of neighboring material points is measured by the (material) *deformation gradient*

$$\mathbf{F}=\operatorname{Grad}\boldsymbol{\Phi}_{t_0}(\boldsymbol{X},t)=\frac{\partial\boldsymbol{x}}{\partial\boldsymbol{X}}=\frac{\partial x^i}{\partial X^j}\boldsymbol{g}_i\otimes\boldsymbol{G}^j=F^i_{\ j}\boldsymbol{g}_i\otimes\boldsymbol{G}^j. \tag{2.8}$$

The coefficients $F^i_{\ j}$ of $\mathbf{F}$ are the coefficients of the Jacobi matrix of the coordinate transformation induced by the vector mapping $\boldsymbol{x}=\boldsymbol{\Phi}_{t_0}(\boldsymbol{X},t)$. Since one of the basis vectors of $\mathbf{F}$ belongs to the reference configuration $(\boldsymbol{G}^j)$ and one belongs to the current configuration $(\boldsymbol{g}_i)$ the deformation gradient is sometimes called a two-field tensor. However, for the description in one Cartesian coordinate system, where the co- and contravariant base systems coincide, one may write

$$\mathbf{F}=\frac{\partial x^i}{\partial X^j}\boldsymbol{e}_i\otimes\boldsymbol{e}_j=F^{ij}\boldsymbol{e}_i\otimes\boldsymbol{e}_j. \tag{2.9}$$

Far more important is the geometrical meaning of the deformation gradient $\mathbf{F}$. The deformation gradient maps material line elements $\boldsymbol{dX}$ (tangent vector of a material line in the reference configuration) into material line elements $\boldsymbol{dx}$ (tangent vector of a material line in the current configuration). In order to demonstrate this, a material line in the reference configuration shall be defined by

$$\boldsymbol{X}=\boldsymbol{C}(\alpha), \tag{2.10}$$

where α is the curve parameter. The same material line in the current configuration is than given by

$$\boldsymbol{x}=\boldsymbol{c}(\alpha)=\boldsymbol{\Phi}_{t_0}(\boldsymbol{C}(\alpha),t). \tag{2.11}$$

The tangent vectors of the material line are

$$\boldsymbol{dX}=\boldsymbol{C}'(\alpha)d\alpha\quad\text{and}\quad\boldsymbol{dx}=\boldsymbol{c}'(\alpha)d\alpha \tag{2.12}$$

in the reference and current configuration, respectively. Insertion of (2.11) into $(2.12)_2$ and application of the chain rule yields

$$\boldsymbol{dx}=\boldsymbol{c}'(\alpha)d\alpha=\frac{\mathrm{d}}{\mathrm{d}\alpha}\boldsymbol{\Phi}_{t_0}(\boldsymbol{C}(\alpha),t)d\alpha=\underbrace{\left(\operatorname{Grad}\ \boldsymbol{\Phi}_{t_0}(\boldsymbol{X},t)|_{\boldsymbol{X}=\boldsymbol{C}(\alpha)}\right)}_{\mathbf{F}}\underbrace{\boldsymbol{C}'(\alpha)d\alpha}_{\boldsymbol{dX}} \tag{2.13}$$

The essential property of the deformation gradient

$$\boldsymbol{dx} = \mathbf{F}\boldsymbol{dX} \tag{2.14}$$

to map tangents of material lines from the reference to the current configuration contains all the information about the local deformation, which will subsequently be used to introduce appropriate strain tensors. From the property (2.14) of the deformation gradient $\mathbf{F}$ the equations

$$\boldsymbol{da} = (\det \mathbf{F})\mathbf{F}^{-T}\boldsymbol{dA} \tag{2.15}$$

$$dv = \det \mathbf{F}\, dV \tag{2.16}$$

can be derived, which describe the deformation of a material surface (volume) element $\boldsymbol{dA}$ (dV) from the reference into the current configuration. The deformation gradient $\mathbf{F}$ is non-symmetric in general and due to its invertibility and the continuity of the motion $\det \mathbf{F} > 0$ holds. Although $\mathbf{F}$ contains all the necessary information about the deformation, it is usually not used directly in constitutive equations, since $\mathbf{F}$ itself is not independent of rigid body motions. To be more precise, $\mathbf{F}$ is independent of rigid body translations but not independent of rigid body rotations.

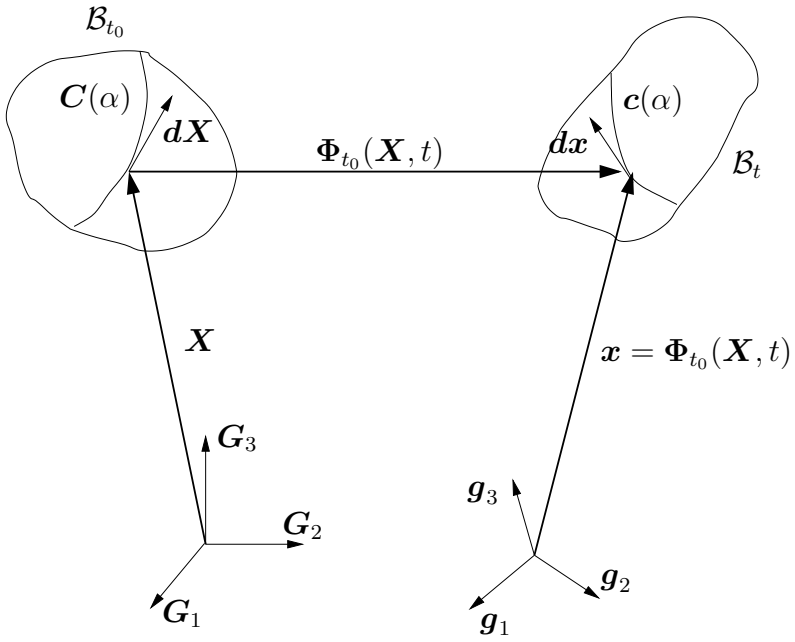

Figure 2.2: Transformation of a material line

Polar decomposition

As a non-singular $(\det \mathbf{F} \neq 0)$ tensor of second order, the deformation gradient $\mathbf{F}$ can be decomposed multiplicatively into an orthogonal tensor $\mathbf{R}$ ($\mathbf{R}^T = \mathbf{R}^{-1},\ \det \mathbf{R} = +1$) and a symmetric, positive definite tensor $\mathbf{U}$ (or $\mathbf{V}$),

$$\mathbf{F} = \mathbf{R}\mathbf{U} = \mathbf{V}\mathbf{R}. \tag{2.17}$$

This decomposition is denoted as the polar decomposition of $\mathbf{F}$. The orthogonal tensor $\mathbf{R}$ describes a pure rotation of a material line element $\boldsymbol{dX}$, whereas $\mathbf{U}$ (or $\mathbf{V}$) describes a pure elongation of the line element $\boldsymbol{dX}$ (or $\mathbf{R}\boldsymbol{dX}$). The tensors $\mathbf{U}$, called right stretch tensor, and $\mathbf{V}$, denoted as left stretch tensor, are related via the similarity relation

$$\mathbf{V} = \mathbf{R}\mathbf{U}\mathbf{R}^{-1}, \tag{2.18}$$

which means that $\mathbf{V}$ and $\mathbf{U}$ have the same eigenvalues. The polar decomposition is unique. With $\mathbf{U}$ and $\mathbf{V}$ two tensors have been found which characterize the deformation and do not dependent on rigid body motions. In order to avoid the non-rational calculation of roots, which is necessary to calculate $\mathbf{U}$ and $\mathbf{V}$ from $\mathbf{F}$, the right Cauchy Green tensor

$$\mathbf{C} = \mathbf{F}^T\mathbf{F} = \mathbf{U}^2 \tag{2.19}$$

and the left Cauchy Green tensor

$$\mathbf{b} = \mathbf{F}\mathbf{F}^T = \mathbf{V}^2 \tag{2.20}$$

are introduced. The tensor $\mathbf{C}$ operates on the reference configuration[1] and the tensor $\mathbf{b}$ operates on the current configuration.[2] With the help of the introduced kinematical quantities a number of strain tensors can be defined, which vanish in the case of pure rigid body motions and characterize the state of strain.

2.1.3 Strain tensors

The Green strain tensor

$$\mathbf{E} = \frac{1}{2}\left(\mathbf{F}^T\mathbf{F} - \mathbf{1}\right) = \frac{1}{2}\left(\mathbf{C} - \mathbf{1}\right) = \frac{1}{2}\left(\mathbf{U}^2 - \mathbf{1}\right) \tag{2.21}$$

operating in the reference configuration and the Almansi strain tensor

$$\mathbf{A} = \frac{1}{2}\left(\mathbf{1} - \mathbf{F}^{-1}\mathbf{F}^{-T}\right) = \frac{1}{2}\left(\mathbf{1} - \mathbf{b}^{-1}\right) = \frac{1}{2}\left(\mathbf{1} - \mathbf{V}^{-2}\right) \tag{2.22}$$

operating in the current configuration are connected by the covariant *push forward* $\mathbf{F}^{-T}(\cdot)\mathbf{F}^{-1}$

$$\mathbf{A} = \mathbf{F}^{-T}\mathbf{E}\mathbf{F}^{-1} \tag{2.23}$$

and *pull back* $\mathbf{F}^T(\cdot)\mathbf{F}$

$$\mathbf{E} = \mathbf{F}^T\mathbf{A}\mathbf{F} \tag{2.24}$$

operations.[3] The tensors $\mathbf{E}$ and $\mathbf{A}$ are embedded in a general class of strain tensors defined with the help of the stretch tensors $\mathbf{U}$ and $\mathbf{V}$, see for example HAUPT AND TSAKMAKIS [70],

$$\mathbf{E}^{(m)} = \begin{cases} \frac{1}{m}\left(\mathbf{U}^m - \mathbf{1}\right) & | \quad m \neq 0 \\ \ln \mathbf{U} & | \quad m = 0 \end{cases} \tag{2.25}$$

$$\mathbf{A}^{(m)} = \begin{cases} \frac{1}{m}\left(\mathbf{V}^m - \mathbf{1}\right) & | \quad m \neq 0 \\ \ln \mathbf{V} & | \quad m = 0 \end{cases} . \tag{2.26}$$

For $m = 2$ the Green strain tensor is retrieved from (2.25) and for $m = -2$ the Almansi tensor is obtained from Eq. (2.26). The tensor $\mathbf{E}^{(0)} = \ln \mathbf{U}$ is known as the Hencky strain tensor (logarithmic strain tensor). Alternative strain tensors, for example, the Piola tensor

$$\mathbf{e} = \frac{1}{2}\left(\mathbf{C}^{-1} - \mathbf{1}\right) \tag{2.27}$$

[1] Actually $\mathbf{C}$ operates on the tangent space of the reference configuration.

[2] Actually $\mathbf{b}$ operates on the tangent space of the current configuration.

[3] The tensors $\mathbf{E}$ and $\mathbf{A}$ are termed covariant because they operate on the tangent spaces of the reference and the current configuration, see HAUPT [67]. Alternative strain tensors operating on the cotangent spaces can be introduced as well, for their transformation contravariant push forward and pull back operations must be used.

and the Finger tensor

$$\mathbf{a} = \frac{1}{2}\left(\mathbf{1} - \mathbf{b}\right), \tag{2.28}$$

operating in the cotangent spaces of the reference and current configurations respectively, can be defined. They are connected through contravariant push forward $\mathbf{F}(\cdot)\mathbf{F}^T$ and pull back $\mathbf{F}^{-1}(\cdot)\mathbf{F}^{-T}$ operations, details can be found in HAUPT [67].

2.1.4 Deformation velocities

The fundamental tensor describing the rate of change of material line, area and volume elements is the (spatial) velocity gradient

$$\mathbf{L} = \operatorname{grad} \boldsymbol{v}(\boldsymbol{x}, t) = \dot{\mathbf{F}}\mathbf{F}^{-1} \tag{2.29}$$

and is calculated from the velocity field $\boldsymbol{v}(\boldsymbol{x}, t)$. The dot denotes the material time derivative, i.e. the total derivative of a function $f(\boldsymbol{X}, t)$ with respect to time t. Material line, area and volume elements change in time according to

$$\dot{\overline{d\boldsymbol{x}}} = \mathbf{L}d\boldsymbol{x}, \tag{2.30}$$

$$\dot{\overline{d\boldsymbol{a}}} = ((\operatorname{tr}\mathbf{L})\mathbf{1} - \mathbf{L}^T)d\boldsymbol{a}, \tag{2.31}$$

$$\dot{\overline{dv}} = (\operatorname{tr}\mathbf{L})dv, \tag{2.32}$$

where tr denotes the trace operator $\operatorname{tr}\mathbf{A} = A_{ii}$. The spatial velocity gradient decomposes additively in a symmetric part $\mathbf{D}$ and a skew symmetric part $\mathbf{W}$,

$$\mathbf{L} = \mathbf{D} + \mathbf{W} \tag{2.33}$$

$$\text{with} \quad \mathbf{D} = \frac{1}{2}\left(\mathbf{L} + \mathbf{L}^T\right) \tag{2.34}$$

$$\text{and} \quad \mathbf{W} = \frac{1}{2}\left(\mathbf{L} - \mathbf{L}^T\right). \tag{2.35}$$

The symmetric part $\mathbf{D}$ is denoted as strain rate tensor and the skew symmetric part is known as spin or vorticity tensor.

2.2 Balance relations and stress tensors

The balance relations of continuum (thermo)mechanics are formulations of fundamental physical principles, in particular, the conservation of momentum, angular momentum and energy. Furthermore, the conservation of mass is valid for the processes considered in continuum mechanics and a balance relation for the entropy will be given. The balance of entropy has to be accompanied by an appropriate formulation of the second law of thermodynamics, which states that the entropy of a closed system never decreases. The balance relations can be formulated either in the current (spatial) or in the reference (material) configuration. They have the general form

$$\frac{\mathrm{d}}{\mathrm{d}t}\int_v \rho(\boldsymbol{x},t)\boldsymbol{\Psi}dv = \int_a \boldsymbol{\Phi}(\boldsymbol{x},t)\boldsymbol{n}da + \int_v \rho(\boldsymbol{x},t)(\varphi(\boldsymbol{x},t)+p(\boldsymbol{x},t))dv \tag{2.36}$$

$$\frac{\mathrm{d}}{\mathrm{d}t}\int_V \rho(\boldsymbol{X},t)\boldsymbol{\Psi}_R dV = \int_A \boldsymbol{\Phi}_R(\boldsymbol{X},t)\boldsymbol{n}_R dA + \int_V \rho_R(\boldsymbol{X},t)(\varphi_R(\boldsymbol{X},t)+p_R(\boldsymbol{X},t))dV \tag{2.37}$$

where $\rho,\ \rho_R$ represent the mass density of the material body in the current and reference configuration respectively. The physical quantity, which is balanced, is represented by $\boldsymbol{\Psi}\ (\boldsymbol{\Psi}_R)$, the flux of the physical quantity through the surface of the material body is denoted as $\boldsymbol{\Phi}\ (\boldsymbol{\Phi}_R)$, whereas the volume distributed exchange of $\boldsymbol{\Psi}\ (\boldsymbol{\Psi}_R)$ with the outside world is represented by $\varphi\ (\varphi_R)$ and the production density of $\boldsymbol{\Psi}\ (\boldsymbol{\Psi}_R)$ is given by $p\ (p_R)$ in the current (reference) configuration. For the representation of conservation laws by means of a balance relation the right hand side of Eqns. (2.36) and (2.37) is zero. The physical quantity $\boldsymbol{\Psi}$ under consideration may be scalar or vector valued. If the physical quantity $\boldsymbol{\Psi}$ is a tensor field of order n, the flux accordingly is a tensor of order $(n+1)$. Under sufficient conditions regarding the continuity and differentiability of the fields one can derive local forms of the balance relations with the help of the divergence-theorem. In the following, the balance of mass, momentum, angular momentum and energy as well as entropy will be stated.

2.2.1 Balance of mass

The mass $m(\mathcal{B},t)$ of a material body $\mathcal{B}$ is a scalar quantity which measures the resistance of the material body against accelerations (inertia) as well as the strength of its gravitational interactions with other masses. Each material point $\mathcal{P}$ is attributed a mass density ρ. Accordingly, the mass of the material body is given by

$$m(t) = \int_V \rho_R(\boldsymbol{X},t)dV = \int_v \rho(\boldsymbol{x},t)dv. \tag{2.38}$$

The conservation of mass states that

$$\frac{\mathrm{d}}{\mathrm{d}t}m(t) = \frac{\mathrm{d}}{\mathrm{d}t}\int_V \rho_R(\boldsymbol{X},t)dV = \frac{\mathrm{d}}{\mathrm{d}t}\int_v \rho(\boldsymbol{x},t)dv = 0. \tag{2.39}$$

The local form in the reference configuration can be derived immediately, since the volume integral over the material body in the reference configuration is time-independent

$$\frac{\partial \rho_R(\boldsymbol{X},t)}{\partial t} = 0 \quad \Leftrightarrow \quad \rho_R(\boldsymbol{X},t) = \rho_R(\boldsymbol{X}). \tag{2.40}$$

In order to obtain the local form in the current configuration, the integral has to be transferred to the reference configuration whereupon the differentiation with respect to time can be exchanged

with the volume integral. Afterwards, the resulting expression is stated in spatial coordinates again using the relation (2.16) between the infinitesimal volume element in the current and the reference configuration

$$\begin{aligned} 0 = \frac{\mathrm{d}}{\mathrm{d}t} m(t) &= \frac{\mathrm{d}}{\mathrm{d}t} \int_v \rho(\boldsymbol{x},t) dv = \frac{\mathrm{d}}{\mathrm{d}t} \int_V \rho \det \mathbf{F} dV \\ &= \int_V \frac{\mathrm{d}}{\mathrm{d}t} (\rho \det \mathbf{F}) dV = \int_V \left(\dot{\rho} \det \mathbf{F} + \rho \det F \underbrace{\mathbf{F}^{-T} \cdot \dot{\mathbf{F}}}_{\operatorname{div} \boldsymbol{v} = \operatorname{tr} \mathbf{L}} \right) dV \\ &= \int_v (\dot{\rho} + \rho \operatorname{div} \boldsymbol{v}) \, dv. \end{aligned} \tag{2.41}$$

Alternatively, the local balance of mass can be written as

$$\dot{\rho} + \rho \operatorname{div} \boldsymbol{v} = 0 \quad \Leftrightarrow \quad \frac{\partial \rho}{\partial t} + \operatorname{div} (\rho \boldsymbol{v}) = 0. \tag{2.42}$$

And due to $\rho_R dV = \rho dv$ and Eq. (2.16) we can also state

$$\rho_R = (\det \mathbf{F}) \, \rho. \tag{2.43}$$

2.2.2 Balance of momentum

The momentum of a material body is the product of mass density and velocity integrated over the domain of the body. The derivative of the momentum with respect to time is equal to the sum of the external forces exerted on the material body

$$\frac{\mathrm{d}}{\mathrm{d}t} \int_v \rho(\boldsymbol{x},t) \boldsymbol{v}(\boldsymbol{x},t) dv = \int_a \boldsymbol{t}(\boldsymbol{x},t) da + \int_v \rho(\boldsymbol{x},t) \boldsymbol{k}(\boldsymbol{x},t) dv. \tag{2.44}$$

The right hand side of (2.44) represents the external forces acting on the material body and the left hand side is the rate of its momentum. In Eq. (2.44) $\boldsymbol{t}(\boldsymbol{x},t)$ denotes the stress vector acting on the surface of the material body. According to Cauchy's theorem the stress vector $\boldsymbol{t}(\boldsymbol{x},t)$ is related to the stress tensor $\mathbf{T}(\boldsymbol{x},t)$ (Cauchy stress tensor) via

$$\boldsymbol{t}(\boldsymbol{x},t,\boldsymbol{n}) = \mathbf{T}\boldsymbol{n}. \tag{2.45}$$

The volume distributed force density acting on the material body is $\rho(\boldsymbol{x},t)\boldsymbol{k}(\boldsymbol{x},t)$ in (2.44). Often $\rho(\boldsymbol{x},t)\boldsymbol{k}(\boldsymbol{x},t) = \rho(\boldsymbol{x},t)\boldsymbol{k}$ are gravitational forces where the acceleration is (in good approximation) constant in space and time. With the help of the divergence-theorem the surface integral can be transformed into a volume integral. With the help of the mass balance in the form $\rho dv = \rho_R dV$ the local form of the balance of momentum reads,

$$\rho(\boldsymbol{x},t) \dot{\boldsymbol{v}}(\boldsymbol{x},t) = \operatorname{div} \mathbf{T}(\boldsymbol{x},t) + \rho(\boldsymbol{x},t) \boldsymbol{k}(\boldsymbol{x},t). \tag{2.46}$$

In the reference configuration the global form of the balance of momentum reads

$$\frac{\partial}{\partial t} \int_V \rho_R(\boldsymbol{X}) \dot{\boldsymbol{\Phi}}_{t_0}(\boldsymbol{X},t) dV = \int_A \boldsymbol{t}_R(\boldsymbol{X},t) dA + \int_V \rho_R(\boldsymbol{X}) \boldsymbol{k}_R(\boldsymbol{X},t) dV \tag{2.47}$$

where the stress vector $\boldsymbol{t}_R$ has been introduced representing the force per area of the reference configuration. In analogy to (2.45) the stress vector $\boldsymbol{t}_R$ is related to the stress tensor $\mathbf{T}_R$ by

$$\boldsymbol{t}_R(\boldsymbol{X},t) = \mathbf{T}_R(\boldsymbol{X},t) \boldsymbol{n}_R, \tag{2.48}$$

which is known as the first Piola-Kirchhoff stress tensor. The local form of the balance of momentum in the reference configuration is given by

$$\rho_R(\boldsymbol{X})\ddot{\boldsymbol{\Phi}}_{t_0}(\boldsymbol{X},t) = \operatorname{Div}\mathbf{T}_R(\boldsymbol{X},t) + \rho_R(\boldsymbol{X})\boldsymbol{k}(\boldsymbol{X},t). \tag{2.49}$$

In Section 2.2.6 a summary of commonly applied stress tensors and their interconnection is compiled.

2.2.3 Balance of angular momentum

The balance of angular momentum (moment of momentum) states that the temporal change of rotational momentum with respect to any fixed point in space $\boldsymbol{c}$ is equal to the sum of external angular momentum due to forces acting on the material body. The spatial form of the balance of angular momentum is

$$\frac{\mathrm{d}}{\mathrm{d}t}\int_v((\boldsymbol{x}-\boldsymbol{c})\times\rho\boldsymbol{v})dv = \int_a((\boldsymbol{x}-\boldsymbol{c})\times\boldsymbol{t})da + \int_v((\boldsymbol{x}-\boldsymbol{c})\times\rho\boldsymbol{k})dv. \tag{2.50}$$

The local form of the balance relation (2.50) together with the balance of mass and momentum implies the symmetry of the Cauchy stress tensor

$$\mathbf{T}^T = \mathbf{T}. \tag{2.51}$$

2.2.4 Balance of energy

In order to establish the balance of energy, the notion *internal energy* of the material body is introduced

$$E = \int_v e\rho dv, \tag{2.52}$$

where e is the (mass) specific internal energy. E represents the total energy content of the material body except for the kinetical energy K given by

$$K = \int_v \frac{\rho}{2}\boldsymbol{v}^2 dv. \tag{2.53}$$

The sum of internal energy E and kinetical energy K represent the total energy content of the material body. The temporal change of this energy content is due to the power of the external forces

$$P_a = \int_a \boldsymbol{v}\cdot(\mathbf{T}\boldsymbol{n})da + \int_v \rho\boldsymbol{k}\cdot\boldsymbol{v}dv \tag{2.54}$$

acting on the material body and also due to the non-mechanical energy exchange, i.e. the heat flux Q given by

$$Q = \int_a qda + \int_v r\rho dv, \tag{2.55}$$

with q denoting the heat flux density and r representing a volume distributed heat supply (analogue to the volume distributed acceleration $\boldsymbol{k}$). The balance of energy for the material body now reads

$$\frac{\mathrm{d}}{\mathrm{d}t}(K+E) = P_a + Q. \tag{2.56}$$

With the help of $q = -\boldsymbol{q} \cdot \boldsymbol{n}$, where $\boldsymbol{q}$ is the Cauchy heat flux vector, the global form of the energy balance in spatial representation is given by

$$\int_v \overset{\cdot}{\left(\frac{1}{2}\boldsymbol{v}^2 + e\right)} \rho dv = \int_a \left((\mathbf{T}^T \boldsymbol{v}) \cdot \boldsymbol{n} - \boldsymbol{q} \cdot \boldsymbol{n}\right) da + \int_v (\boldsymbol{k} \cdot \boldsymbol{v} + r)\, \rho dv. \tag{2.57}$$

Application of the divergence-theorem to the surface integral in (2.57) and using the symmetry $\mathbf{T} = \mathbf{T}^T$ together with the product rule in the form $\operatorname{div}\left(\mathbf{T}^T \boldsymbol{v}\right) = (\operatorname{div} \mathbf{T}) \cdot \boldsymbol{v} + \mathbf{T} \cdot \operatorname{grad} v = (\operatorname{div} \mathbf{T}) \cdot \boldsymbol{v} + \mathbf{T} \cdot \mathbf{D}$ yields

$$\int_v \left[(\rho \dot{\boldsymbol{v}} - \operatorname{div} \mathbf{T} + \rho \boldsymbol{k}) \cdot \boldsymbol{v} + \rho \dot{e} + \operatorname{div} \boldsymbol{q} - \rho r - \mathbf{T} \cdot \mathbf{D}\right] dv = 0. \tag{2.58}$$

This can be simplified with the help of the balance of momentum giving the local form of the energy balance in spatial representation

$$\dot{e} = -\frac{1}{\rho} \operatorname{div} \boldsymbol{q} + r + \frac{1}{\rho} \mathbf{T} \cdot \mathbf{D}. \tag{2.59}$$

Alternatively the balance of energy can be formulated on the reference configuration and reads in local form

$$\dot{e} = -\frac{1}{\rho_R} \operatorname{Div} \boldsymbol{q}_R + r + \frac{1}{\rho_R} \tilde{\mathbf{T}} \cdot \dot{\mathbf{E}}. \tag{2.60}$$

2.2.5 Balance of entropy and dissipation inequality

In continuum mechanics the entropy content S of a material body is defined as the volume integral of the entropy density s over the realm of the material body

$$S = \int_v s \rho dv. \tag{2.61}$$

Every heat exchange of the material body with its surroundings is likewise an exchange of entropy. The total exchange of entropy H is the sum of the entropy exchange through the surface Σ of the material body and a volume distributed entropy exchange σ,

$$H = \int_a \Sigma da + \int_v \sigma \rho dv. \tag{2.62}$$

In addition to the exchange of entropy with the surroundings a volume distributed entropy production within the material body is introduced via

$$\Gamma = \int_v \gamma \rho dv. \tag{2.63}$$

The entropy flux Σ through the surface in (2.62) is $\Sigma = -\boldsymbol{\Sigma} \cdot \boldsymbol{n}$ with the entropy flux vector $\boldsymbol{\Sigma}$, given by

$$\boldsymbol{\Sigma} = \frac{\boldsymbol{q}}{T}, \tag{2.64}$$

where T denotes the absolute temperature. Accordingly the volume distributed entropy supply is

$$\sigma = \frac{r}{T}. \tag{2.65}$$

The entropy balance states that

$$\dot{S} = H + \Gamma \tag{2.66}$$

and the second law of thermodynamics demands that

$$\Gamma = \dot{S} - H \geq 0. \tag{2.67}$$

This means that the entropy production within a material body during all processes is always positive. The entropy production represents a measure for the irreversibility of the considered process. Under idealized assumptions the entropy production during a process may at most be zero, which is equivalent to the statement that the process is reversible. With the assumptions on the entropy exchange of the material body with its surroundings in Eqns. (2.64) and (2.65), Eq. (2.67) can be written in the form

$$\Gamma = \frac{\mathrm{d}}{\mathrm{d}t} \int_v s\rho dv + \int_a \frac{\boldsymbol{q} \cdot \boldsymbol{n}}{T} da - \int_v \frac{r}{T} \rho dv \geq 0 \tag{2.68}$$

which is known as the Clausius-Duhem inequality in continuum mechanics, see HAUPT [67]. The local form in spatial representation reads

$$\gamma = \dot{s} + \frac{1}{\rho T} \left(\operatorname{div} \boldsymbol{q} - \rho r \right) - \frac{1}{\rho T^2} \boldsymbol{q} \cdot \boldsymbol{g} \tag{2.69}$$

with the spatial temperature gradient $\boldsymbol{g} = \operatorname{grad} T$. Using the energy balance in local form (2.59), we can rewrite Eq. (2.69) and obtain

$$T\gamma = -\dot{e} + T\dot{s} + \frac{1}{\rho} \mathbf{T} \cdot \mathbf{D} - \frac{1}{\rho T} \boldsymbol{q} \cdot \boldsymbol{g} \geq 0. \tag{2.70}$$

The term $T\gamma$ on the left-hand side of (2.70) is called dissipation. We will use the Clausius-Duhem inequality later to define a constitutive model which is a priori thermodynamically consistent, i.e. it fulfills the second law of thermodynamics in all processes. Instead of the internal energy e, the (Helmholtz) free energy $\psi = e - sT$ will be used; introducing this into Eq. (2.70) yields

$$-\dot{\psi} - s\dot{T} + \frac{1}{\rho} \mathbf{T} \cdot \mathbf{D} - \frac{1}{\rho T} \boldsymbol{q} \cdot \boldsymbol{g} \geq 0. \tag{2.71}$$

For isothermal processes ($\dot{T} = 0$) and a uniform temperature distribution ($\boldsymbol{g} = \mathbf{0}$), to which we will restrict our considerations, Eq. (2.71) simply becomes

$$\mathbf{T} \cdot \mathbf{D} - \rho \dot{\psi} \geq 0. \tag{2.72}$$

2.2.6 Stress tensors

In (2.45) we have already introduced the Cauchy stress tensor $\mathbf{T}$ through $\boldsymbol{t}(\boldsymbol{x}, t, \boldsymbol{n}) = \mathbf{T}\boldsymbol{n}$, with $\boldsymbol{t}$ being the stress vector in the current configuration. The stress vector $\boldsymbol{t}$ is also called true stress vector. The current force $\boldsymbol{df}$, acting on a cutting plane with the surface $da (= \boldsymbol{da} \cdot \boldsymbol{n})$ and the surface normal $\boldsymbol{n}$ through the point $\boldsymbol{x}$, is divided by the surface element in the current configuration da,

$$\boldsymbol{t} = \frac{\boldsymbol{df}}{da} = \mathbf{T}\boldsymbol{n}. \tag{2.73}$$

If the actual force $\boldsymbol{df}$ is divided by the surface element in the reference configuration dA, we obtain the stress vector

$$\boldsymbol{t}_R = \frac{\boldsymbol{df}}{dA} = \mathbf{T}_R \boldsymbol{n}_R, \tag{2.74}$$

which has already been introduced in (2.48). In contrast to the true stress tensor $\mathbf{T}$, the stress tensor $\mathbf{T}_R$ is denoted as a nominal stress tensor, see ALTENBACH AND ALTENBACH [6]. A pseudo stress tensor $\tilde{\mathbf{T}}$ is gained, as soon as the force vector $\boldsymbol{df}$ is transferred to the reference configuration in the same manner as a material line element $\boldsymbol{dx}$ and then divided by the surface in the reference configuration,

$$\tilde{\boldsymbol{t}} = \mathbf{F}^{-1} \frac{\boldsymbol{df}}{dA} = \tilde{\mathbf{T}} \boldsymbol{n}_R. \tag{2.75}$$

The stress tensor $\tilde{\mathbf{T}}$ is called the second Piola-Kirchhoff tensor and is used in constitutive models more frequently than the first Piola-Kirchhoff stress tensor since $\tilde{\mathbf{T}}$ is symmetric. Table 2.1 summarizes the introduced stress tensors and gives the transformation formulas to calculate them from each other. In addition to the stress tensors $\mathbf{T}$, $\mathbf{T}_R$ and $\tilde{\mathbf{T}}$ introduced so far, Table 2.1 contains the weighted Cauchy stress tensor $\mathbf{S}$ (Kirchhoff stress tensor), which is frequently used in constitutive models. Furthermore, Table 2.1 shows the stress tensor $\hat{\mathbf{T}}$ and the Mandel stress tensor $\hat{\mathbf{P}}$, which operate on the plastic intermediate configuration. They will be introduced in Section 2.3.3 and are applied later on to formulate the constitutive model.

Table 2.1: Stress tensors

	1. Piola-Kirchhoff $\mathbf{T}_R$	2. Piola-Kirchhoff $\tilde{\mathbf{T}}$	weighted Cauchy $\mathbf{S}$	Cauchy $\mathbf{T}$	$\hat{\mathbf{T}}$	Mandel $\hat{\mathbf{P}}$
$\mathbf{T}_R$		$\mathbf{F}\tilde{\mathbf{T}}$	$\mathbf{S}\mathbf{F}^{-T}$	$J\mathbf{T}\mathbf{F}^{-T}$	$\hat{\mathbf{F}}_\mathrm{e}\hat{\mathbf{T}}\mathbf{F}_\mathrm{p}^{-T}$	$\mathbf{F}_\mathrm{e}^{-T}\hat{\mathbf{P}}\mathbf{F}_\mathrm{p}^{-T}$
$\tilde{\mathbf{T}}$	$\mathbf{F}^{-1}\mathbf{T}_R$		$\mathbf{F}^{-1}\mathbf{S}\mathbf{F}^{-T}$	$J\mathbf{F}^{-1}\mathbf{T}\mathbf{F}^{-T}$	$\mathbf{F}^{-1}\hat{\mathbf{T}}\mathbf{F}_\mathrm{p}^{-T}$	$\mathbf{F}^{-1}\mathbf{F}_\mathrm{e}^{-T}\hat{\mathbf{P}}\mathbf{F}_\mathrm{p}^{-T}$
$\mathbf{S}$	$\mathbf{T}_R\mathbf{F}^T$	$\mathbf{F}\tilde{\mathbf{T}}\mathbf{F}^T$		$J\mathbf{T}$	$\hat{\mathbf{F}}_\mathrm{e}\hat{\mathbf{T}}\mathbf{F}_\mathrm{e}^T$	$\mathbf{F}_\mathrm{e}^{-T}\hat{\mathbf{P}}\mathbf{F}_\mathrm{e}^T$
$\mathbf{T}$	$\frac{1}{J}\mathbf{T}_R\mathbf{F}^T$	$\frac{1}{J}\mathbf{F}\tilde{\mathbf{T}}\mathbf{F}^T$	$\frac{1}{J}\mathbf{S}$		$\frac{1}{J}\hat{\mathbf{F}}_\mathrm{e}\hat{\mathbf{T}}\mathbf{F}_\mathrm{e}^T$	$\frac{1}{J}\mathbf{F}_\mathrm{e}^{-T}\hat{\mathbf{P}}\mathbf{F}_\mathrm{e}^T$
$\hat{\mathbf{T}}$	$\mathbf{F}_\mathrm{e}^{-1}\mathbf{T}_R\mathbf{F}_\mathrm{p}^T$	$\mathbf{F}_\mathrm{p}\tilde{\mathbf{T}}\mathbf{F}_\mathrm{p}^T$	$\mathbf{F}_\mathrm{e}^{-1}\mathbf{S}\mathbf{F}_\mathrm{e}^{-T}$	$J\mathbf{F}_\mathrm{e}^{-1}\mathbf{T}\mathbf{F}_\mathrm{e}^{-T}$		$\mathbf{C}_\mathrm{e}^{-1}\hat{\mathbf{P}}$
$\hat{\mathbf{P}}$	$\mathbf{F}_\mathrm{e}^T\mathbf{T}_R\mathbf{F}_\mathrm{p}^T$	$\mathbf{F}_\mathrm{e}^T\mathbf{F}\tilde{\mathbf{T}}\mathbf{F}_\mathrm{p}^T$	$\mathbf{F}_\mathrm{e}^T\mathbf{S}\mathbf{F}_\mathrm{e}^{-T}$	$J\mathbf{F}_\mathrm{e}^T\mathbf{T}\mathbf{F}_\mathrm{e}^{-T}$	$\mathbf{C}_\mathrm{e}\hat{\mathbf{T}}$	

2.3 Fundamental issues of constitutive modeling

The third cornerstone of continuum mechanics is the theory of material behavior (material theory). It is obvious that the system of equations formed by the balance of mass, momentum angular momentum and energy together with the entropy inequality is not sufficient to determine the unknown fields velocity $\boldsymbol{v}$, temperature T, density ρ, Cauchy stress $\mathbf{T}$, internal energy e, heat flux vector $\boldsymbol{q}$ and the entropy s. The entropy inequality (2.69) can not be used directly to determine these fields, it rather acts as a constraint, which needs to be fulfilled by all solutions of the basic equations. Taking into account the balance of angular momentum in the form $\mathbf{T} = \mathbf{T}^T$, 5 scalar equations[4] remain for the 16 unknown fields $\boldsymbol{v}$[3], T[1], ρ[1], $\mathbf{T}$[6], e[1], $\boldsymbol{q}$[3] and s[1]. If pure mechanical processes are considered, the situation is slightly better, since there are 4 scalar equations[5] for 10 unknown fields[6]. In order to close the system of equations, additional relations between the unknowns must be established. These additional equations are called constitutive equations. At least 11 additional equations in the thermomechanical case and at least 6 additional equations in the pure mechanical case are required. In many cases the constitutive equations introduce additional unknowns (internal variables), increasing thereby the number of unknowns and, consequently, the number of required equations as well.

In contrast to the kinematical description of the motion of a material body in Section 2.1 and the balance relations described in Section 2.2 the constitutive equations are not valid for all material bodies. They rather define the behavior of the individual material under consideration. Material theory provides a number of essential rules, which should be obeyed by the constitutive equations in order to ensure that the constructed mathematical model is consistent with observations. Obviously, the constitutive equations are not allowed to contradict the balance relations. Additionally, the constitutive equations should not produce a contradiction to the second law of thermodynamics for any solution under any initial and boundary conditions. This can either be checked after a constitutive equation has been stated, which might become rather difficult. Alternatively, the second law of thermodynamics in the form of the Clausius-Duhem inequality can be used to construct constitutive equations, which are a priori thermodynamically consistent, i.e. fulfill the second law in any thermomechanical process.

Moreover, a constitutive theory should follow further principles like the principle of determinism, local action and frame-indifference (material objectivity), see HAUPT [67, P.257]. The principle of determinism states that the current state at each point of the material body may depend on the current state of strain and the complete strain history in each and every material point of the material body. In essence, this principle excludes a dependence of the current state of the material on future strains. The principle of local action states that the current state of stress at a material point is influenced only by the strain history of this material point. Further assumptions, which promote the development of constitutive theories, are for example the principles of equipresence and fading memory, see for details ALTENBACH AND ALTENBACH [6]. The principle of frame-indifference (material objectivity) will be discussed in some detail in the following subsection. Afterwards the concept of dual variables introduced by HAUPT AND TSAKMAKIS [69] is discussed and subsequently the multiplicative decomposition of the deformation gradient $\mathbf{F}$ due to LEE [93] and LEE AND LIU [94], which is a fundamental assumption for the formulation of finite strain plasticity, is introduced. Besides the rules for the formulation of constitutive equations, two major concerns of material theory are the utilization of symmetries of the material

[4] balance of mass [1], balance of momentum [3] and balance of energy [1]

[5] balance of mass [1], balance of momentum [3]

[6] namely the velocity field $\boldsymbol{v}$[3], the density ρ[1] and the Cauchy stress $\mathbf{T}$[6]

as well as the inclusion of kinematical constraints, e.g. incompressibility, in the formulation of the constitutive models. These subjects will not be addressed here, but details can be found in ALTENBACH AND ALTENBACH [6], HAUPT [67], GREVE [53], HUTTER AND JÖHNK [76].

2.3.1 Objectivity

The principle of material objectivity (material frame-indifference) states that the constitutive equations should be indifferent under so called Euclidean transformations (2.76), which represent a general change of frame of reference

$$\boldsymbol{x}^* = \mathbf{Q}(t)\boldsymbol{x} + \boldsymbol{c}(t), \qquad t^* = t - a. \tag{2.76}$$

In the Euclidean transformation (2.76) the time t and spatial coordinates $\boldsymbol{x}$ of an arbitrary event in the unstarred coordinate system are transferred into a second frame of reference (the starred system). The functions $\mathbf{Q}(t)$ and $\boldsymbol{c}(t)$ define a rigid body motion of the reference frame consisting of a time dependent rotation $\mathbf{Q}(t)$ and a time-dependent translation of the origin described by $\boldsymbol{c}(t)$.[7]

In order to make the verification of the material objectivity of a constitutive equation possible, it is useful to analyze the transformation behavior of physical quantities under Euclidean transformations. Furthermore, the transformation behavior under Euclidean transformations is used to subdivide the quantities into objective and non-objective quantities. A scalar a, vector $\boldsymbol{a}$ or second order tensor $\mathbf{A}$ valued quantity is called objective if it transforms under Euclidean transformations according to

$$a^* = a, \tag{2.77}$$
$$\boldsymbol{a}^* = \mathbf{Q}(t)\boldsymbol{a}, \tag{2.78}$$
$$\mathbf{A}^* = \mathbf{Q}(t)\mathbf{A}\mathbf{Q}^T(t). \tag{2.79}$$

This definition of objectivity agrees with the definitions used, for example, in TRUESDELL AND NOLL [134], ALTENBACH AND ALTENBACH [6], HAUPT [67], BETTEN [18]. According to this definition the deformation gradient $\mathbf{F}$, which transforms like $\mathbf{F}^* = \mathbf{Q}(t)\mathbf{F}$ and the right Cauchy Green tensor $\mathbf{C}$ which transforms like $\mathbf{C}^* = \mathbf{C}$, are called non-objective. It should be mentioned that several authors, e.g. MALVERN [102], DOGHRI [40], GREVE [53], HUTTER AND JÖHNK [76], would also refer to $\mathbf{F}$ and $\mathbf{C}$ as objective quantities, since $\mathbf{F}$ transforms like 3 objective vectors and $\mathbf{C}$ transforms like 9 objective scalars. A definition yielding this kind of separation in objective and non-objective quantities can be found in DOGHRI [40] and is there traced back to HUGHES [75] and reads

"A tensor $A_{ij...kAB...C}$ transforms objectively if under the transformation (14.116) it transforms according to the following rule: $A^+_{ij...kAB...C} = Q_{il}Q_{jm}...Q_{km}A_{lm...nAB...C}$"[8]

In this thesis a scalar, vector or tensor is called objective only if it fulfills the transformation behavior stated in (2.78)-(2.79). As stated by HAUPT [67, P.168] one possibility is to establish the objectivity of a physical quantity individually, a priori by virtue of its definition, like in the

[7] A well-known subset of the Euclidean transformations are the Galilei transformations, which are characterized by a time independent rotation $\mathbf{Q}(t) = \mathbf{Q}_0$ and a translation with a constant velocity $\boldsymbol{c}(t) = \boldsymbol{c}_0 + \boldsymbol{c}_1 t$.

[8] The transformation in 14.116 to which DOGHRI [40] refers is the euclidean transformation Eq.(2.76), the lower case indices are for the current and the upper case indices are for the reference configuration.

case of mass, force, internal energy, heat, entropy, temperature and entropy flux. This definition also implies the objectivity of the corresponding density functions mass density, Cauchy stress vector, Cauchy stress tensor, volume force density, specific internal energy, specific entropy and heat flux vector. The other possibility is to confirm the objectivity by calculation based on earlier definitions. Without proof a list of important objective quantities is given in the following itemization:

- $\boldsymbol{dx}$, $\boldsymbol{da}$, dv: Line, surface and volume element
- $\mathbf{V}$, $\mathbf{b}$: Left stretch tensor, left Cauchy Green tensor
- $\mathbf{A}$: Almansi strain tensor
- $\mathbf{D}$: Deformation velocity tensor

Furthermore, a list of non-objective quantities is presented with the transformation behavior of the considered quantity:

- $\mathbf{F}^* = \mathbf{QF}$, $\mathbf{R}^* = \mathbf{QR}$: Deformation gradient and rotational tensor
- $\mathbf{U}^* = \mathbf{U}$, $\mathbf{C}^* = \mathbf{C}$: Right stretch tensor and right Cauchy Green tensor
- $\mathbf{E}^* = \mathbf{E}$, $\mathbf{L}^* = \mathbf{QLQ}^T + \dot{\mathbf{Q}}\mathbf{Q}^T$: Green strain tensor and velocity gradient
- $\mathbf{W}^* = \mathbf{QWQ}^T + \dot{\mathbf{Q}}\mathbf{Q}^T$, $\mathbf{T}_R^* = \mathbf{Q}$: Vorticity tensor and first Piola-Kichhoff stress tensor
- $\tilde{\mathbf{T}}^* = \tilde{\mathbf{T}}$: Second Piola-Kichhoff stress tensor

Additionally, it can be shown, see HAUPT [67] for a proof, that the set of objective quantities is closed with respect to algebraic operations, e.g. if $\boldsymbol{a}$ and $\boldsymbol{b}$ are objective vectors, $\boldsymbol{a} \cdot \boldsymbol{b}$ is an objective scalar. With these prerequisites the material objectivity of a constitutive equation is guaranteed, if all quantities within it are objective and are combined only by operations which preserve objectivity. Although the principle of material frame indifference seems perfectly plausible, especially for mechanical processes, some criticism can be found in the literature, see e.g. JOU ET AL. [77] and the literature cited therein. These authors state that there are indications in some fields that frame dependence of constitutive equations may be necessary and should not be ruled out a priori.

Objective vector, tensor rates

Unfortunately, the material time derivative of an objective vector or tensor is not objective. We consider the Cauchy stress tensor for example, which is objective and transforms accordingly as

$$\mathbf{T}^* = \mathbf{QTQ}^T, \tag{2.80}$$

whereas the material time derivative of $\mathbf{T}^*$ reads

$$\dot{\mathbf{T}}^* = \mathbf{Q}\dot{\mathbf{T}}\mathbf{Q}^T + \dot{\mathbf{Q}}\mathbf{T}\mathbf{Q}^T + \mathbf{QT}\dot{\mathbf{Q}}^T, \tag{2.81}$$

which is not objective due to the additional terms $\dot{\mathbf{Q}}\mathbf{TQ}^T$ and $\mathbf{QT}\dot{\mathbf{Q}}^T$. In order to overcome the problem that material time derivatives of objective tensors are not objective several tensor

rates can be introduced, which are objective, see for example HAUPT [67] or ALTENBACH AND ALTENBACH [6]. In this work so called Oldroyd rates are applied, which are defined by

$$\overset{\triangle}{\mathbf{T}} = \dot{\mathbf{T}} + \mathbf{L}^T\mathbf{T} + \mathbf{T}\mathbf{L}, \tag{2.82}$$

$$\overset{\triangledown}{\mathbf{T}} = \dot{\mathbf{T}} - \mathbf{L}\mathbf{T} + \mathbf{T}\mathbf{L}^T. \tag{2.83}$$

The concept of dual variables, which is due to HAUPT AND TSAKMAKIS [69], provides further insights about which tensors and which tensor rates should be chosen and connected to each other in constitutive equations. These aspects are discussed in the next section.

2.3.2 Dual variables

The concept of dual variables introduced by HAUPT AND TSAKMAKIS [69] can be considered as a guideline for the choice of stress and strain measures as well as their objective rates especially for the formulation of constitutive equations of evolutionary type. The starting point for the concept of dual variables is the observation that products of the quantities $\tilde{\mathbf{T}}$ (second Piola-Kirchhoff stress tensor) and $\mathbf{E}$ (Green strain tensor) and their material time derivatives $\dot{\tilde{\mathbf{T}}}$ and $\dot{\mathbf{E}}$ appear in the formulation of physical principles on the reference configuration. The balance of energy (2.60) formulated on the reference configuration contains the specific stress power $\frac{1}{\rho_R}\tilde{\mathbf{T}} \cdot \dot{\mathbf{E}}$. Furthermore, the product $\tilde{\mathbf{T}} \cdot \delta\mathbf{E}$ emerges in the principle of d'Alembert and the principle of virtual displacements and the term $\dot{\tilde{\mathbf{T}}} \cdot \delta\dot{\mathbf{E}}$ (incremental virtual stress power) appears in the incremental form of d'Alemberts principle (principle of virtual velocities). The fact that the product $\tilde{\mathbf{T}} \cdot \dot{\mathbf{E}}$ yields the stress power is usually described by denoting the pair $\tilde{\mathbf{T}}$ and $\mathbf{E}$ as conjugated variables. HAUPT AND TSAKMAKIS [69] introduce the term dual variables for $\tilde{\mathbf{T}}$ and $\mathbf{E}$ in the sense that they (and their material time derivatives) emerge in the physically significant scalar products

$$\tilde{\mathbf{T}} \cdot \dot{\mathbf{E}} \quad \text{stress power} \tag{2.84}$$

$$\dot{\tilde{\mathbf{T}}} \cdot \mathbf{E} \quad \text{complementary stress power} \tag{2.85}$$

$$\dot{\tilde{\mathbf{T}}} \cdot \dot{\mathbf{E}} \quad \text{incremental stress power} \tag{2.86}$$

$$\tilde{\mathbf{T}} \cdot \mathbf{E} \quad \text{accumulated work} \tag{2.87}$$

Stress and strain tensors operating on other than the reference configuration are called dual to each other if they, together with suitable tensor rates, preserve all four products introduced in (2.84) - (2.87). In the following it is demonstrated how a pair of dual variables (dual derivatives) can be constructed for a given (intermediate) configuration, which arises from a multiplicative decomposition of the deformation gradient $\mathbf{F}$

$$\mathbf{F} = \mathbf{F}_b\mathbf{F}_a = (\mathbf{F}\mathbf{F}_a^{-1})\mathbf{F}_a. \tag{2.88}$$

Dual stress and strain tensors on the intermediate configuration induced by $\mathbf{F}_a$ as well as their rates are then gained from the transformations

$$\boldsymbol{\Pi} = \mathbf{F}_a^{-T}\mathbf{E}\mathbf{F}_a^{-1} \tag{2.89}$$

$$\overset{\triangle}{\boldsymbol{\Pi}} = \mathbf{F}_a^{-T}\dot{\mathbf{E}}\mathbf{F}_a^{-1} = \dot{\boldsymbol{\Pi}} + \boldsymbol{\Lambda}^T\boldsymbol{\Pi} + \boldsymbol{\Pi}\boldsymbol{\Lambda} \tag{2.90}$$

$$\boldsymbol{\Sigma} = \mathbf{F}_a\tilde{\mathbf{T}}\mathbf{F}_a^T \tag{2.91}$$

$$\overset{\triangledown}{\boldsymbol{\Sigma}} = \mathbf{F}_a\dot{\tilde{\mathbf{T}}}\mathbf{F}_a^T = \dot{\boldsymbol{\Pi}} - \boldsymbol{\Lambda}\boldsymbol{\Sigma} + \boldsymbol{\Sigma}\boldsymbol{\Lambda}^T \tag{2.92}$$

with the tensor $\mathbf{\Lambda}$ defined by

$$\mathbf{\Lambda} = \dot{\mathbf{F}}_a \mathbf{F}_a^{-1}. \tag{2.93}$$

With the choice $\mathbf{F}_a = \mathbf{F}$ the dual quantities of the current configuration are retrieved

$$\mathbf{A} = \mathbf{F}^{-T}\mathbf{E}\mathbf{F}^{-1}, \quad \overset{\triangle}{\mathbf{A}} = \mathbf{F}^{-T}\dot{\mathbf{E}}\mathbf{F}^{-1} = \dot{\mathbf{A}} + \mathbf{L}^T\mathbf{A} + \mathbf{A}\mathbf{L} \tag{2.94}$$

$$\mathbf{S} = \mathbf{F}\tilde{\mathbf{T}}\mathbf{F}^T, \quad \overset{\triangledown}{\mathbf{S}} = \mathbf{F}\dot{\tilde{\mathbf{T}}}\mathbf{F}^T = \dot{\mathbf{S}} - \mathbf{L}\mathbf{S} - \mathbf{S}\mathbf{L}^T \tag{2.95}$$

with $\mathbf{\Lambda} \equiv \mathbf{L}$. In Section 2.3.3 the concept of dual variables is applied to introduce stress and strain measures (and appropriate rates) operating on the so-called plastic intermediate configuration, which arises from the multiplicative decomposition $\mathbf{F} = \hat{\mathbf{F}}_\mathrm{e}\mathbf{F}_\mathrm{p}$ and will later be used for the formulation of the constitutive model. It should be mentioned that the transformations introduced here belong to the first family of dual variables. A second family of dual variables can be introduced based on the Piola tensor $\mathbf{e}$ and the convected stress tensor $\tilde{\mathbf{t}} = \mathbf{F}^T\mathbf{S}\mathbf{F}$. Since they are not used in this work, the reader is referred to HAUPT AND TSAKMAKIS [69] or HAUPT [67] for further details.

2.3.3 The multiplicative decomposition $\mathbf{F} = \hat{\mathbf{F}}_\mathbf{e}\mathbf{F}_\mathbf{p}$

One fundamental concept for the modeling of elastoplastic material behavior is the subdivision of the model in two parts. One part is the formulation of an elasticity relation, which operates on a stress-free intermediate configuration and the other part is the representation of the evolution of this intermediate configuration. In order to obtain the stress free intermediate configuration the multiplicative decomposition of $\mathbf{F}$ is introduced,

$$\mathbf{F} = \hat{\mathbf{F}}_\mathrm{e}\mathbf{F}_\mathrm{p}, \quad \text{with} \quad \det\hat{\mathbf{F}}_\mathrm{e} > 0,\ \det\mathbf{F}_\mathrm{p} > 0. \tag{2.96}$$

This decomposition is not of mere kinematical nature, since the evolution of $\mathbf{F}_\mathrm{p}$ is defined through constitutive equations. The decomposition established in (2.96) defines the plastic intermediate configuration, see Figure 2.3. The stresses are defined by a constitutive equation, which depends on $\hat{\mathbf{F}}_\mathrm{e}$ like

$$\mathbf{T} = \mathbf{f}(\hat{\mathbf{F}}_\mathrm{e}) \quad \text{with} \quad \mathbf{f}(\mathbf{1}) = \mathbf{0}, \tag{2.97}$$

to ensure that the intermediate configuration is stress free. One can imagine the intermediate configuration to arise from a local unloading process, see HAUPT [67, P.432]. After a given deformation the material body is assumed to be separated in (small) volume elements with external forces applied to their surfaces according to the free-body principle. Reduction of these surface forces (stresses) to zero (local unloading) gives rise to a deformation which is related to the local state of stress whereas the remaining deformation relative to the reference configuration is assumed to be given by $\mathbf{F}_\mathrm{p}$. Since this assumed unloading happens locally in each individual volume the resulting volume elements of the material body will in general no longer fit together, because they change their shape independent of each other. This is described with the notion that the plastic intermediate configuration is (in general) incompatible. Following the concept of dual variables and identifying $\mathbf{F}_a = \mathbf{F}_\mathrm{p}$, we introduce the following set of dual stress and strain tensors operating on the intermediate configuration and their associated dual rates. The quantity $\dot{\mathbf{F}}_a\mathbf{F}_a^{-1}$ becomes $\dot{\mathbf{F}}_\mathrm{p}\mathbf{F}_\mathrm{p}^{-1}$ and is denoted as the plastic velocity gradient

$$\hat{\mathbf{L}}_\mathrm{p} = \dot{\mathbf{F}}_\mathrm{p}\mathbf{F}_\mathrm{p}^{-1}. \tag{2.98}$$

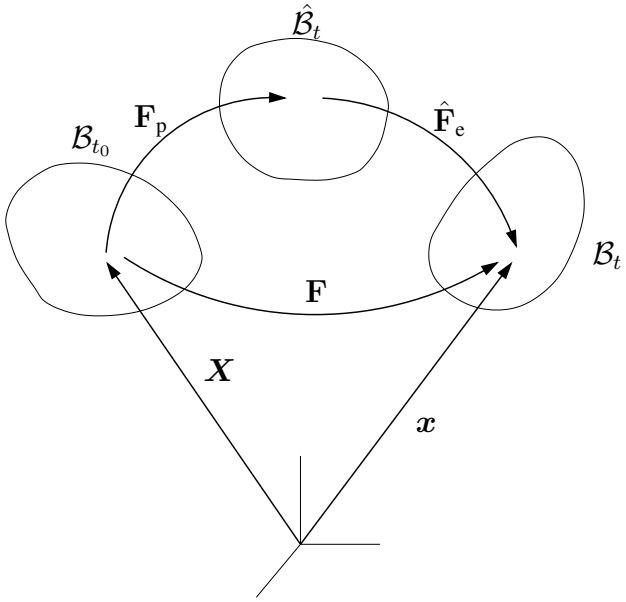

Figure 2.3: Multiplicative decomposition and intermediate configuration

The rates $\overset{\triangle}{\hat{\mathbf{\Gamma}}}$ and $\overset{\triangledown}{\hat{\mathbf{T}}}$ represent Oldroyd derivatives formed with $\hat{\mathbf{L}}_\mathrm{p}$:

$$\hat{\mathbf{\Gamma}} = \mathbf{F}_\mathrm{p}^{-T}\mathbf{E}\mathbf{F}_\mathrm{p}^{-1}, \quad \overset{\triangle}{\hat{\mathbf{\Gamma}}} = \mathbf{F}_\mathrm{p}^{-T}\dot{\mathbf{E}}\mathbf{F}_\mathrm{p}^{-1} = \dot{\hat{\mathbf{\Gamma}}} + \mathbf{L}_\mathrm{p}^{T}\hat{\mathbf{\Gamma}} + \hat{\mathbf{\Gamma}}\hat{\mathbf{L}}_\mathrm{p} \tag{2.99}$$

$$\hat{\mathbf{T}} = \mathbf{F}_\mathrm{p}\tilde{\mathbf{T}}\mathbf{F}_\mathrm{p}^{T}, \quad \overset{\triangledown}{\hat{\mathbf{T}}} = \mathbf{F}_\mathrm{p}\dot{\tilde{\mathbf{T}}}\mathbf{F}_\mathrm{p}^{T} = \dot{\hat{\mathbf{T}}} - \mathbf{L}_\mathrm{p}\hat{\mathbf{T}} - \hat{\mathbf{T}}\mathbf{L}_\mathrm{p}^{T} \tag{2.100}$$

In Figure 2.5 the strain tensors and rates operating on the intermediate configuration and the relations with strain tensors (and their rates) of the reference and current configuration are depicted. The stress tensors of the three configurations, their rates and transformations are presented in Figure 2.4. The strain tensor $\hat{\mathbf{\Gamma}}$ decomposes in the intermediate configuration additively in a

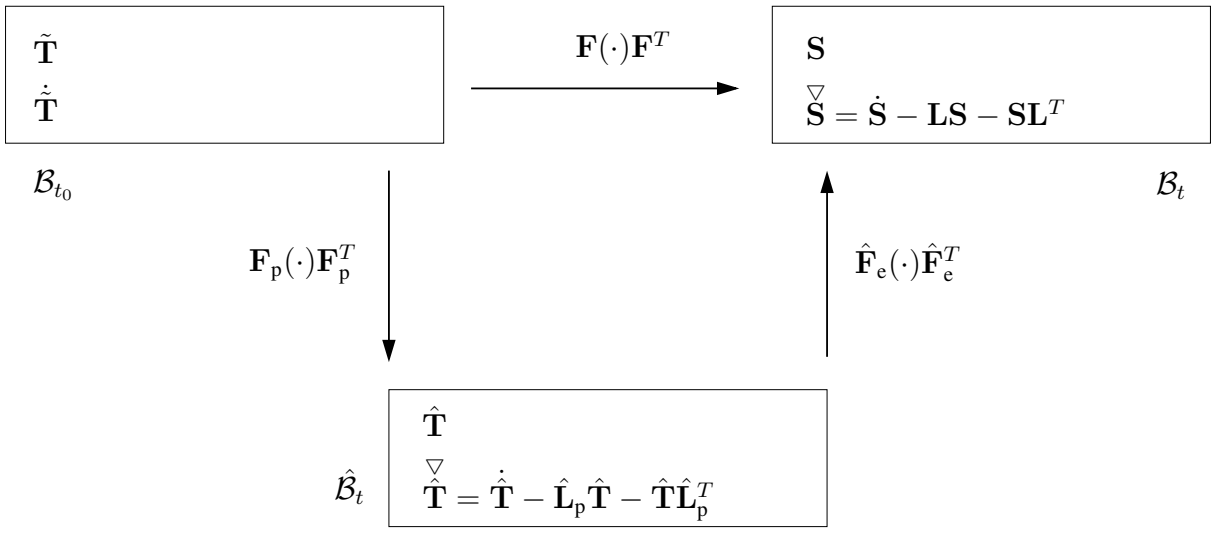

Figure 2.4: Stress tensor in the reference, intermediate and current configuration

pure elastic part (depending only on $\hat{\mathbf{F}}_{\mathrm{e}}$) and a pure plastic part (depending only on $\mathbf{F}_{\mathrm{p}}$).

$$\hat{\boldsymbol{\Gamma}} = \hat{\boldsymbol{\Gamma}}_{\mathrm{e}} + \hat{\boldsymbol{\Gamma}}_{\mathrm{p}} \tag{2.101}$$

$$\hat{\boldsymbol{\Gamma}}_{\mathrm{e}} = \frac{1}{2}\left(\hat{\mathbf{F}}_{\mathrm{e}}^{T}\hat{\mathbf{F}}_{\mathrm{e}} + \mathbf{1}\right) \tag{2.102}$$

$$\hat{\boldsymbol{\Gamma}}_{\mathrm{p}} = \frac{1}{2}\left(\mathbf{1} - \mathbf{F}_{\mathrm{p}}^{-T}\mathbf{F}_{\mathrm{p}}^{-1}\right) \tag{2.103}$$

Furthermore, the plastic deformation rate $\overset{\triangle}{\hat{\boldsymbol{\Gamma}}}_{\mathrm{p}}$ is also purely plastic (depends only on $\mathbf{F}_{\mathrm{p}}$) and is identical with the symmetric part of the plastic velocity gradient

$$\overset{\triangle}{\hat{\boldsymbol{\Gamma}}}_{\mathrm{p}} = \hat{\mathbf{D}}_{\mathrm{p}} \quad \text{with} \quad \hat{\mathbf{D}}_{\mathrm{p}} = \frac{1}{2}\left(\hat{\mathbf{L}}_{\mathrm{p}} + \hat{\mathbf{L}}_{\mathrm{p}}^{T}\right). \tag{2.104}$$

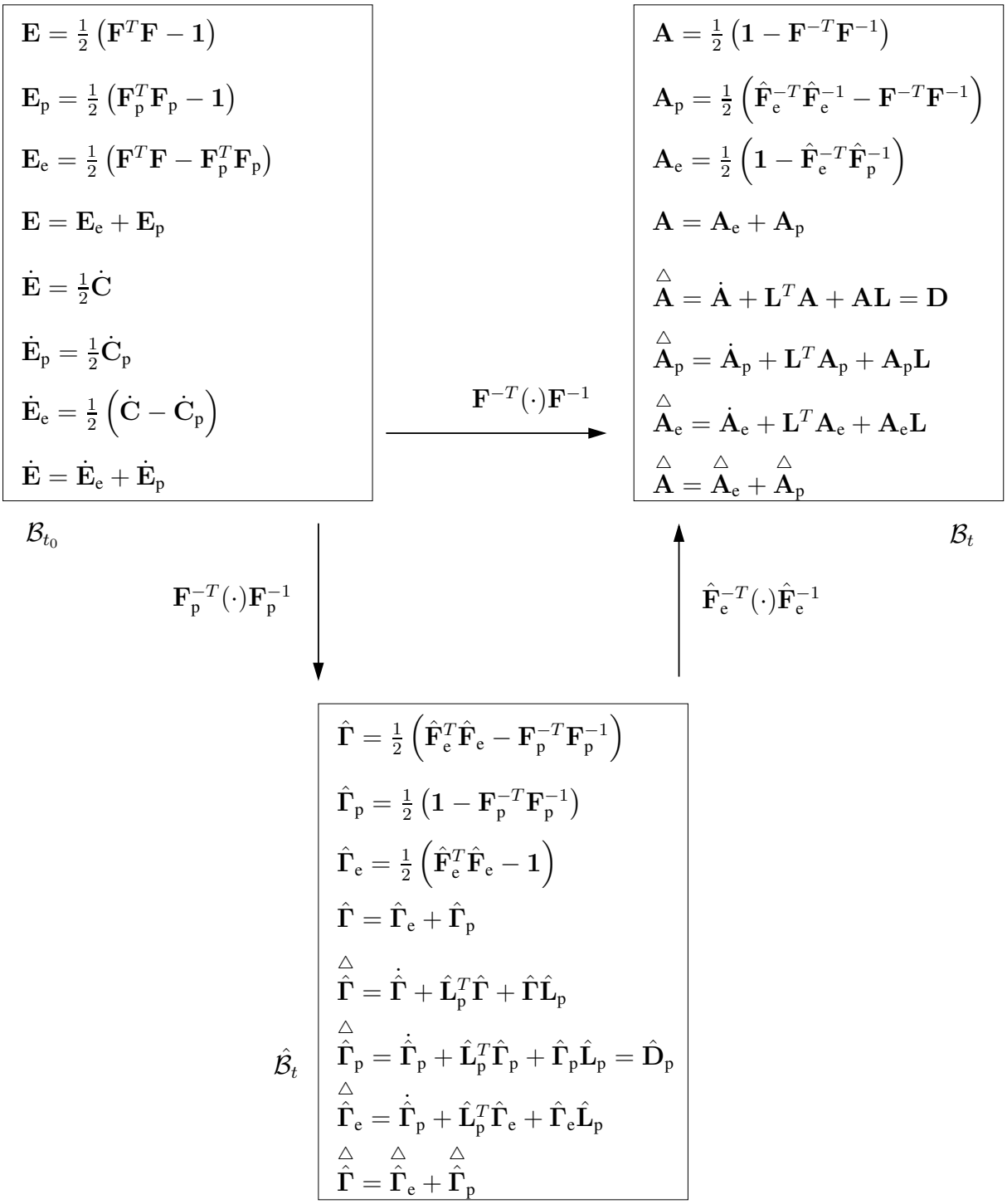

Figure 2.5: Strain tensors and strain tensor rates in the reference, intermediate and current configuration

Chapter 3

Constitutive modeling of metal powder

At first the constitutive model is developed within the framework of elastoplasticity for finite strains and is subsequently generalized to viscoplasticity. The elastic behavior is modeled using an elasticity relation derived from a free energy function (hyperelasticity). The model is yield function based and the developed pressure-dependent yield function is adapted to reproduce the behavior of metal powders, see BIER AND HARTMANN [19]. Section 3.1 provides a motivation for the application of a finite strains elastoplasticity model based on available experimental data. Furthermore, the structure of an elastoplasticity model is introduced. Subsequently, the backbone of the three-dimensional constitutive model, which is the pressure-dependent yield function is described. There, we start with a review of existing formulations and their application in the constitutive modeling of metal powder compaction (Section 3.2). Afterwards, in Section 3.3 the other ingredients of the elastoplasticity model are introduced. Finally, in Section 3.4 the expansion of the model to viscoplasticity is discussed.

3.1 Motivation

Taking a look at experimental data in Fig. 4.8 from a uniaxial constrained compression experiment with intermediate unloading and reloading cycles, we notice that during unloading and reloading the material deforms elastically. The boundaries of this elastic domain in stress space increase with the amount of preloading the material has undergone. Such a behavior can be described by a model of elastoplasticity. One of the special things to consider is that initially the elastic domain is essentially non-existent. However, it grows subsequently under compressive loading.

The main ingredients of an elastoplasticity constitutive model are summarized in Tab. 3.1. The *yield function* defines the border of the elastic domain and determines through the *loading condition* the onset of plastic deformations and an evolution of the internal variables. The *elasticity relation* is valid during elastic as well as plastic loading. The *flow rule* defines the evolution of the plastic strains during plastic loading. Often the flow rule is connected to the yield function such that the direction of the plastic strain rate is perpendicular to the yield function (*associative flow rule*). The *evolution equations* determine how the *internal variables* besides the plastic strains evolve during plastic loading. They are ordinary differential equations of first order.

Table 3.1: General structure of elastoplasticity constitutive model (for brevity a small strain-state is considered) formulated with the stress measure $\boldsymbol{\sigma}$, the strain measure $\boldsymbol{\epsilon}$ and the internal variables $\boldsymbol{q}$ which contain the plastic strain measure $\boldsymbol{\epsilon}_{\mathrm{p}}$. The proportionality factor λ is denoted as plastic multiplier.

yield function	$f(\boldsymbol{\sigma}, \boldsymbol{q}) = 0$	
loading condition	$f < 0 \ \vee \ f = 0 \ \wedge \ \dot{f}\|_{\boldsymbol{q}\text{ fixed}} < 0$	$f = 0 \ \wedge \ \dot{f}\|_{\boldsymbol{q}\text{ fixed}} \geq 0$
	elastic	elastoplastic
elasticity relation	$\boldsymbol{\sigma} = \mathbf{h}(\boldsymbol{\epsilon}, \boldsymbol{q})$	
flow rule	$\dot{\boldsymbol{\epsilon}}_{\mathrm{p}} = 0$	$\dot{\boldsymbol{\epsilon}}_{\mathrm{p}} = \lambda \boldsymbol{r}_{\mathrm{p}}(\boldsymbol{\epsilon}, \boldsymbol{q})$
evolution equations	$\dot{\boldsymbol{q}} = 0$	$\dot{\boldsymbol{q}} = \lambda \boldsymbol{r}_{\mathrm{q}}(\boldsymbol{\epsilon}, \boldsymbol{q})$

3.2 Yield functions for pressure dependent material behavior

The yield function is one of the most important ingredients of an elastoplasticity model. It defines the size and shape of the elastic domain in stress space, i.e. whether a given state of stress leads to plastic deformations or not. The state of stress in each material point is defined by the stress tensor $\mathbf{T}$, which is symmetric, i.e. $\mathbf{T}$ has six independent components. As a symmetric tensor of second order $\mathbf{T}$ can be represented (diagonalization) by the three principal stresses σ_1, σ_2 and σ_3,

$$\mathbf{T} = \sum_{k=1}^{3} \sigma_k \vec{n}_k \otimes \vec{n}_k. \tag{3.1}$$

With respect to the principal directions $\vec{n}_k$, the state of stress is given by the three coordinates σ_1, σ_2 and σ_3, which define a point in the three-dimensional principal stress space. In this principal stress space the yield function defines a surface which encloses the elastic domain. It is possible to use the principal stresses σ_1, σ_2 and σ_3 for the mathematical definition of the yield surface, but usually the yield surface is defined using the invariants I_1, I_2 and I_3 of the stress tensor or a combination of one invariant I_1 of the stress tensor and invariants of the deviator of the stress tensor J_2, J_3 or quantities which can be derived from these invariants (Haigh-Westergaard coordinates, octahedral stresses). We define the invariants of the stress tensor

$$I_1 = \operatorname{tr} \mathbf{T}, \quad I_2 = \frac{1}{2} \mathbf{T} \cdot \mathbf{T}, \quad I_3 = \det \mathbf{T} \tag{3.2}$$

as well as the invariants of the deviator

$$J_1 = \operatorname{tr} \mathbf{T}^D = 0, \quad J_2 = \frac{1}{2} \mathbf{T}^D \cdot \mathbf{T}^D, \quad J_3 = \det \mathbf{T}^D = \frac{1}{3} \mathbf{T}^D \cdot (\mathbf{T}^D \mathbf{T}^D) \tag{3.3}$$

with the deviator being defined through

$$\mathbf{T}^D = \mathbf{T} - \frac{1}{3} (\operatorname{tr} \mathbf{T}) \, \mathbf{1}. \tag{3.4}$$

Alternatively, Haigh-Westergaard coordinates can be introduced via the definitions, see CHEN AND HAN [28],

$$\pi = \frac{1}{\sqrt{3}} I_1, \quad \varrho = \sqrt{2 J_2}, \quad \theta = \frac{1}{3} \arccos \left(\frac{\sqrt{27}}{2} \frac{J_3}{J_2^{3/2}} \right). \tag{3.5}$$

The Haigh-Westergaard representation corresponds to the introduction of a cylindrical coordinates like coordinate system in principal stress space. The coordinate π measures the hydrostatic component of the state of stress and is connected to the hydrostatic pressure via $\pi = -\sqrt{3}p$ with p being the hydrostatic pressure $-p = \frac{1}{3}(\sigma_1 + \sigma_2 + \sigma_3) = \frac{1}{3}I_1$. The coordinate ϱ measures the distance from the hydrostatic axis and θ is an angle between $0°$ and $60°$, which defines the position of the stress state relative to the projections of the axis of the principal stresses upon the deviatoric plane. The deviatoric plane may be any plane in the principal stress space perpendicular to the hydrostatic axis, i.e. all stresses in the plane have the same hydrostatic stress component. Instead of θ in Eq. (3.5) the angle

$$\Theta = \frac{1}{3}\arcsin\left((\sqrt{27}/2)(J_3/J_2^{3/2})\right) \quad -30° \leq \Theta \leq 30° \tag{3.6}$$

may be used. In this thesis the yield surface is defined, using the first invariant of the stress tensor I_1 and the second and third invariant of its deviator J_2, J_3, where the dependence on the third invariant is usually neglected, i.e. a circular shape of the yield surface in the deviator plane is assumed and the discussion of the shape of the yield surface is restricted mostly to the I_1-$\sqrt{J_2}$-plane.

The famous von Mises yield function (3.7) for metals defines a cylinder around the hydrostatic axis, i.e. in the I_1-$\sqrt{J_2}$-plane it is represented by a straight line parallel to the hydrostatic axis and in the deviator plane it is represented by a circle with its center on the hydrostatic axis, see Figure 3.1(b),

$$F = \sqrt{J_2} - \kappa = 0. \tag{3.7}$$

The simplest expansion of the von Mises yield function to incorporate a pressure dependence is due to Drucker and Prager

$$F = \sqrt{J_2} - \beta I_1 - \kappa = 0, \tag{3.8}$$

which is represented by a circle in the deviatoric plane, where the radius of the circle depends on I_1, which can be seen from the representation in the I_1-$\sqrt{J_2}$-plane. There, the Drucker-Prager yield function defines a straight line with the slope β and the intersection $-\kappa/\beta$ with the hydrostatic axis, see Figure 3.1(b). The following discussion of yield functions from the literature and the subsequent introduction of a new yield function will be restricted to the I_1-$\sqrt{J_2}$-plane, i.e. it is assumed that the yield function is independent of the third invariant of the deviator J_3. Other authors have discussed and introduced yield functions with a rounded triangular like shape in the deviatoric plane, e.g. EHLERS [42] or BIGONI AND PICCOLROAZ [20]. It can be shown that the new yield function can be expanded to incorporate a dependence on the third invariant following, for example, the suggestion of EHLERS [42]. Due to lack of experimental data to identify the shape in the deviatoric plane a dependence on the third invariant will actually not be included in the proposed constitutive model.

3.2.1 A review of existing pressure dependent yield functions

With respect to the modeling of metal powder compaction processes, it is very common to introduce the notion of *relative density*,

$$\rho_{\text{rel}}(\boldsymbol{x}, t) = \rho(\boldsymbol{x}, t)/\rho_{\text{particle material}} \tag{3.9}$$

where ρ is the bulk density in the current configuration. The density of the particle material $\rho_{\text{particle material}}$ is assumed to be a constant and represents the density of the (pore free) base material. In our experiments, see Section 4, we made use of copper with $\rho_{\text{particle material}} = 8.96\,\text{g/cm}^3$.

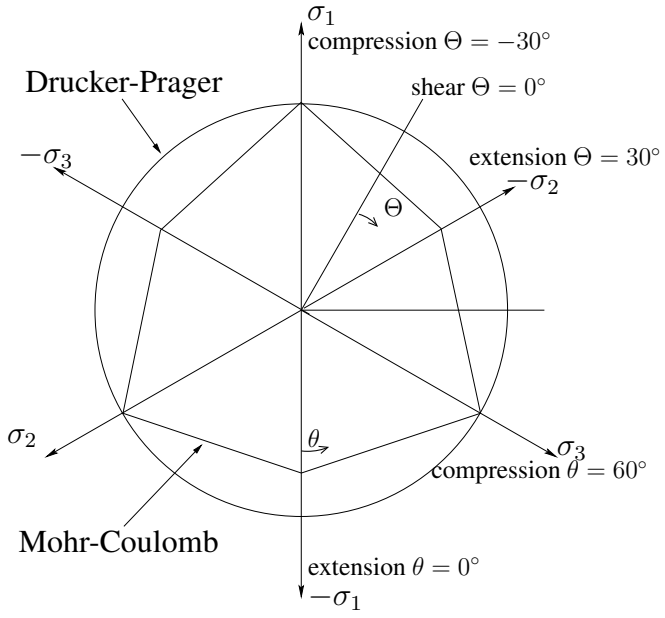

(a) von Mises (or likewise Drucker-Prager) and Mohr-Coulomb yield function in deviatoric plane

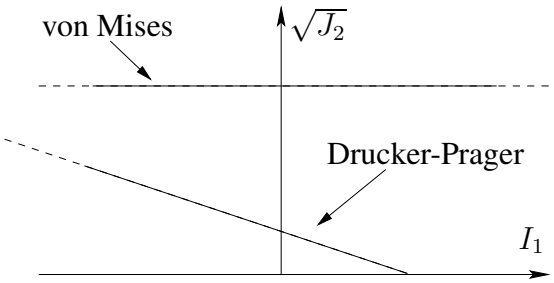

(b) von Mises and Drucker-Prager yield function in $I_1 - \sqrt{J_2}$-plane

Figure 3.1: Von Mises and Drucker-Prager yield surface as well as Mohr-Coulomb yield function

From the balance of mass in the form of the continuity equation (2.43) we obtain in view of Eq. (3.9) the relations

$$\frac{\rho}{\rho_{\text{particle material}}}(\det \mathbf{F}) = \frac{\rho_R}{\rho_{\text{particle material}}} \quad \Rightarrow \quad \rho_{\text{rel}} \det \mathbf{F} = \rho_{R,\text{rel}}. \tag{3.10}$$

Where $\rho_{R,\text{rel}}$ denotes the initial relative density of the bulk powder. Accordingly, the material time derivative reads

$$\left(\frac{\mathrm{d}}{\mathrm{d}t}\rho_{\text{rel}}\right) \det \mathbf{F} + \rho_{\text{rel}} \frac{\mathrm{d}}{\mathrm{d}t} \det \mathbf{F} = 0 \tag{3.11}$$

because the density $\rho_R(\boldsymbol{X})$ and, hence $\rho_{R,\text{rel}}$ are independent of time t. Using the property $\mathrm{d}(\det \mathbf{F})/\mathrm{d}t = (\det \mathbf{F})\mathrm{tr}\,\mathbf{L} = (\det \mathbf{F})\mathrm{tr}\,\mathbf{D}$, with $\mathbf{L}$ being the spatial velocity gradient, see Eq. (2.29), and $\mathbf{D}$ its symmetric part, see Eq. (2.34), we obtain the result of the balance of mass in the local form

$$\frac{\mathrm{d}}{\mathrm{d}t}\rho_{\text{rel}} = -\rho_{\text{rel}} \mathrm{tr}\,\mathbf{D}. \tag{3.12}$$

Sometimes Eq. (3.12) is written in terms of plastic variables. This can be obtained applying the multiplicative decomposition of the deformation gradient, see Eq. (2.96), which implies $\det \mathbf{F} = (\det \hat{\mathbf{F}}_{\text{e}})(\det \mathbf{F}_{\text{p}})$. The polar decomposition, see Eq. (2.17), of the elastic part $\hat{\mathbf{F}}_{\text{e}} = \mathbf{R}_{\text{e}}\mathbf{U}_{\text{e}}$, $\det \mathbf{R}_{\text{e}} = 1$, $\mathbf{R}_{\text{e}}^T = \mathbf{R}_{\text{e}}^{-1}$, yields, together with the assumption of small elastic strains, $\mathbf{U}_{\text{e}} \approx \mathbf{1}$

$$\det \mathbf{F} \approx \det \mathbf{F}_{\text{p}}. \tag{3.13}$$

Consequently, we obtain from (3.11)

$$\frac{\mathrm{d}}{\mathrm{d}t}\rho_{\text{rel}} = -\rho_{\text{rel}}(\mathrm{tr}\,\mathbf{D}_{\text{p}}) \tag{3.14}$$

using the relation

$$\frac{\mathrm{d}}{\mathrm{d}t}\det\mathbf{F}_\mathrm{p} = (\det\mathbf{F}_\mathrm{p})(\mathrm{tr}\,\mathbf{L}_\mathrm{p}) = (\det\mathbf{F}_\mathrm{p})(\mathrm{tr}\,\mathbf{D}_\mathrm{p}) \tag{3.15}$$

with $\mathbf{L}_\mathrm{p}$ and $\mathbf{D}_\mathrm{p}$ from Eqns. (2.98) and (2.104). Equation (3.14) is, for example, proposed in GOVINDARAJAN AND ARAVAS [51]. Of course, this holds in the case of rigid plasticity, $\mathbf{D} = \mathbf{D}_\mathrm{p}$, as well. After these introductory remarks about the notion relative density we actually start the review of existing pressure dependent yield functions with ellipsoidal shaped yield functions.

Ellipsoidal shaped yield functions

The earliest proposals to describe the compaction behavior of metal powders using yield functions are due to KUHN AND DOWNEY [89] as well as GREEN [52]. They proposed independent of each other yield functions of the form

$$F = AJ_2 + BI_1^2 - C\kappa^2 = 0, \tag{3.16}$$

which can be conceived as modifications of the von Mises surface introducing a dependence upon the first invariant of the stress tensor (hydrostatic pressure). KUHN AND DOWNEY [89] were interested in the description of the constitutive behavior of already sintered powder compacts during forging and repressing, while GREEN [52] developed the model for a metal with isotropically distributed voids or cracks. The parameters A, B and C in (3.16) are usually assumed to be density dependent in such a way, that for a fully dense material ($\rho_\mathrm{rel} = 1$) the von Mises yield function (3.7) is retrieved from (3.16) and accordingly κ represents the von Mises yield strength of the base material.

Several authors like SHIMA AND OYANE [122], CORAPCIOGLU AND UZ [32] as well as KUHN AND DOWNEY [89] and GREEN [52] themselves have proposed specific dependencies of the given parameters on the relative density. A compilation of the proposed dependencies can be found in DORAIVELU ET AL. [41], where DORAIVELU ET AL. [41] propose an additional one, based on their experimental observations. The proposals of KUHN AND DOWNEY [89], GREEN [52] and SHIMA AND OYANE [122] are visualized in Figures 3.2(a) - 3.2(c) showing that the yield surface grows with increasing relative density in different manners towards the von Mises yield function. These elliptical shaped yield functions are still applied in more recent publications on powder compaction problems, for example by PEREZ-FOGUET ET AL. [110], OLIVER ET AL. [105] and RODRIGUEZ-FERRAN ET AL. [118].

Based upon numerous experiments ABOU-CHEDID [3] proposed a simple modification of the elliptical yield function as depicted in Figure 3.3. ABOU-CHEDID [3] suggested shifting the ellipse along the hydrostatic axis in order to take the limited strength under tensile and shear conditions of the metal powder into account. This idea has been adopted for the proposal of a constitutive model for metal powders by TSZENG AND WU [136].

Gurson model

A pressure-dependent yield function for porous ductile media, quite similar to the ellipse, has been developed by GURSON [55]. The yield function is given in (3.17) and has been derived from micro-mechanical considerations,

$$F = \frac{J_2}{\kappa^2} + 2n\cosh\left(\frac{I_1}{2\sqrt{3}\kappa}\right) - (1+n^2) = 0, \tag{3.17}$$

$$F = \frac{J_2}{\kappa^2} + 2q_1 n\cosh\left(\frac{q_2 I_1}{2\sqrt{3}\kappa}\right) - (1+(q_1 n)^2) = 0. \tag{3.18}$$

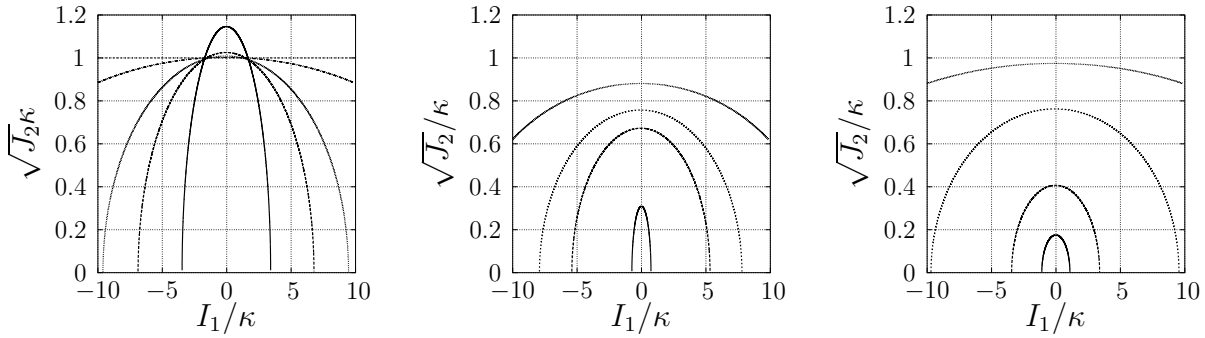

(a) KUHN AND DOWNEY [89] for the relative densities $\rho_{\text{rel}} = \{0.5, 0.9, 0.95, 0.99, 1.0\}$ with $A(\rho_{\text{rel}}) = 2 + \rho_{\text{rel}}^2$,$B(\rho_{\text{rel}}) = \frac{1-\rho_{\text{rel}}^2}{3}$ and $C = 1$.

(b) GREEN [52] for the relative densities $\rho_{\text{rel}} = \{0.5, 0.9, 0.95, 0.99\}$ with $A = 3$,$B(\rho_{\text{rel}}) = \frac{1}{4(\ln(1-\rho_{\text{rel}}))^2}$ and $C(\rho_{\text{rel}}) = \frac{3(1-(1-\rho_{\text{rel}})^{1/3})^2}{3-2(1-\rho_{\text{rel}})^{1/4}}$.

(c) SHIMA AND OYANE [122] for the relative densities $\rho_{\text{rel}} = \{0.5, 0.7, 0.9, 0.99\}$ with $A = 3$,$B(\rho_{\text{rel}}) = \frac{2.49(1-\rho_{\text{rel}})^{0.514}}{9\rho_{\text{rel}}^5}$ and $C(\rho_{\text{rel}}) = \rho_{\text{rel}}^5$.

Figure 3.2: Dependence of ellipsoidal yield function on relative density according to KUHN AND DOWNEY [89], GREEN [52] and SHIMA AND OYANE [122].

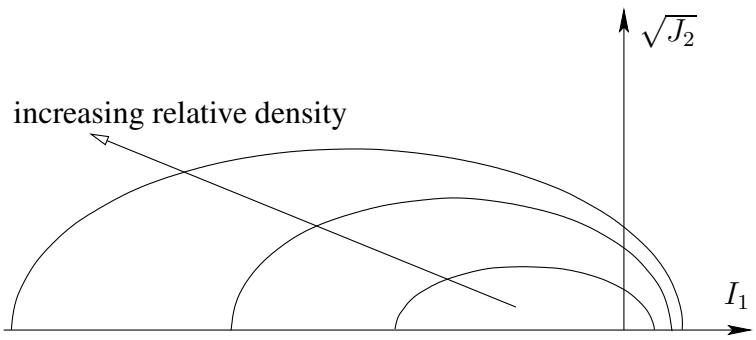

Figure 3.3: Suggested modification of elliptical yield function due to ABOU-CHEDID [3]

The quantity n in (3.17) and (3.18) represents the porosity. The assumptions entering the micro-mechanical derivation of the yield function (3.17) are only valid for high relative densities (void ratio $\leq$ 15 %). For this reason the yield function of GURSON [55] is sometimes applied in combination with micro-mechanically motivated models for low relative densities due to FLECK ET AL. [48], for example, by REDANZ [115, 116], REDANZ AND FLECK [117], CEDERGREN ET AL. [26] and CEDERGREN ET AL. [27]. Actually, a modified version of the yield function of GURSON [55] is applied in these publications. The modifications are due to TVERGAARD [137, 138] and introduce two adjustable parameters q_1, q_2 to the yield function proposed by GURSON [55], see (3.18).

Cap models

The most widespread kind of yield functions applied to metal powder compaction problems are so-called cap-models. Cap-models form a yield function by combination of two (or more) yield functions. Usually the Drucker-Prager yield function (3.8) (DPC) is used in combination with

a cap, which is part of an ellipse, see for example WATSON AND WERT [139], ABAQUS [1], COUBE [33] and COUBE AND RIEDEL [34]. Instead of the Drucker-Prager cone some authors use the exponential yield (failure) function tracing back to DIMAGGIO AND SANDLER [39], see for example CHTOUROU ET AL. [30], SHAMLOO ET AL. [121] or KHOEI AND AZIZI [83], which has been proposed originally for granular materials like soil, sand or rock. The combination of the Mohr-Coulomb yield function[1], which gives a non-smooth shape in the deviatoric plane with a usually elliptical cap (MCEC), has been considered in LEWIS AND KHOEI [96], KHOEI AND LEWIS [79], KHOEI AND LEWIS [80], LEWIS AND KHOEI [97] and GU ET AL. [54]. Instead of a cap, which is part of an ellipse, KIM ET AL. [84], KIM ET AL. [85] and LEE AND KIM [95] applied a hyperbolic cap of the form

$$F_{\text{hyperbolic cap}} = C - A\cosh(Bp) - q = 0, \quad \text{with} \quad q = \sqrt{3J_2}, \quad p = -\frac{1}{3}I_1 \tag{3.19}$$

with A, B, C being parameters depending on the relative density. In addition to the failure surface (Drucker-Prager, Mohr-Coulomb or exponential) and the cap, some authors, e.g. CHTOUROU ET AL. [30], COUBE AND RIEDEL [34] and KHOEI AND AZAMI [82] introduce an additional tension cut-off of the form

$$F_{\text{tension cut off}} = T_C - I_1 = 0 \tag{3.20}$$

to limit the hydrostatic tensile stresses. Furthermore, COUBE AND RIEDEL [34] introduce a von Mises cut off to the applied DPC function of the form

$$F_{\text{von Mises cut off}} = Y - \sqrt{J_2} = 0. \tag{3.21}$$

The non-smooth intersection between the yield surfaces that are combined, lead to difficulties

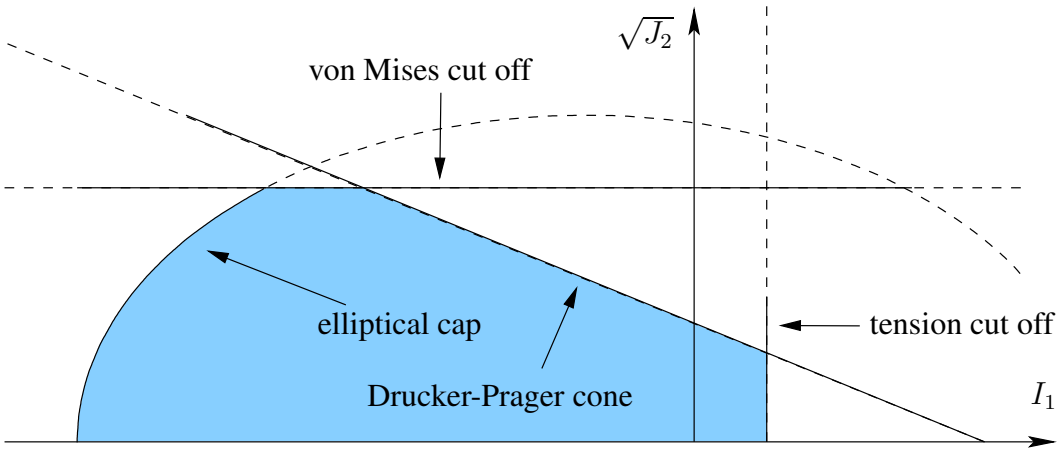

Figure 3.4: Drucker-Prager-Cap yield function with tension and von Mises cut off.

when associative flow rules are applied, which is very common, since the normal is not defined uniquely at the intersection points. These difficulties can be addressed either by local smoothing techniques, see, for example, BEJARANO ET AL. [16], or by special considerations (corner modes) in the numerical treatment of the equations, see, for example, CHTOUROU ET AL. [29].

[1] The Mohr-Coulomb yield function reads $F = \sqrt{J_2} - \frac{\frac{I_1}{3}\sin(\phi) + c\cos(\phi)}{\cos(\Theta) - \frac{\sin(\Theta)\sin(\phi)}{\sqrt{3}}} = 0$, c and ϕ being material parameters usually referred to as cohesion and friction angle respectively.

In addition to the corners associated with the intersections of the yield functions, there is a singularity also at the intersection of the Drucker-Prager or Mohr-Coulomb cone with the hydrostatic axis for which ABBO AND SLOAN [2] have proposed a suitable smoothing procedure.

Cam-clay models

The yield functions proposed as parts of the so-called "Cam-clay" and "modified Cam-clay" models are not frequently applied to metal powder compaction processes. Therefore, they are addressed only briefly. On the other hand, SUN ET AL. [128] reports good agreement with experimental data for the application of a modified Cam-clay model to a uniaxial powder compaction problem. The Cam-clay models go back to the 1960s and have been suggested to describe the constitutive behavior of granular media like soils, clay or rock. According to CALLARI ET AL. [22] the yield function of the original Cam-clay model can be written in the form

$$F = q + Mp \ln\left(\frac{p}{p_c}\right) = 0 \tag{3.22}$$

whereas the modified Cam-clay model reads

$$F = \frac{q^2}{M^2} + p(p - p_c) = 0 \tag{3.23}$$

with $q = \sqrt{3J_2}$ and $p = -\frac{1}{3}I_1$ and M representing the slope of the so called critical state line in the $p - q$-plane. This critical state line is the line through the origin of the $p - q$-plane and the maximum of the yield function plotted in the $p - q$-plane. The parameter p_c usually called preconsolidation pressure represents the intersection of the yield function with the hydrostatic (p) axis, see 3.5(a) and 3.5(b). The yield function of the modified Cam-clay model, see Eq. (3.23), is going back to ROSCOE AND BURLAND [119]. It is just an ellipse in the $p - q$-plane (or likewise the $I_1 - \sqrt{J_2}$-plane) going through the origin of the $p - q$-plane and its center lies on the hydrostatic axis. This means that the yield function of the modified Cam-clay model can be considered as a special case of the generalized elliptical model proposed by ABOU-CHEDID [3] discussed earlier.

Micro-mechanically motivated models

There is a significant number of publications on the derivation of macroscopic constitutive models (with an emphasis on the formulation of yield surfaces) motivated from micro-mechanical models of the powder material. One common starting point for such a derivation can be the model assumption that the powder consists of equal-sized spherical particles which behave perfectly plastic with a uniaxial yield stress σ_Y. Of course, modifications of these assumptions regarding the constitutive behavior, shape and contact laws of and between the particles have been studied leading to a variety of macroscopic yield surfaces. In an arrangement of densely packed spherical powder particles an external macroscopic load is transferred within the powder through the contacts between the powder particles. If the local load at the contact between two particles exceeds the yield strength σ_Y of the material, then the particles start to deform plastically. In case of an compressive external load the centers of the spherical particles come closer to each other and the number of contacts Z (coordination number) and the size of the contact area A_c increases. This change of A_c and Z leads to a macroscopic hardening. ARZT [11] proposed relations for the dependencies of A_c and Z on the achieved relative density during an isostatic

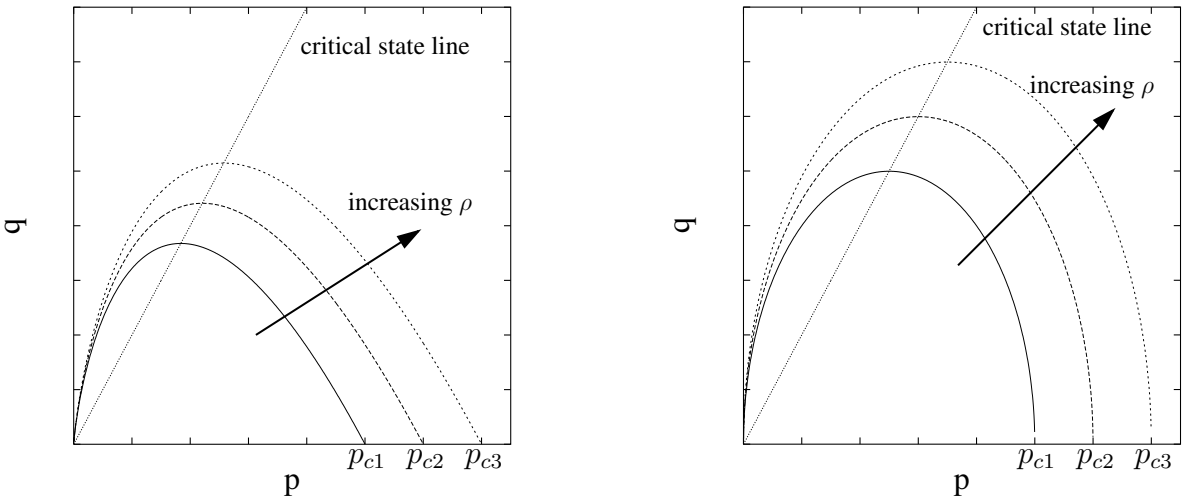

(a) Cam-clay yield surface in the $p-q$-plane.

(b) Modified Cam-clay yield surface in the $p-q$-plane.

Figure 3.5: Cam-clay and modified Cam-clay yield function.

compaction and HELLE ET AL. [72] derived a relation for the macroscopic yield stress under isostatic external load (3.24), which is also the starting point for the derivation of a macroscopic yield surface presented in the very influential publication of FLECK ET AL. [48].

$$p_Y = 2.97 D^2 \frac{D - D_0}{1 - D_0} \sigma_Y \tag{3.24}$$

In Eq. (3.24) D denotes the relative density of the particle assemblage and D_0 is the initial relative density which is $D_0 = 0.64$ for a dense packing of spherical particles. A detailed discussion of the development of micro-mechanical based yield surfaces for powder materials can be found in ASM [13]. An overview can also be found in the thesis of MEYER [103] or COUBE [33] and a brief summary is given in COCKS [31]. FLECK ET AL. [48] derives expressions for the yield function under axisymmetric loading conditions formulated in the deviatoric stress Σ and the means stress Σ_m ($F(\Sigma, \Sigma_m) = 0$) and derives afterwards approximations to these expressions formulated in second deviatoric invariant $\Sigma_e = \sqrt{3 J_2}$ and the mean stress $\Sigma_m = \frac{1}{3} I_1$ which are

$$\text{(linear approx.) } F = \frac{2}{3}\frac{\Sigma_e}{p_Y} + \frac{\Sigma_m}{p_Y} - 1 = 0 \quad | \quad \frac{p_Y}{3} \leq \Sigma_m \leq p_Y \tag{3.25}$$

$$\text{(linear approx.) } F = \frac{2}{3}\frac{\Sigma_e}{p_Y} - \frac{\Sigma_m}{p_Y} - 1 = 0 \quad | \quad -p_Y \leq \Sigma_m \leq -\frac{p_Y}{3} \tag{3.26}$$

$$\text{(quadratic approx.) } F = \left(\frac{\sqrt{5}\Sigma_m}{3 p_Y}\right)^2 + \left(\frac{5\Sigma_e}{18 p_Y} + \frac{2}{3}\right)^2 - 1 = 0 \tag{3.27}$$

$$\tag{3.28}$$

for more general loading conditions. The shape of the quadratic approximation is depicted in Figure 3.6. The micro-mechanically motivated models based on the assumption of spheres in contact with each other by isolated (non-overlapping) contact areas can only be considered to

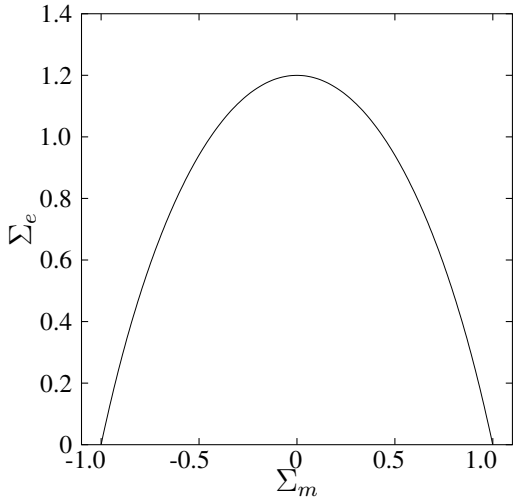

Figure 3.6: Quadratic approximation to the micro-mechanical motivated yield surface proposed by FLECK ET AL. [48].

be valid at comparatively low relative densities. For higher relative densities $D > 0.9$ FLECK ET AL. [48] recommends the use of the likewise micro-mechanically motivated Gurson model, see GURSON [55]. For intermediate relative densities between $D = 0.75$ and $D = 0.9$ he suggests defining a transition from his yield function to the Gurson model. This combination of the model of FLECK ET AL. [48], actually the more advanced model incorporating limited tensile strength of the contacts due to FLECK [47], and the model of GURSON [55] have been applied successfully for example by REDANZ [115], REDANZ [116] and REDANZ AND FLECK [117] to simulate metal powder compaction problems.

MEYER [103] discusses in his thesis the influence of friction between the particles as well as the influence of the contact assumption between the particles (from full cohesive contact to cohesionless contact). Furthermore, he demonstrates that the micro-mechanical model also predicts a dependence of the yield surface on the third invariant of stress. A common feature of the micro-mechanical motivated yield surfaces is the existence of vertices, which make their application in numerical simulations more difficult since the normal to the yield surface is not uniquely defined in the vertices. There is a growing number of publications dealing with the derivation of yield surfaces using discrete or finite element simulations of particle arrangements (often two-dimensional) to compute macroscopic yield surfaces from the simulation of compaction of these particle assemblages, see, for example, XIN ET AL. [141], HEYLIGER AND MCMEEKING [73] and PROCOPIO AND ZAVALIANGOS [112]. LARSSON ET AL. [92] and STORAKERS ET AL. [127] considered more realistic constitutive models for the particles and SHRIDHAR AND FLECK [123] considered the compaction of composite powders to mention only a few of the many publications dealing with the extension of the ideas introduced in the original works on the micro-mechanical modeling of the powder behavior.

Single surface models

Another way to circumvent the problems related to corners in the yield function is the application of single surface yield functions, which resemble the shape of cone-cap yield functions. These kind of single surface yield functions are predominantly applied in constitutive models for granular materials like soils, sand and rock, see among others DESAI [37], LADE AND KIM [90],

DE BOER AND DRESENKAMP [35]. The three yield functions which will be discussed in Section 3.2.2 in some detail fall also in this kind of yield function. They exhibit the special feature of being very flexible with respect to shape due to 7 (5) parameters that determine their shape. Up to 5 parameters define their shape in the I_1-$\sqrt{J_2}$-plane and up to 2 parameters modify the shape in the deviatoric plane from circular to almost triangular. Recently, in KHOEI AND AZAMI [82] a single surface yield function for powder materials (metals) was proposed and adapted to experimental data of the literature.

3.2.2 General 7(5) parameter yield functions

For the purpose of replacing multi-surface cone-cap yield functions by a smooth single surface yield function, less than five parameters are sufficient for reproducing a teardrop-like shape in the I_1-$\sqrt{J_2}$-plane, see, for example, DE BOER AND DRESENKAMP [35], KHOEI AND AZAMI [82]. The following discussion deals with the general, very shape flexible yield functions proposed by EHLERS [42], BIGONI AND PICCOLROAZ [20], and AUBERTIN AND LI [14]. All these authors provide (among other representations) one representation of their yield function of the form[2]

$$F = \sqrt{J_2} - F_h(I_1)F_d(\Theta) \quad \text{or} \quad F = \sqrt{J_2} - F_h(I_1)F_d(\theta) \tag{3.29}$$

with θ and Θ defined in Eq. $(3.5)_3$ and Eq. (3.6):

EHLERS [42]

$$F_h(I_1) = \left[(\varepsilon^2-\delta^2)I_1^4 + 2\beta\varepsilon I_1^3 + \left(\beta^2 - \frac{1}{2}\alpha - 2\varepsilon\kappa\right) I_1^2 - 2\beta\kappa I_1 + \kappa^2\right]^{1/2} \tag{3.30}$$

$$F_d(\Theta) = \left[1 + \frac{2}{\sqrt{27}}\gamma\sin(3\Theta)\right]^{-m/2} \tag{3.31}$$

$$\text{parameters} : \{\alpha, \beta, \gamma, \delta, \varepsilon, m, \kappa\}$$

BIGONI AND PICCOLROAZ [20]

$$F_h(I_1) = \begin{cases} Mp_c\sqrt{(\Phi-\Phi^m)[2(1-\alpha)\Phi+\alpha]} & \Phi \in [0,1] \\ \infty & \Phi \notin [0,1] \end{cases} \tag{3.32}$$

$$F_d(\theta) = \frac{1}{\cos\left[\beta\frac{\pi}{6} - \frac{1}{3}\arccos(\gamma\cos(3\theta))\right]} \tag{3.33}$$

$$\text{parameters} : \{M, p_c, c, \alpha, m, \beta, \gamma\}, \quad \Phi = \frac{c - \frac{1}{3}I_1}{c + p_c}$$

AUBERTIN AND LI [14]

$$F_h(I_1) = \left[\alpha^2(I_1^2 - 2a_1I_1) + a_2^2 - a_3\langle I_1 - I_c\rangle^2\right]^{1/2} \tag{3.34}$$

$$F_d(\Theta) = \left(\frac{b}{\left[b^2 + (1-b^2)\sin^2(45^\circ - 1.5\Theta)\right]^{1/2}}\right)^{\nu} \tag{3.35}$$

$$\text{parameters} : \{a_1, a_2, a_3, \alpha, I_c, b, \nu\}^{\,3}$$

Here, $F_d(\Theta)$ determines the shape in the deviatoric plane and $F_h(I_1)$ defines the shape in the I_1-$\sqrt{J_2}$-plane. These models have in common that they use up to 7 parameters to specify the

[2] Actually BIGONI AND PICCOLROAZ [20] does use $p = -\frac{1}{3}I_1$ and $q = \sqrt{3J_2}$ instead of I_1 and $\sqrt{J_2}$ to formulate the yield function, the expressions have been transformed.

shape of the yield function. Up to 5 of these parameters are used for establishing the shape in the I_1-$\sqrt{J_2}$-plane. The large shape flexibility, which is achieved by using 5(7) parameters for the definition of the yield function has the potential to cause several difficulties. Since we are currently not interested in the dependence on Θ, Θ is assumed to be constant. This allows to simplify Eq. (3.29) into $J_2 = F_h(I_1)$ for representing the yield surface. In the proposal of EHLERS [42] as well as in some other single surface yield functions, e.g. DE BOER AND DRESENKAMP [35], KHOEI AND AZAMI [82], $F_h(I_1)$ takes the special form

$$F_h(I_1) = \sqrt{\sum_{k=0}^{n} a_k I_1^k}. \tag{3.36}$$

The polynomials under the root can have more than 2 solutions depending on their degree n and the choice of parameters. This means that solutions to $F = 0$ can exist outside the elastic domain, see, for example, Figure 3.7 where the situation is depicted for the yield function of EHLERS [42]. The yield surface proposed by AUBERTIN AND LI [14] shares this problem. In their

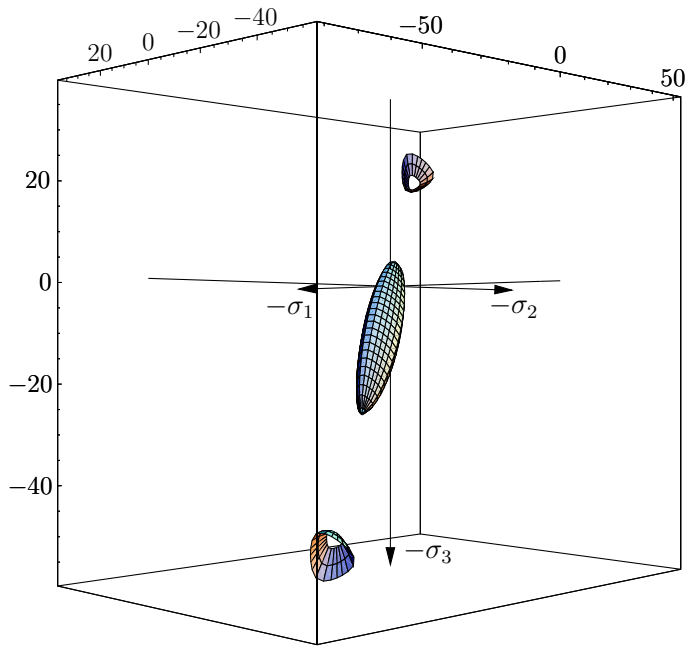

Figure 3.7: Yield surface in stress space with solutions to $F = 0$ away from the elastic domain.

proposal the sum of a second order polynomial and another second order polynomial in Macauley brackets is applied leading to up to three roots of $F_h(I_1)$. The existence of further solutions to $F = 0$ for points in principal stress space beyond the elastic domain causes difficulties using these yield functions in finite elements in view of predictor-corrector schemes usually applied. BIGONI AND PICCOLROAZ [20] avoid this problem by a special case distinction in their yield function formulation setting $F = \infty$ for points with I_1 beyond the I_1 range of the elastic domain. On the other hand, their yield function can no longer be used as a flow potential, since the gradient is not defined in the aforementioned regions in stress space.

The second difficulty encountered in the case of the yield function of EHLERS [42] and also with the yield function proposed by KHOEI AND AZAMI [82] is that convexity of the yield surface is not guaranteed for all admissible choices of parameters. If the shape of the yield

function depends on internal variables, evolving according to differential equations to describe the hardening behavior of the material, additional effort is necessary to ensure the convexity throughout the process.

3.2.3 A new pressure dependent yield function based on log-interpolation

In order to circumvent difficulties like non-convexity throughout the process, corner edges, non-uniqueness in stress-space, a new yield function concept is proposed. The new yield function is constructed with the aim to be comparably shape flexible as the functions proposed by EHLERS [42], BIGONI AND PICCOLROAZ [20] and AUBERTIN AND LI [14] circumventing the problems of guaranteeing convexity by simple constraints on the parameters. Furthermore, it avoids solutions to the yield function beyond the elastic domain, which would make the application of predictor-corrector schemes in the numerical treatment essentially impossible. The basic idea for the new yield function concept is founded on the cap-models described earlier. The two simple yield functions constituting the cap-model are combined by a so-called log-interpolation introducing two additional parameters resulting in a smooth, convex single surface yield function without the difficulty of solutions beyond the elastic domain. The first simple yield function constituent of the new proposal is the generalized ellipse due to ABOU-CHEDID [3] with its center shifted along the hydrostatic axis. The second is the exponential function due to DIMAGGIO AND SANDLER [39] also frequently applied in cap models. After an introduction of the log-interpolation concept, it will be applied directly to the yield function formulation in the form $\sqrt{J_2} = F_h(I_1)$. For the application in the constitutive model a modified approach is chosen, which will be discussed subsequently, leading to a more suitable formulation for the numerical treatment. Furthermore, an expansion of the model to viscoplasticity, where also stress states with $F > 0$ become admissible, is discussed. In BIER AND HARTMANN [19] the application of the elastoplastic constitutive model to describe data from a compaction experiment of a metal powder taken from CARNAVAS AND PAGE [24] has been presented. Additionally, in BIER AND HARTMANN [19] the shape flexibility of the new yield function is demonstrated by adapting it to a variety of materials including sand, soil and metal powders, for which experimental data could be found in the literature.

Log-interpolation

In KREISSELMEIER AND STEINHAUSER [88] and ARNOLD AND FRISCHMUTH [10] the interpolation formula (weighted mean) of two scalar functions $y_1 = f_1(x)$ and $y_2 = f_2(x)$ was proposed, defined by

$$f(x) = -c \ln \left(\frac{e^{-f_1(x)/c} + e^{-f_2(x)/c}}{2} \right), \qquad c > 0. \tag{3.37}$$

The following properties hold for this function:

- $f(x_0) = f_1(x_0) = f_2(x_0)$ holds at the intersection point x_0 of both functions.
- In a certain distance from the intersection point, the resulting function $f(x)$ tends towards the function with the smaller values. In order to see this, the interpolation function (3.37)

is written in the form

$$f(x) = -c \ln \left(\frac{1}{2} e^{-f_1(x)/c} \left(1 + e^{-(f_2(x)-f_1(x))/c} \right) \right) = \\ = f_1(x) + c \ln 2 - c \ln \left(1 + e^{-(f_2(x)-f_1(x))/c} \right). \tag{3.38}$$

If we assume that $f_2(x) \gg f_1(x)$ and monotonicity of $f_1(x)$ and $f_2(x)$ is given, then, the difference of the second and third term converges towards zero and the function $f(x)$ tends towards $f_1(x)$. Even without monotonicity the difference between $f(x)$ and the smaller function (here $f_1(x)$) is always less than $c \ln 2$.

- If $f_2(x) \gg f_1(x)$ holds, $\lim_{c \to 0} f(x) = f_1(x)$ is obviously satisfied in Eq. (3.38), i.e. the weighting factor c enforces the rate of approximation towards the smaller one of the two functions $f_1(x)$ and $f_2(x)$. Actually, the difference between $f(x)$ and the smaller one of the two functions can always be reduced below an arbitrary limit by choosing c sufficiently small.

- The value of the interpolated function $f(x)$ is enclosed between the two function values $f_1(x)$ and $f_2(x)$ for all x.

- If one changes the sign of c, $f(x)$ tends towards the function with larger values.

- If the functions $f_1(x)$ and $f_2(x)$ are convex ($f_1''(x) \leq 0$ and $f_2''(x) \leq 0$), the resulting function $f(x)$ is also convex ($f''(x) \leq 0$). In order to see this, we calculate

$$f'(x) = \frac{e^{f_2/c} f_1' + e^{f_1/c} f_2'}{e^{f_1/c} + e^{f_2/c}}, \tag{3.39}$$

$$f''(x) = \underbrace{-\frac{e^{(f_1+f_2)/c} (f_1' - f_2')^2}{c (e^{f_1/c} + e^{f_2/c})^2}}_{<0} + \frac{e^{f_2/c} f_1'' + e^{f_1/c} f_2''}{e^{f_1/c} + e^{f_2/c}}. \tag{3.40}$$

  Obviously, the convexity of $f_1(x)$ and $f_2(x)$ implies the convexity of $f(x)$. The prime indicates the derivative with respect to the arguments. One can also see that $f'(x)$ is smooth and does not show any jumps if $f_1'(x)$ and $f_2'(x)$ are continuous.

- In the case of $c \to \infty$ one obtains the mean value of the two functions

$$\lim_{c \to \infty} f(x) = \frac{f_1(x) + f_2(x)}{2}. \tag{3.41}$$

Direct application of the log-interpolation

In the following, the main objective is to deal with the application of the interpolation concept to a combination of two yield functions. In the first step, there is no interest in a curved triangular shaped yield function in the deviatoric plane, which is related to the third invariant $(3.3)_3$. If we assume that the yield function $F(I_1, \sqrt{J_2}, J_3)$ is independent of the third invariant J_3, it describes a circular form in the deviatoric plane. Thus, one can confine one's considerations to the I_1-$\sqrt{J_2}$-plane. According to a proposal of ABOU-CHEDID [3], an ellipsoidal shaped yield function is assumed, which is described by its center 3ξ in I_1 direction, the intersection point $I_0 > 0$ with the hydrostatic axis, as well as the ratio $\sqrt{\alpha}$ of the two principal axes of the ellipse in $\sqrt{J_2}$ and I_1 direction. In Fig. 3.8 the functions are depicted. The ellipse has the representation

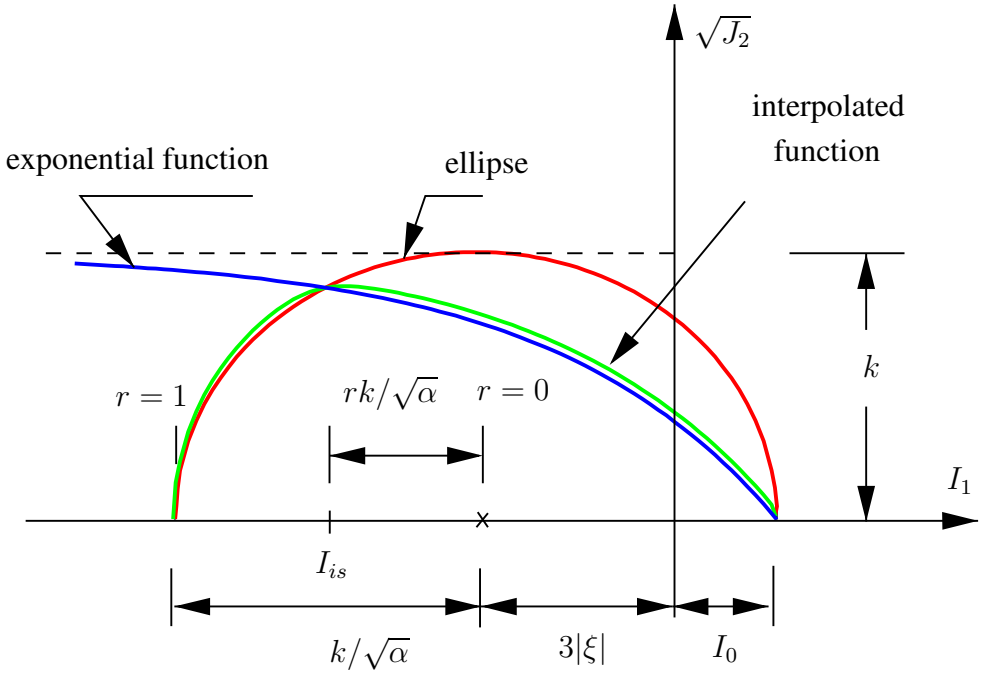

Figure 3.8: Interpolation of ellipse and exponential function and its intersections

$$f_1(I_1) = \sqrt{k^2 - \alpha(I_1 - 3\xi)^2} \qquad \text{with} \qquad k = \sqrt{\alpha(I_0 - 3\xi)^2}. \tag{3.42}$$

In order to obtain a drop-like form, which is more suitable for representing the shear failure region, use is made of an exponential function

$$f_2(I_1) = A_1 - A_2 e^{A_3 I_1}. \tag{3.43}$$

Such a function is fully specified by three (positive) parameters. Here A_1 symbolizes the limit value $A_1 = \lim_{I_1 \to -\infty} f_2(I_1)$. A_2 defines (together with A_1) the intersection with the $\sqrt{J_2}$-axis, $f_2(0) = A_1 - A_2$. A_3 specifies (together with A_2) the slope of f_2 at the intersection with the $\sqrt{J_2}$-axis, $f_2'(0) = -A_2 A_3$. If we demand that f_2 and f_1 intersect the hydrostatic axis at I_0, and if we fix the limit value $A_1 = k$ as well as specifying the second intersection point with the ellipse f_1 using the parameter r, see Fig. 3.8, then the coefficients of the exponential function have the representation

$$A_1 = k, \quad A_2 = \frac{k}{\left(1 - \sqrt{1 - r^2}\right)^{I_0/((3\xi - I_0)(1+r))}}, \quad A_3 = \ln(k/A_2)/I_0. \tag{3.44}$$

According to the interpolation (3.37), Fig. 3.8 shows the resulting function $f(I_1)$ as well as the ellipse $f_1(I_1)$ and the exponential function $f_2(I_1)$.

A yield function is built, if we subtract the interpolated function (3.37) from the ordinate $\sqrt{J_2}$,

$$\begin{aligned} F(I_1, \sqrt{J_2}) &= \sqrt{J_2} - f(I_1) = \\ &= \sqrt{J_2} + c \ln \left(\frac{e^{-f_1(I_1)/c} + e^{-f_2(I_1)/c}}{2} \right). \end{aligned} \tag{3.45}$$

This function is a convex single surface because the ellipse and the exponential function are convex.

The parameters contained in the yield function $f(I_1)$ of Eq.(3.37) can be chosen in such a way that f mirrors some of the well known yield functions, at least in the physically relevant region of stress space, which may be defined as large as needed. In other words, the yield function concept is able to approximate other known yield functions, such as

- the Drucker-Prager yield function,
- the ellipse, either centered or shifted in the stress space, as well as
- the von Mises yield function.

This is shown in Appendix A. These approximations are shown in order to demonstrate the flexibility of the concept.

Modified yield function formulation based on log interpolation

Principally, one could finish the presentation of the previous sections using the yield function (3.45). However, an essential drawback arises in view of the application of an elastic predictor and plastic corrector scheme usually applied in the finite element method. If an elastic predictor computes a stress state outside the range of I_1, where the ellipse function $f_1(I_1)$ is not defined, $f(I_1)$ is not defined either. Thus, a modified approach has to be taken into account. The functions (3.42) and (3.43) are reformulated into the form

$$g_1(I_1, \sqrt{J_2}) = \sqrt{J_2 + \alpha \left(I_1 - 3\xi\right)^2} - k \tag{3.46}$$

$$g_2(I_1, \sqrt{J_2}) = \sqrt{J_2} - A_1 + A_2 e^{A_3 I_1} \tag{3.47}$$

(from $\sqrt{J_2} - f_k(I_1) = 0$, $k = 1, 2$, one obtains (3.46) and (3.47) by reordering). The extension of the interpolation (3.37) to a function in two variables leads to the final yield function

$$F(I_1, \sqrt{J_2}) = ck \ln \left(\frac{e^{g_1(I_1, \sqrt{J_2})/(ck)} + e^{g_2(I_1, \sqrt{J_2})/(ck)}}{2} \right), \tag{3.48}$$

where the interpolation weight c is replaced by ck. This is done for two reasons: first, it normalizes the value range of g_1 and g_2 for the points inside the yield surface to the interval $(0, 1)$, and, accordingly, reduces a process dependence of the interpolation. Second, the value of the argument is reduced which is favorable in view of evaluating the exponential function. Apparently, the factor ck in front of the $\ln$ in Eq.(3.48) could be omitted in the case of $F = 0$. However, for didactic reasons it is preserved in the following. Fig. 3.9(a) shows the modified yield function for $F(I_1, \sqrt{J_2}) \geq 0$, where for $F = 0$ the intersection of both surfaces represents the curve depicted in Fig. 3.8. Here, it must be emphasized that the interpolation formula (3.48) tends towards the larger of the two functions. In the following, it is required that $I_0 \geq 0$ and $\xi \leq 0$ in order to guarantee that the origin of stress space lies within the yield surface. Furthermore, the conditions $0 \leq r \leq 1$, $0 \leq \alpha < \infty$, and $c > 0$ are assumed. In Fig. 3.9(b) the yield surface $F = 0$ is depicted in principal stress space showing its drop-like form.

Since the resulting single surface yield function (3.48) is a function of I_1 and $\sqrt{J_2}$, it obviously differs from Eq. (3.37). Thus, a proof of convexity has to be adapted. In other words, it must be shown that

$$F(I_1, \sqrt{J_2}) = G(g_1(I_1, \sqrt{J_2}), g_2(I_1, \sqrt{J_2})) \tag{3.49}$$

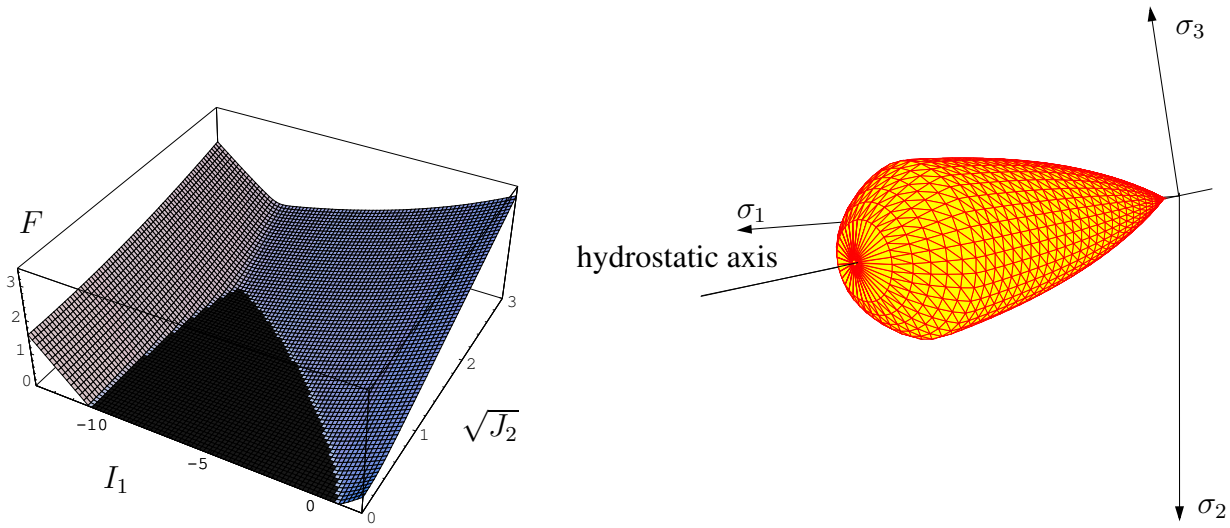

(a) Modified yield function $F(I_1, \sqrt{J_2})$

(b) Principal stress space representation

Figure 3.9: Proposed yield function in various representations

is a convex function in I_1 and $\sqrt{J_2}$. This is shown in Appendix B.

The reformulation of the yield function produces one difficulty. Although $F(I_1, \sqrt{J_2})$ in its original form (3.45) is smooth everywhere, this does not hold for the formulation given in Eq. (3.48). The new form exhibits one corner at the intersection of the yield envelope with the hydrostatic axis at $I_1 = I_0$. Since such a corner might lead to numerical difficulties a rounding off of the yield function following a proposal of ABBO AND SLOAN [2] can be considered. This can be done by changing $g_2(I_1, \sqrt{J_2})$ from Eq. (3.47) in the following way,

$$g_2(I_1, \sqrt{J_2}) = \sqrt{J_2 + \delta} - A_1 + A_2 e^{A_3 I_1}, \qquad \delta > 0. \tag{3.50}$$

Replacing Eq. (3.47) by (3.50) still guarantees the convexity of the yield function. The constant δ should be chosen small enough in order to ensure that the elastic domain still includes the origin of principal stress space and big enough to remove the corner efficiently.

3.3 Rate-independent constitutive model

On the basis of the proposed yield function in the previous section, a new constitutive model for metal powder compaction is developed. The finite strain constitutive model is derived in such a way that it cannot produce contradictions to the Clausius-Duhem inequality, see Section 2.2.5 (thermo-mechanically consistent).

Since the yield function represents an interpolation between an ellipsoid and an exponential function, ξ controls the hardening in the direction of the hydrostatic stress state and α influences the form of the drop-like yield function. $\mathrm{I}_1 = \mathrm{tr}\,\hat{\mathbf{P}}$ and $\mathrm{J}_2 = 1/2\,\hat{\mathbf{P}}^D \cdot \hat{\mathbf{P}}^D$ symbolize invariants of the concerned stress tensor $\hat{\mathbf{P}}$. In the constitutive model proposed later, $\hat{\mathbf{P}}$ defines the Mandel stress tensor, see definition (3.68). Within the proposed constitutive model the yield function given in Eq.(3.48) is applied. In contrast to the general formulation given in Eq.(3.48), where only the dependence on the invariants of the stress tensor (and its deviator) is considered the

dependence on the internal variable α and the accumulated plastic strain through the variable ξ are explicitly assumed in the following. Furthermore, we replace $\sqrt{\mathrm{J}_2}$ by J_2. This reads in detail

$$\hat{F}(\mathrm{I}_1, \mathrm{J}_2, \xi, \alpha) := F(\mathrm{I}_1, \sqrt{\mathrm{J}_2}, \xi, \alpha) = ck \ln \left(\frac{e^{g_1(I_1, \sqrt{J_2})/(ck)} + e^{g_2(I_1, \sqrt{J_2})/(ck)}}{2} \right) \tag{3.51}$$

where the dependence on α and ξ is contained in g_1 and g_2 given by Eq.(3.46) and Eq.(3.47) which is omitted in the representation for brevity. The associative flow rule

$$\overset{\triangle}{\hat{\mathbf{\Gamma}}}_{\mathrm{p}} = \lambda \frac{\partial \hat{F}}{\partial \hat{\mathbf{P}}} = \lambda \left(\frac{\partial \hat{F}}{\partial \mathrm{I}_1} \mathbf{I} + \frac{\partial \hat{F}}{\partial \mathrm{J}_2} \hat{\mathbf{P}}^D \right) \tag{3.52}$$

is assumed with λ defining the plastic multiplier. Here, the derivatives

$$\frac{\partial \hat{F}}{\partial \mathrm{I}_1} = \frac{\partial F}{\partial \mathrm{I}_1} = \frac{\partial F}{\partial g_1} \frac{\partial \hat{g}_1}{\partial \mathrm{I}_1} + \frac{\partial F}{\partial g_2} \frac{\partial \hat{g}_2}{\partial \mathrm{I}_1}, \tag{3.53}$$

$$\frac{\partial \hat{F}}{\partial \mathrm{J}_2} = \frac{1}{2\sqrt{\mathrm{J}_2}} \frac{\partial F}{\partial \sqrt{\mathrm{J}_2}} = \frac{1}{2\sqrt{\mathrm{J}_2}} \left(\frac{\partial F}{\partial g_1} \frac{\partial \hat{g}_1}{\partial \sqrt{\mathrm{J}_2}} + \frac{\partial F}{\partial g_2} \frac{\partial \hat{g}_2}{\partial \sqrt{\mathrm{J}_2}} \right) \tag{3.54}$$

occur due to the application of the chain rule, which requires the derivatives

$$\frac{\partial F}{\partial g_1} = \frac{e^{g_1/(ck)}}{e^{g_1/(ck)} + e^{g_2/(ck)}}, \qquad \frac{\partial F}{\partial g_2} = \frac{e^{g_2/(ck)}}{e^{g_1/(ck)} + e^{g_2/(ck)}}, \tag{3.55}$$

$$\frac{\partial \hat{g}_1}{\partial \mathrm{I}_1} = \frac{\alpha(\mathrm{I}_1 - 3\xi)}{\sqrt{\mathrm{J}_2 + \alpha(\mathrm{I}_1 - 3\xi)^2}}, \qquad \frac{\partial \hat{g}_2}{\partial \mathrm{I}_1} = A_2 A_3 e^{A_3 \mathrm{I}_1}, \tag{3.56}$$

$$\frac{\partial \hat{g}_1}{\partial \sqrt{\mathrm{J}_2}} = \frac{\sqrt{\mathrm{J}_2}}{\sqrt{\mathrm{J}_2 + \alpha(\mathrm{I}_1 - 3\xi)^2}}, \qquad \frac{\partial \hat{g}_2}{\partial \sqrt{\mathrm{J}_2}} = 1. \tag{3.57}$$

In order to motivate a constitutive model in a thermo-mechanically consistent framework, use is made of the concept of dual variables of Section 2.3.2, particularly, family 1 variables (HAUPT AND TSAKMAKIS [69], HAUPT AND TSAKMAKIS [70]). Furthermore, the approach proposed by TSAKMAKIS [135] and LÄMMER AND TSAKMAKIS [91] is extended to the case of the pressure-dependent yield function (3.48). Accordingly, an additive split of the specific free-energy into an elastic and a plastic part is assumed,

$$\hat{\psi}(\hat{\mathbf{\Gamma}}_{\mathrm{e}}, r_K, r_D) = \hat{\psi}_e(\hat{\mathbf{\Gamma}}_{\mathrm{e}}) + \hat{\psi}_p(r_K, r_D). \tag{3.58}$$

Furthermore, the plastic part is assumed to decompose into two parts, where $\hat{\psi}_K$ results from kinematic and $\hat{\psi}_D$ from distortional hardening processes

$$\hat{\psi}_p(r_K, r_D) = \hat{\psi}_K(r_K) + \hat{\psi}_D(r_D). \tag{3.59}$$

r_D defines a strain-like scalar-valued internal variable and

$$r_K = \hat{r}_K(\mathbf{C}_{\mathrm{p}}) = \ln(\det \mathbf{C}_{\mathrm{p}})/2 = \ln(\det \mathbf{F}_{\mathrm{p}}) \tag{3.60}$$

is related to the plastic volume change,

$$\dot{r}_K = \frac{\dot{\ln(\det \mathbf{C}_{\mathrm{p}})}}{2} = \frac{1}{2} \dot{\mathbf{C}}_{\mathrm{p}} \cdot \mathbf{C}_{\mathrm{p}}^{-1} = \mathrm{tr} \overset{\triangle}{\hat{\mathbf{\Gamma}}}_{\mathrm{p}}. \tag{3.61}$$

Under the assumption of isothermal processes, the Clausius-Duhem inequality (2.72) reads

$$\tilde{\mathbf{T}} \cdot \dot{\mathbf{E}} - \rho_{\mathrm{R}} \dot{\hat{\psi}} = \mathbf{S} \cdot \mathbf{D} - \rho_{\mathrm{R}} \dot{\hat{\psi}} = \hat{\mathbf{T}} \cdot \overset{\triangle}{\hat{\mathbf{\Gamma}}} - \rho_{\mathrm{R}} \dot{\hat{\psi}} \geq 0. \tag{3.62}$$

with the stress tensor operating on the plastic intermediate configuration

$$\hat{\mathbf{T}} = \hat{\mathbf{F}}_{\mathrm{e}}^{-1} \mathbf{S} \hat{\mathbf{F}}_{\mathrm{e}}^{-T} = \mathbf{F}_{\mathrm{p}} \tilde{\mathbf{T}} \mathbf{F}_{\mathrm{p}}^{T}, \tag{3.63}$$

see Section 2.2.6 and Tab. 2.1. If the specific free-energy (3.58) is inserted into the dissipation inequality (3.62), one obtains

$$\left(\hat{\mathbf{T}} - \rho_{\mathrm{R}} \frac{\mathrm{d}\hat{\psi}_e}{\mathrm{d}\hat{\mathbf{\Gamma}}_{\mathrm{e}}} \right) \cdot \overset{\triangle}{\hat{\mathbf{\Gamma}}}_{\mathrm{e}} + \hat{\mathbf{T}} \cdot \overset{\triangle}{\hat{\mathbf{\Gamma}}}_{\mathrm{p}} + \rho_{\mathrm{R}} \frac{\mathrm{d}\hat{\psi}_e}{\mathrm{d}\hat{\mathbf{\Gamma}}_{\mathrm{e}}} \hat{\mathbf{\Gamma}}_{\mathrm{e}} \cdot \mathbf{L}_{\mathrm{p}}^{T} + \rho_{\mathrm{R}} \hat{\mathbf{\Gamma}}_{\mathrm{e}} \frac{\mathrm{d}\hat{\psi}_e}{\mathrm{d}\hat{\mathbf{\Gamma}}_{\mathrm{e}}} \cdot \mathbf{L}_{\mathrm{p}} - \rho_{\mathrm{R}} \dot{\hat{\psi}}_p \geq 0, \tag{3.64}$$

where use is made of definitions (2.101)-(2.103). Firstly, the potential relation

$$\hat{\mathbf{T}} = \rho_{\mathrm{R}} \frac{\mathrm{d}\hat{\psi}_e}{\mathrm{d}\hat{\mathbf{\Gamma}}_{\mathrm{e}}} = 2\rho_{\mathrm{R}} \frac{\mathrm{d}\overline{\psi}_e}{\mathrm{d}\hat{\mathbf{C}}_{\mathrm{e}}} \tag{3.65}$$

with the property of isotropy is assumed, as is customary. This implies the commutativity of

$$\hat{\mathbf{\Gamma}}_{\mathrm{e}} \frac{\mathrm{d}\hat{\psi}_e}{\mathrm{d}\hat{\mathbf{\Gamma}}_{\mathrm{e}}} = \frac{\mathrm{d}\hat{\psi}_e}{\mathrm{d}\hat{\mathbf{\Gamma}}_{\mathrm{e}}} \hat{\mathbf{\Gamma}}_{\mathrm{e}} \tag{3.66}$$

leading to the remaining dissipation inequality

$$\mathcal{D}_p = \hat{\mathbf{P}} \cdot \overset{\triangle}{\hat{\mathbf{\Gamma}}}_{\mathrm{p}} - \rho_{\mathrm{R}} \dot{\hat{\psi}}_p \geq 0, \tag{3.67}$$

where the Mandel stress tensor

$$\hat{\mathbf{P}} = (\mathbf{I} + 2\hat{\mathbf{\Gamma}}_{\mathrm{e}}) \hat{\mathbf{T}} = \hat{\mathbf{C}}_{\mathrm{e}} \hat{\mathbf{T}} = \hat{\mathbf{T}} \hat{\mathbf{C}}_{\mathrm{e}} \tag{3.68}$$

has been introduced. Secondly, a hydrostatic stress part is separated introducing the stress-like variable ξ

$$\mathcal{D}_p = (\hat{\mathbf{P}} - \xi \mathbf{I}) \cdot \overset{\triangle}{\hat{\mathbf{\Gamma}}}_{\mathrm{p}} + \xi \mathbf{I} \cdot \overset{\triangle}{\hat{\mathbf{\Gamma}}}_{\mathrm{p}} - \rho_{\mathrm{R}} \dot{\hat{\psi}}_p \geq 0. \tag{3.69}$$

If the flow rule (3.52) is inserted into the first term and if the definitions

$$\xi := \rho_{\mathrm{R}} \frac{\mathrm{d}\hat{\psi}_K}{\mathrm{d}r_K} \qquad \text{and} \qquad \alpha := \rho_{\mathrm{R}} \frac{\mathrm{d}\hat{\psi}_D}{\mathrm{d}r_D} \tag{3.70}$$

are taken into account, the remaining inequality

$$\mathcal{D}_p = \frac{\dot{s}}{\chi} (\hat{\mathbf{P}} - \xi \mathbf{I}) \cdot \frac{\partial F}{\partial \hat{\mathbf{P}}} + \xi \mathrm{tr} \overset{\triangle}{\hat{\mathbf{\Gamma}}}_{\mathrm{p}} - \xi \dot{r}_K - \alpha \dot{r}_D \geq 0 \tag{3.71}$$

arises. Here, the plastic multiplier λ is replaced by the rate of the plastic arc-length

$$\dot{s} = \sqrt{\overset{\triangle}{\hat{\mathbf{\Gamma}}}_{\mathrm{p}} \cdot \overset{\triangle}{\hat{\mathbf{\Gamma}}}_{\mathrm{p}}} = \lambda \chi \tag{3.72}$$

with

$$\chi = \hat{\chi}(\mathrm{I}_1, \mathrm{J}_2, \xi, \alpha) = \sqrt{3\left(\frac{\partial \hat{F}}{\partial \mathrm{I}_1}\right)^2 + 2\mathrm{J}_2\left(\frac{\partial \hat{F}}{\partial \mathrm{J}_2}\right)^2}, \tag{3.73}$$

where use is made of the flow rule (3.52).

In view of the definitions (3.70) the partial specific free-energies

$$\rho_{\mathrm{R}}\hat{\psi}_K(r_K) = \frac{a_1}{a_2^2}e^{-a_2 r_K} + \frac{c_K}{2}r_K^2 \tag{3.74}$$

$$\rho_{\mathrm{R}}\hat{\psi}_D(r_D) = \frac{c_D}{2}r_D^2 \tag{3.75}$$

are assumed, leading to the internal variable α and its evolution equation

$$\alpha = c_D r_D \qquad \longrightarrow \qquad \dot{\alpha} = c_D \dot{r}_D \tag{3.76}$$

as well as to the hardening variable

$$\xi = -\frac{a_1}{a_2}e^{-a_2 r_K} + c_K r_K. \tag{3.77}$$

ξ describes the kinematic hardening behavior in the sense that the center of the yield function moves in the direction of the hydostatic axis, and r_K is related to the plastic volume change, see Eq. (3.60).

We consider again the remaining inequality (3.71) of the form

$$\mathcal{D}_p = \mathcal{D}_K + \mathcal{D}_D \geq 0. \tag{3.78}$$

The term

$$\mathcal{D}_K = \xi(\mathrm{tr}\,\overset{\triangle}{\hat{\mathbf{\Gamma}}}_{\mathrm{p}} - \dot{r}_K) \geq 0 \tag{3.79}$$

holds due to definition (3.60) and the time derivative (3.61). Additionally,

$$\mathcal{D}_D = \frac{\dot{s}}{\chi}(\hat{\mathbf{P}} - \xi\mathbf{I}) \cdot \frac{\partial F}{\partial \hat{\mathbf{P}}} - \alpha\dot{r}_D = \tag{3.80}$$

$$= \alpha\left(\frac{\dot{s}}{\alpha\chi}(\hat{\mathbf{P}} - \xi\mathbf{I}) \cdot \frac{\partial F}{\partial \hat{\mathbf{P}}} - \frac{\dot{\alpha}}{c_D}\right) \geq 0 \tag{3.81}$$

must hold, where use is made of $(3.76)_2$. This inequality can be satisfied for

$$\frac{\dot{s}}{\alpha\chi}(\hat{\mathbf{P}} - \xi\mathbf{I}) \cdot \frac{\partial F}{\partial \hat{\mathbf{P}}} - \frac{\dot{\alpha}}{c_D} = \alpha\frac{b_D}{c_D}\dot{s}, \tag{3.82}$$

with $b_D > 0$, $c_D > 0$. In other words, inequality (3.81) is fulfilled, owing to the evolution equation

$$\dot{\alpha} = \left(\frac{c_D}{\alpha\chi}(\hat{\mathbf{P}} - \xi\mathbf{I}) \cdot \frac{\partial F}{\partial \hat{\mathbf{P}}} - \alpha b_D\right)\dot{s}. \tag{3.83}$$

Since α has always to be positive, this ordinary differential equation, which is briefly studied in Appendix C, has to be investigated. Only in the case of non-negative first term, i.e. $(\hat{\mathbf{P}} - \xi\mathbf{I}) \cdot \partial F/\partial\hat{\mathbf{P}} \geq 0$, $\alpha \geq 0$ is guaranteed. This inequality is related to the convexity of the yield function. Shortly spoken, a function is convex if and only if $f(\mathbf{y}) \geq f(\mathbf{x}) + \{\partial f(\mathbf{x})/\partial\mathbf{x}\}^T\{\mathbf{y}-\mathbf{x}\}$

is satisfied (see, for example, LUENBERGER [99]). For the stress state $\mathbf{x}\hat{=}\hat{\mathbf{P}}$ satisfying the yield condition $F(\hat{\mathbf{P}}) = 0$, and the center of the ellipsoid $\mathbf{y}\hat{=}\xi\mathbf{I}$, this condition reads

$$F(3\xi, 0, \xi, \alpha) \geq \frac{\partial F(\mathrm{I}_1, \sqrt{\mathrm{J}_2}, \xi, \alpha)}{\partial \hat{\mathbf{P}}} \cdot (\xi\mathbf{I} - \hat{\mathbf{P}}). \tag{3.84}$$

In view of Eq.(3.51) one obtains $F(3\xi, 0, \xi, \alpha) \leq 0$ so that

$$\frac{\partial F(\mathrm{I}_1, \sqrt{\mathrm{J}_2}, \xi, \alpha)}{\partial \hat{\mathbf{P}}} \cdot (\hat{\mathbf{P}} - \xi\mathbf{I}) = (\mathrm{I}_1 - 3\xi)\frac{\partial F}{\partial \mathrm{I}_1} + \sqrt{\mathrm{J}_2}\frac{\partial F}{\partial \sqrt{\mathrm{J}_2}} \geq 0 \tag{3.85}$$

is satisfied. Whether α increases or decreases is mainly controlled by the material parameters c_D and b_D and depends also on the initial condition $\alpha(0) = \alpha_0$.

The elastic deformations are very small in comparison to the inelastic strains. Thus, use is made of a rather simple strain-energy function in Eq. (3.58), see also (3.65), proposed by SIMO AND PISTER [125],

$$\rho_{\mathrm{R}}\overline{\psi}_e(\hat{\mathbf{C}}_{\mathrm{e}}) = \frac{\Lambda}{2}\left(\ln(J_e)\right)^2 - \mu \ln J_e + \frac{\mu}{2}(\operatorname{tr}\hat{\mathbf{C}}_{\mathrm{e}} - 3) \tag{3.86}$$

with $J_e = (\det \hat{\mathbf{C}}_{\mathrm{e}})^{1/2}$. In view of the potential relation (3.65) we obtain

$$\hat{\mathbf{T}} = (\Lambda \ln J_e - \mu)\hat{\mathbf{C}}_{\mathrm{e}}^{-1} + \mu\mathbf{I} \tag{3.87}$$

i.e.

$$\hat{\mathbf{P}} = \hat{\mathbf{C}}_{\mathrm{e}}\hat{\mathbf{T}} = (\Lambda \ln J_e - \mu)\mathbf{I} + \mu\hat{\mathbf{C}}_{\mathrm{e}}, \tag{3.88}$$

($\hat{\mathbf{P}}^D = \mu\hat{\mathbf{C}}_{\mathrm{e}}^D$).

In conclusion, the constitutive model, which is recapped in Tab. 3.2, is thermo-mechanically consistent in the sense of fulfilling the Clausius-Duhem inequality. Beside the flow rule, one evolution equation for α, see Eq.(3.83), describes the distortional hardening behavior and the kinematical hardening variable ξ is described by Eq.(3.77). The variables control the hardening behavior and are connected to the geometrical idea of the center and the axes-ratio of ellipsoidal part of the yield function. The proposed model, formulated with quantities relative to the reference configuration, is collected in Tab. 3.3.

3.4 Expansion to viscoplasticity

Despite the fact that the rate-dependent effects at ambient temperature might be negligible for metal powders, it has been decided to generalize the original elastoplasticity model to viscoplasticity. This has the further merit of easing the numerical solution of the constitutive equations of evolutionary type. The expansion of the model from elastoplasticity to viscoplasticity is straightforward. The elasticity relation remains unchanged. The loading condition, see Tab. 3.3, is simplified in such a way that for $\hat{F} \leq 0$ the behavior is assumed to be elastic and for $\hat{F} > 0$ the behavior is viscoplastic. The yield function still represents the border of the elastic domain, however it does no longer serve as an additional constraint from which the plastic multiplier could be calculated. Accordingly, the plastic multiplier in the flow rule and the evolution equation,

	elasticity	*elastoplasticity*
loading condition	$\hat{F} < 0$ or $\hat{F} = 0 \wedge \dot{\hat{F}}\big\vert_{\dot{\hat{\mathbf{q}}}=\mathbf{0}} < 0$	$\hat{F} = 0 \wedge \dot{\hat{F}}\big\vert_{\dot{\hat{\mathbf{q}}}=\mathbf{0}} \geq 0$
free energy	$\hat{\psi}(\hat{\mathbf{\Gamma}}_\mathrm{e}, r_K, r_D) = \hat{\psi}_e(\hat{\mathbf{\Gamma}}_\mathrm{e}) + \hat{\psi}_K(r_K) + \hat{\psi}_D(r_D)$ $\hat{\psi}_e(\hat{\mathbf{\Gamma}}_\mathrm{e}) = \frac{1}{\rho_\mathrm{R}}\left(\frac{\Lambda}{2}\left(\ln(J_e)\right)^2 - \mu \ln J_e + \mu \mathrm{tr}\,\hat{\mathbf{\Gamma}}_\mathrm{e}\right)$ $\hat{\psi}_K(r_K) = \frac{1}{\rho_\mathrm{R}}\frac{a_1}{a_2^2}e^{-a_2 r_K} + \frac{c_K}{2}r_K^2, \quad \hat{\psi}_D(r_D) = \frac{1}{\rho_\mathrm{R}}\frac{c_D}{2}r_D^2$	
elasticity relation	$\hat{\mathbf{P}} = (\Lambda \ln J_e - \mu)\mathbf{I} + \mu \hat{\mathbf{C}}_\mathrm{e}$	
flow rule	$\overset{\triangle}{\hat{\mathbf{\Gamma}}}_\mathrm{p} = \mathbf{0}$	$\overset{\triangle}{\hat{\mathbf{\Gamma}}}_\mathrm{p} = \lambda\left(\frac{\partial \hat{F}}{\partial \mathrm{I}_1}\mathbf{I} + \frac{\partial \hat{F}}{\partial \mathrm{J}_2}\hat{\mathbf{P}}^D\right)$
distortional hardening	$\dot{\alpha} = 0$	$\dot{\alpha} = \lambda\left(\frac{c_D}{\alpha}\left((\mathrm{I}_1 - 3\xi)\frac{\partial \hat{F}}{\partial \mathrm{I}_1} + \sqrt{\mathrm{J}_2}\frac{\partial \hat{F}}{\partial \sqrt{\mathrm{J}_2}}\right) - b_D \alpha \chi\right)$
abbrev.	$\mathrm{I}_1 = \mathrm{tr}\,\hat{\mathbf{P}}$, $\mathrm{J}_2 = (\hat{\mathbf{P}}^D \cdot \hat{\mathbf{P}}^D)/2$, $J_e = (\det \hat{\mathbf{C}}_\mathrm{e})^{1/2}$ $r_K = \ln(\det \mathbf{C}/\det \hat{\mathbf{C}}_\mathrm{e})/2$, $\xi = -\frac{a_1}{a_2}e^{-a_2 r_K} + c_K r_K$	

Table 3.2: Constitutive model expressed with quantities relative to the intermediate configuration (with $\hat{\mathbf{q}} = \{s, \mathbf{F}_\mathrm{p}, \alpha\}$)

	elasticity	*elastoplasticity*
loading condition	$\hat{F} < 0$ or $\hat{F} = 0 \wedge \dot{\hat{F}}\big\vert_{\dot{\mathbf{C}}_\mathrm{p}=\mathbf{0}} < 0$	$\hat{F} > 0$ or $\hat{F} = 0 \wedge \dot{\hat{F}}\big\vert_{\dot{\mathbf{C}}_\mathrm{p}=\mathbf{0}} \geq 0$
elasticity relation	$\tilde{\mathbf{T}} = (\Lambda \ln J_e - \mu)\mathbf{C}^{-1} + \mu \mathbf{C}_\mathrm{p}^{-1}$	
flow rule	$\dot{\mathbf{C}}_\mathrm{p} = \mathbf{0}$	$\dot{\mathbf{C}}_\mathrm{p} = \lambda 2\left(\frac{\partial \hat{F}}{\partial \mathrm{I}_1}\mathbf{I} + \frac{\partial \hat{F}}{\partial \mathrm{J}_2}(\mathbf{C}\tilde{\mathbf{T}} - (\mathrm{I}_1/3)\mathbf{I})\right)\mathbf{C}_\mathrm{p}$
distortional hardening	$\dot{\alpha} = 0$	$\dot{\alpha} = \lambda\left(\frac{c_D}{\alpha}\left((\mathrm{I}_1 - 3\xi)\frac{\partial \hat{F}}{\partial \mathrm{I}_1} + \sqrt{\mathrm{J}_2}\frac{\partial \hat{F}}{\partial \sqrt{\mathrm{J}_2}}\right) - b_D \alpha \chi\right)$
abbrev.	$\mathrm{I}_1 = \mathrm{tr}\,(\tilde{\mathbf{T}}\mathbf{C})$, $\mathrm{J}_2 = (\mathbf{C}\tilde{\mathbf{T}} \cdot \tilde{\mathbf{T}}\mathbf{C} - \mathrm{I}_1^2/3)/2$, $J_e = ((\det \mathbf{C})/(\det \mathbf{C}_\mathrm{p}))^{1/2}$ $r_K = \ln(\det \mathbf{C}_\mathrm{p})/2$, $\xi = -\frac{a_1}{a_2}e^{-a_2 r_K} + c_K r_K$	

Table 3.3: Constitutive model expressed with quantities relative to the reference configuration

see Tab. 3.3, is replaced by the additional variable $\tilde{\lambda}$, which is calculated from the additional constitutive equation, see PERZYNA [111],

$$\tilde{\lambda} = \left\langle \frac{\hat{F}}{\sigma_0} \right\rangle^{r_{vp}} \frac{1}{\eta}. \tag{3.89}$$

Here, the three parameters η, σ_0 and r_{vp} have been introduced. It is worthwhile mentioning that for $\eta = 0$ the original equations of elastoplasticity are retrieved, see HAUPT ET AL. [68]. Thus, the implementation of the model of viscoplasticity includes the limit case of elastoplasticity in a very simple manner. The parameter σ_0 is needed to make the expression in the Macauley brackets $\langle \cdot \rangle$ dimensionless. The viscoplasticity model is summarized in Tab. 3.4 expressed in quantities relative to the reference configuration.

	elasticity	*viscoplasticity*
loading condition	$\hat{F} \leq 0$	$\hat{F} > 0$
elasticity relation	$\tilde{\mathbf{T}} = (\Lambda \ln J_e - \mu)\mathbf{C}^{-1} + \mu \mathbf{C}_\mathrm{p}^{-1}$	
flow rule	$\dot{\mathbf{C}}_\mathrm{p} = \mathbf{0}$	$\dot{\mathbf{C}}_\mathrm{p} = \tilde{\lambda} 2 \left(\frac{\partial \hat{F}}{\partial \mathrm{I}_1} \mathbf{I} + \frac{\partial \hat{F}}{\partial \mathrm{J}_2} (\mathbf{C}\tilde{\mathbf{T}} - (\mathrm{I}_1/3)\mathbf{I}) \right) \mathbf{C}_\mathrm{p}$
distortional hardening	$\dot{\alpha} = 0$	$\dot{\alpha} = \tilde{\lambda} \left(\frac{c_D}{\alpha} \left((\mathrm{I}_1 - 3\xi) \frac{\partial \hat{F}}{\partial \mathrm{I}_1} + \sqrt{\mathrm{J}_2} \frac{\partial \hat{F}}{\partial \sqrt{\mathrm{J}_2}} \right) - b_D \alpha \chi \right)$
abbrev.	$\mathrm{I}_1 = \mathrm{tr}\,(\tilde{\mathbf{T}}\mathbf{C})$, $\mathrm{J}_2 = (\mathbf{C}\tilde{\mathbf{T}} \cdot \tilde{\mathbf{T}}\mathbf{C} - \mathrm{I}_1^2/3)/2$, $J_e = ((\det \mathbf{C})/(\det \mathbf{C}_\mathrm{p}))^{1/2}$ $r_K = \ln(\det \mathbf{C}_\mathrm{p})/2$, $\xi = -\frac{a_1}{a_2} e^{-a_2 r_K} + c_K r_K$, $\tilde{\lambda} = \left\langle \frac{\hat{F}}{\sigma_0} \right\rangle^{r_{vp}} \frac{1}{\eta}$	

Table 3.4: Constitutive model (viscoplasticity) expressed with quantities relative to the reference configuration

Chapter 4

Material parameter identification

This chapter deals with the material parameter identification of the constitutive model. First, a survey of the literature available on the topic of material parameter identification from experiments on metal powders is provided. Afterwards, the experiments that have been developed and conducted in close cooperation with Prof. Frage at the Ben Gurion University of the Negev in Beer Sheva, Israel are described. This includes the description of the experimental setup as well as the characterization of the treatment of the raw data. Subsequently, the material parameter identification itself is discussed and the results are provided.

4.1 Experimental-based parameter determination

All constitutive models contain a number of material parameters. While the general behavior of a material is already defined by the structure of the constitutive equations, the material parameters provide the possibility to adapt quantitatively the model behavior to experimental results. Usually, the material parameters are determined from simple experiments (leading to a homogeneous deformation), which are only or at least dominantly influenced by one or a subset of the material parameters. With respect to the material parameter identification of the metal powder compaction models, various authors have proposed different approaches which invoke different levels of experimental effort.

Among the publications which suggest an elaborate experimental program for the parameter identification, are, for example, the thesis of COUBE [33] and the article of CHTOUROU ET AL. [30]. In CHTOUROU ET AL. [30] the material parameter identification for a cap model (elasto-plasticity) is discussed in some detail. They apply resonant frequency tests on pre-compacted specimen of various relative densities, which were machined into rectangular bars, in order to determine the elastic properties of the material. For identifying the hardening properties (growth of cap surface due to densification) they apply hydrostatic compression experiments. Additionally, they use a triaxial apparatus to superimpose an increasing axial stress on a number of hydrostatic pre-compaction stress states in order to determine the shape of the cap yield surface. Furthermore, they perform free uniaxial compression tests on pre-compacted specimen for the determination of the shear failure surface. A somewhat similar approach, which does also rest mainly upon testing of pre-compacted samples, is presented by COUBE [33] for his Drucker-Prager cap model. He uses data from free compression and "Brazilian disc" tests on pre-compacted specimens of various densities for the identification of the failure line (Drucker-Prager cone) and applies ultrasonic tests on machined pre-compacts to determine the elasticity parameters. Furthermore, results from triaxial and die compaction testing (iso-density points) are used for the

identification of the cap surface and its evolution. Tests to determine the tensile cut-off value are described, which are conducted with the help of a special two-part die, tearing the compacted specimen apart with rather small tensile stresses of about 1-2 MPa (increasing with density). On the one hand, a detailed experimental analysis of a given powder material is of course desirable for the material parameter identification. On the other hand, such experimental effort may not always be feasible and some of the experiments mentioned above, especially the ones conducted with pre-compacted and machined specimens are questionable in view of their reliability in respect to material parameter identification of a metal powder model.

One of the earliest publications suggesting the application of a Drucker-Prager cap model for metal powder compaction problems is due to WATSON AND WERT [139]. They also suggest and use the application of ultrasonic wave speed measurements to determine the elasticity parameters of pre-compacts (aluminum powder). Furthermore, they determine the yield function and its evolution from hydrostatic compression, constrained compression (die compaction), free compression and unconstrained tension tests. Since the die used is not fully instrumented, they have to calculate the radial stress state inside the die from the elasticity parameters identified previously and the measured axial stress.

In the thesis of CARNAVAS [23] experimental data on several metal powders is proposed, obtained in uniaxial constrained compression and triaxial experiments. In addition to the pure loading experiments, he reports loading experiments with intermediate unloading and reloading cycles. Since the apparatus is fully instrumented, the radial stress as well as the axial stress are known during loading and unloading and can be used to determine the elasticity parameters as presented in CARNAVAS AND PAGE [24]. This way of determining the elastic properties has the merit that the experiments are not conducted on machined pre-compacts. The unloading and reloading behavior of the compacted powder is studied directly, so that there is no intermediate process (machining) which might have undesired influence on the results. On the other hand, this procedure demands the determination of the radial stress inside the die, which is a non-trivial task. CARNAVAS [23] solves this problem by measuring the hoop strains (with strain gauges) on the outer surface of the die calibrating the apparatus by pressurizing castor oil (hydrostatic pressure) inside the die. A similar procedure to determine the radial stress during die compaction is used by GEINDREAU ET AL. [50], who also measure the circumferential strains at the outer die surface and calibrate their apparatus using an unspecified incompressible material.

In BIER AND HARTMANN [19] the experimental data from die compaction experiments reported by CARNAVAS [23] has been used to identify the material parameters of the constitutive model defined in the previous chapter. Additionally, it is shown that the model response, adapted to die compaction data only, does also represent the triaxial data reported by CARNAVAS [23] for the same powder fairly well, see Fig. 4.1 taken from BIER AND HARTMANN [19]. The positive experience with the parameter identification from (fully instrumented) die compaction data gives reason to rely mainly on this kind of experiment for the parameter identification for the powder under consideration, which is discussed in the following section.

4.2 Description of the experiments

The investigated material, within this project is a fine grained copper powder with irregular morphology as shown in the SEM image of the loose powder (Fig. 4.2). The copper powder has been purchased from Alfa under Stock number 13990. The density of the particle base material (Cu) is 8.96 g/cm^3. The average particle size of the powder particles, as stated by the supplier, is 8-11 μm with less than 10% of the powder particles greater than 44 μm (+325 mesh).

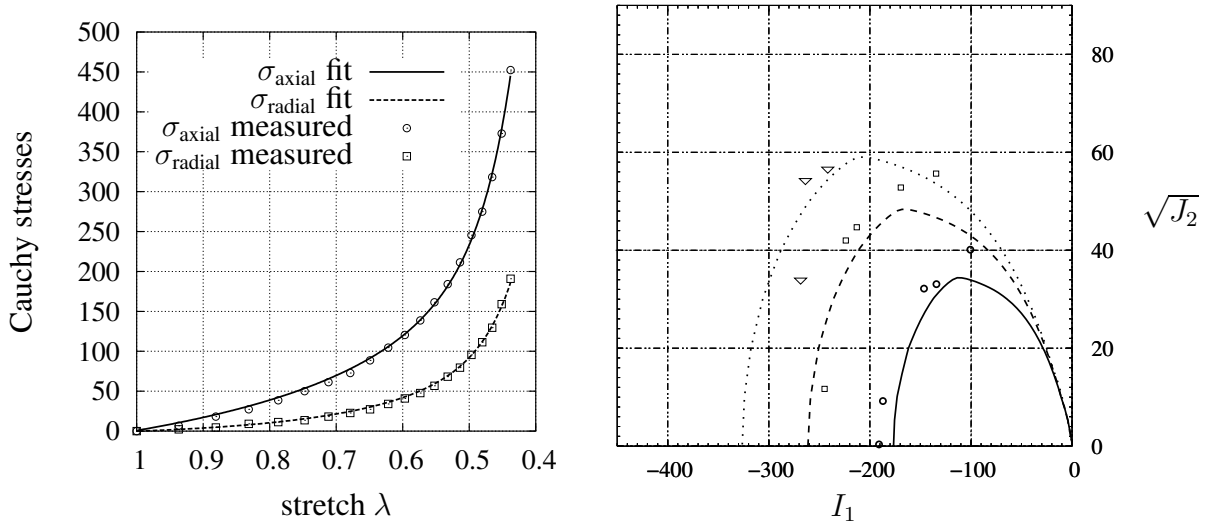

(a) Experimental die compaction data of a copper powder with irregular shaped particles and fitted loading curve.

(b) Comparison of the reported iso-density points ($\circ \hat{=} \rho_{\text{rel}} = 0.7$, $\square \hat{=} \rho_{\text{rel}} = 0.8$, $\triangledown \hat{=} \rho_{\text{rel}} = 0.85$) from triaxial loading experiments of the copper powder with irregular shaped particles. Shown is the yield surface (relative densities $\rho_{\text{rel}} = 0.70, 0.80, 0.85$) using the parameter identified from the experimental data of Fig.4.1.

Figure 4.1: Response of parameter identification applied to data of CARNAVAS [23], see BIER AND HARTMANN [19].

A number of uniaxial constrained compression experiments in a cylindrical die are performed with the experimental setup described in Subsection 4.2.1. In addition to the axial displacement (axial stretch) and the axial stress (compaction pressure), the setup allows the determination of the radial stress (radial pressure) inside the die through the measurement of the radial expansion of the die. Details about the processing of the measured data and the calibration are provided in Subsection 4.2.2. The rate-dependence of the material is checked in three compaction experiments at different velocities of the upper punch. In addition to pure loading experiments, which are predominantly used to identify the material parameters in the evolution equation, the yield function and the flow rule, a number of experiments with intermediate unloading and reloading cycles are performed and used to identify the elasticity parameters from the initial part of the unloading curve, which is assumed to be elastic. Details about the parameter identification procedure are provided in Section 4.3.

4.2.1 Experimental setup

The loose powder is compacted in a cylindrical die, with an internal and external diameter of 14 mm and 22 mm, respectively. Two true scale drawings of the setup are provided in Fig. 4.4 and Fig. 4.5 containing all the relevant dimensions of the setup. Pictures of the setup as well as pictures of the disjointed setup are shown in Fig. 4.3 providing a better impression. The pressure is applied by an "Instron 1186" testing machine and measured by the load cell below the depicted

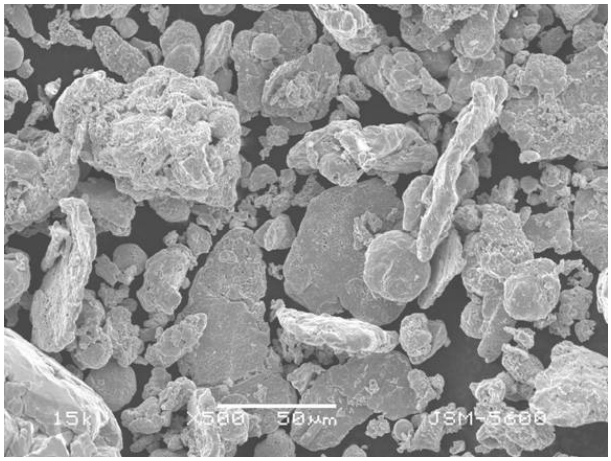

Figure 4.2: SEM image of the loose powder

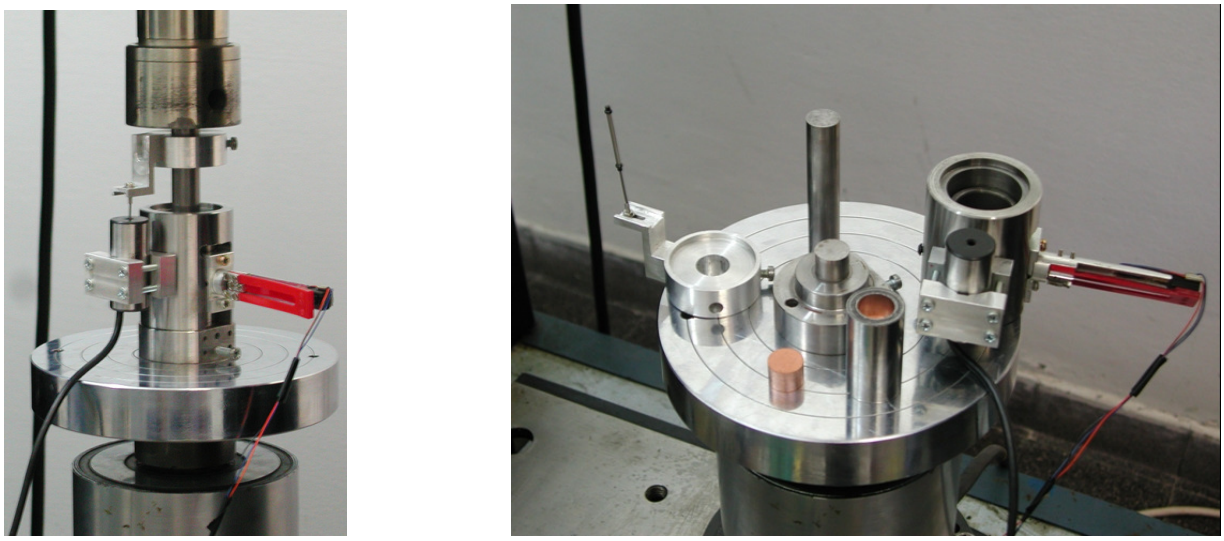

(a) Setup in action

(b) Disjointed setup

Figure 4.3: Images of the setup and of the disjointed setup

setup. The axial load (axial stress) is transferred from the testing machine to the powder inside the die via the upper and bottom punches. The axial displacement of the upper punch is measured with a ”Solartron dc miniature” displacement transducer. The rod of the displacement transducer is attached to the top punch, see Fig. 4.4, and the displacement transducer’s body is fixed to the outermost cylinder of the setup. The small radial expansion of the die, caused by the radial pressure exerted by the powder onto the inner die wall, is measured at one fixed position. The radial expansion of the die at this position is amplified mechanically by a newly developed device and measured at the end of its arm with the help of a Hall effect sensor allowing the determination of the radial expansion of the die. Assuming a linear elastic behavior of the die, the radial pressure inside the die can be calculated from the measured deflection, see Subsection 4.2.2. In order to reduce the friction between the powder particles and the die wall, the punches and the die are mechanically cleaned (in acetone and alcohol environment) and are lubricated with ”silicon mold

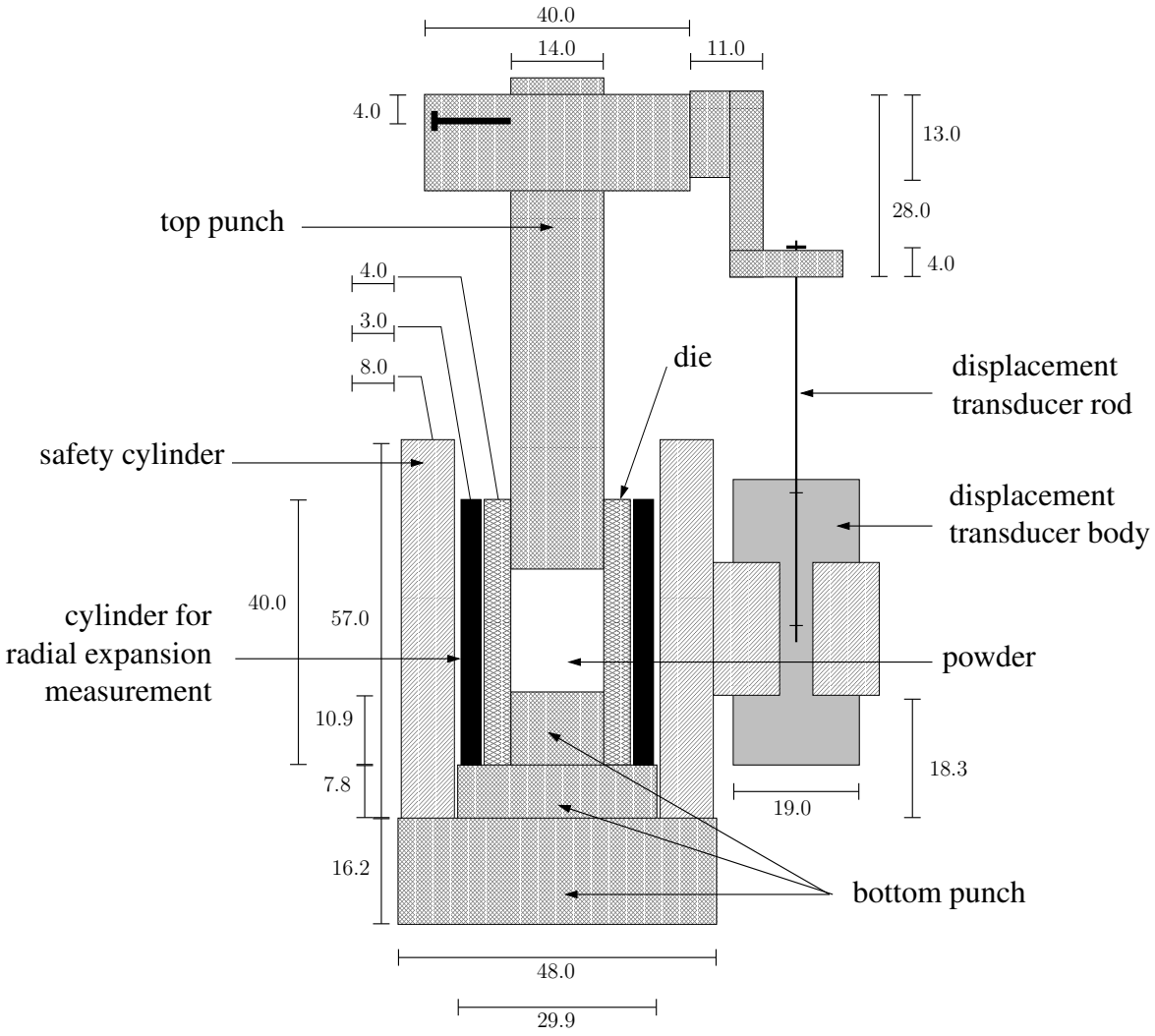

Figure 4.4: Drawing of the setup showing the instrumentation for the determination of the axial displacements (all dimensions are in mm)

release". The die and the punches are fabricated from 4340 steel, with Young's modulus $E = 200$ GPa, Poisson ratio $\nu = 0.3$ and a yield strength of $\sigma_{\mathrm{Y}} = 1300$ MPa.

4.2.2 Treatment of experimental data

A limited number of compaction experiments are conducted and analyzed with the setup described above. In each compaction experiment an amount of 10 g copper powder is poured in the die and compacted up to a final axial stress of approximately 500 MPa. Except for the experiments to check the rate dependence of the material, which were conducted at higher velocities of the machines traverse, the velocity is kept constant at 0.05 cm/min during the compaction phase. The axial stress, the axial displacement of the upper punch and the radial expansion of the die are recorded every 1.5 seconds. In Fig. 4.6 the measured axial stress and the measured radial displacement (expansion of the die) are each plotted versus the axial displacement of the upper punch. Since the stresses are always negative (pressure), the sign is omitted throughout this section and compressive stresses are counted with positive sign. The observed reproducibility in the three depicted runs is satisfactory. In order to check the rate-dependence of the material, the

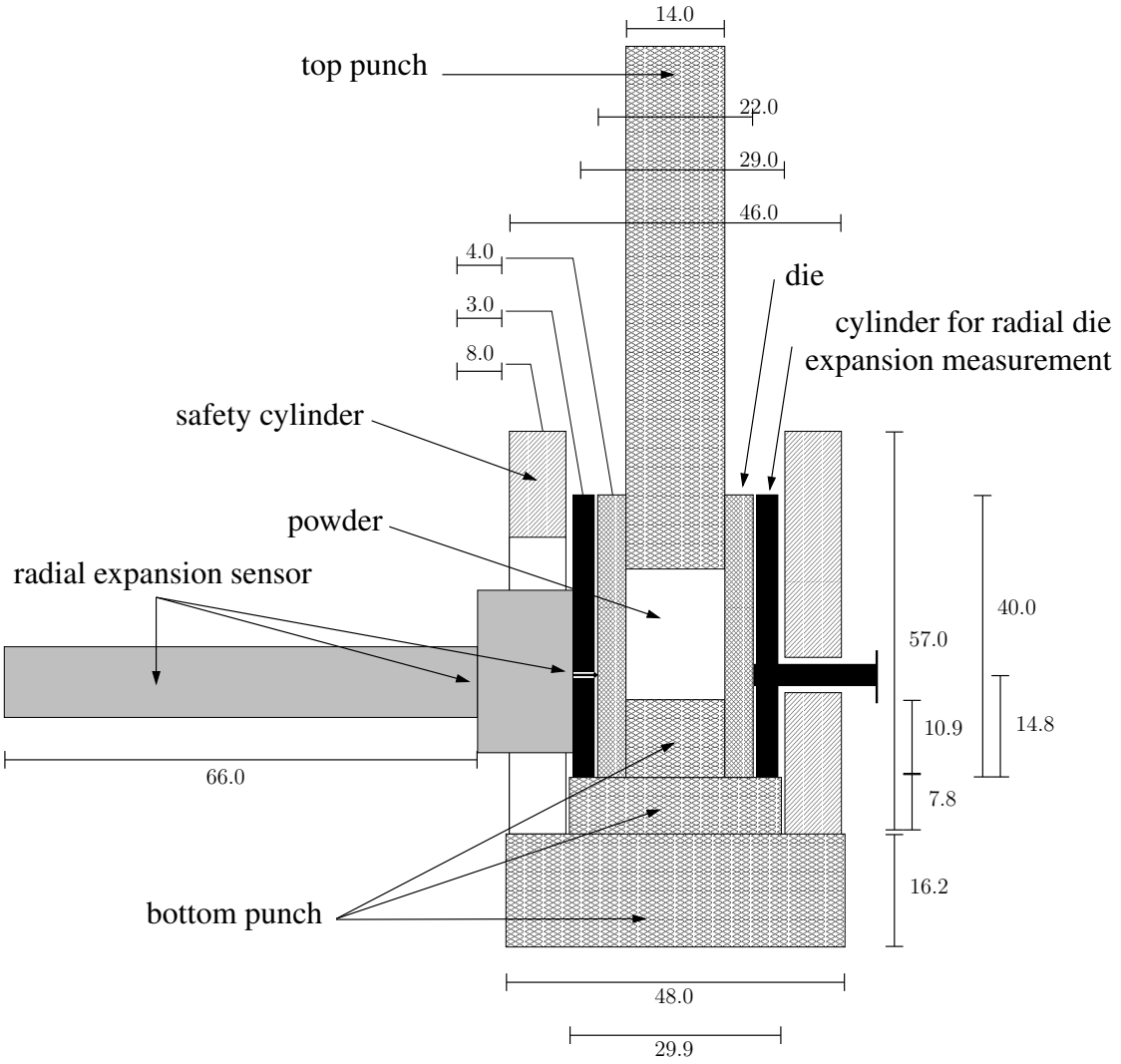

Figure 4.5: Drawing of the setup showing the instrumentation for the determination of the radial expansion of the die (all dimensions are in mm)

same experiment is repeated with different displacement velocities (1x = 0.05cm/min, 4x ,10x) of the machine's traverse. The raw data obtained in these experiments are depicted in Fig. 4.7. For the studied velocities no significant rate-dependence is observed. At higher velocities a rate-dependent behavior may of course be present, but will be ignored due to the lack of experimental data. In addition to the pure loading tests, experiments with intermediate unloading ($\sigma_{\text{axial}} = 0$) and reloading cycles are conducted. The measured data of one of the three conducted experiments is shown in Fig. 4.8. In order to be able to use the obtained experimental results to identify the material parameters of the developed constitutive model, it is necessary to derive relations between the axial stress σ_{axial} and the axial stretch λ, see Eq. (4.3), as well as the radial stress σ_{radial} and the axial stretch λ. The main relevant issue is the calculation of the radial stress σ_{radial} from the measured radial expansion of the die. First of all, the determination of the axial stretch λ from the measured axial displacement u_{axial}, which contains the compliance of the system (punches) is addressed.

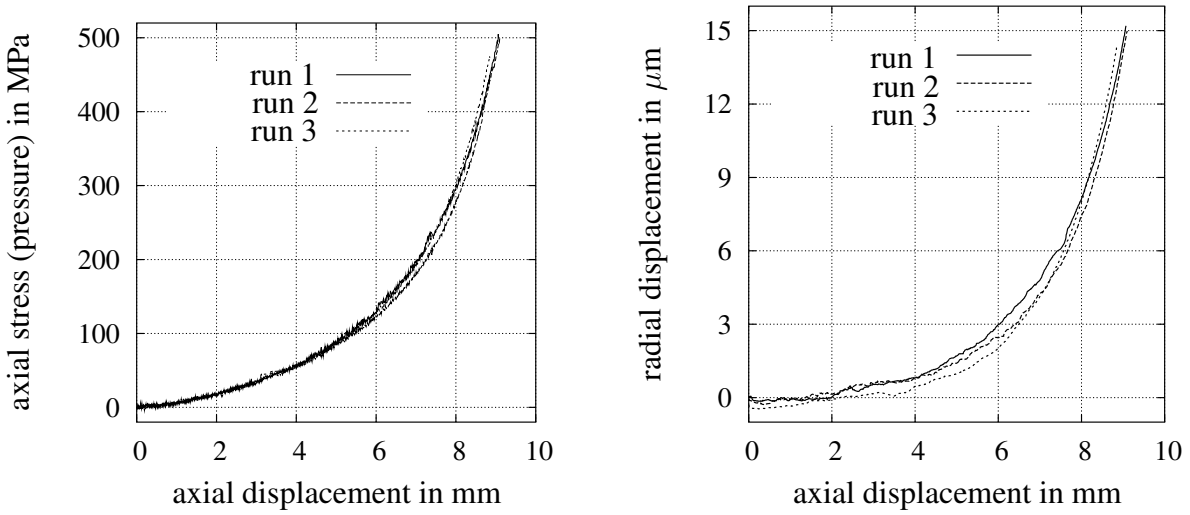

(a) Axial stress vs. axial displacements

(b) Radial displacement vs. axial displacement

Figure 4.6: Raw data obtained in the pure loading compaction experiments.

Correction of axial displacements for compliance of system

The measured axial displacement u_{axial} is the sum of the change in height of the powder $u_{\text{axial}}^{\text{pow}}$ and the change in length of the upper and the bottom punch $u_{\text{axial}}^{\text{sys}}$

$$u_{\text{axial}} = u_{\text{axial}}^{\text{pow}} + u_{\text{axial}}^{\text{sys}} \quad \Leftrightarrow \quad u_{\text{axial}}^{\text{pow}} = u_{\text{axial}} - u_{\text{axial}}^{\text{sys}}. \tag{4.1}$$

The length change of the setup $u_{\text{axial}}^{\text{sys}}$ depends on the applied pressure and can be calculated from the measured axial stress assuming a linear elastic behavior of the punches,

$$u_{\text{axial}}^{\text{sys}} = \frac{\sigma_{\text{axial}}}{E} L_0, \tag{4.2}$$

with the Young's modulus E of the punches and the reference length $L_0 = 85$ mm. L_0 is the sum of the undeformed length of the upper punch from the point, where the displacement transducer's rod is fixed to the upper punch down to the powder (66.5 mm) and an equivalent undeformed length of the bottom punch (18.5 mm), which takes into account the pyramid like shape of the bottom punch. The axial stretch λ is then given by

$$\lambda = \frac{h_0 - u_{\text{axial}}}{h_0}, \tag{4.3}$$

where h_0 is the initial height of the powder.

Since in most of the literature on powder materials the stresses and other quantities are related to the relative density, the correlation between the stretch λ and the relative density is briefly addressed, see also Subsection 3.2.1 for further details about the notion relative density. For this purpose it is assumed that the radial expansion of the die can be neglected. Therefore, the relative density is

$$\rho_{\text{rel}} = \frac{\rho_{R,\text{rel}}}{\lambda} \tag{4.4}$$

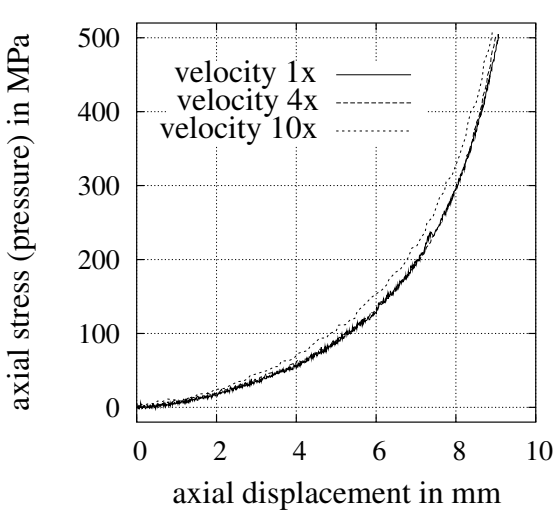

(a) Axial stress vs. axial displacements

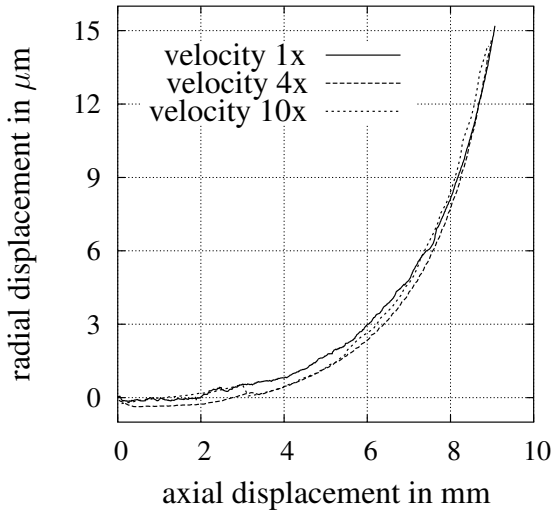

(b) Radial displacement vs. axial displacement

Figure 4.7: Raw data obtained in the pure loading compaction experiments at increased velocities of the machines traverse (1x≙0.05cm/min).

assuming a given initial relative density $\rho_{R,\text{rel}}$ and $\det \mathbf{F} = \lambda$. For an arbitrary homogeneous deformation described by the deformation gradient $\mathbf{F}$, Eq. (4.4) must be replaced by

$$\rho_{\text{rel}} = \frac{\rho_{R,\text{rel}}}{\det \mathbf{F}}. \tag{4.5}$$

In Fig. 4.9 the axial stress is plotted versus the measured axial displacement u_{axial} as well as the axial displacement $u^{\text{pow}}_{\text{axial}}$ corrected for the compliance of the system $u^{\text{sys}}_{\text{axial}}$ as described above. This gives an impression of the influence of this correction, which becomes visible, especially, during the unloading and reloading.

The precise determination of the initial powder height h_0 is practically not feasible. This is partly due to the uncertainty in the amount of powder inside the die (10 ± 0.05g). Another reason is that the powder height inside the die cannot be measured directly; instead it is deduced from the measured height of the whole setup (length of punches + powder height). Moreover, the initial powder height may deviate from one experiment to another on account of the deviations in the initial relative density after "tapping" the powder within the die. For the calculation of the stretch λ, the mean value of the determined initial powder heights from the three loading experiments, which is $h_0 = 17.3$ mm ± 0.2 mm, is used. The uncertainty is estimated from the variance of the three measured values. In order to take this uncertainty into account, an offset to the measured axial displacements of each individual experiment is introduced in the initial conditions. This offset is determined in such a way that all three curves of axial stress versus axial displacement pass through the same point at a certain axial stress level. Here, a value of 460 MPa has been used. At that axial stress the mean value of the measured axial displacements was 8.90 mm. This means that it has been assumed that the same amount of powder will have the same height at a high axial pressure, while the initial height at approximately zero axial pressure may vary due to differences in the density of the loose powder.

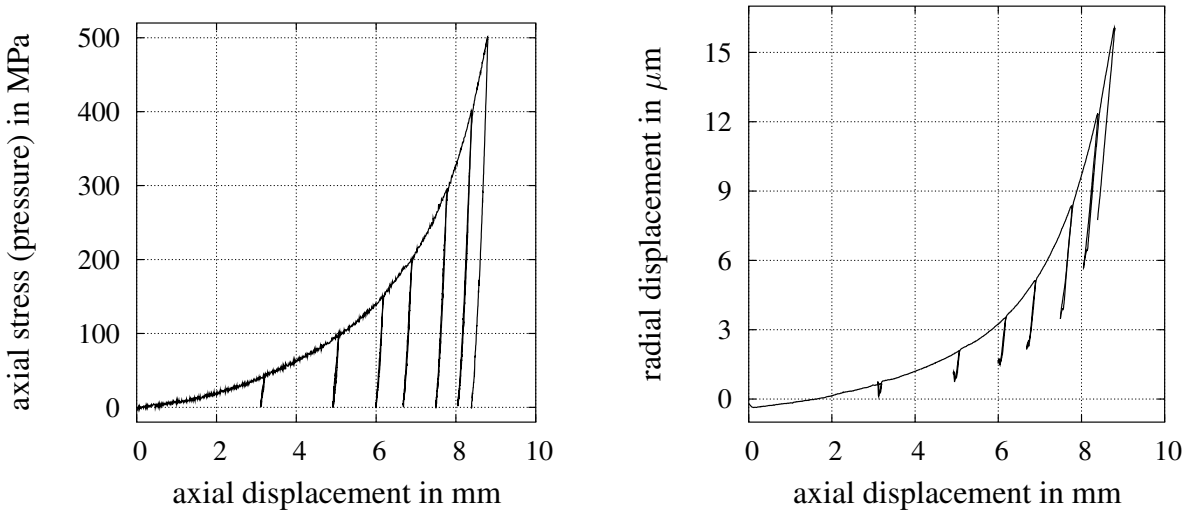

(a) Axial stress vs. axial displacements

(b) Radial displacement vs. axial displacement

Figure 4.8: Raw data obtained in loading experiment with intermediate unloading and reloading cycles.

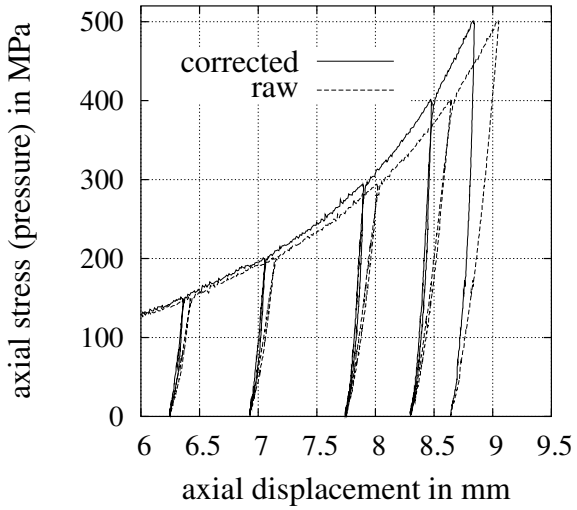

Figure 4.9: Exemplary plot to show influence of the compliance of the system

REMARK 4.1
The upper punch is forced inside the die by hand until it cannot be pushed further. It seems reasonable to assume that the initial density of the powder reached this way may vary much more than the height obtained at the rather high axial pressure of 460 MPa, which is the reason for the offsets that have been introduced. □

Conversion of radial displacements to radial stresses

The radial stress inside the die is calculated from the measured radial displacement outside the die. Under the assumption of a linear relation between the pressure (radial stress σ_{radial}) inside the die and the radial expansion Δd of the die at a fixed position and with the proportionality factor q depending on the current powder height one obtains

$$\sigma_{\text{radial}} = q(h)\Delta d. \tag{4.6}$$

The function $q(h)$ can be found from several finite element simulations with different powder heights h. In each FE-simulation a pressure of $\sigma_{\text{radial}} = 1$ MPa is applied to the inner die wall as boundary condition over the height h of the powder, see Fig. 4.11. The result of the computation is the radial displacement Δd at the position of the sensor H. Therefore, the proportionality factor is

$$q(h) = \frac{\Delta d}{\sigma_{\text{radial}}} = \frac{\Delta d}{1\,\text{MPa}}. \tag{4.7}$$

The proportionality factor $q(h)$ is determined several times according to (4.7) for different powder heights. These computations have been performed by Prof. Yosibash[1]. In Fig. 4.10 the results for $q(h)$ are plotted versus the powder height, together with a third order polynomial in the powder height starting from an initial powder height of 14.6 mm. The fitted function for $q(h)$ is used to convert the measured radial expansion Δd into radial stresses within the die, taking the continously changing height of the powder during the compaction process into account. In

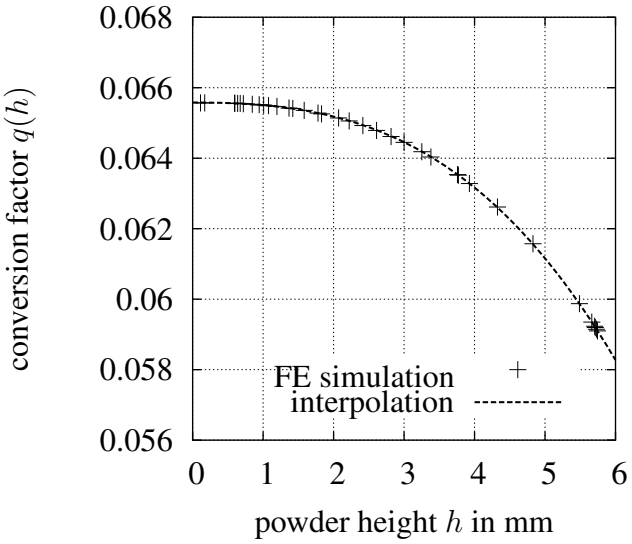

Figure 4.10: Proportionality factor $q(h)$ versus powder height. Third order polynomial is used to represent the data points obtained by Prof. Yosibash continously.

Fig. 4.11 the geometry and the mesh of the FE-simulation for the computation of the dies expansion is given. To this end the Young's modulus E and the Poisson ratio ν of the die's material

[1]Radial stress measurements in a die during compaction, Internal report for GIF project, BGU, Computatinal Mechanics Lab, Beer-Sheva, Israel, October 2004, by Idit Cohen and Zohar Yosibash

have been determined from ultrasonic measurements to be 203.4 GPa and $\nu = 0.3$. These material parameters have been used in the calculations using the commercial p-finite element code StressCheck, see ESRD [46]. The p-version of the finite element method applies higher order ansatz-functions and can achieve precise solutions with a comparatively coarse mesh. Various computations with increasing p-level (order) up to 8^{th} order have been performed in order to see convergence to the "exact" solution. For a theoretical background of the high-order p-FE analysis, see SZABÓ AND BABUŠKA [131]. The estimated error in energy norm is below 1 % for all analyzed powder heights. This "computational" approach of determining the proportionality factor $q(h)$ is preferred because of its simplicity over the "experimental" alternatives, e.g. used by CARNAVAS [23] or GEINDREAU ET AL. [50].

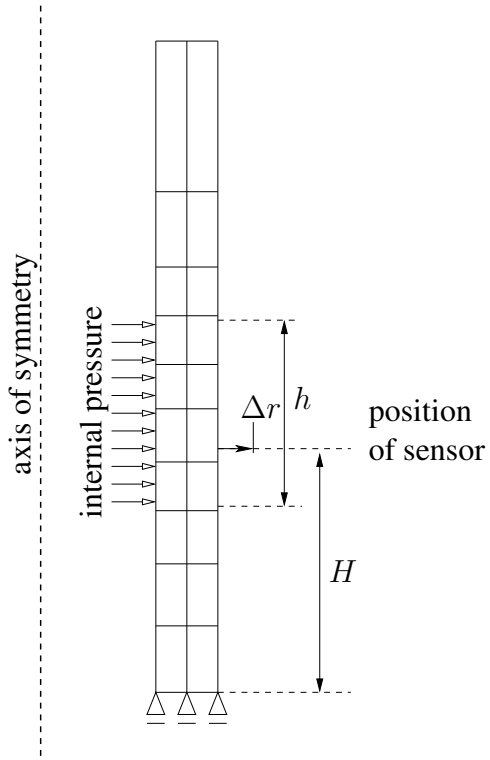

Figure 4.11: Axisymmetric geometry of die and p-FE mesh with boundary conditions used to determine the conversion factor $q(h)$

4.3 Parameter identification procedure

The material parameters contained in the constitutive model, which has been defined in Chapter 3.3 are gathered in Tab. 4.1. Since the available experimental data is not exhaustive with respect to the determination of all parameters, some parameters are set a priori. The elasticity parameters Λ and μ determine the behavior within the elastic domain. The parameters α_0, b_D, c_D define the evolution of the internal variable α, which is the squared ratio of the axis of the elliptical part of the yield function. The size of the yield function, or, to be more precise, the dependence of the size on the plastic volumetric deformations is described with the help of a_1, a_2, c_{K}. They determine the function $\xi(r_{\text{K}})$, with ξ representing the center of the yield function lying on the hydrostatic axis (actually the center of the elliptical part of the yield function). The parameters

I_0, r and c influence the shape of the yield function. Due to the lack of experimental data that would provide reliable information about the shape of the yield function, the latter parameters are specified a priori in such a way that a reasonable shape of the yield function is obtained. This means that only the function $\xi(r_{\mathrm{K}})$, i.e. the parameters a_1, a_2, c_{K}, are used to model the increase in size of the yield surface during a compaction process.

The compaction experiments, which study the rate-dependence of the material behavior, give no evidence of a rate dependence within the studied range of compaction velocities. This means that an identification of the corresponding viscosity parameters is not necessary, since the experimental data can be reproduced for $\eta = 0$ (elastoplasticity) very well. However, the introduction of a small viscosity ($\eta > 0$) can reduce the numerical effort, without changing the stress results of a finite element calculation significantly. Therefore we will consider in the numerical examples (chapter 6) in addition to the choice $\eta = 0$ (elastoplasticity) the alternative choice $\eta > 0$, $\sigma_0 = 1$, $r_{vp} = 1$ (viscoplasticity). The undetermined material parameters of the constitutive model have been collected and grouped in Tab. 4.1. The parameters from the groups "elasticity", "function $\xi(r_{\mathrm{K}})$" and "evolution of α" are identified with the help of the available experimental data from the pure loading and the experiments with intermediate unloading and reloading cycles. The parameters in the groups "yield surface" and "viscosity" from Tab. 4.1 are not identified. For the viscosity parameter $\eta = 0$ (no viscous effects) is assumed, leaving $r_{vp} = 1$ and $\sigma_0 = 1$ MPa without influence.[2] For the "yield surface" parameters I_0, r and c reasonable choices are made a priori. These are $I_0 = 1$ MPa, giving the powder a fixed small strength against hydrostatic tensile loading and guaranteeing a uniaxial tensile strength which grows during densification but remains small. The parameters r, c are chosen to be $r = 0.3$ and $c = 0.01$. This choice ensures a drop like shape of the yield surface in the I_1-$\sqrt{J_2}$-plane being sufficiently smooth to be handled numerically in an adequate way. For the parameter identification of the remaining free parameters, it is taken advantage of the fact that the behavior of the material during plastic loading is hardly influenced by the elasticity parameters Λ and μ. Likewise, the behavior during unloading and reloading in the elastic range is dominated by these two parameters. This gives reason to apply an iterative two stage identification procedure. In the first step of this procedure the elastic parameters Λ and μ are roughly estimated to be both equal to 20 GPa. This estimation corresponds to an Young's modulus of $E = 50$ GPa and a Poisson ratio of $\nu = 0.25$. These values have been reported by CARNAVAS AND PAGE [24] for another copper powder compacted to a relative density of about 85 %. It will be shown that, although this initial guess for the elasticity parameters is very rough, the identification procedure can be stopped after two iterative steps. In this respect, it must be emphasized that, although Λ and μ correspond to the Lame constants for small strains, we have to identify the elasticity parameters of the nonlinear elasticity relation (3.87). In other words, the influence of the current plastic strains upon the unloading behavior must be taken into account.

Stage I: Identification of inelastic parameters from loading curve

The hardening behavior of the material is modeled by the growth of the yield surface, which is described by the dependence of ξ (with 3ξ being the center of the ellipse on the hydrostatic axis) on the volumetric plastic strain, see Fig. 3.8. Relation (3.77) contains the parameters a_1, a_2 and c_{K}. The initial condition at $t = 0$ for $\mathbf{C}_{\mathrm{p}}$ is $\mathbf{C}_{\mathrm{p}} = \mathbf{I}$, which implies $r_{\mathrm{K}} = 0$ in the beginning. Additionally, the initial condition α_0 for the internal variable α and the two parameters

[2] The expansion of the model to viscosity will be used only in view of its influence on the numerical treatment of the model.

Table 4.1: Collection of material parameters

symbol	group	description of parameter
Λ	elasticity	elasticity parameter corresponding to the Lame constant for small deformations, see Tab. 3.3
μ	elasticity	elasticity parameter corresponding to the Lame constant for small deformations, see Tab. 3.3
a_1	function $\xi(r_{\mathrm{K}})$	defines together with a_2 the value of ξ for $r_{\mathrm{K}} = 0$ and together with c_{K} the initial slope of $\xi(r_{\mathrm{K}})$, i.e. the start of compaction, see Eq.(3.77)
a_2	function $\xi(r_{\mathrm{K}})$	defines together with a_2 the value of ξ for $r_{\mathrm{K}} = 0$, i.e. start of compaction and how fast ξ grows as r_{K} approaches $-\infty$, see Eq.(3.77)
c_{K}	function $\xi(r_{\mathrm{K}})$	determines together with a_1 the initial slope of $\xi(r_{\mathrm{K}})$, i.e. the start of compaction, see Eq.(3.77)
α_0	evolution of α	initial value of α, see Eq.(3.83)
b_D	evolution of α	parameter in evolution equation for α , see Eq.(3.83)
c_D	evolution of α	parameter in evolution equation for α , see Eq.(3.83)
I_0	yield surface	defines intersection of the elliptical part of the yield function with the hydrostatic axis (tensile) , see Fig. 3.8
r	yield surface	defines intersection of the elliptical part and the exponential part of the yield function, see Fig. 3.8
c	yield surface	defines the smoothness of the transition between the elliptical part and the exponential part of the yield function, see Fig. 3.8
σ_0	viscosity	makes the expression in the Mccauley brackets dimensionless and can normalize the yield function value, see Tab. 3.4
r_{vp}	viscosity	parameter used to model rate dependence , see Tab. 3.4
η	viscosity	parameter used to model rate dependence , see Tab. 3.4

b_D and c_D defining its evolution need to be identified. For the identification of this whole set of parameters (a_1, a_2, c_{K}, b_D, c_D, α_0) the die compaction experiment is idealized by assuming a homogeneous deformation inside the die, which is described by the deformation gradient $\mathbf{F} = \vec{e}_r \otimes \vec{e}_r + \vec{e}_\vartheta \otimes \vec{e}_\vartheta + \lambda \vec{e}_z \otimes \vec{e}_z$. This means that friction between the powder and the die as well as the influence of the die's radial expansion are neglected. $\vec{e}_r$ $\vec{e}_\vartheta$, $\vec{e}_z$ are the basis vectors in cylindrical coordinates. For the assumed deformation gradient the constitutive equations, see Tab. 3.3, are integrated numerically to reproduce the measured stress-stretch curves. With the help of an optimization tool of SPELLUCCI [126], which is able to handle inequality constraints of the parameters specified in Tab. 4.2, the numerical integration procedure is called with differ-

ent values of the parameters repeatedly. The new values are generated by the optimization tool in order to minimize the difference between the computed stress-stretch relation and the smoothed representation of the measured data. In this procedure a weighting technique described by HARTMANN ET AL. [66] is applied. The residuals from the axial and radial stresses are weighted in the objective function of the optimization by the inverse of the maximal value occurring in the data in order to achieve an equally well representation of axial and radial stresses.

$$\text{objective function} = \sum_{\text{all data points}} \left(\frac{\sigma^{\text{mod}}_{\text{axial}} - \sigma^{\text{exp}}_{\text{axial}}}{\max(\sigma^{\text{exp}}_{\text{axial}})} \right)^2 + \left(\frac{\sigma^{\text{mod}}_{\text{radial}} - \sigma^{\text{exp}}_{\text{radial}}}{\max(\sigma^{\text{exp}}_{\text{radial}})} \right)^2 \quad \rightarrow \quad \text{min} \qquad (4.8)$$

The fit results of the first iterative step using $\Lambda = \mu = 20$ GPa are presented in column 3 (1^{st} fit result) of Tab. 4.2. These parameters are used subsequently in the second stage of the identification procedure to identify the elasticity parameters Λ and μ.

REMARK 4.2
In principle it would have been possible to identify all parameters using the optimization tool of SPELLUCCI [126] *by fitting the model response to the experimental data with intermediate unloading and reloading cycles. However, there are two strong reasons against this procedure. First, as mentioned before, we would not exploit the fact that the unloading and reloading phases are majorly influenced by the elasticity parameters Λ, μ and that the plastic loading phase is predominantly influenced by the other parameters (a_1, a_2, c_K, b_D, c_D, α_0). Second the inclusion of unloading and reloading phases would have led to a number of technical problems like the definition of points where unloading should start, and the problem that the stretch would not increase monotonically. So the decision has been made, giving favor to the two stage identification procedure.* □

Table 4.2: List of parameters, constraints and fit results

parameter	constraint	1^{st} fit result ($\Lambda = \mu = 20$ GPa)	2^{nd} fit result ($\Lambda = 5.3$ GPa, $\mu = 8.3$ GPa)
a_1	≥ 0	0.440×10^1	0.445×10^1
a_2	≥ 0	0.649×10^1	0.662×10^1
c_{K}	≥ 0	0.433×10^2	0.427×10^2
b_D	≥ 0	0.256×10^1	0.268×10^1
c_D	$\geq 0.1 \times 10^{-3}$	0.1×10^{-3}	0.1×10^{-3}
α_0	> 0	0.532	0.558

Stage II: Identification of elasticity parameters from unloading curves

For the identification of the elasticity parameters, the three experiments with inserted axial unloading and reloading, see Fig. 4.8, are analyzed. The two parameters in the elasticity relation, Λ and μ, can be deduced from the slopes B_{axial} and B_{radial} of the unloading curves of the axial

stress and the radial stress over the stretch λ. The equations, which connect the slopes with the parameters, are derived in the following. From the elasticity relation, see Tab. 3.3, one finds the Cauchy stress tensor $\mathbf{T}$ by inserting the information about the deformation

$$\mathbf{F} = \begin{pmatrix} 1 & 0 & 0 \\ 0 & 1 & 0 \\ 0 & 0 & \lambda \end{pmatrix}, \quad \mathbf{C} = \begin{pmatrix} 1 & 0 & 0 \\ 0 & 1 & 0 \\ 0 & 0 & \lambda^2 \end{pmatrix}, \quad \mathbf{C}_\mathrm{p} = \begin{pmatrix} \lambda_\mathrm{pq} & 0 & 0 \\ 0 & \lambda_\mathrm{pq} & 0 \\ 0 & 0 & \lambda_\mathrm{p}^2 \end{pmatrix} \tag{4.9}$$

and performing a push-forward of the 2. Piola-Kirchhoff stress tensor $\tilde{\mathbf{T}}$ to the current configuration

$$\mathbf{T} = \frac{1}{\det \mathbf{F}} \mathbf{F} \left(\mu \mathbf{C}_\mathrm{p}^{-1} + \left(\frac{1}{2} \Lambda \ln \left(\det \left(\mathbf{C}_\mathrm{p}^{-1} \mathbf{C} \right) \right) - \mu \right) \mathbf{C}^{-1} \right) \mathbf{F}^T. \tag{4.10}$$

Therefore, the axial and the radial Cauchy stresses are written as

$$\sigma_\mathrm{axial} = \sigma_\mathrm{axial}\left(\lambda, \lambda_\mathrm{p}, \lambda_\mathrm{pq}, \Lambda, \mu\right) = \frac{\mu\lambda}{\lambda_\mathrm{p}^2} - \frac{\mu}{\lambda} + \frac{\Lambda}{2\lambda} \ln\left(\frac{\lambda^2}{\lambda_\mathrm{p}^2 \lambda_\mathrm{pq}^4} \right), \tag{4.11}$$

$$\sigma_\mathrm{radial} = \sigma_\mathrm{radial}\left(\lambda, \lambda_\mathrm{p}, \lambda_\mathrm{pq}, \Lambda, \mu\right) = \frac{\mu}{\lambda_\mathrm{pq}^2 \lambda} - \frac{\mu}{\lambda} + \frac{\Lambda}{2\lambda} \ln\left(\frac{\lambda^2}{\lambda_\mathrm{p}^2 \lambda_\mathrm{pq}^4} \right). \tag{4.12}$$

During unloading λ_p and λ_pq are constant (as long as the unloading leads to a stress state inside the elastic domain). Thus, the initial slope of the unloading curve at a certain stretch λ_0 can be expressed in the following form:
Slope of σ_axial during loading:

$$B_\mathrm{axial} = \left. \frac{\partial \sigma_\mathrm{axial}}{\partial \lambda} \right|_{\lambda=\lambda_0} = C_1(\lambda_0, \lambda_\mathrm{p}, \lambda_\mathrm{pq})\Lambda + C_2(\lambda_0, \lambda_\mathrm{p}, \lambda_\mathrm{pq})\mu \tag{4.13}$$

Slope of σ_radial during unloading:

$$B_\mathrm{radial} = \left. \frac{\partial \sigma_\mathrm{radial}}{\partial \lambda} \right|_{\lambda=\lambda_0} = C_3(\lambda_0, \lambda_\mathrm{p}, \lambda_\mathrm{pq})\Lambda + C_4(\lambda_0, \lambda_\mathrm{p}, \lambda_\mathrm{pq})\mu \tag{4.14}$$

Inserting the slopes of the experimental unloading curves B_axial and B_radial, which are determined by a simple linear regression fit to the experimental data (initial 50% of unloading curves) into these equations, one obtains a system of linear equations for the unknown parameters μ and Λ. The solution of this system of linear equations reads

$$\Lambda = \frac{2\lambda_0^2 \left(B_\mathrm{axial} \lambda_p^2 \left(\lambda_\mathrm{pq}^2 - 1 \right) - B_\mathrm{radial} \lambda_\mathrm{pq}^2 \left(\lambda_\mathrm{p}^2 + \lambda_0^2 \right) \right)}{\left(\lambda_\mathrm{p}^2 + \lambda_\mathrm{pq}^2 \lambda_0^2 \right) \left(\ln\left(\frac{\lambda_0^2}{\lambda_\mathrm{p}^2} \lambda_\mathrm{pq}^4 \right) - 2 \right)}, \tag{4.15}$$

$$\mu = \frac{\left(B_\mathrm{axial} - B_\mathrm{radial} \right) \lambda_0^2 \lambda_\mathrm{p}^2 \lambda_{pq}^2}{\lambda_\mathrm{p} + \lambda_\mathrm{pq}^2 \lambda_0^2}. \tag{4.16}$$

In each of the n_exp experiments with inserted unloading processes, there are $n_\mathrm{up} = 7$ points $\lambda_0^j,\ j = 1..., n_\mathrm{up}$, at which unloading starts. This means that one finds $n_\mathrm{exp} \times n_\mathrm{up}$ individual values μ_i^j and Λ_i^j corresponding to the j^th unloading in the i^th experiment, $i = 1, ..., n_\mathrm{exp}$. The results for Λ_i^j and μ_i^j, which are calculated from (4.15) and (4.16), depend not only on the stretch λ_0^j at which the unloading starts, but also on the respective plastic stretches λ_p^j and λ_pq^j. The values of λ_p^j and λ_pq^j are taken from the computation of the pure loading process with the parameters of

Tab. 4.2, (column 3). The resulting mean values of the n_{exp} experiments at j^{th} unloading point are

$$\overline{\mu}^j = \frac{1}{n_{\text{exp}}} \sum_{i=1}^{n_{\text{exp}}} \mu_i^j, \quad \overline{\Lambda}^j = \frac{1}{n_{\text{exp}}} \sum_{i=1}^{n_{\text{exp}}} \Lambda_i^j. \tag{4.17}$$

The overall mean values after the first iteration are given by

$$\overline{\mu} = \frac{1}{n_{\text{exp}} n_{\text{up}}} \sum_{i=1}^{n_{\text{exp}}} \sum_{j=1}^{n_{\text{up}}} \mu_i^j, \quad \overline{\Lambda} = \frac{1}{n_{\text{exp}} n_{\text{up}}} \sum_{i=1}^{n_{\text{exp}}} \Lambda_i^j \tag{4.18}$$

and read $\mu = \overline{\mu} = 8.3$ GPa and $\Lambda = \overline{\Lambda} = 5.3$ GPa. Since the material parameters of the inelastic part of the constitutive model are influenced by the choice μ and Λ, the two-stage procedure has to be repeated. In Tab. 4.2 (column 4) the identified material parameters are compiled. Obviously, the parameters are not drastically influenced by the alteration of the elasticity parameters μ and Λ. Computing μ and Λ once again by (4.17) and (4.18) yields $\mu = \overline{\mu} = 8.3$ GPa and $\Lambda = \overline{\Lambda} = 5.2$ GPa, which is only a very small change and, consistently, no further iteration is necessary. Fig. 4.12 shows the result of the identification for the monotonic loading process

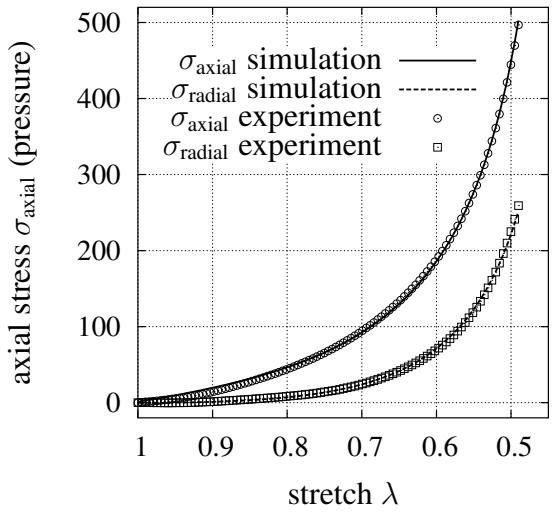

Figure 4.12: Stress-stretch behavior calculated with model after optimization of parameters together with smooth representation of experimental data

using the parameters of Tab. 4.2 (column 4). The results of the identification of the elasticity parameters are depicted in Fig. 4.13. There, the displayed error bars in ordinate-direction represent the standard deviation of the mean value $\overline{\Lambda}^j$ and $\overline{\mu}^j$ from the three unloading experiments at the relative density ρ_{rel}, see Eq. (4.4) corresponding to the j^{th} unloading. The displayed error bars on the abscissa (uncertainty of the relative density) are estimated according to quadratic error propagation from the uncertainties of the mass of the powder (± 0.05 g), the initial powder height (± 0.2 mm), the diameter of the die (± 0.02 mm) and the axial displacement (± 0.03 mm). In addition to the values for μ and Λ derived from our experiments, Fig. 4.13 contains values for μ and Λ which have been calculated from values of E and ν reported by CARNAVAS AND PAGE [24,

THEIR FIGURES 6B, 6C AND 8] for two copper powders consisting of irregular (irr.) and dendritic (dend.) shaped particles. The data based on the experiments of Carnavas has been included in Fig. 4.13 to demonstrate the plausibility of the identified values for the elasticity parameters μ and Λ. Finally, the results of the model, using the identified set of parameters of Tab. 4.2 (column

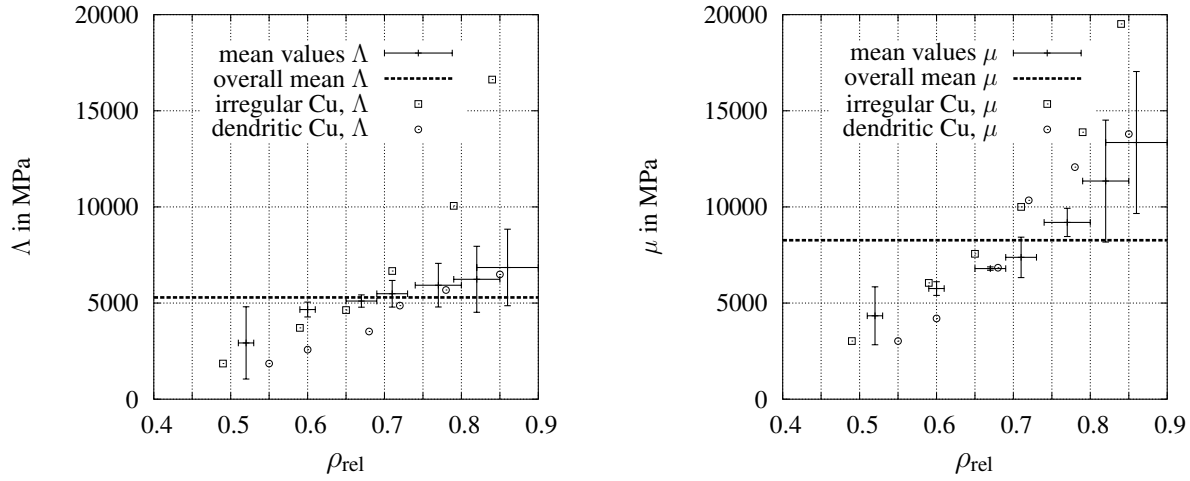

(a) elasticity parameter Λ

(b) elasticity parameter μ

Figure 4.13: Elasticity parameters identified from all three experiments with inserted unloading and reloading processes and calculated from values of E and ν reported in CARNAVAS AND PAGE [24].

4), are compared to an experiment with inserted unloading. In the computation, the unloading continues until $\sigma_{\text{axial}} = 0$ is reached. In Fig. 4.14 the output of the model for the axial as well as the radial stress is presented together with the experimental data. The model captures the general behavior during loading and unloading. In particular, the residual radial stress after unloading to $\sigma_{\text{axial}} = 0$ is reproduced remarkably well.

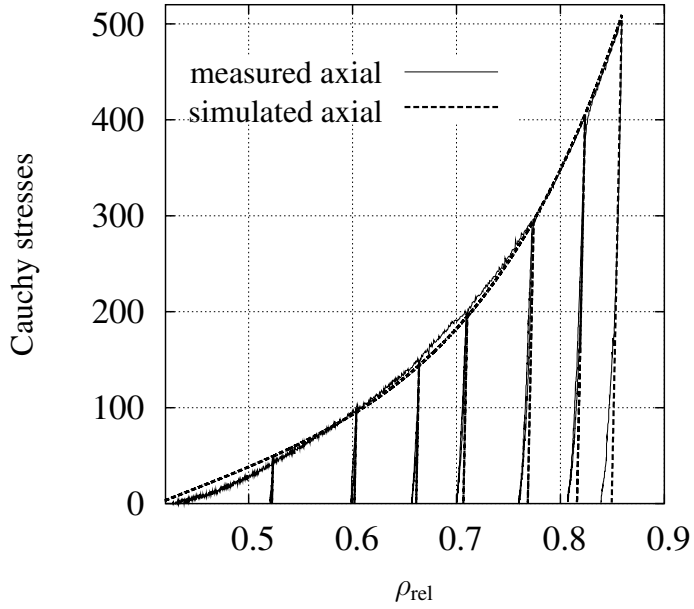

(a) Axial stresses

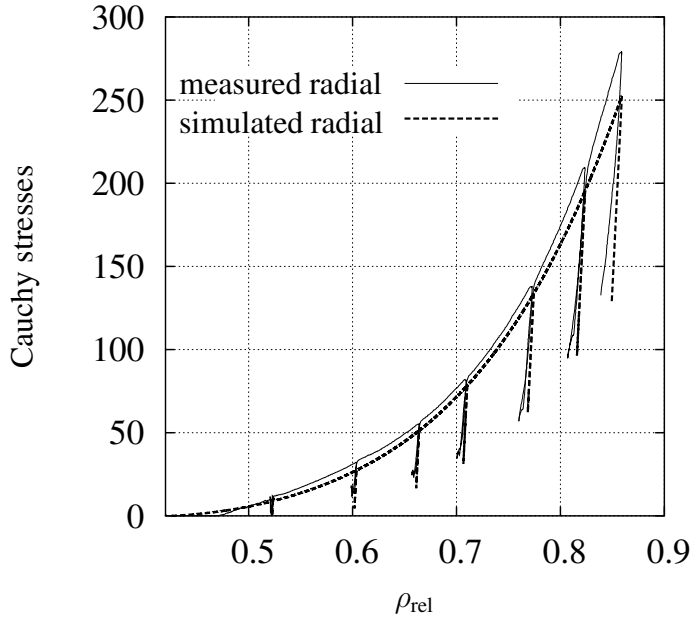

(b) Radial stresses

Figure 4.14: Axial and radial stress from experiment with inserted unloading-reloading and results of similar computation with the identified set of parameters.

Chapter 5

Numerical treatment using finite elements

This chapter deals with the numerical treatment of the initial boundary value problem (IBVP) in the context of finite elements that is formed by the balance relations and the constitutive equations together with given initial and boundary conditions. The applied solution strategy is explained in Section 5.2 in a step by step manner starting with the formulation of the principle of virtual displacements (Section 5.2.1). Afterwards the space discretization of this principle (Section 5.2.2) leads to a system of differential-algebraic equations (DAE-system). This DAE-system is integrated in time with the help of diagonally implicit Runge-Kutta (DIRK) methods[1], see Section 5.2.3, demanding the computation of nonlinear systems of equations at each stage of the integration scheme. These nonlinear systems are solved with the help of the Multilevel-Newton algorithm, which exploits the coupled structure of the equations. On the local level of the Multilevel-Newton algorithm a nonlinear system of equations that results from the constitutive model has to be solved. Furthermore, the consistent tangent matrix is calculated on the local level. Frequently, the nonlinear system on local level is solved using the Newton method. The analytical reduction of the number of equations resulting from the constitutive model proposed in Section 3.3 and 3.4 to one equation as proposed by LÜHRS ET AL. [100] or HARTMANN ET AL. [65] in the context of metal plasticity is not feasible. Furthermore, the application of the standard Newton algorithm lead to convergence problems so that several globalization strategies for Newton's method are studied, see Section 5.2.4, leading to particular stress algorithms.

In order to make this chapter more comprehensible, some of the applied mathematical concepts are introduced in Section 5.1 in some detail. This introduction is somewhat more general, however, already suited for the later application discussed in Section 5.2.

[1] In the simplest case with the implicit Euler method.

5.1 Mathematical basics

This section introduces some of the less well known mathematical concepts, which will be applied in the solution process of the IBVP. In Subsection 5.1.1 diagonally implicit Runge-Kutta methods, which are applied for the solution of the DAE-system resulting from the space discretization within finite elements, are introduced. Subsequently, the Multilevel-Newton algorithm, which is applied to solve the nonlinear systems in each stage of the Runge-Kutta scheme, is introduced. Finally, in Section 5.1.3 a number of globalization strategies for the Newton method, which are applied on local level to solve the nonlinear system of equations, are introduced.

5.1.1 Solution of DAEs with DIRK methods

A system of explicit ordinary differential equations of first order can be written in the form

$$\dot{\boldsymbol{y}}(t) = \boldsymbol{f}(t, \boldsymbol{y}(t)), \quad \boldsymbol{f} \in \mathbb{R}^m \tag{5.1}$$

and a solution $\boldsymbol{y}(t)$ with $t \in [t_0, T]$ can either be found analytically (if possible) or numerically for given initial conditions $\boldsymbol{y}(t_0) = \boldsymbol{y}_0$. A more general class of problems are so-called implicit ordinary differential equations of first order

$$\boldsymbol{F}(t, \boldsymbol{y}(t), \dot{\boldsymbol{y}}(t)) = \boldsymbol{0} \tag{5.2}$$

where an algebraic transformation to the form (5.1) is not feasible. The space discretization of the principle of virtual displacements (see Section 5.2.2) will lead to a system of differential equations of first order possessing the special structure

$$\boldsymbol{F}(t, \boldsymbol{y}(t), \dot{\boldsymbol{y}}(t)) \equiv \left\{ \begin{array}{c} \boldsymbol{g}(t, \boldsymbol{u}(t), \boldsymbol{q}(t)) \\ \boldsymbol{A}\dot{\boldsymbol{q}} - \boldsymbol{r}(t, \boldsymbol{u}(t), \boldsymbol{q}(t)) \end{array} \right\} = \boldsymbol{0} \tag{5.3}$$

with

$$\boldsymbol{y}(t) = \left\{ \begin{array}{c} \boldsymbol{u}(t) \\ \boldsymbol{q}(t) \end{array} \right\} \quad \text{and} \quad \boldsymbol{y}(t_0) = \left\{ \begin{array}{c} \boldsymbol{u}(t_0) \\ \boldsymbol{q}(t_0) \end{array} \right\} = \left\{ \begin{array}{c} \boldsymbol{u}_0 \\ \boldsymbol{q}_0 \end{array} \right\} = \boldsymbol{y}_0. \tag{5.4}$$

This structure is called a (semi-explicit) system of nonlinear differential algebraic equations of first order, shortly denoted as a DAE-system. The part $\boldsymbol{g} = \boldsymbol{0}$ is referred to as the algebraic part of the DAE-system and the part $\boldsymbol{A}\dot{\boldsymbol{q}} - \boldsymbol{r} = \boldsymbol{0}$ as the differential part, where $\boldsymbol{A}$ can be singular, which would make the differential part a DAE-system of its own (elastoplasticity). Later on a special class of Runge-Kutta methods will be introduced in order to solve problems of the form (5.3). However, we start the introduction of the method considering Eq. (5.1) and will generalize it afterwards. We are interested in the solution $\boldsymbol{y}(t)$ of Eq. (5.1) in the time interval $t \in [t_0, T]$ which is subdivided into N subintervals $t_0 < t_1 < \ldots < t_n < t_{n+1} < \ldots < t_N \equiv T$ with the time stepsize $\Delta t_n = t_{n+1} - t_n$ from time t_n to time t_{n+1}. Assuming that we start with a point of the exact solution $(t_n, \boldsymbol{y}(t_n))$, we seek the solution at time t_{n+1} by integration of Eq. (5.1)

$$\boldsymbol{y}(t_{n+1}) = \boldsymbol{y}(t_n) + \int_{t_n}^{t_{n+1}} \boldsymbol{f}(t, \boldsymbol{y}(t)) dt. \tag{5.5}$$

With the help of a coordinate transformation $(t = t_n + \tau \Delta t_n)$ the integration can be conducted over the unit interval $[0, 1]$

$$\boldsymbol{y}(t_{n+1}) = \boldsymbol{y}(t_n) + \Delta t_n \int_0^1 \boldsymbol{f}(t_n + \tau \Delta t_n, \boldsymbol{y}(t_n + \tau \Delta t_n)) d\tau. \tag{5.6}$$

Table 5.1: Butcher tableau for Runge-Kutta methods with s stages

c_1	a_{11}	a_{12}	$\dots$	a_{1s}
c_2	a_{21}	a_{22}	$\dots$	a_{2s}
$\vdots$	$\vdots$	$\vdots$	$\ddots$	$\vdots$
c_s	a_{1s}	a_{2s}	$\dots$	a_{ss}
	b_1	b_2	$\dots$	b_s

The integral in Eq. (5.6) is now solved applying a quadrature formula

$$I = \int_0^1 f(\tau)d\tau \approx \sum_{i=1}^{s} b_i f(c_i), \quad i = 1, \dots, s \tag{5.7}$$

with the weights b_i and the stages c_i leading to the discrete form of Eq. (5.6)

$$\boldsymbol{y}(t_{n+1}) \approx \boldsymbol{y}_{n+1} = \boldsymbol{y}(t_n) + \Delta t_n \sum_{i=1}^{s} b_i \boldsymbol{f}(t_n + c_i \Delta t_n, \boldsymbol{y}(t_n + c_i \Delta t_n)) \tag{5.8}$$

The quantities $\boldsymbol{y}(t_n + c_i \Delta t_n)$ are unknown. They are determined as well by applying a quadrature rule using new weights a_{ij} but the same stages $c_j,\ j = 1, \dots, s$, as before

$$\boldsymbol{y}(t_n + c_i \Delta t_n) \approx \boldsymbol{Y}_{ni} = \boldsymbol{y}(t_n) + \Delta t_n \sum_{j=1}^{s} a_{ij} \boldsymbol{f}(t_n + c_j \Delta t_n, \boldsymbol{Y}_{nj}). \tag{5.9}$$

Eq. (5.9) is in general a system of $s \times m$ equations for the $s \times m$ unknowns $\boldsymbol{Y}_{ni} \in \mathbb{R}^m$, $i = 1, \dots, s$, with s being the number of stages of the Runge-Kutta method and m being the dimension of the system of differential equations, i.e. the dimension of $\boldsymbol{y}$. The solution of this system is inserted into Eq. (5.8) to compute the solution $\boldsymbol{y}_{n+1}$ looked for. The coefficients of the Runge-Kutta scheme are usually compiled in Butcher arrays, see Tab. 5.1. According to their coefficients Runge-Kutta methods can be subdivided into

- explicit (ERK), if $a_{ij} = 0 \,\forall\, j \geq i$,
- implicit (IRK), if at least one $a_{ij} \neq 0$ with $j \geq i$.

A special kind of implicit Runge-Kutta methods is called diagonally-implicit (DIRK), if $a_{ij} = 0 \,\forall\, j > i$. The term stiffly accurate is used if $a_{sj} = b_j$. Individual RK-methods differ in the choice of coefficients leading to different properties of the algorithm with respect to efficiency, stability and accuracy, see for example HAIRER AND WANNER [58] for more details. In the following, we demonstrate that the Runge-Kutta algorithm can be applied to solve the more general implicit differential equation (5.2) as well, including also the case (5.3). At each stage of the RK-method the stage values are given through

$$\boldsymbol{Y}_{ni} = \boldsymbol{y}_n + \Delta t_n \sum_{j=1}^{s} a_{ij} \dot{\boldsymbol{Y}}_{nj}, \quad i = 1, \dots, s \tag{5.10}$$

Exploitation of the implicit differential equation (5.2) at each stage $T_{ni} = t_n + c_i \Delta t_n$ with $i = 1, \ldots, s$, yields

$$\boldsymbol{F}(T_{ni}, \underbrace{\boldsymbol{y}_n + \Delta t_n \sum_{j=1}^{s} a_{ij} \dot{\boldsymbol{Y}}_{nj}}_{\boldsymbol{Y}_{ni}}, \dot{\boldsymbol{Y}}_{ni}) = \boldsymbol{0}, \quad i = 1, \ldots, s. \tag{5.11}$$

From this (usually) non-linear system the stage derivatives $\dot{\boldsymbol{Y}}_{ni}$, $i = 1, \ldots, s$, can be computed. With the help of the stage derivatives the sought solution at time t_{n+1} is obtained

$$\boldsymbol{y}_{n+1} = \boldsymbol{y}_n + \Delta t_n \sum_{i=1}^{s} b_i \dot{\boldsymbol{Y}}_{ni}. \tag{5.12}$$

The application of a fully implicit RK-method with at least one $a_{ij} \neq 0$ for $j > i$ results in a coupling of all the stage values, so that a system of $s \times m$ equations has to be solved. In the case of explicit RK-methods the stage values can be calculated from already known values of the earlier stages, so instead of the iterative solution of a nonlinear system only function evaluations are necessary. However, the stability properties of the explicit scheme are of course much poorer. For the class of stiffly accurate DIRK methods, which will be applied later on, the diagonally implicit property $a_{ij} = 0$ for $j > i$ implies that at each stage j the nonlinear system depends only on the current stage derivatives $\dot{\boldsymbol{Y}}_{nj}$ and the previously calculated stage derivatives $\dot{\boldsymbol{Y}}_{ni}$ with $i < j$ so that instead of $s \times m$ equations (fully implicit) only a system of m equations needs to be solved at each of the s stages. The stiffly accurate property, $a_{ji} = b_i$, has the additional merit that the final stage value $\boldsymbol{Y}_{ns}$ is already the sought solution $\boldsymbol{y}_{n+1}$ and that in the case of application to the DAE-system the algebraic equation is also satisfied at time t_{n+1}. In the case of stiffly accurate DIRK methods, Eq. (5.10) reduces to

$$\boldsymbol{Y}_{ni} = \boldsymbol{y}_n + \Delta t_n \sum_{j=1}^{i} a_{ij} \dot{\boldsymbol{Y}}_{nj} = \boldsymbol{S}_{ni} + \Delta t_n a_{ii} \dot{\boldsymbol{Y}}_{ni} \tag{5.13}$$

with the starting value

$$\boldsymbol{S}_{ni} = \boldsymbol{y}_n + \Delta t_n \sum_{j=1}^{i-1} a_{ij} \dot{\boldsymbol{Y}}_{nj} \tag{5.14}$$

which depends only on already calculated stage derivatives. This implies that the stage derivatives can be computed in each stage from (5.13) giving

$$\dot{\boldsymbol{Y}}_{ni} = \frac{\boldsymbol{Y}_{ni} - \boldsymbol{S}_{ni}}{\Delta t_n a_{ii}}. \tag{5.15}$$

Inserting this into (5.11) yields the non-linear system

$$\boldsymbol{R}_{ni}(\boldsymbol{Y}_{ni}) \equiv \boldsymbol{F}\left(T_{ni}, \boldsymbol{Y}_{ni}, \frac{\boldsymbol{Y}_{ni} - \boldsymbol{S}_{ni}}{\Delta t_n a_{ii}}\right) = \boldsymbol{0}, \quad i = 1, \ldots, s \tag{5.16}$$

which has to be solved in each stage, where the unknown stage values $\boldsymbol{Y}_{ni}$ can be computed and allowing afterwards the computation of the stage derivatives $\dot{\boldsymbol{Y}}_{ni}$ using Eq. (5.15).

Application of a stiffly accurate DIRK-method to the DAE-system (5.3) implies the solution of the following coupled nonlinear system

$$\boldsymbol{R}_{ni}(\boldsymbol{Y}_{ni}) = \left\{ \begin{array}{c} \boldsymbol{G}_{ni}(\boldsymbol{U}_{ni}, \boldsymbol{Q}_{ni}) \\ \boldsymbol{L}_{ni}(\boldsymbol{U}_{ni}, \boldsymbol{Q}_{ni}) \end{array} \right\} = \boldsymbol{0} \tag{5.17}$$

at each stage T_{ni} of the time step from t_n to t_{n+1}, with

$$\boldsymbol{G}_{ni}(\boldsymbol{U}_{ni}, \boldsymbol{Q}_{ni}) \equiv \boldsymbol{g}(T_{ni}, \boldsymbol{U}_{ni}, \boldsymbol{Q}_{ni}) \tag{5.18}$$

and

$$\boldsymbol{L}_{ni}(\boldsymbol{U}_{ni}, \boldsymbol{Q}_{ni}) \equiv \boldsymbol{A} \left\{ \frac{\boldsymbol{Q}_{ni} - \boldsymbol{S}^q_{ni}}{\Delta t_n a_{ii}} \right\} - \boldsymbol{r}(T_{ni}, \boldsymbol{U}_{ni}, \boldsymbol{Q}_{ni}). \tag{5.19}$$

Where $\boldsymbol{S}^q_{ni}$ is given by, see Eq. (5.14),

$$\boldsymbol{S}^q_{ni} = \boldsymbol{Q}_n + \Delta t_n \sum_{j=1}^{i-1} a_{ij} \dot{\boldsymbol{Q}}_{nj}. \tag{5.20}$$

The partition of the quantities is

$$\boldsymbol{y}_n = \left\{ \begin{array}{c} \boldsymbol{u}_n \\ \boldsymbol{q}_n \end{array} \right\}, \quad \boldsymbol{Y}_{ni} = \left\{ \begin{array}{c} \boldsymbol{U}_{ni} \\ \boldsymbol{Q}_{ni} \end{array} \right\}, \quad \boldsymbol{S}_{ni} = \left\{ \begin{array}{c} \boldsymbol{S}^u_{ni} \\ \boldsymbol{S}^q_{ni} \end{array} \right\} \tag{5.21}$$

With this partition we obtain from Eq. (5.12) the solution in the form

$$\boldsymbol{u}_{n+1} = \boldsymbol{u}_n + \Delta t_n \sum_{i=1}^{s} b_i \dot{\boldsymbol{U}}_{ni} \tag{5.22}$$

$$\boldsymbol{q}_{n+1} = \boldsymbol{q}_n + \Delta t_n \sum_{i=1}^{s} b_i \dot{\boldsymbol{Q}}_{ni} \tag{5.23}$$

As mentioned before, the case of elastoplasticity with yield function leads to a singular matrix $\boldsymbol{A}$ if the consistency condition is not used to compute the plastic multiplier analytically but is added as an additional unknown and the yield function itself represents an additional algebraic equation.

The coefficients of three Runge-Kutta methods, which will be applied later on, are summarized in Tab. 5.2. The Backward Euler method is included as a special case with one stage only in that class of methods, see Tab. 5.2(a). The second row of coefficients $\hat{b}_i$ in the Butcher tableaus (Tab. 5.2(b)(c)) is explained in the following paragraph, which explains how embedded Runge-Kutta methods can be used to implement an efficient stepsize control.

Time-adaptivity

The choice of an appropriate time stepsize is one major issue in the business of solving ordinary differential equations as well as differential-algebraic equations. One point is that, although the algebraic part of equation (5.17) at time stage $T_{ns} = t_{n+1}$ is satisfied, the integration step (5.17) can be an inaccurate approximation of the solution. Another common desire is the specification of tolerances ensuring that the integration error keeps limited. Furthermore, a time adaptive procedure can be very efficient, especially in problems with different time scales, since it adapts to the underlying solution path. In order to minimize the computational effort of the time adaptive

Table 5.2: Butcher tableaus of three of the applied Runge-Kutta methods

(a) Backward Euler ($s = 1, p = 1$)

$$\begin{array}{c|c} 1 & 1 \\ \hline & 1 \end{array}$$

(b) Ellsiepen's coefficients [44, S.89] ($s = 2, p = 2, \hat{p} = 1$)

$$\begin{array}{c|cc} \alpha & \alpha & \\ 1 & 1-\alpha & \alpha \\ \hline & 1-\alpha & \alpha \\ & 1-\hat{\alpha} & \hat{\alpha} \end{array} \qquad \alpha = 1 - \tfrac{1}{2}\sqrt{2}, \qquad \hat{\alpha} = 2 - \tfrac{5}{4}\sqrt{2}$$

(c) Cash's coefficients [25] ($s = 3, p = 3, \hat{p} = 2$)

$$\begin{array}{c|ccc} \gamma & \gamma & & \\ \delta & \tau-\gamma & \gamma & \\ 1 & \alpha & \beta & \gamma \\ \hline & \alpha & \beta & \gamma \\ & \hat{\alpha} & \hat{\beta} & 0 \end{array}$$

$$\begin{aligned} \gamma &= 0.4358665215084580 \\ \tau-\gamma &= 0.2820667392457705 \\ \alpha &= 1.2084966491760101 \\ \beta &= -0.6443631706844691 \\ \delta &= 0.7179332607542295 \\ \hat{\alpha} &= 0.7726301276675511 \\ \hat{\beta} &= 0.2273698723324489 \end{aligned}$$

procedure, so-called embedded methods are applied. For these procedures a method to estimate a suitable time step size is outlined below, for further details see HAIRER ET AL. [57] and HAIRER AND WANNER [58]. The adaptation of the stepsize is done on the basis of the estimation of the so-called local integration error. The current value $\boldsymbol{y}(t_n)$ is assumed to be given (exactly). The local integration error δ is the difference of the exact solution $\boldsymbol{y}(t_{n+1})$ (unknown) and the numerical solution $\boldsymbol{y}_{n+1}$, which is known from the integration step with the applied Runge-Kutta method:

$$\begin{aligned} \delta(t_{n+1}, \boldsymbol{y}; \Delta t_n) &= \boldsymbol{y}(t_{n+1}) - \boldsymbol{y}_{n+1} \\ &= \boldsymbol{y}(t_{n+1}) - \underbrace{\{\boldsymbol{y}(t_n) + \Delta t_n \boldsymbol{\Phi}(t_n, \boldsymbol{y}; \Delta t_n)\}}_{\text{Runge-Kutta method}} \\ &= \underbrace{\Delta t_n^{p+1} \Psi(t_n, \boldsymbol{y})}_{\text{main part of local integration error}} + O(\Delta t_n^{p+2}) \end{aligned} \tag{5.24}$$

In Eq. (5.24) $\boldsymbol{\Phi}$ is the so-called increment function of the method, see HAIRER ET AL. [57]. This function is only formally explicit and incorporates implicit algorithms. Equation (5.24) stems from the Taylor expansion of the exact solution and the solution produced by the chosen Runge-Kutta method, where p is the order of the applied Runge-Kutta method. The local integration error can be separated into the main part and a part of the order Δt_n^{p+2}. The main part of the local integration error is used to estimate the stepsize in order to control the integration error. To this end, we assume that there are two numerical integration methods with different integration order,

$$\boldsymbol{y}_{n+1} = \boldsymbol{y}(t_n) + \Delta t_n \boldsymbol{\Phi}(t_n, \boldsymbol{y}; \Delta t_n) \tag{5.25}$$

$$\hat{\boldsymbol{y}}_{n+1} = \boldsymbol{y}(t_n) + \Delta t_n \hat{\boldsymbol{\Phi}}(t_n, \hat{\boldsymbol{y}}; \Delta t_n) \tag{5.26}$$

leading to the local integration errors

$$\delta = \boldsymbol{y}(t_{n+1}) - \boldsymbol{y}_{n+1} = \Delta t_n^{p+1} \Psi(t_n, \boldsymbol{y}) + O(\Delta t_n^{p+2}) \tag{5.27}$$

$$\hat{\delta} = \boldsymbol{y}(t_{n+1}) - \hat{\boldsymbol{y}}_{n+1} = \Delta t_n^{\hat{p}+1} \hat{\Psi}(t_n, \boldsymbol{y}) + O(\Delta t_n^{\hat{p}+2}). \tag{5.28}$$

Here, we assume $\hat{p} < p$. From the difference of both errors, the error of the lower order method $\hat{p}$ can be estimated,

$$\delta - \hat{\delta} = \hat{\boldsymbol{y}}_{n+1} - \boldsymbol{y}_{n+1} = \Delta t_n^{\hat{p}+1} \hat{\Psi}(t_n, \boldsymbol{y}) + o(\Delta t_n^{\hat{p}+2}) \approx \Delta t_n^{\hat{p}+1} \hat{\Psi}(t_n, \boldsymbol{y}). \tag{5.29}$$

Now, we can demand that the absolute value of the error should be smaller than a chosen tolerance

$$\|\Delta t_n^{\hat{p}+1} \hat{\Psi}(t_n, \boldsymbol{y})\| \approx \|\hat{\boldsymbol{y}}_{n+1} - \boldsymbol{y}_{n+1}\| \leq \varepsilon_r \|\hat{\boldsymbol{y}}_n\| + \varepsilon_a \tag{5.30}$$

with ε_a and ε_r being user defined absolute and relative error tolerances. With the help of the assumption that the error $\|\hat{\Psi}(t_n, \boldsymbol{y})\| \approx C$ shall be constant from one step to the next, Eq. (5.30) gives

$$\|\hat{\boldsymbol{y}}_{n+1} - \boldsymbol{y}_{n+1}\| \approx C \Delta t_n^{\hat{p}+1} \tag{5.31}$$

and can be used to compute the new stepsize Δt_{new} from the prescribed error tolerances

$$C \Delta t_{\text{new}}^{\hat{p}+1} = \varepsilon_r \|\hat{\boldsymbol{y}}_n\| + \varepsilon_a \tag{5.32}$$

and Eq. (5.31) by elimination of the constant C,

$$\Delta t_{\text{new}} = \Delta t_n \left(\frac{\varepsilon_r \|\hat{\boldsymbol{y}}_n\| + \varepsilon_a}{\|\hat{\boldsymbol{y}}_{n+1} - \boldsymbol{y}_{n+1}} \right)^{\frac{1}{\hat{p}+1}} \tag{5.33}$$

To stabilize the stepsize behavior, i.e. avoid oscillations of the stepsize or the rejection of stepsizes small modifications to (5.33) should be made. Furthermore, the application of suitable norms $\|\cdot\|$ for solution vectors containing quantities with different scales should be considered. For the application within finite elements for material models with internal variables the decomposition of the local error $\boldsymbol{y}_{\text{err}} = \hat{\boldsymbol{y}}_{n+1} - \boldsymbol{y}_{n+1}$ in

$$\boldsymbol{u}_{\text{err}} = \hat{\boldsymbol{u}}_{n+1} - \boldsymbol{u}_{n+1} \quad \text{and} \quad \boldsymbol{q}_{\text{err}} = \hat{\boldsymbol{q}}_{n+1} - \boldsymbol{q}_{n+1} \tag{5.34}$$

for the displacements $\boldsymbol{u}$ and the internal variables $\boldsymbol{q}$ has been suggested by DIEBELS ET AL. [38] and EHLERS AND ELLSIEPEN [43] and has been applied by HARTMANN [60] and ELLSIEPEN AND HARTMANN [45]. Furthermore, they suggested weighted norms

$$e_u := \sqrt{\frac{1}{n_u} \sum_{l=1}^{n_u} \left(\frac{u_{\text{err}}^l}{\epsilon_r |u_n^l| + \epsilon_a^l} \right)^2}, \quad e_q := \max_k \left| \frac{q_{\text{err}}^k}{\epsilon_r |q_n^k| + \epsilon_a^k} \right| \tag{5.35}$$

The maximum $e_m = \max(e_u, e_q)$ of these partial error measures can now be used to determine the new stepsize

$$\Delta t_{\text{new}} = \Delta t_n \begin{cases} \max(f_{\min}, f_{\text{safety}}, e_m^{-1/(\hat{p}+1)}) & | \quad e_m > 1 \\ \min(f_{\max}, f_{\text{safety}}, e_m^{-1/(\hat{p}+1)}) & | \quad e_m \leq 1. \end{cases} \tag{5.36}$$

The factor $0 < f_{\text{safety}} < 1$ prohibits oscillations and the factors $f_{\min}$ and $f_{\max}$ prohibit too big stepsize changes, see HAIRER ET AL. [57] and HAIRER AND WANNER [58]. Practical values for $f_{\text{safety}}, f_{\min}, f_{\max}$ are $0.8 \leq f_{\text{safety}} \leq 0.9$, $0.2 \leq f_{\min} \leq 0.5$ and $2 \leq f_{\max} \leq 3$.

The main advantage of the choice of an embedded method for the computation of the solution $\hat{\boldsymbol{y}}_{n+1}$ with order $\hat{p}$ is that it uses the same coefficients a_{ij} and c_i as the higher order method (p) with other coefficients $\hat{b}_i$, see Table 5.2. Thus, the solution is

$$\hat{\boldsymbol{y}}_{n+1} = \boldsymbol{y}_n + \Delta t_n \sum_{i+1}^{s} \hat{b}_i \dot{\boldsymbol{Y}}_{ni}. \tag{5.37}$$

The stage derivative $\dot{\boldsymbol{Y}}_{ni}$ are already known from the method of order p. Accordingly, the error $\boldsymbol{y}_{\text{err}} = \hat{\boldsymbol{y}}_{n+1} - \boldsymbol{y}_{n+1}$ can be calculated from

$$\boldsymbol{y}_{\text{err}} = \hat{\boldsymbol{y}}_{n+1} - \boldsymbol{y}_{n+1} = \Delta t_n \sum_{i+1}^{s} (\hat{b}_i - b_i)\, \dot{\boldsymbol{Y}}_{ni} \tag{5.38}$$

without significant additional computational effort.

5.1.2 Multilevel-Newton algorithm

It has been demonstrated in Section 5.1.1 that the application of stiffly accurate DIRK methods to DAE-systems leads to nonlinear systems of equations

$$\boldsymbol{F}(\boldsymbol{y}) = \boldsymbol{0}, \qquad \boldsymbol{F}, \boldsymbol{y} \in \mathbb{R}^{n_u + n_Q} \tag{5.39}$$

with the structure

$$\boldsymbol{F}(\boldsymbol{y}) = \left\{ \begin{array}{c} \boldsymbol{L}(\boldsymbol{U}, \boldsymbol{Q}) \\ \boldsymbol{G}(\boldsymbol{U}, \boldsymbol{Q}) \end{array} \right\} = \boldsymbol{0}, \qquad \begin{array}{l} \boldsymbol{G}, \boldsymbol{U} \in \mathbb{R}^{n_u} \\ \boldsymbol{L}, \boldsymbol{Q} \in \mathbb{R}^{n_Q} \end{array} \tag{5.40}$$

and the unknowns

$$\boldsymbol{y} = \left\{ \begin{array}{c} \boldsymbol{U} \\ \boldsymbol{Q} \end{array} \right\}. \tag{5.41}$$

This corresponds to (5.17), but for the sake of readability the indices ni, which mark the i^{th} stage in the n^{th} time step have been dropped. In this section the Multilevel-Newton algorithm is introduced, which is one way to solve the nonlinear equations, which arise from the application of the nonlinear finite element method. This method has been introduced in order to solve DAE-systems appearing for the computation of electric circuits, see RABBAT ET AL. [113]. In the field of nonlinear finite elements it has been applied by HARTMANN [60] and is discussed in detail in HARTMANN [61]. In view of the application of the method within nonlinear finite element analysis, the used notation in the structured nonlinear system (5.40) becomes comprehensible. $\boldsymbol{L}$ represents the "local" level, i.e. equations which can be solved on element level, and $\boldsymbol{G}$ represents the equations which have to be solved on the "global" level. If Eq. (5.40) stems from a finite element analysis $\boldsymbol{U}$ usually represents the unknown nodal displacements and $\boldsymbol{Q}$ the unknown internal variables emerging from all Gauss points.

Instead of $\boldsymbol{F}(\boldsymbol{y}) = \boldsymbol{0}$, we start with the coupled nonlinear system of equations

$$\boldsymbol{L}(\boldsymbol{U}, \boldsymbol{Q}) = \boldsymbol{0} \tag{5.42}$$

$$\boldsymbol{G}(\boldsymbol{U}, \boldsymbol{Q}) = \boldsymbol{0} \tag{5.43}$$

and apply the implicit function theorem to Eq. (5.42). The implicit function theorem states that a function $\boldsymbol{Q}(\boldsymbol{U})$ exists in the neighborhood of the solution of $\boldsymbol{L}(\boldsymbol{U}, \boldsymbol{Q}) = \boldsymbol{0}$, presuming sufficient continuity properties of $\boldsymbol{L}$. Introducing this (unknown) function $\boldsymbol{Q}(\boldsymbol{U})$ into equation (5.43) yields a nonlinear system of equations

$$\boldsymbol{G}(\boldsymbol{U}, \boldsymbol{Q}(\boldsymbol{U})) = \boldsymbol{0} \tag{5.44}$$

in the unknowns $\boldsymbol{U}$. Applying the classical Newton method to (5.44) means that in each iteration step indicated by $^{(m)}$ the linear system

$$\left[\frac{\partial \boldsymbol{G}}{\partial \boldsymbol{U}} + \frac{\partial \boldsymbol{G}}{\partial \boldsymbol{Q}} \frac{\mathrm{d}\boldsymbol{Q}}{\mathrm{d}\boldsymbol{U}} \right]^{(m)} \Delta \boldsymbol{U} = -\boldsymbol{G}(\boldsymbol{U}^{(m)}, \boldsymbol{Q}^{(m)}) \tag{5.45}$$

Table 5.3: Multilevel-Newton algorithm in stage i of the time step from t_n to t_{n+1}

Already known or given:	$\boldsymbol{U}_{ni}^{(0)} = \boldsymbol{u}_n,\ \boldsymbol{Q}_{ni}^{(0)} = \boldsymbol{q}_n,\ \Delta t_n,\ T_{ni},\ a_{ii},\ \boldsymbol{S}_{ni}$
Repeat	$m = 0, 1, \ldots$
	local level (abbreviation: $\boldsymbol{z} \equiv (\boldsymbol{U}_{ni}^{(m)}, \boldsymbol{Q}_{ni}^{(m)})$, given: $\boldsymbol{U}_{ni}^{(m)}$) local integration step $\boldsymbol{L}(\boldsymbol{U}_{ni}^{(m)}, \boldsymbol{Q}_{ni}^{(m)}) = \boldsymbol{0} \quad \rightarrow \quad \boldsymbol{Q}_{ni}^{(m)}$ consistent linearization $\left[\frac{\partial \boldsymbol{L}}{\partial \boldsymbol{Q}}\Big|_{\boldsymbol{z}}\right] \frac{\mathrm{d}\boldsymbol{Q}}{\mathrm{d}\boldsymbol{U}} = -\frac{\partial \boldsymbol{L}}{\partial \boldsymbol{U}}\Big|_{\boldsymbol{z}} \quad \rightarrow \quad \frac{\mathrm{d}\boldsymbol{Q}}{\mathrm{d}\boldsymbol{U}}\Big|_{\boldsymbol{z}}$
	global level solve linear system of equations $\left[\frac{\partial \boldsymbol{G}}{\partial \boldsymbol{U}}\Big|_{\boldsymbol{z}} + \frac{\partial \boldsymbol{G}}{\partial \boldsymbol{Q}}\Big|_{\boldsymbol{z}} \frac{\mathrm{d}\boldsymbol{Q}}{\mathrm{d}\boldsymbol{U}}\Big|_{\boldsymbol{z}}\right] \Delta \boldsymbol{U}_{ni} = -\boldsymbol{G}(\boldsymbol{z}) \quad \rightarrow \quad \Delta \boldsymbol{U}_{ni}$ update global variables $\boldsymbol{U}_{ni}^{(m+1)} = \boldsymbol{U}_{ni}^{(m)} + \Delta \boldsymbol{U}_{ni} \quad \rightarrow \quad \boldsymbol{U}_{ni}^{(m+1)}$
Until	Convergence criteria are fulfilled

has to be solved for the increment $\Delta \boldsymbol{U}$ which is subsequently used to update the unknowns $\boldsymbol{U}^{(m+1)} = \boldsymbol{U}^{(m)} + \Delta \boldsymbol{U}$. The quantities $\boldsymbol{Q}^{(m)} = \boldsymbol{Q}(\boldsymbol{U}^{(m)})$ in (5.45) are obtained from the solution of the nonlinear system

$$\boldsymbol{L}(\boldsymbol{U}^{(m)}, \boldsymbol{Q}^{(m)}) = \boldsymbol{0} \tag{5.46}$$

with given $\boldsymbol{U}^{(m)}$. Furthermore, one needs on the left-hand side of (5.45) for the determination of the Jacobi-matrix of the Newton algorithm the derivatives $\partial \boldsymbol{G}/\partial \boldsymbol{U}$ and $\partial \boldsymbol{G}/\partial \boldsymbol{Q}$, which can be computed from (5.43). In addition to this, the total derivative of the (unknown) function $\boldsymbol{Q}(\boldsymbol{U})$ with respect to $\boldsymbol{U}$ is needed. Applying the chain rule to the function

$$\boldsymbol{L}(\boldsymbol{U}, \boldsymbol{Q}(\boldsymbol{U})) = \boldsymbol{0} \tag{5.47}$$

yields

$$\frac{\partial \boldsymbol{L}}{\partial \boldsymbol{U}} + \frac{\partial \boldsymbol{L}}{\partial \boldsymbol{Q}} \frac{\mathrm{d}\boldsymbol{Q}}{\mathrm{d}\boldsymbol{U}} = \boldsymbol{0} \ \Rightarrow \ \left[\frac{\partial \boldsymbol{L}}{\partial \boldsymbol{Q}}\right] \frac{\mathrm{d}\boldsymbol{Q}}{\mathrm{d}\boldsymbol{U}} = -\frac{\partial \boldsymbol{L}}{\partial \boldsymbol{U}}. \tag{5.48}$$

This is a system of linear equations with several right hand sides $\partial \boldsymbol{L}/\partial \boldsymbol{U}$ for the unknown total derivative $\mathrm{d}\boldsymbol{Q}/\mathrm{d}\boldsymbol{U}$. Summarizing the Multilevel-Newton algorithm we can state that one has to solve a linear system of equations on the global level in each iteration. In order to build the right-hand side of this linear equation system, the quantity $\boldsymbol{Q}^{(m)}$ must be computed on the local level by solving the nonlinear system of equations (5.46). This is usually done with the classical Newton method resulting in a local iteration. In the case of the constitutive model proposed in this thesis the application of the classical Newton method to solve (5.46) leads to severe convergence problems. To overcome these convergence problems a number of algorithms (globalization of Newton method) are applied. These algorithms are presented in the subsequent section. In addition to the solution of the nonlinear system a linear system with several right hand sides has to be calculated for the determination of the total derivative $\mathrm{d}\boldsymbol{Q}/\mathrm{d}\boldsymbol{U}$. The Multilevel-Newton algorithm is summarized in Tab.5.3.

5.1.3 Globalization of Newton's method

The treatment of the nonlinear system (5.46) for given $\boldsymbol{U}^{(m)}$ on the local level with the classical Newton-method might lead to convergence problems, i.e. the algorithm often diverges. For this reason some globalization strategies for the Newton-algorithm are applied. Although these algorithms can mostly be found in textbooks like SCHWETLICK AND KRETZSCHMAR [120] or ORTEGA AND RHEINBOLDT [106] they are explained in some detail here for the sake of comprehensibility.

Classical Newton-algorithm

The reason why Newton's method is one of the most favored methods for solving systems of nonlinear equations is that it exhibits a quadratic rate of convergence. Of course, this is only true for starting points, which are "close" to the solution, otherwise the algorithm does not reach a quadratic rate of convergence initially, or may even diverge. The classical Newton-algorithm applied to the nonlinear system $\mathbf{L}(\mathbf{Q}) = \mathbf{0}$ is summarized in Tab. 5.4.

Table 5.4: Newton-algorithm to solve the nonlinear system of equations $\mathbf{L}(\mathbf{Q}) = \mathbf{0}$

Initialization:	$\mathbf{Q}^{(0)} = \mathbf{Q}_n, \quad k = 0$
Repeat	$k = 0, 1, \ldots$
	Compute right-hand side $\mathbf{L}(\mathbf{Q}^{(k)})$
	Compute Jacobian $\mathbf{J} = \mathbf{L}'(\mathbf{Q}^{(k)}) = \mathsf{J}_{ij} = \dfrac{\partial \mathsf{L}_i(\mathbf{Q}^{(k)})}{\partial \mathsf{Q}_j}$
	Compute the increment from $\mathbf{J}\left[\Delta\mathbf{Q}^{(k)}\right] = -\mathbf{L}(\mathbf{Q}^{(k)})$
	Update the unknowns $\mathbf{Q}^{(k+1)} = \mathbf{Q}^{(k)} + \Delta\mathbf{Q}^{(k)}$ $k = k + 1$
Until	Convergence criteria are fulfilled

Newton with damping

Even a small modification of the Newton-method can enhance its stability significantly. The idea of the damped Newton-method is to reduce the increment (of the Newton-method) as long as one is not "close" to the solution. The decision, whether one is "close" to the solution or not, can be made based upon the value of the right-hand side $\|\mathbf{L}(\mathbf{Q}^{(k)})\|$. Therefore, the norm of the right-hand side is compared to an appropriate "critical radius" r_{crit} in each iteration. As long as the norm exceeds the critical radius r_{crit} only a fraction (e.g. $1/2$) of the full increment is added to the vector of unknowns. Otherwise the original full increment is used resulting again in a quadratic rate of convergence. The described damping method for the Newton-algorithm is summarized in Tab. 5.5. It has the merit that it is inexpensive from a computational point of view.

Commonly one finds under the keyword "damped Newton-method" more elaborate algorithms, which demand additional evaluations of $\mathbf{L}$ in each iteration. Therefore, these algorithms have not been implemented. Instead other, more sophisticated and computationally more expensive algorithms, have been studied, in order to increase the stability of Newton's method.

Table 5.5: Newton algorithm with damping

Initialization:	$\mathbf{Q}^{(0)} = \mathbf{Q}_n, \quad k = 0, \quad$ choose critical distance r_{crit}
Repeat	$k = 0, 1, \ldots$
	Compute right hand side $\mathbf{L}(\mathbf{Q}^{(k)})$
	Compute Jacobian $\mathbf{J} = \mathbf{L}'(\mathbf{Q}^{(k)}) = \mathsf{J}_{ij} = \frac{\partial \mathsf{L}_i(\mathbf{Q}^{(k)})}{\partial \mathsf{Q}_j}$
	Compute the full increment from $\mathbf{J}\left[\Delta\mathbf{Q}^{(k)}\right] = -\mathbf{L}(\mathbf{Q}^{(k)})$
	Compute "distance" from solution $\|\mathbf{L}(\mathbf{Q}^{(k)})\|$
	if $\|\mathbf{L}(\mathbf{Q}^{(k)})\| < r_{\text{crit}}$ then
	$\beta = 1$
	else
	$\beta = 0.5$
	endif
	Update the unknowns $\mathbf{Q}^{(k+1)} = \mathbf{Q}^{(k)} + \beta\Delta\mathbf{Q}^{(k)}$ $k = k + 1$
Until	Convergence criteria are fulfilled

Newton-algorithm with line-search

In this section another common expansion of Newton's method by a so-called line-search algorithm is introduced in order to achieve convergence for starting points, which are not close to the solution. The unknowns of the nonlinear system, which has to be solved on the local level, have to obey certain inequality constraints. This problem is addressed afterwards and it is explicitly shown how these constraints can be incorporated in the algorithm. The idea of the line search expansion is similar to the idea of the damping. Again a reduction of the increment resulting in an update of the unknowns of the form $\mathbf{Q}^{(k+1)} = \mathbf{Q}^{(k)} + \beta\Delta\mathbf{Q}^{(k)}$ is used. But now the para-meter β is not fixed. Instead β is determined in each iteration from an appropriate minimization problem. The line-search algorithm is described in the following and summarized in Tab. 5.6.

It is obvious that the solution of $\mathbf{L}(\mathbf{Q}) = \mathbf{0}$ is also the solution of the minimization problem

$$\varphi(\mathbf{Q}) = \frac{1}{2}\mathbf{L}^T(\mathbf{Q})\mathbf{L}(\mathbf{Q}) \;\rightarrow\; \min \tag{5.49}$$

since $\varphi(\mathbf{Q}) = 0$ is true for $\mathbf{L}(\mathbf{Q}) = \mathbf{0}$ and due to the quadratic structure of Eq.(5.49) $\varphi(\mathbf{Q}) \geq 0$ for all $\mathbf{Q}$. Since the direction $\Delta\mathbf{Q}^{(k)}$ of Newton's method applied to the nonlinear system $\mathbf{L} = \mathbf{0}$ represents a descent direction for the minimization problem $\varphi(\mathbf{Q}) \rightarrow \min$, the convergence of the algorithm to a local minimum can be guaranteed by the application of a line-search scheme, see, for example, LUENBERGER [99], BERTSEKAS [17] or DENNIS AND SCHNABEL [36]. To this end the merit function

$$\hat{\varphi}(\beta) = \varphi(\mathbf{Q}^{(k)} + \beta\Delta\mathbf{Q}^{(k)}) \tag{5.50}$$

is introduced. Now, the line-search parameter β is determined from the approximate minimization of $\hat{\varphi}(\beta)$. The approximate minimizer of $\hat{\varphi}(\beta)$ is obtained as the minimizer of a quadratic fit to the function $\hat{\varphi}(\beta)$. The fit is based on

$$\hat{\varphi}(0) = \varphi(\mathbf{Q}^{(k)}) = \frac{1}{2}\mathbf{L}^T\mathbf{L}, \tag{5.51}$$

$$\hat{\varphi}'(0) = -2\varphi(\mathbf{Q}^{(k)}), \tag{5.52}$$

$$\hat{\varphi}(1) = \varphi(\mathbf{Q}^{(k)} + \Delta\mathbf{Q}^{(k)}) \tag{5.53}$$

with the minimum of the quadratic function defined by equations (5.51), (5.52) and (5.53) being at

$$\beta_{\text{min}} = \frac{-\hat{\varphi}(0)}{2\left(\hat{\varphi}(1) - \hat{\varphi}'(0) - \hat{\varphi}(0)\right)}. \tag{5.54}$$

The calculated line-search parameter $\beta^{(k)}$ in the k^{th} iteration has to satisfy the so-called Goldstein conditions

$$\hat{\varphi}(\beta^{(k)}) \leq \hat{\varphi}(0) + \varepsilon\hat{\varphi}'(0)\beta^{(k)} \tag{5.55}$$

$$\hat{\varphi}(\beta^{(k)}) > \hat{\varphi}(0) + (1-\varepsilon)\hat{\varphi}'(0)\beta^{(k)} \tag{5.56}$$

to guarantee convergence to the minimum of φ. Alternative conditions like Armijo's rule or the Wolfe test, see LUENBERGER [99] for details, may be used as well. Usually, the obtained minimum of φ will coincide with the solution of the original nonlinear problem $\mathbf{L}(\mathbf{Q}) = \mathbf{0}$. However, as stated by DENNIS AND SCHNABEL [36] in rare cases one might end up in a local minimum. If this happens one may only try to restart the search from another starting point. The algorithm is presented in Tab. 5.6, it is an adapted version of the "primal closest point projection" algorithm with line-search (unconstrained) described in PEREZ-FOGUET AND ARMERO [107]. In that publication and the companion article ARMERO AND PEREZ-FOGUET [9] several algorithms for elasto- and viscoplastic problems and the theoretical background, originating from the interpretation as optimization problems, are discussed. Also the incorporation of the constraint that the plastic multiplier needs to be positive is presented in PEREZ-FOGUET AND ARMERO [107]. The concepts in these very enlightening articles have been generalized to incorporate several inequality constraints to the unknowns, which becomes necessary for the equations resulting from the numerical treatment of the previously proposed constitutive model.

It should be noted that the second Goldstein condition (5.56), which requires that the line-search parameter β is not too small, is taken into account, by demanding $\beta^{(k)}_{(j+1)} \geq \nu\beta^{(k)}_{(j)}$. This approach has been proposed by PEREZ-FOGUET AND ARMERO [107] and is based on the work of SHULTZ ET AL. [124]. In the implementation the choices for $\nu = 0.1$ and $\varepsilon = 10^{-4}$ recommended by PEREZ-FOGUET AND ARMERO [107] have been adopted.

Table 5.6: Newton-algorithm with line-search

Initialization:	$\mathbf{Q}^{(0)} = \mathbf{Q}_n, \quad k = 0,$ Set line-search parameters: maximum number of curve fits $j_{\max}$, convergence tolerance ε, ensure finite line-search parameter ν
Repeat	$k = 0, 1, \ldots$
	Compute right-hand side $\mathbf{L}(\mathbf{Q}^{(k)})$
	Compute Jacobian $\mathbf{J} = \mathbf{L}'(\mathbf{Q}^{(k)}) = \mathsf{J}_{ij} = \dfrac{\partial \mathsf{L}_i(\mathbf{Q}^{(k)})}{\partial \mathsf{Q}_j}$
	Compute the full increment from $\mathbf{J}\left[\Delta\mathbf{Q}^{(k)}\right] = -\mathbf{L}(\mathbf{Q}^{(k)})$
	Initialize line search: $j = 0$, $\beta_{(0)}^{(k)} = 1$, $\hat{\varphi}^{(k)}(0) = \frac{1}{2}\mathbf{L}^{(k)T}\mathbf{L}^{(k)}$, $\hat{\varphi}'^{(k)} = -2\hat{\varphi}^{(k)}$
	Repeat $j = 0, 1, \ldots$
	$\mathbf{Q}_{(j)}^{(k+1)} = \mathbf{Q}_{(j)}^{(k)} + \beta_{(j)}^{(k)}\Delta\mathbf{Q}^{(k)}$
	$\mathbf{L}_{(j)}^{(k+1)} = \mathbf{L}(\mathbf{Q}_{(j)}^{(k+1)})$
	$\hat{\varphi}_{(j)}^{(k+1)} = \frac{1}{2}\mathbf{L}_{(j)}^{(k+1)T}\mathbf{L}_{(j)}^{(k+1)}$
	$\beta_{j+1}^{(k)} = \max\left(\nu\beta_{(j)}^{(k)}, \dfrac{-\left(\beta_{(j)}^{(k)}\right)^2\hat{\varphi}'^{(k)}}{2\left(\hat{\varphi}_{(j)}^{(k+1)} - \hat{\varphi}^{(k)} - \beta_{(j)}^{(k)}\hat{\varphi}'^{(k)}\right)}\right)$
	$j = j + 1$
	Until $\hat{\varphi}_{(j)}^{(k+1)} \leq \left(1 - 2\varepsilon\beta_{(j)}^{(k)}\right)\hat{\varphi}^{(k)}$ **or** $j = j_{\max}$
	if $j = j_{\max}$ then post WARNING !
	Update the unknowns $\mathbf{Q}^{(k+1)} = \mathbf{Q}_{(j)}^{(k+1)}$, $k = k + 1$
Until	Convergence criteria are fulfilled

Line-search for constrained problems

The incorporation of inequality constraints in the Newton scheme with line-search has been discussed with respect to the non-negativity of the plastic multiplier in the case of an elastoplastic model by PEREZ-FOGUET AND ARMERO [107]. The approach presented there is based on the treatment of simply constraint minimization problems, which is described in BERTSEKAS [17, PP.76] in detail. In addition to solve the nonlinear system $\mathbf{L}(\mathbf{Q}) = \mathbf{0}$, which again minimizes the function Eq.(5.49), we consider a set of constraints on some of the components of the vector of unknowns,

$$\mathsf{Q}_i \geq \mathsf{Q}_{i,\min}, \qquad i \in \mathrm{I}_{\mathrm{con}}. \tag{5.57}$$

With $\mathrm{I_{con}}$ being the set of indices of the components of $\mathbf{Q}$ for which constraints are defined[2]. In the problem of interest in this thesis the constraints which need to be considered are the non-negativity of ζ and the non-negativity of the diagonal elements of $\mathrm{C_p}$, see Eq.(5.115) - (5.117). The algorithm described in the previous section without consideration of the constraints can be generalized in order to take into account (5.57). To this end we introduce the vector function

$$\langle \mathbf{Q} \rangle_{\mathrm{I_{con}}} \; : \; \mathbb{R}^n \rightarrow \mathbb{R}^{n-n_{\mathrm{con}}} \times [\mathsf{Q}_{n-n_{\mathrm{con}}+1,\mathrm{min}}, \infty) \times \ldots \times [\mathsf{Q}_{n,\mathrm{min}}, \infty) \tag{5.58}$$

defined in components by

$$\left[\langle \mathbf{Q} \rangle_{\mathrm{I_{con}}}\right]_i = \mathsf{Q}_i \; \forall i \notin \mathrm{I_{con}} \quad \text{and} \quad \left[\langle \mathbf{Q} \rangle_{\mathrm{I_{con}}}\right]_i = \langle \mathsf{Q}_i \rangle \; \forall i \in \mathrm{I_{con}}. \tag{5.59}$$

With $\langle \cdot \rangle$ denoting a modified version of the Macauley brackets defined as

$$\langle \mathsf{Q}_i \rangle \; : \; \mathbb{R} \rightarrow [\mathsf{Q}_{i,\mathrm{min}}, \infty) \; \text{with} \; \langle \mathsf{Q}_i \rangle = \begin{cases} \mathsf{Q}_i & \text{if } \mathsf{Q}_i > \mathsf{Q}_{i,\mathrm{min}} \\ \mathsf{Q}_{i,\mathrm{min}} & \text{if } \mathsf{Q}_i \leq \mathsf{Q}_{i,\mathrm{min}} \end{cases} \tag{5.60}$$

When one of the constraints is *active*, i.e. if any

$$\left[\mathbf{Q}^{(k)}\right]_i = \mathsf{Q}_{i,\mathrm{min}} \quad \text{for} \quad i \in \mathrm{I_{con}} \tag{5.61}$$

and

$$\left[\nabla \varphi(\mathbf{Q}^{(k)})\right]_i = \left[\left(\mathbf{J}(\mathbf{Q}^{(k)})\right)^T \mathbf{L}(\mathbf{Q}^{(k)})\right]_i > 0 \quad \text{for} \quad i \in \mathrm{I_{con}} \tag{5.62}$$

with $\mathbf{J} = \dfrac{\partial \mathsf{L}_i(\mathbf{Q}^{(k)})}{\partial \mathsf{Q}_j}$ being the Jacobian. That means that if the i^{th} component of $\mathbf{Q}$ is at the bound $\mathsf{Q}_{i,\mathrm{min}}$ and the original update direction $\Delta\mathbf{Q}$ would lead to a further decrease of the i^{th} component of $\mathbf{Q}$. Accordingly, instead of the original update direction $\Delta\mathbf{Q}$ (from the Newton method) a modified update direction has to be found which does not lead to a further reduction of the components having already reached their limit value. This direction is given by

$$\Delta\mathbf{Q}^{(k)} = -\mathbf{D}^{(k)} \nabla \varphi(\mathbf{Q}^{(k)}) = -\mathbf{D}^{(k)} \left(\mathbf{J}(\mathbf{Q}^{(k)})\right)^T \mathbf{L}(\mathbf{Q}^{(k)}) \tag{5.63}$$

for φ defined in Eq.(5.49) and $\mathbf{D}$ defined in components by

$$\left[\mathbf{D}^{(k)}\right]_{ij} = \left[\left(\mathbf{J}(\mathbf{Q}^{(k)})\right)^{-1} \left(\mathbf{J}(\mathbf{Q}^{(k)})\right)^{-T}\right]_{ij} \quad \forall \; i,j < n_{\mathrm{con}} \text{ or } i = j \in \mathrm{I_{con}} \tag{5.64}$$

$$\left[\mathbf{D}^{(k)}\right]_{ij} = \left[\mathbf{D}^{(k)}\right]_{ji} = 0 \quad \forall i \in \mathrm{I_{con}} \text{ and } j \neq i \tag{5.65}$$

This means that the original Newton update direction is used if none of the constraints is active, otherwise the modified search direction is used. Accordingly, the previously described line search scheme has to be adapted in order to take into account the constraints, i.e. instead of $\hat{\varphi}_{(j)}^{(k)} = \varphi\left(\mathbf{Q}^{(k)} + \beta_{(j)}^{(k)} \Delta\mathbf{Q}^{(k)}\right)$ with the classical Newton update direction $\Delta\mathbf{Q}^{(k)}$ we have to use

$$\hat{\varphi}_{(j)}^{(k)} = \varphi\left(\left\langle \varphi\mathbf{Q}^{(k)} + \beta_{(j)}^{(k)} \Delta\mathbf{Q}^{(k)} \right\rangle_{\mathrm{I_{con}}}\right) \tag{5.66}$$

with $\Delta\mathbf{Q}^{(k)}$ from Eq.(5.63) and $\langle \cdot \rangle_{\mathrm{I_{con}}}$ as defined in Eq.(5.60). The final algorithm, where also the evaluation of the Goldstein condition has been adapted, is summarized in Tab. 5.7.

[2]Without loss of generality, in the following we will assume that there are constraints for the last n_{con} components of $\mathbf{Q}$ while the first $n - n_{\mathrm{con}}$ components of $\mathbf{Q}$ are unconstrained. (This can always be achieved by reordering the components of $\mathbf{Q}$)

Table 5.7: Newton-algorithm with line-search and constraints

Initialization: $\mathbf{Q}^{(0)} = \mathbf{Q}_n, \quad k = 0, \quad$ Set line-search parameters: $j_{\max}$, ε, ν, see Tab. 5.7

Repeat $k = 0, 1, \ldots$

Compute right-hand side and Jacobian

$$\mathbf{L}(\mathbf{Q}^{(k)}), \quad \mathbf{J} = \mathbf{L}'(\mathbf{Q}^{(k)}) = \mathsf{J}_{ij} = \frac{\partial \mathsf{L}_i(\mathbf{Q}^{(k)})}{\partial \mathsf{Q}_j}$$

Detection of active constraints

if $\mathsf{Q}_i = \mathsf{Q}_{i,\min}$ then $aux_i = (\operatorname{grad} \hat{\varphi})_i = \left(\mathbf{J}^T \mathbf{L}\right)_i \quad i \in \mathrm{I}_{\mathrm{con}}$

Determine update direction

if $(aux_i \leq 0 \, \forall \, i \in \mathrm{I}_{\mathrm{c}})$ then

$flag =$true, $\quad \Delta\mathbf{Q} = -\mathbf{J}^{-1}\mathbf{L}$

else

$flag =$false

$$\left(\mathbf{D}^{(k)}\right)_{lm} = \begin{cases} 0 \mid l, m = i \text{ with } aux_i \geq 0, \mathsf{Q}_i = \mathsf{Q}_{i,\min}, l \neq m \\ \left(\mathbf{J}^{-1}\mathbf{J}^{-T}\right)_{lm} \mid \text{otherwise} \end{cases}$$

endif

Initialize line search:

$$j = 0, \beta_{(0)}^{(k)} = 1, \hat{\varphi}^{(k)}(0) = \tfrac{1}{2}\mathbf{L}^{(k)T}\mathbf{L}^{(k)}, \hat{\varphi}'^{(k)} = \begin{cases} -2\hat{\varphi}^{(k)} \mid flag = \text{true} \\ \mathbf{L}^{(k)T}(\mathbf{J}\Delta\mathbf{Q}) \mid flag = \text{false} \end{cases}$$

Repeat $j = 0, 1, \ldots$

Compute new values of unknowns and the merit function for current β

$$\mathbf{Q}_{(j)}^{(k+1)} = \left\langle \mathbf{Q}_{(j)}^{(k)} + \beta_{(j)}^{(k)} \Delta\mathbf{Q}^{(k)} \right\rangle$$
$$\mathbf{L}_{(j)}^{(k+1)} = \mathbf{L}(\mathbf{Q}_{(j)}^{(k+1)})$$
$$\hat{\varphi}_{(j)}^{(k+1)} = \tfrac{1}{2}\mathbf{L}_{(j)}^{(k+1)T}\mathbf{L}_{(j)}^{(k+1)}$$

Check first Goldstein condition

$$bound = \begin{cases} \left(1 - 2\varepsilon\beta_{(j)}^{(k)}\hat{\varphi}^{(k)}\right) \mid flag = \text{true} \ \wedge \ \text{no constraint active} \\ \hat{\varphi}^{(k)} + \varepsilon\left(\mathbf{L}^T\left(\mathbf{J}^{(k)}\left(\mathbf{Q}_{(j)}^{(k+1)} - \mathbf{Q}^{(k)}\right)\right)\right) \mid \text{otherwise} \end{cases}$$

Compute new β as minimizer of quadratic fit

$$\beta_{j+1}^{(k)} = \max\left(\nu\beta_{(j)}^{(k)}, \frac{-\left(\beta_{(j)}^{(k)}\right)^2 \hat{\varphi}'^{(k)}}{2\left(\hat{\varphi}_{(j)}^{(k+1)} - \hat{\varphi}^{(k)} - \beta_{(j)}^{(k)}\hat{\varphi}'^{(k)}\right)}\right)$$

Next curve fit

$j = j + 1$

Until $\hat{\varphi}_{(j)}^{(k+1)} \leq bound$ **or** $j = j_{\max}$

if $j = j_{\max}$ then post WARNING !

Update the unknowns

$\mathbf{Q}^{(k+1)} = \mathbf{Q}_{(j)}^{(k+1)}$

$k = k + 1$

Until Convergence criteria are fulfilled

Embedded Newton-algorithm (homotopy)

An alternative approach for the globalization of Newton's method is the so-called *homotopy Newton method*, which is also known under the name *embedded Newton method*. In order to be able to apply this kind of algorithm, one has to remember that the nonlinear system, which has to be solved on local level, depends on the nodal displacements, or, to be more precise, on the deformation represented in our case by the right Cauchy-Green tensor C. For this tensor we use, in the numerical implementation, the 6x1 vector representation $\mathbf{C}$,

$$\mathbf{L}(\mathbf{C}(\boldsymbol{U}^{(m)}), \mathbf{Q}) = \mathbf{0}. \tag{5.67}$$

We suppose that a solution at time t_n is known

$$\mathbf{L}(\mathbf{C}^{(n)}, \mathbf{Q}^{(n)}) = \mathbf{0}. \tag{5.68}$$

By introduction of the increment $\Delta\mathbf{C} = \mathbf{C} - \mathbf{C}^{(n)}$ the nonlinear system to be solved can be rewritten

$$\mathbf{L}(\mathbf{C}^{(n)} + \lambda\Delta\mathbf{C}, \mathbf{Q}) = \mathbf{0} \tag{5.69}$$

where the scalar "load" parameter λ has been introduced. With $\lambda = 0$ Eq. (5.69) is fulfilled for $\mathbf{Q}^{(n)}$. For $\lambda = 1$ Eq. (5.69) represents again the nonlinear equation, for which a solution is sought. The idea is now to increase λ in steps k from $\lambda = 0$ to $\lambda = 1$ solving in each step k the nonlinear system (5.69) for which the solution of the previous step represents a "good" starting vector, at least for a sufficiently small stepsize. The nonlinear system of equations is solved with the classical Newton algorithm in each step, which will converge quadratically for sufficiently small steps. The algorithm is summarized in Tab. 5.8, for more details about this algorithm see, for example, SCHWETLICK AND KRETZSCHMAR [120] or TÖRNIG AND SPELLUCCI [133].

Table 5.8: Homotopy Newton algorithm

Initialization: $\mathbf{Q}^{(0)} = \mathbf{Q}_n$, choose $\tau_{\max}$

Repeat $k = 0, 1, \ldots$

if $(\lambda^{(k)} + \tau^{(k)} > 1)$ then $\tau^{(k)} = 1 - \lambda^{(k)}$

jumplabel 1: Increase λ

$$\lambda^{(k+1)} = \lambda^{(k)} + \tau^{(k)}, \quad \mathbf{Q}^{(k,0)} = \mathbf{Q}^{(k)}$$

Repeat $i = 0, 1, \ldots$

Compute right hand side

$$\mathbf{L}(\mathbf{Q}^{(k,i)}, \lambda^{(k+1)})$$

Compute Jacobian

$$\mathbf{J} = \frac{\partial \mathbf{L}}{\partial \mathbf{Q}}(\mathbf{Q}^{(k,i)})$$

Compute increment $\Delta\mathbf{Q}^{(k,i)}$ from

$$\mathbf{J}[\Delta\mathbf{Q}^{(k,i)}] = -\mathbf{L}(\mathbf{Q}^{(k,i)})$$

Update the unknowns

$$\mathbf{Q}^{(k,i+1)} = \mathbf{Q}^{(k,i)} + \Delta\mathbf{Q}^{(k,i)}$$

Sufficient descent check

if $(\|\mathbf{L}(\mathbf{Q}^{(k,i+1)}, \lambda^{(k+1)})\| \leq \mu \|\mathbf{L}(\mathbf{Q}^{(k,i)}, \lambda^{(k+1)})\|)$ then

next Newton step $i = i + 1$

else

reduce step size and retry $\tau^{(k)} = \rho\tau^{(k)}$ goto jumplabel 1

endif

Until Convergence $\|\mathbf{L}(\mathbf{Q}^{(k,i+1)}, \lambda^{(k+1)})\| < \varepsilon$

New step size $\tau^{(k+1)} = \min(\tau^{(k)}/\rho, \tau_{\max})$

Update the unknowns

$$\mathbf{Q}^{(k+1)} = \mathbf{Q}^{(k,i+1)}, \quad k = k + 1$$

Until $\lambda^{(k)} = 1$

5.2 Numerical solution of the initial boundary value problem

Analytical solutions for initial boundary value problems (IBVPs), which are formed by the balance relations in combination with the constitutive equations and problem-dependent initial and boundary conditions, can only be found for very few, simple problems. In general a numerical solution procedure is necessary. One method is the finite element method, which is applied and described here. The constitutive equations are formulated, such that the balance of rotational momentum is fulfilled (symmetric $\mathbf{T}$). Furthermore, only isothermal, quasi-static problems are discussed, i.e. only the balance of momentum Eq. (2.46) (without the inertia term) needs to be considered:

$$\operatorname{div} \mathbf{T}(\boldsymbol{x}, t) + \rho \boldsymbol{k} = \mathbf{0} \tag{5.70}$$

The constitutive model(s) considered in this work are of the form

$$\tilde{\mathbf{T}} = \tilde{\mathbf{h}}(\mathbf{C}(\boldsymbol{X}, t), \mathbf{q}(\boldsymbol{X}, t)) \tag{5.71}$$

$$\tilde{\mathbf{A}}\dot{\mathbf{q}} - \tilde{\mathbf{r}}(\mathbf{C}(\boldsymbol{X}, t), \mathbf{q}(\boldsymbol{X}, t)) = \mathbf{0} \quad \text{with} \quad \mathbf{q}(\boldsymbol{x}, t_0) = \mathbf{q}_0 \tag{5.72}$$

They consist of an elasticity relation, which depends, in addition to the deformation (displacements), on a number of internal variables that evolve according to a set of differential equations of 1^{st} order with problem specific initial conditions. Furthermore, in the case of elastoplasticity, we have to consider the algebraic constraint, namely the yield condition. In that case the matrix $\tilde{\mathbf{A}}$ becomes singular. The treatment of the IBVP constituted by equations (5.70) - (5.72) with the help of the finite element method is demonstrated in the following subsections. After the introduction of the principle of virtual displacements, see Section 5.2.1, its spatial discretization is discussed leading to a set of differential-algebraic equations (DAE), which is treated with DIRK-methods, see Subsection 5.2.3. In each stage of the applied DIRK-method a nonlinear system of equations has to be solved. Here, the Multilevel-Newton algorithm is applied to this end. This solution procedure sustains the structure of current implicit finite element implementations, e.g. ANSYS INC. [7], ABAQUS [1]. The treatment of the nonlinear system that is solved on the local level needs special attention. Its solution with the help of globalized Newton methods is discussed in Subsection 5.2.4. Afterwards, we address the computation of the consistent tangent matrix, see Section 5.2.5, which is necessary within the Multilevel-Newton algorithm of Section 5.1.2, see Eq. (5.45).

5.2.1 The principle of virtual displacements

The principle of virtual displacements (weak form of the equilibrium equation) formulated with quantities of the current configuration reads

$$\begin{aligned}
\pi(t, \boldsymbol{u}, \delta\boldsymbol{u}, \boldsymbol{q}) &= \int_v \mathbf{T} \cdot \frac{1}{2}\left(\operatorname{grad}\delta\boldsymbol{u}(\boldsymbol{x}) + \operatorname{grad}^T\delta\boldsymbol{u}(\boldsymbol{x})\right) dv - \int_v \rho\boldsymbol{k}\cdot\delta\boldsymbol{u}dv - \int_a \boldsymbol{t}\cdot\delta\boldsymbol{u}da \\
&= \int_v \mathbf{T}\cdot\operatorname{sym}\delta\mathbf{h}dv - \underbrace{\int_v \rho\boldsymbol{k}\cdot\delta\boldsymbol{u}dv - \int_a \boldsymbol{t}\cdot\delta\boldsymbol{u}da}_{\pi_{\text{ext}}(\delta\boldsymbol{u},t)} \\
&= \int_v \operatorname{sym}\delta\mathbf{h}\cdot\mathbf{S}dV - \pi_{\text{ext}}(\delta\boldsymbol{u}, t) = 0
\end{aligned} \tag{5.73}$$

with the virtual spatial displacement gradient

$$\delta\mathbf{h} = \operatorname{grad}\delta\boldsymbol{u}(\boldsymbol{x}). \tag{5.74}$$

The weak form can be derived from the balance of momentum (2.46) without acceleration term by multiplying the balance of momentum (scalar product) in its local form with arbitrary "test functions" (virtual displacements $\delta\boldsymbol{u}$) and integrating the resulting equation over the volume of the material body. With the help of the identity

$$\operatorname{div}\mathbf{T}\cdot\delta\boldsymbol{u}=\operatorname{div}\left(\mathbf{T}^T\delta\boldsymbol{u}\right)-\mathbf{T}^T\cdot\operatorname{grad}\delta\boldsymbol{u} \tag{5.75}$$

and the Gauss theorem

$$\int_v(\operatorname{div}\boldsymbol{v})dv=\int_a\boldsymbol{v}\cdot\boldsymbol{n}da \tag{5.76}$$

one obtains Eq. (5.73). The virtual displacements $\delta\boldsymbol{u}$ have to fulfill the geometrical boundary conditions, i.e. they have to be zero at the part of the boundary of the material body, where geometrical boundary conditions are given. On the other part of the boundary, where no geometrical boundary conditions are given, the stress has to be given on the boundary. The stress tensor $\mathbf{T}$ depends, via $\tilde{\mathbf{h}}(\mathbf{C}(\boldsymbol{X},t),\mathbf{q}(\boldsymbol{X},t))$, on the displacements $\boldsymbol{u}$ due to the dependence of the right Cauchy Green tensor $\mathbf{C}=\mathbf{C}(\boldsymbol{u})$ on the displacements. The relation between the Cauchy stress tensor $\mathbf{T}$ in the principle of virtual displacements (5.73) and the second Piola-Kirchhoff stress tensor $\tilde{\mathbf{T}}$ in the constitutive equation (5.71) can be taken from Tab.2.1, i.e. $\mathbf{T}=J^{-1}\mathbf{F}\tilde{\mathbf{T}}\mathbf{F}^T$.

5.2.2 Space discretization of the principle of virtual displacements

In order to solve the IBVP posed by (5.73) together with the constitutive equations for the evolution of the internal variables (5.72), the following approach within the framework of the finite element method is chosen. In the first step the space discretization is realized. This includes the partition of the body into elements, the introduction of ansatz functions for the displacements and the virtual displacements and the formulation of the coordinate transformation of the elements into a reference element (i.e. introduction of local coordinates). Furthermore, this first step includes the (numerical) solution of the integrals within Eq. (5.73), for example, with the Gauss quadrature. This procedure yields a system of nonlinear equations in the nodal displacements, that still contains the dependence on the internal variables evolving according to differential equations. All in all we have a system of differential-algebraic equations in the unknown internal variables and the unknown nodal displacements. In the second step, i.e. the time discretization, the DIRK-methods, already introduced in Section 5.1.1, are applied to solve this DAE-system, preserving the structure of current implicit FE implementations. This approach of separating space and time integration is known as "method of lines" within the framework of methods for solving partial differential equations. Conducting the space discretization first and subsequently the time discretization is denoted as vertical method of lines.

The displacements $\boldsymbol{u}(\boldsymbol{x},t)$ and the virtual displacements $\delta\boldsymbol{u}(\boldsymbol{x})$ are expressed with the help of the nodal displacements $\boldsymbol{u}_j(t)\in\mathbb{R}^3$, and the virtual nodal displacements $\delta\boldsymbol{u}_j\in\mathbb{R}^3$ and the ansatz-functions $N_j(\boldsymbol{x})$ of the node j with $j=1,\ldots,n_{\text{nodes}}$, and $\boldsymbol{x}\in\Omega$. The original domain of the material body V is approximated by Ω and its surface A is approximated by Γ. The brief description presented here is restricted to a displacement formulation for three-dimensional continuum elements in the current configuration with

$$\boldsymbol{u}^h(\mathbf{x},t)=\sum_{j=1}^{n_{\text{nodes}}}N_j(\mathbf{x})u_j(t)=\boldsymbol{N}_a(\mathbf{x})\boldsymbol{u}_a(t)\quad\boldsymbol{u}^h\in\mathbb{R}^3 \tag{5.77}$$

$$\delta\boldsymbol{u}^h(\mathbf{x})=\sum_{j=1}^{n_{\text{nodes}}}N_j(\mathbf{x})\delta u_j=\boldsymbol{N}_a(\mathbf{x})\delta\boldsymbol{u}_a(t)\quad\delta\boldsymbol{u}^h\in\mathbb{R}^3. \tag{5.78}$$

In (5.77) we have introduced the vector $\boldsymbol{u}_a(t) \in \mathbb{R}^{n_{\text{dof}}}$ containing all nodal displacements and in (5.78) the vector of all virtual displacements $\delta\boldsymbol{u}_a \in \mathbb{R}^{n_{\text{dof}}}$ as well as the matrix of ansatz functions $\boldsymbol{N}_a(\mathbf{x}) \in \mathbb{R}^{3\times n_{\text{dof}}}$. The index a is added in order to emphasize that the vectors $\boldsymbol{u}_a(t)$ and $\delta\boldsymbol{u}_a$ contain all nodal displacements. The vectors of all displacements and all virtual displacements are subdivided (formally) into known and unknown components with $\boldsymbol{u}(t) \in \mathbb{R}^{n_{\text{u}}}$ representing the vector of unknown and $\overline{\boldsymbol{u}}(t) \in \mathbb{R}^{n_{\text{p}}}$ representing the vector of known (prescribed) nodal displacements, $n_{\text{dof}} = n_{\text{u}} + n_{\text{p}}$. For the nodes with prescribed displacements, the virtual displacements have to vanish, i.e. $\delta\overline{\boldsymbol{u}} = \boldsymbol{0} \in \mathbb{R}^{n_{\text{p}}}$, while the other virtual nodal displacements $\delta\boldsymbol{u} \in \mathbb{R}^{n_{\text{u}}}$ are arbitrary. Taking into account this subdivision of the nodal displacements for the ansatz (5.77) and (5.78) leads to

$$\boldsymbol{u}^h(\mathbf{x},t) = \underbrace{\left[\boldsymbol{N}(\mathbf{x})\,\overline{\boldsymbol{N}}(\mathbf{x})\right]}_{\boldsymbol{N}_a(\mathbf{x})} \underbrace{\left\{\begin{array}{c}\boldsymbol{u}(t)\\ \overline{\boldsymbol{u}}(t)\end{array}\right\}}_{\boldsymbol{u}_a(t)} = \boldsymbol{N}(\mathbf{x})\mathbf{u}(t) + \overline{\boldsymbol{N}}(\mathbf{x})\overline{\boldsymbol{u}}(t) \tag{5.79}$$

$$\delta\boldsymbol{u}^h(\mathbf{x},t) = \underbrace{\left[\boldsymbol{N}(\mathbf{x})\,\overline{\boldsymbol{N}}(\mathbf{x})\right]}_{\boldsymbol{N}_a(\mathbf{x})} \underbrace{\left\{\begin{array}{c}\delta\boldsymbol{u}\\ \delta\overline{\boldsymbol{u}} = \boldsymbol{0}\end{array}\right\}}_{\delta\boldsymbol{u}_a(t)} = \boldsymbol{N}(\mathbf{x})\delta\boldsymbol{u}(t) \tag{5.80}$$

with

$$\boldsymbol{u}_a(t) = \left\{\begin{array}{c}\boldsymbol{u}(t)\\ \overline{\boldsymbol{u}}(t)\end{array}\right\} \quad \text{and} \quad \delta\boldsymbol{u}_a(t) = \left\{\begin{array}{c}\delta\boldsymbol{u}\\ \delta\overline{\boldsymbol{u}}\end{array}\right\} = \left\{\begin{array}{c}\delta\boldsymbol{u}\\ \boldsymbol{0}\end{array}\right\}. \tag{5.81}$$

This ansatz for the displacements and virtual displacements depends on the spatial coordinates $\mathbf{x}$, which depend on the deformation through $\mathbf{x} = \chi_R(\mathbf{X},t)$.

The coordinate transformation between the actual element and the reference element can be performed, using the same ansatz functions as for the nodal displacements (isoparametric finite element formulation). For the reference element considered here (3D - continuum element) the local coordinates of the reference element $\boldsymbol{\xi} \in \Omega_{\text{ref}}$ have the ranges, $-1 \le \xi \le 1$, $-1 \le \eta \le 1$, $-1 \le \zeta \le 1$. The coordinate transformation is given by

$$\mathbf{X} = \chi^e(\boldsymbol{\xi}), \quad \boldsymbol{\xi} = \varphi^e(\mathbf{X}) = \chi^{e-1}(\mathbf{X}) \tag{5.82}$$

Furthermore, it is evident that the globally defined displacements $\boldsymbol{u}^h(\mathbf{x},t) = \boldsymbol{N}_a(\mathbf{x})\boldsymbol{u}_a(t)$ have to be equal to the locally defined displacements $\mathbf{N}^e\mathbf{u}^e(t)$ within each element. A formal allocation between the nodal displacements $\mathbf{u}^e(t)$ of element e and the vector of all displacements $\boldsymbol{u}_a(t)$ can be written in the form

$$\mathbf{u}^e = \boldsymbol{Z}_a^e\boldsymbol{u}_a \quad \text{with} \quad \boldsymbol{Z}_a^e \in \mathbb{R}^{n_{\text{en}}\times n_{\text{dof}}}. \tag{5.83}$$

The so-called coincidence Matrix $\boldsymbol{Z}_a^e$ subdivides according to the subdivision of the nodal displacements into one part $\overline{\boldsymbol{Z}}^e$ allocating the known nodal displacements and one part $\boldsymbol{Z}^e$ allocating the unknown nodal displacements

$$\mathbf{u}^e = \boldsymbol{Z}^e\boldsymbol{u} + \overline{\boldsymbol{Z}}^e\overline{\boldsymbol{u}} \quad \text{with} \quad \boldsymbol{Z}_a^e = \left[\boldsymbol{Z}^e\,\overline{\boldsymbol{Z}}^e\right]. \tag{5.84}$$

Based on the ansatz for the displacements $\boldsymbol{u}^h(\mathbf{x},t)$ and the virtual displacements $\delta\boldsymbol{u}^h(\mathbf{x})$ the strain tensor(s) needed in the constitutive equation (elasticity relation) within the principle of virtual displacements as well as the virtual strain tensor appearing directly in the principle of virtual displacements can be derived.

Inserting the approximations ($V \rightarrow \Omega$, $A \rightarrow \Gamma$, $\boldsymbol{u} \rightarrow \boldsymbol{u}^h$, $\delta\boldsymbol{u} \rightarrow \delta\boldsymbol{u}^h$) into the principle of virtual displacements (5.73) formulated in the current configuration and splitting the integral over the material body into integrals over the domains of the individual elements yields

$$\boldsymbol{g}(t,\boldsymbol{u},\boldsymbol{q}) = \sum_{e=1}^{n_e} \mathbf{Z}^{eT} \int_{\Omega^e} \mathbf{B}^{eT}\mathbf{S}^e d\Omega^e - \overline{\boldsymbol{p}}(t) = \sum_{e=1}^{n_e} \mathbf{Z}^{eT} \int_{\Omega^e} \mathbf{B}^{eT}\mathbf{F}_{23}^e\tilde{\mathbf{T}}^e d\Omega^e - \overline{\boldsymbol{p}}(t) = \boldsymbol{0} \quad (5.85)$$

with $\overline{\boldsymbol{p}}(t) \in \mathbb{R}^{n_u}$ being the total external load consisting of volume distributed, surface distributed and nodal forces $\overline{\boldsymbol{F}}(t) \in \mathbb{R}^{n_u}$

$$\overline{\boldsymbol{p}}(t) \equiv \underbrace{\int_\Omega \boldsymbol{N}^T(\boldsymbol{x})\rho\boldsymbol{k}d\Omega}_{\text{volume distributed load}} + \underbrace{\int_\Gamma \boldsymbol{N}^T(\boldsymbol{x})\boldsymbol{t}d\Gamma}_{\text{surface distributed load}} + \underbrace{\overline{\boldsymbol{F}}(t)}_{\text{nodal forces}} \quad (5.86)$$

and with $\mathbf{B}^e = \left[\mathbf{B}_1^e \dots \mathbf{B}_{n_{en}}^e\right]$ and the strain displacement matrix for the a^{th} node of element e

$$\mathbf{B}_a^e = \begin{bmatrix} n_{a,x}^e & 0 & 0 \\ 0 & n_{a,y}^e & 0 \\ 0 & 0 & n_{a,z}^e \\ n_{a,y}^e & n_{a,x}^e & 0 \\ 0 & n_{a,z}^e & n_{a,y}^e \\ n_{a,z}^e & n_{a,x}^e & 0 \end{bmatrix}, \qquad a = 1,\dots,n_{\text{en}}, \quad (5.87)$$

which looks like the strain-displacement matrix in the case of small deformations. The matrix $\mathbf{F}_{23}^e$ reads

$$\mathbf{F}_{23}^e = \begin{bmatrix} F_{11}^eF_{11}^e & F_{12}^eF_{12}^e & F_{13}^eF_{13}^e & 2F_{11}^eF_{12}^e & 2F_{12}^eF_{13}^e & 2F_{13}^eF_{11}^e \\ F_{21}^eF_{21}^e & F_{22}^eF_{22}^e & F_{23}^eF_{23}^e & 2F_{21}^eF_{22}^e & 2F_{22}^eF_{23}^e & 2F_{23}^eF_{21}^e \\ F_{31}^eF_{31}^e & F_{32}^eF_{32}^e & F_{33}^eF_{33}^e & 2F_{31}^eF_{32}^e & 2F_{32}^eF_{33}^e & 2F_{33}^eF_{31}^e \\ F_{11}^eF_{21}^e & F_{12}^eF_{22}^e & F_{13}^eF_{23}^e & F_{11}^eF_{22}^e + F_{12}^eF_{21}^e & F_{12}^eF_{23}^e + F_{13}^eF_{22}^e & F_{13}^eF_{21}^e + F_{11}^eF_{23}^e \\ F_{21}^eF_{31}^e & F_{22}^eF_{32}^e & F_{23}^eF_{33}^e & F_{21}^eF_{32}^e + F_{22}^eF_{31}^e & F_{22}^eF_{33}^e + F_{23}^eF_{32}^e & F_{23}^eF_{31}^e + F_{21}^eF_{33}^e \\ F_{31}^eF_{11}^e & F_{32}^eF_{12}^e & F_{33}^eF_{13}^e & F_{31}^eF_{12}^e + F_{32}^eF_{11}^e & F_{32}^eF_{13}^e + F_{33}^eF_{12}^e & F_{33}^eF_{11} + F_{31}^eF_{13}^e \end{bmatrix} \quad (5.88)$$

and is the matrix representation (6x6 matrix) of the fourth order tensor, which maps the second Piola-Kirchhoff tensor from the reference configuration upon the weighted Cauchy stress tensor (Kirchhoff stress tensor) of the current configuration. Further details about the applied matrix notation can be found in HARTMANN [60, APPENDIX A2]. In Eq. (5.85) the quantity $\tilde{\mathbf{T}}^e = \left\{\tilde{T}_{11}^h, \tilde{T}_{22}^h, \tilde{T}_{33}^h, \tilde{T}_{12}^h, \tilde{T}_{23}^h, \tilde{T}_{31}^h\right\}^T$ is the 6x1 vector notation of the symmetric second Piola-Kirchhoff tensor.

The numerical solution of the integrals over the domain of the individual elements by application of a Gauss-quadrature after transformation of the element to the reference element can be expressed by

$$\boldsymbol{g}(t,\boldsymbol{u},\boldsymbol{q}) = \sum_{e=1}^{n_e} \boldsymbol{Z}^{eT} \left\{ \sum_{j=1}^{n_\xi}\sum_{k=1}^{n_\eta}\sum_{l=1}^{n_\zeta} w_j w_k w_l \mathbf{B}^{eT}\left(\boldsymbol{\xi}_{jkl}\right) \tilde{\mathrm{h}}(\mathbf{C}^e(\boldsymbol{\xi}_{jkl}), \mathbf{q}_{jkl}^e) \det \mathbf{J}^e(\boldsymbol{\xi}_{jkl}) \right\} - \overline{\boldsymbol{p}}(t) = \boldsymbol{0}, \quad (5.89)$$

where we have introduced the Gauss-point coordinates and the weights w_j, w_k, w_l of the Gauss quadrature with n_ξ, n_η, n_ζ being the number of Gauss-points in the ξ, η, ζ direction, respectively.

$\mathbf{J}^e$ is the Jacobian of the coordinate transformation $\boldsymbol{X} = \chi^e(\boldsymbol{\xi})$. The internal variables $\boldsymbol{q}(t)$ have to be evaluated at each integration (Gauss) point, i.e. the system of evolution equations (5.72) reads

$$\boldsymbol{A}\dot{\boldsymbol{q}}(t) - \boldsymbol{r}(t, \boldsymbol{u}(t), \boldsymbol{q}(t)) = \boldsymbol{0}, \quad \boldsymbol{q}(t_0) = \boldsymbol{q}_0. \tag{5.90}$$

Here $\boldsymbol{q}(t) \in \mathbb{R}^{n_Q}$ is the vector of all internal variables at all Gauss points with $n_Q = n_i \times n_q$, where n_i is the (total) number of Gauss points and n_q the number of internal variables of each Gauss point. As in the case of the nodal displacements a coincidence matrix $\boldsymbol{Z}_q^{e(ijk)}$ can be introduced

$$\mathbf{q}^e_{jkl}(t) = \boldsymbol{Z}_q^{e(jkl)}\boldsymbol{q}(t), \quad \mathbf{q}^e_{jkl} \in \mathbb{R}^{n_q}. \tag{5.91}$$

Unlike the nodal displacements the internal variables at each Gauss-point do only depend on quantities of the same Gauss-point (uncoupled)

$$\mathbf{A}\dot{\mathbf{q}}^e_{jkl}(t) - \mathbf{r}(\mathbf{C}^e_{jkl}(t), \mathbf{q}^e_{jkl}(t)) = \mathbf{0}, \quad \mathbf{q}^e_{jkl}(t_0) = \mathbf{q}^e_{jkl,0}. \tag{5.92}$$

5.2.3 Solving the DAE-system with DIRK methods and the Multilevel-Newton algorithm

The nonlinear system of equations obtained from the space discretization of the principle of virtual displacements formulated with respect to the current configuration (5.89) form together with the evolution equations for all internal variables of each integration point (5.90) a DAE-system

$$\boldsymbol{F}(t, \boldsymbol{y}(t), \dot{\boldsymbol{y}}(t)) = \left\{ \begin{array}{c} \boldsymbol{g}(t, \boldsymbol{u}(t), \boldsymbol{q}(t)) \\ \boldsymbol{A}\dot{\boldsymbol{q}}(t) - \boldsymbol{r}(t, \boldsymbol{u}(t), \boldsymbol{q}(t)) \end{array} \right\} = \boldsymbol{0}, \quad \boldsymbol{F} \in \mathbb{R}^{n_u + n_Q} \tag{5.93}$$

with

$$\boldsymbol{y}(t) = \left\{ \begin{array}{c} \boldsymbol{u}(t) \\ \boldsymbol{q}(t) \end{array} \right\}, \quad \boldsymbol{y}(t_0) = \left\{ \begin{array}{c} \boldsymbol{u}(t_0) \\ \boldsymbol{q}(t_0) \end{array} \right\}, = \left\{ \begin{array}{c} \boldsymbol{u}_0 \\ \boldsymbol{q}_0 \end{array} \right\} = \boldsymbol{y}_0, \quad \boldsymbol{y}(t) \in \mathbb{R}^{n_u + n_Q} \tag{5.94}$$

The unknowns of this DAE-system (5.93) are the nodal displacements $\boldsymbol{u}(t) \in \mathbb{R}^{n_u}$ and all internal variables $\boldsymbol{q}(t)$. The discretized principle of virtual displacements (5.89) represents the algebraic part of the DAE-system, whereas the evolution equations (5.90) represent the differential part. In Section 5.1.1 we have introduced diagonally implicit Runge-Kutta (DIRK) methods as a possible approach for the solution of DAE-systems. According to (5.17), with the short notation introduced in (5.18) and (5.19), we have to solve the nonlinear system given by

$$\begin{aligned} \boldsymbol{G}_{ni}(\boldsymbol{U}_{ni}, \boldsymbol{Q}_{ni}) \;=\; & \sum_{e=1}^{n_e} \boldsymbol{Z}^{eT} \left\{ \sum_{j=1}^{n_\xi} \sum_{k=1}^{n_\eta} \sum_{l=1}^{n_\zeta} w_j w_k w_l \mathbf{B}^{eT}(\boldsymbol{\xi}_{jkl}, \mathbf{U}^{e(jkl)}_{ni}) \right. \\ & \left. \tilde{\mathbf{h}}(\mathbf{C}^{e(jkl)}_{ni}(\mathbf{U}^{e(jkl)}_{ni}), \mathbf{Q}^{e(jkl)}_{ni}) \det \mathbf{J}^e(\boldsymbol{\xi}_{jkl}) \right\} - \overline{\boldsymbol{p}}(T_{ni}) = \boldsymbol{0} \end{aligned} \tag{5.95}$$

$$\boldsymbol{L}_{ni}(\boldsymbol{U}_{ni}, \boldsymbol{Q}_{ni}) = \boldsymbol{A} \left\{ \frac{\boldsymbol{Q}_{ni} - \boldsymbol{S}^q_{ni}}{\Delta t_n a_{ii}} \right\} - \boldsymbol{r}(T_{ni}, \boldsymbol{U}_{ni}, \boldsymbol{Q}_{ni}) = \boldsymbol{0} \tag{5.96}$$

in each stage T_{ni} (i^{th} stage of the n^{th} time step). This implies that the discretized principle of virtual displacements (equilibrium) represented by $\boldsymbol{G}_{ni} = \boldsymbol{0}$ is satisfied in each stage of the DIRK-method. The nonlinear system resulting from the integration of the differential part of the DAE-system decomposes into small nonlinear systems of equations at each Gauss-point. Since

the evolution equations at distinct Gauss-points are not coupled with the evolution equations at any other Gauss-point, each of the small systems

$$\mathbf{L}_{ni}^{e(jkl)}\left(\mathbf{C}_{ni}^{e(jkl)}(\mathbf{U}_{ni}^{e}),\mathbf{Q}_{ni}^{e(jkl)}\right)=\mathbf{A}\left\{\frac{\mathbf{Q}_{ni}^{e(jkl)}-\mathbf{S}_{ni}^{qe(jkl)}}{\Delta t_n a_{ii}}\right\}-\mathbf{r}\left(\mathbf{C}_{ni}^{e(jkl)}(\mathbf{U}_{ni}^{e(jkl)}),\mathbf{Q}_{ni}^{e(jkl)}\right)=\mathbf{0} \tag{5.97}$$

has to be satisfied by itself. The combination of all systems of equations (5.97) can be achieved by application of the coincidence matrices (5.91)

$$\boldsymbol{L}_{ni}(\boldsymbol{U}_{ni},\boldsymbol{Q}_{ni})=\sum_{e=1}^{n_e}\left\{\sum_{j=1}^{n_\xi}\sum_{k=1}^{n_\eta}\sum_{l=1}^{n_\zeta}\boldsymbol{Z}_{q}^{e(jkl)T}\mathbf{L}_{ni}^{e(jkl)}\left(\mathbf{C}_{ni}^{e(jkl)}(\mathbf{U}_{ni}^{e(jkl)}),\mathbf{Q}_{ni}^{e(jkl)}\right)\right\}=\boldsymbol{0} \tag{5.98}$$

leading to Eq. (5.96). We apply the Multilevel-Newton algorithm introduced in Subsection 5.1.2 to solve the nonlinear system of equations given by (5.95) and (5.96). This implies that on local level (at each Gauss-point of each element) for the given displacements $\boldsymbol{U}_{ni}^{(m)}$ in each global iteration m the nonlinear system (5.97)

$$\mathbf{L}_{ni}^{e(jkl)}=\mathbf{0}\quad\Rightarrow\quad\mathbf{Q}_{ni}^{e(jkl)} \tag{5.99}$$

has to be solved. The common solution procedure for this nonlinear system is the Newton-algorithm, since the Newton-algorithm fails to converge already for moderate time (load) increments in the case of the constitutive model of Tab. 3.3 or Tab. 3.4, several globalization strategies for Newton's method have to be applied, see Section 5.1.3 and 5.2.4.

Within the Multilevel-Newton algorithm, we make use of the fact that a function $\boldsymbol{Q}(\boldsymbol{U})$ exists in the neighborhood of the solution of $\boldsymbol{F}=\boldsymbol{0}$. This (undetermined) function $\boldsymbol{Q}(\boldsymbol{U})$ is inserted into $\boldsymbol{G}(\boldsymbol{U},\boldsymbol{Q})=\boldsymbol{0}$ resulting in $\boldsymbol{G}(\boldsymbol{U},\boldsymbol{Q}(\boldsymbol{U}))=\boldsymbol{0}$. Solving this nonlinear system with Newton's method necessitates the linearization of $\boldsymbol{G}(\boldsymbol{U},\boldsymbol{Q}(\boldsymbol{U}))=\boldsymbol{0}$ with respect to $\boldsymbol{U}$, see Tab. 5.3.

For the formulation on the current configuration the linearization of (5.85) with respect to the displacements reads

$$\begin{aligned}\mathrm{D}_{\boldsymbol{u}}\boldsymbol{g}(t,\boldsymbol{u},\boldsymbol{q}(\boldsymbol{u})[\Delta\boldsymbol{u}] &= \left[\sum_{e=1}^{n_e}\boldsymbol{Z}^{eT}\left[\int_{\Omega^e}J^e\mathbf{B}^{eT}\mathbf{C}_{\mathrm{L}}^{e}\mathbf{B}^{e}d\Omega^e\right.\right.\\ &\quad\left.\left.+\int_{\Omega^e}\mathbf{B}_{\mathrm{NL}}^{eT}\mathbf{M}_{\mathrm{S}}^{e}\mathbf{B}_{\mathrm{NL}}^{e}d\Omega^e\right]\mathbf{Z}^{e}\right]\Delta\boldsymbol{u} &(5.100)\\ &= \left[\sum_{e=1}^{n_e}\boldsymbol{Z}^{eT}\mathbf{k}^{e}\boldsymbol{Z}^{e}\right]\Delta\boldsymbol{u} &(5.101)\end{aligned}$$

where the element stiffness matrix $\mathbf{k}^e=\mathbf{k}_{\mathrm{C}}^{e}+\mathbf{k}_{\mathrm{G}}^{e}$ decomposes additively into a constitutive part

$$\mathbf{k}_{\mathrm{C}}^{e}=\int_{\Omega^e}J^e\mathbf{B}^{eT}\mathbf{C}_{\mathrm{L}}^{e}\mathbf{B}^{e}d\Omega^e=\int_{\omega^e}\mathbf{B}^{eT}\mathbf{C}_{\mathrm{L}}^{e}\mathbf{B}^{e}d\omega^e \tag{5.102}$$

with the spatial tangent operator

$$\mathbf{C}_{\mathrm{L}}^{e}=\frac{1}{J^e}\mathbf{F}_{23}^{e}\tilde{\mathbf{C}}_{\mathrm{L}}^{e}\mathbf{F}_{23}^{eT}\quad\text{with}\quad\tilde{\mathbf{C}}_{\mathrm{L}}^{e}=2\left[\frac{\partial\tilde{\mathbf{h}}}{\partial\mathbf{C}^e}+\frac{\partial\tilde{\mathbf{h}}}{\partial\mathbf{q}^e}\frac{\mathrm{d}\mathbf{q}^e}{\mathrm{d}\mathbf{C}^e}\right] \tag{5.103}$$

and the part emerging from the geometrical nonlinearity

$$\mathbf{k}_{\mathrm{G}}^{e} = \int_{\Omega^e} \mathbf{B}_{\mathrm{NL}}^{eT} \mathbf{M}_{\mathbf{S}}^{e} \mathbf{B}_{\mathrm{NL}}^{e} d\Omega^e = \int_{\omega^e} \frac{1}{J^e} \mathbf{B}_{\mathrm{NL}}^{eT} \mathbf{M}_{\mathbf{S}}^{e} \mathbf{B}_{\mathrm{NL}}^{e} d\omega^e \tag{5.104}$$

with ω_e representing the approximated volume in the current configuration. In (5.100) the matrices

$$\mathbf{B}_{\mathrm{NL}}^{e} = \begin{bmatrix} n_{1,x}^e & 0 & 0 & n_{2,x}^e & 0 & 0 & \dots & n_{n_{\mathrm{en}},x}^e & 0 & 0 \\ 0 & n_{1,y}^e & 0 & 0 & n_{2,y}^e & 0 & \dots & 0 & n_{n_{\mathrm{en}},y}^e & 0 \\ 0 & 0 & n_{1,z}^e & 0 & 0 & n_{2,z}^e & \dots & 0 & 0 & n_{n_{\mathrm{en}},z}^e \\ n_{1,y}^e & 0 & 0 & n_{2,y}^e & 0 & 0 & \dots & n_{n_{\mathrm{en}},y}^e & 0 & 0 \\ 0 & n_{1,z}^e & 0 & 0 & n_{2,z}^e & 0 & \dots & 0 & n_{n_{\mathrm{en}},z}^e & 0 \\ 0 & 0 & n_{1,x}^e & 0 & 0 & n_{2,x}^e & \dots & 0 & 0 & n_{n_{\mathrm{en}},x}^e \\ n_{1,z}^e & 0 & 0 & n_{2,z}^e & 0 & 0 & \dots & n_{n_{\mathrm{en}},z}^e & 0 & 0 \\ 0 & n_{1,x}^e & 0 & 0 & n_{2,x}^e & 0 & \dots & 0 & n_{n_{\mathrm{en}},x}^e & 0 \\ 0 & 0 & n_{1,y}^e & 0 & 0 & n_{2,y}^e & \dots & 0 & 0 & n_{n_{\mathrm{en}},y}^e \end{bmatrix}, \tag{5.105}$$

and

$$\mathbf{M}_{\mathbf{S}}^{e} = \begin{bmatrix} S_{11}^e & 0 & 0 & S_{12}^e & 0 & 0 & S_{31}^e & 0 & 0 \\ 0 & S_{22}^e & 0 & 0 & S_{23}^e & 0 & 0 & S_{12}^e & 0 \\ 0 & 0 & S_{33}^e & 0 & 0 & S_{31}^e & 0 & 0 & S_{23}^e \\ S_{12}^e & 0 & 0 & S_{22}^e & 0 & 0 & S_{23}^e & 0 & 0 \\ 0 & S_{23}^e & 0 & 0 & S_{33}^e & 0 & 0 & S_{31}^e & 0 \\ 0 & 0 & S_{31}^e & 0 & 0 & S_{11}^e & 0 & 0 & S_{12}^e \\ S_{31}^e & 0 & 0 & S_{23}^e & 0 & 0 & S_{33}^e & 0 & 0 \\ 0 & S_{12}^e & 0 & 0 & S_{31}^e & 0 & 0 & S_{11}^e & 0 \\ 0 & 0 & S_{23}^e & 0 & 0 & S_{12}^e & 0 & 0 & S_{22}^e \end{bmatrix}. \tag{5.106}$$

have been introduced. For a derivation of the linearization of the formulation in the current configuration the reader is referred to HARTMANN [60, SECTION 5.1.4].

Within the specified linearizations of the principle of virtual displacements the linear system which has to be solved in each iteration contains in the tangent matrix, see (5.104), the unknown total derivative of the internal variables with respect to the displacements $\mathrm{d}\boldsymbol{Q}/\mathrm{d}\boldsymbol{U}$, see also Section 5.1.2 ((5.45) - (5.48)). This means that at each Gauss-point a linear system with several right-hand sides

$$\frac{\partial \mathbf{L}_{ni}^{e(jkl)}}{\partial \mathbf{Q}_{ni}^{e(jkl)}} \frac{\mathrm{d}\mathbf{Q}_{ni}^{e(jkl)}}{\mathrm{d}\mathbf{C}_{ni}^{e(jkl)}} = -\frac{\partial \mathbf{L}_{ni}^{e(jkl)}}{\partial \mathbf{C}_{ni}^{e(jkl)}} \tag{5.107}$$

has to be solved in order to receive the expression $\mathrm{d}\mathbf{Q}_{ni}^{e(jkl)}/\mathrm{d}\mathbf{C}_{ni}^{e(jkl)}$ which is necessary to build up the material matrix $\tilde{\mathbf{C}}_{\mathrm{L}}^{e}$.

5.2.4 Application of globalized Newton algorithms to solve the local nonlinear system (stress computation)

In this subsection the solution of the nonlinear system (5.99) with $\mathbf{L}$ defined in Eq. (5.97) resulting from the implicit integration of the flow rule, the evolution equation for the internal variable α and the auxiliary equation for $\tilde{\lambda}$ is described. Since the insertion of the resulting internal variables $\mathbf{Q}^{(n+1)} = \{\mathbf{C}_{\mathrm{p}}^{(n+1)}, \alpha^{(n+1)}\}$ into the elasticity relation (5.108) yields the new state of stress, this

procedure is therefore referred to as the stress computation or stress algorithm. The result of this local computation, i.e. on Gauss-point level, is needed to build up the right-hand side on the linear system on the global level of the Multilevel-Newton algorithm, see Tab. 5.3. Frequently, the Newton method is the first choice to solve the non-linear system of equations (5.99). It is shown, see Section 6.3, that the Newton method is not the best choice for the problem at hand and leads frequently to a non-converging algorithm. In order to investigate the different solution methods introduced in Subsection 5.1.3, i.e. globalization strategies for the Newton method, a particular problem is studied. Before we start the discussion of this problem, let us recapitulate the relevant constitutive equations from Tab. 3.4 formulated with quantities of the reference configuration.

$$\tilde{\mathbf{T}} = \tilde{\mathbf{h}}(\mathbf{C}, \mathbf{C}_\mathrm{p}) = \left(\frac{\Lambda}{2} \ln \left(\frac{\det \mathbf{C}}{\det \mathbf{C}_\mathrm{p}} \right) - \mu \right) \mathbf{C}^{-1} + \mu \mathbf{C}_\mathrm{p}^{-1} \tag{5.108}$$

$$\dot{\mathbf{C}}_\mathrm{p} = \tilde{\lambda} 2 \left(\frac{\partial \hat{F}}{\partial \mathrm{I}_1} \mathbf{I} + \frac{\partial \hat{F}}{\partial \mathrm{J}_2} (\mathbf{C}\tilde{\mathbf{T}} - (\mathrm{I}_1/3)\mathbf{I}) \right) \mathbf{C}_\mathrm{p} \tag{5.109}$$

$$\dot{\alpha} = \tilde{\lambda} \left(\frac{c_D}{\alpha} \left((\mathrm{I}_1 - 3\xi) \frac{\partial \hat{F}}{\partial \mathrm{I}_1} + \sqrt{\mathrm{J}_2} \frac{\partial \hat{F}}{\partial \sqrt{\mathrm{J}_2}} \right) - b_D \alpha \chi \right) \tag{5.110}$$

$$\tilde{\lambda} = \left\langle \frac{\hat{F}}{\sigma_0} \right\rangle^{r_{vp}} \frac{1}{\eta} \tag{5.111}$$

By means of the elasticity relation these equations can be reformulated into the abbreviated form

$$\dot{\mathbf{C}}_\mathrm{p} = \tilde{\lambda} \mathbf{h}_1 \left(\mathbf{C}, \mathbf{C}_\mathrm{p}, \alpha \right), \tag{5.112}$$

$$\dot{\alpha} = \tilde{\lambda} h_2 \left(\mathbf{C}, \mathbf{C}_\mathrm{p}, \alpha \right), \tag{5.113}$$

$$\tilde{\lambda} = \left\langle \frac{\hat{F}}{\sigma_0} \right\rangle^{r_{vp}} \frac{1}{\eta}, \tag{5.114}$$

where we have introduced the abbreviations $\mathbf{h}_1$ and h_2, which are specified in Eq. (D.3) and Eq. (D.4) of the Appendix D. In the time discretized equations (5.97) the quantity $\tilde{\lambda}$ is replaced with the quantity $\zeta = \tilde{\lambda} \Delta t_n a_{ii}$ leading to

$$0 = \mathbf{C}_\mathrm{p}^{ni} - \mathbf{C}_\mathrm{p}^{(n)} - \zeta \mathbf{h}_1 \left(\mathbf{C}, \mathbf{C}_\mathrm{p}^{ni}, \alpha^{ni} \right) \tag{5.115}$$

$$0 = \alpha^{ni} - \alpha^{(n)} - \zeta h_2 \left(\mathbf{C}, \mathbf{C}_\mathrm{p}^{ni}, \alpha^{ni} \right) \tag{5.116}$$

$$0 = F^{r_{vp}} - \zeta \sigma_0^{r_{vp}} \frac{\eta}{\Delta t_n a_{ii}} \tag{5.117}$$

which corresponds to Eq. (5.99). Where a_{ii} represents the corresponding coefficients from the applied DIRK method. Afterwards the stresses can be computed from the elasticity relation with the updated internal variables $\mathbf{Q}^{(n+1)} = \{\mathbf{C}_\mathrm{p}^{(n+1)}, \alpha^{(n+1)}\}$. The system of equations (5.115) - (5.117) for the 8 unknowns[3] $\mathbf{C}_\mathrm{p}, \alpha, \zeta$ is solved with the help of Newton's method and the modified Newton algorithms described in Section 5.1.3. In order to study and compare the algorithms a fixed value of $\mathbf{C}_\mathrm{p}, \alpha$ and ζ is chosen to represent the values from the previous equilibrium. Now, different deformations are prescribed by $\mathbf{C}$ and the number of iterations needed to converge (or non-convergence) is determined. The prescribed deformations represented by $\mathbf{C}$ are inserted into

[3] $\mathbf{C}_\mathrm{p}$ is symmetric, i.e. it contains only 6 independent components.

the elasticity relation, together with the internal variables from the previous equilibrium ($\mathbf{C}_\mathrm{p}$ from the last equilibrium) leading to the so-called predictor stress, which is an intermediate state of stress which may lay outside the elastic domain. The predictor stresses do not represent the final stresses, since the integration step for the flow rule and the evolution equations has not yet been performed. However, the predictor stresses represent the starting point for the iterative solution of the nonlinear system (5.115)-(5.117) (or (5.99)) and it has been realized that the difficulty of finding a solution, i.e. the number of iterations necessary to converge, is correlated to the relative position of the predictor stresses and the yield function.[4]

To study the convergence behavior of Newton's method and the modified Newton algorithms of Subsection 5.1.3, the following test problem is set up. The initial conditions (previous equilibrium) for $\mathbf{C}_\mathrm{p}$ and α are assumed to be resulting from a die compaction process with $\mathbf{C} = \mathrm{diag}(0.5, 1, 1)$ leading to $\mathbf{C}_\mathrm{p} = \mathrm{diag}(0.51, 1.001, 1.001)$ and $\alpha = 0.14$. From the starting conditions, the given $\mathbf{C}_\mathrm{p}$ and the prescribed deformation $\mathbf{C}$ the invariants I_1 and J_2 can be calculated by means of the elasticity relation (invariants of Cauchy predictor stress).[5] The convergence behavior is visualized graphically, and to this end the number of iterations needed to converge is represented by a specific color (grey scale) at each studied starting point (I_1,$\sqrt{J_2}$). All starting points are visualized as positions in the two-dimensional diagram of the first invariant $I_1(\mathbf{T})$ of the Cauchy stress tensor and the square root of the second invariant of its deviator $J_2(\mathbf{T})$, see definitions $(3.2)_1$ and $(3.3)_2$. In this diagram also the yield surface corresponding to the assumed internal variables is depicted, see Fig. 5.1. For all algorithms it is obvious that the number of necessary iterations depends strongly on the relative position of the predictor stress invariants (starting point) and the yield surface. Similar graphically representations have been used by PEREZ-FOGUET AND ARMERO [107] also for different starting points in the deviatoric plane, where a yield surface with a dependence on the third invariant is studied. In Fig. 5.1(a) the convergence performance of Newton's method is depicted. The plot clearly shows wide regions of non-convergence. Furthermore, the performance of the Newton-method with damping (Fig. 5.1(b)), with line-search Fig. 5.1(c) and with constraint line-search Fig. 5.1(d) are depicted. For the constraint line search algorithm the plastic multiplier as well as the diagonal elements of $\mathbf{C}_\mathrm{p}$ are demanded to be positive. It is obvious that the globalization strategies reduce the areas of non-convergence significantly allowing bigger load steps and leading to a stress algorithm with a significantly better stability. Where the studied line search algorithm with constraints outperforms the other algorithms.

After solving the nonlinear system (5.115)-(5.117), i.e. Eq. (5.99), the internal variables have to be inserted in the elasticity relation (5.108). In addition to the stresses the consistent tangent within the Multilevel-Newton algorithm is needed, see Tab. 5.3, the computation of the consistent tangent is treated in the following Subsection 5.2.5.

5.2.5 Computation of the consistent tangent matrix

Since the Multilevel-Newton algorithm, see Tab. 5.3 and Subsection 5.1.2, is based on the implicit function theorem, the total derivative $\mathrm{d}\tilde{\mathbf{h}}/\mathrm{d}\mathbf{C}$ is necessary for the global iteration. The

[4] When the stress tensor and the yield function are represented in a suitable invariant space, here the first invariant of the Cauchy stress tensor and the second invariant of its deviator are applied.

[5] Actually I_1 and $\sqrt{J_2}$ are specified, and a corresponding $\mathbf{C}$ is determined under the assumption that $\mathbf{C}$ is of the form $\mathrm{diag}(^2, \lambda_q^2, \lambda_q^2)$ (triaxial compression), resulting in non-linear equations for λ and λ_q which have to be solved.

derivative of $\tilde{\mathbf{h}}(\mathrm{C}, \mathrm{C_p})$ can be derived from the elasticity relation (5.108) applying the chain rule

$$\frac{\mathrm{d}\tilde{\mathbf{h}}}{\mathrm{d}\mathrm{C}} = \underbrace{\frac{\partial\tilde{\mathbf{h}}}{\partial\mathrm{C}}}_{\text{term I}} + \underbrace{\frac{\partial\tilde{\mathbf{h}}}{\partial\mathrm{C_p}}}_{\text{term II}} \underbrace{\frac{\mathrm{d}\mathrm{C_p}}{\mathrm{d}\mathrm{C}}}_{\text{term III}} \tag{5.118}$$

(for the case $F > 0$). Here and in the following, all indices characterizing the Gauss-point, the time and the iteration are omitted for brevity. Both the term I and the term II are calculated from the elasticity relation. In the case of $F \leq 0$ (elasticity) the internal variables do not change and term III does not occur implying that term I defines the consistent tangent $\tilde{\mathbf{C}}^{e}_{\mathrm{L}}$. In the case $F > 0$ (viscoplasticity) the internal variables are computed from the system of non-linear equations (5.115) - (5.117). This system is also required for the computation of term III namely the derivative of the plastic right Cauchy-Green tensor $\mathrm{C_p}$ with respect to C. Therefore, Eqns. (5.115) - (5.117) is written in the abbreviated form:

$$\mathbf{L}(\mathbf{C}; \mathbf{Q}(\mathbf{C})) = \mathbf{0} \Leftrightarrow \begin{array}{rl} \mathbf{L}_p(\mathbf{C}, \mathbf{C}_\mathrm{p}(\mathbf{C}), \alpha(\mathbf{C}), \zeta(\mathbf{C})) = & \mathbf{0} \\ \mathsf{L}_\alpha(\mathbf{C}, \mathbf{C}_\mathrm{p}(\mathbf{C}), \alpha(\mathbf{C}), \zeta(\mathbf{C})) = & 0 \\ \mathsf{L}_F(\mathbf{C}, \mathbf{C}_\mathrm{p}(\mathbf{C}), \alpha(\mathbf{C}), \zeta(\mathbf{C})) = & 0 \end{array} \tag{5.119}$$

By applying the implicit function theorem, see also Subsection 5.1.2 Eq. (5.48), term III can be calculated by the chain rule

$$\frac{\mathrm{d}\mathbf{L}}{\mathrm{d}\mathbf{U}} \rightarrow \frac{\mathrm{d}\mathbf{L}}{\mathrm{d}\mathbf{C}} = \frac{\partial\mathbf{L}}{\partial\mathbf{C}} + \frac{\partial\mathbf{L}}{\partial\mathbf{Q}}\frac{\mathrm{d}\mathbf{Q}}{\mathrm{d}\mathbf{C}} = \mathbf{0} \tag{5.120}$$

$$\Rightarrow \quad \underbrace{\left[\frac{\partial\mathbf{L}}{\partial\mathbf{Q}}\right]}_{\text{term A}} \underbrace{\left(\frac{\mathrm{d}\mathbf{Q}}{\mathrm{d}\mathbf{C}}\right)}_{\text{includes term III}} = -\underbrace{\left(\frac{\partial\mathbf{L}}{\partial\mathbf{C}}\right)}_{\text{term B}} \tag{5.121}$$

which reads in more detail

$$\begin{bmatrix} \dfrac{\partial\mathbf{L}_\mathrm{p}}{\partial\mathbf{C}_\mathrm{p}} & \dfrac{\partial\mathbf{L}_\mathrm{p}}{\partial\alpha} & \dfrac{\partial\mathbf{L}_\mathrm{p}}{\partial\zeta} \\ \left\{\dfrac{\partial\mathsf{L}_\alpha}{\partial\mathbf{C}_\mathrm{p}}\right\}^T & \dfrac{\partial\mathsf{L}_\alpha}{\partial\alpha} & \dfrac{\partial\mathsf{L}_\alpha}{\partial\zeta} \\ \left\{\dfrac{\partial\mathsf{L}_F}{\partial\mathbf{C}_\mathrm{p}}\right\}^T & \dfrac{\partial\mathsf{L}_F}{\partial\alpha} & \dfrac{\partial\mathsf{L}_F}{\partial\zeta} \end{bmatrix} \begin{pmatrix} \dfrac{\mathrm{d}\mathbf{C}_\mathrm{p}}{\mathrm{d}\mathbf{C}} \\ \left\{\dfrac{\mathrm{d}\alpha}{\mathrm{d}\mathbf{C}}\right\}^T \\ \left\{\dfrac{\mathrm{d}\zeta}{\mathrm{d}\mathbf{C}}\right\}^T \end{pmatrix} = - \begin{pmatrix} \dfrac{\partial\mathbf{L}_\mathrm{p}}{\partial\mathbf{C}} \\ \left\{\dfrac{\partial\mathsf{L}_\alpha}{\partial\mathbf{C}}\right\}^T \\ \left\{\dfrac{\partial F}{\partial\mathbf{C}}\right\}^T \end{pmatrix}. \tag{5.122}$$

In order to be able to compute term III, we need to solve a system of linear equations with several right-hand sides (in the 3D-case these are 6). The coefficient matrix, called term A, is known from the Newton method applied to the non-linear system (5.115) - (5.117). Additionally, the right hand-side term B, i.e. the partial derivative of $\mathbf{L}$ with respect to $\mathbf{C}$ has to be computed. The derivation of analytical expressions for this term is similar to the derivation of the analytical expression for term A. The only difference is that the equations need to be differentiated with respect to $\mathbf{C}$ instead of $\mathbf{C}_\mathrm{p}$. The solution of the linear system (5.122) yields term III needed for the computation of the consistent tangent from (5.118). Analytical expressions for the proposed model are supplied in the Appendix D. Alternatively, numerical differentiation techniques can be applied to compute the necessary derivatives. The advantage of numerical differentiation is that one can skip the cumbersome derivation and implementation of all the necessary derivatives. On the other hand, one has to know that the numerical computation of the derivatives needs more

computational time and are less accurate than analytical derivatives. Since in our case already the function evaluation is quite expensive, only a simple forward difference scheme is applied to compute the derivatives (Jacobi matrix of local nonlinear system, consistent tangent matrix). A comparison for one example computation between numerical and analytical derivatives is provided in Section 6.3.

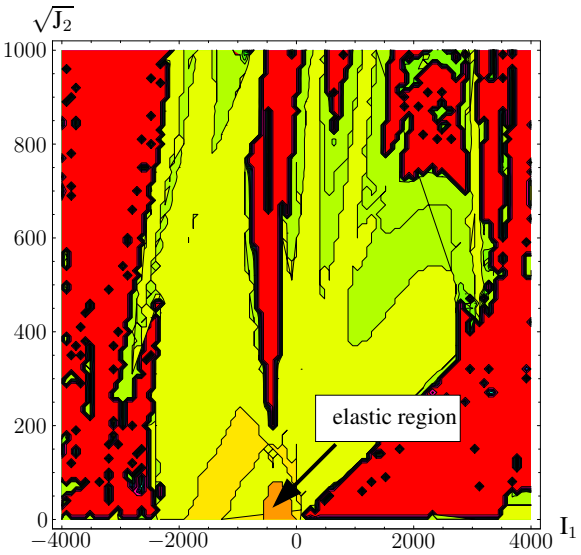

(a) Classical Newton-method

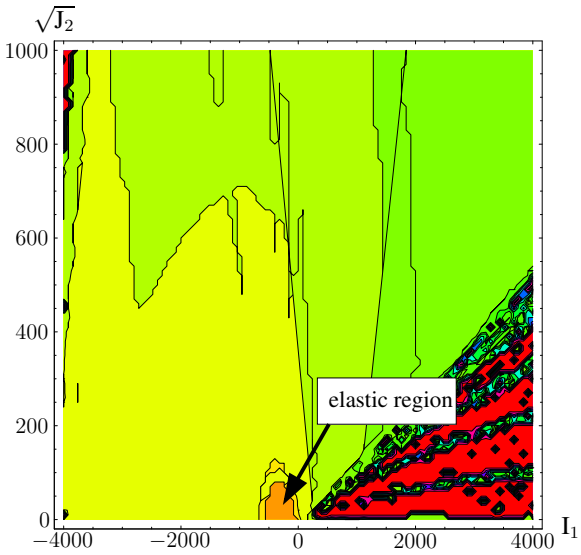

(b) Newton-method with damping

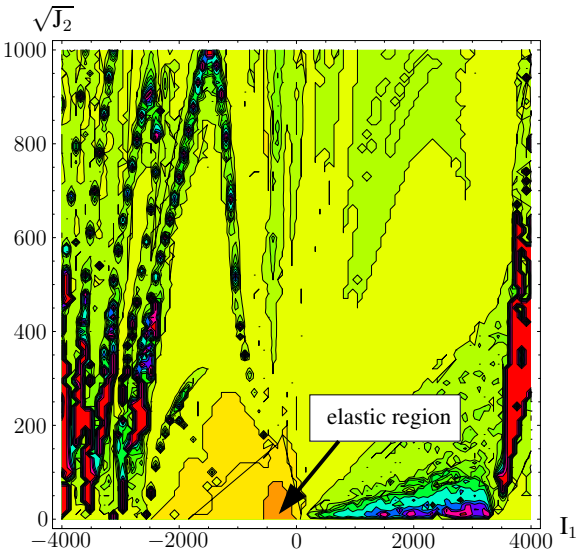

(c) Newton with line-search

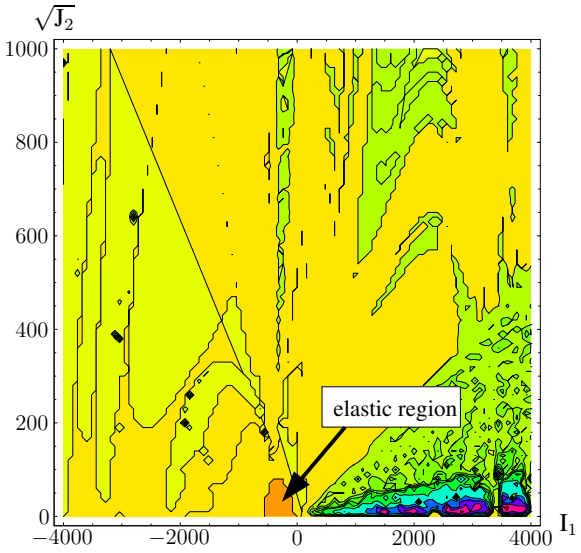

(d) Line-search with constraints

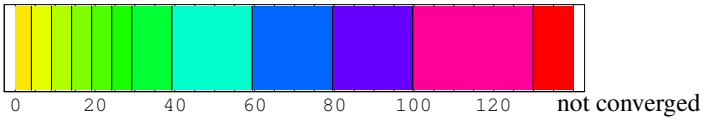

(e) Number of iterations needed to converge

Figure 5.1: Examples for convergence result

Chapter 6

Numerical studies and examples

The constitutive model introduced in Sections 3.3 and 3.4 is implemented into the finite element code TASA-FEM, see HARTMANN [62], which supports the application of higher order time integration as discussed in Section 5.2.3 as well as time adaptive strategies aiming to keep the accumulated error induced by the numerical time integration within reasonable tolerances while allowing time steps as big as possible in order to keep the overall computation time reasonable. The stress algorithm applies Newton's method or alternatively one of the globalized versions of Newton's method for the solution of the nonlinear system of equations on local level. The Jacobian of the local Newton iteration can be computed either analytically (analytical expressions for the proposed constitutive model can be found in Appendix D) or numerically. Furthermore, the computation of the consistent tangent matrix can also be done fully numerical or using the derived analytical expressions, see Appendix D. For the numerical studies presented in this chapter, three different structures with increasing complexity are considered. The simplest geometry consisting of only two elements is used in Section 6.1 in order to investigate the influence of the viscosity on the reached accuracy order of the applied Runge-Kutta methods. In Section 6.2 an essentially two-dimensional problem (L-shaped profile) is used to study the spatial distribution of the time integration error, when a time adaptive method is applied. The model geometry contains a spatial singularity, which influences the time integration error. However, even in the vicinity of the singularity the integration error can be kept small if a proper time adaptive algorithm is applied. In Section 6.3 the geometry of the example problem described in Section 6.2 is extended to a three-dimensional washer disc like part. The time step behavior for $\eta = 0$ (elastoplasticity) and $\eta = 1$ (viscoplasticity) using two different time adaptive approaches is checked. Afterwards, the merit, with respect to computational time, of the globalized Newton methods is demonstrated using this three-dimensional example. Furthermore, the computation time using either numerical or analytical consistent tangent operator and numerical or analytical Jacobian in the local iteration is compared. This example indicates that the implementation of analytical expressions is very beneficial in this respect.

Some of the results presented in this chapter have been shown in HARTMANN AND BIER [64] and the results of additional numerical studies using the proposed constitutive model can be found in SZANTO ET AL. [132] and HEISSERER ET AL. [71] using an implementation of the constitutive model in the finite elements codes Abaqus and Adhoc respectively.

6.1 Simple die compaction (order reduction phenomenon)

In order to study the higher order time integration methods described in Section 5.1.1 a very simple test case (2 elements) is considered. We consider the configuration of two elements depicted in Figure 6.1. The boundary conditions are that all nodes are fixed in y and z-direction. Furthermore, the nodes at the bottom are constrained in x-direction as well and the top nodes perform the prescribed motion down. The structure in whole is compressed to half of its initial size. The whole compaction process is carried out within one second (in the rate-independent case

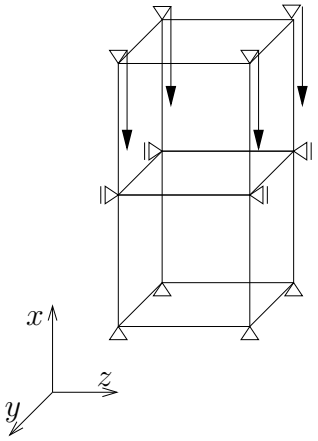

Figure 6.1: Boundary conditions of simple test structure

of elastoplasticity this has no influence). In order to check the accuracy obtained with the time integration methods specified in Section 5.1.1, first, a reference solution is generated using the diagonally implicit Runge Kutta method of 4^{th} order proposed by HAIRER AND WANNER [58], and the embedded 3^{rd} order method is used to estimate the integration error and subsequently control the step-size.

REMARK 6.1
The following settings have been used within the input file for TASA-FEM, see HARTMANN [62], *in order to generate the reference solution: nintv=7, i.e. DIRK method proposed by* HAIRER AND WANNER [58], *iscon=3, i.e. the embedded DIRK method is used for step-size control, istop=3, i.e. both toldu and tolphi are considered when convergence of global Newton-iteration is checked, with toldu representing the convergence tolerance for the displacement increment and tolphi the convergence tolerance for the residual, toldu* $= 0.1 \times 10^{-10}$, *tolphi* $=0.1 \times 10^{-8}$. *The absolute error tolerances (tolabu, tolabe and tolabs) and the relative error tolerances (tolreu, tolree and tolres) for the step size control on the basis of the embedded DIRK method are all set to* 0.1×10^{-8} *for the generation of the reference solution. The convergence criterion for the local Newton-like iteration is set to* 0.1×10^{-10} *for the generation of the reference solution. For the other computations discussed in subsection 6.1 no step-size control is considered (iscon=1) and the following convergence tolerances of the global Newton-iteration are used toldu* $= 0.1 \times 10^{-8}$, *tolphi* $=0.1 \times 10^{-6}$. *The convergence criterion for the local Newton-like iteration is set to* 0.1×10^{-8}.

REMARK 6.2
In view of the findings shown in this paragraph, it is questionable that the 4^{th} *order method really does reach* 4^{th} *order applied to the proposed constitutive model. However, due to the stricter*

convergence criterion enforcing a smaller step-size the produced solution can be considered to be sufficiently accurate to be used as a reference solution.

For comparison of the different methods the total pressure, which needs to be exerted on the top surface of the structure to produce the prescribed compaction, is used. First, the case of elastoplasticity is studied, i.e. $\eta = 0$. In this case the index of the DAE-system, which arises after the space discretization, is 2 due to the algebraic constraint (yield function) on the local level. For the definition of the index of a DAE-system see, for example, HAIRER AND WANNER [58] or ASCHER AND PETZOLD [12]. Roughly spoken the (differentiation) index of a DAE-system is the minimum number of differentiations needed (together with algebraic operations) to transform the DAE-system into a system of ordinary differential equations (ODE) in explicit form.

It can be observed from Figure 6.2(a) that the Backward-Euler method reaches as expected order 1, i.e. the relative error is reduced by half if the time step-size is halfed. In the double logarithmic plot of the relative error over the step-size Figure 6.2(a) the order of the method is simply given by the slope of the curves for the different methods. The 2^{nd} order method of Ellsiepen (ELLSIEPEN [44]) reaches order 2 whereas the 3^{rd} order method does only reach order 2. The order reduction in the case of a third order method applied to an elastoplasticity model has also been reported in the case of von Mises plasticity without hardening by ELLSIEPEN [44], see also ELLSIEPEN AND HARTMANN [45].

From Figure 6.2(b) it can be observed that the computational effort, here measured by the number of global Newton iterations of the Multilevel-Newton algorithm, is significantly lower for the methods of Ellsiepen (ELLSIEPEN [44]) or Alexander, see ALEXANDER [5], than for the Backward-Euler method. The difference increases with increasing accuracy requirements and there can easily be a factor of ten to one hundred between the number of iterations needed with the methods of Ellsiepen or Alexander and the Backward-Euler method.

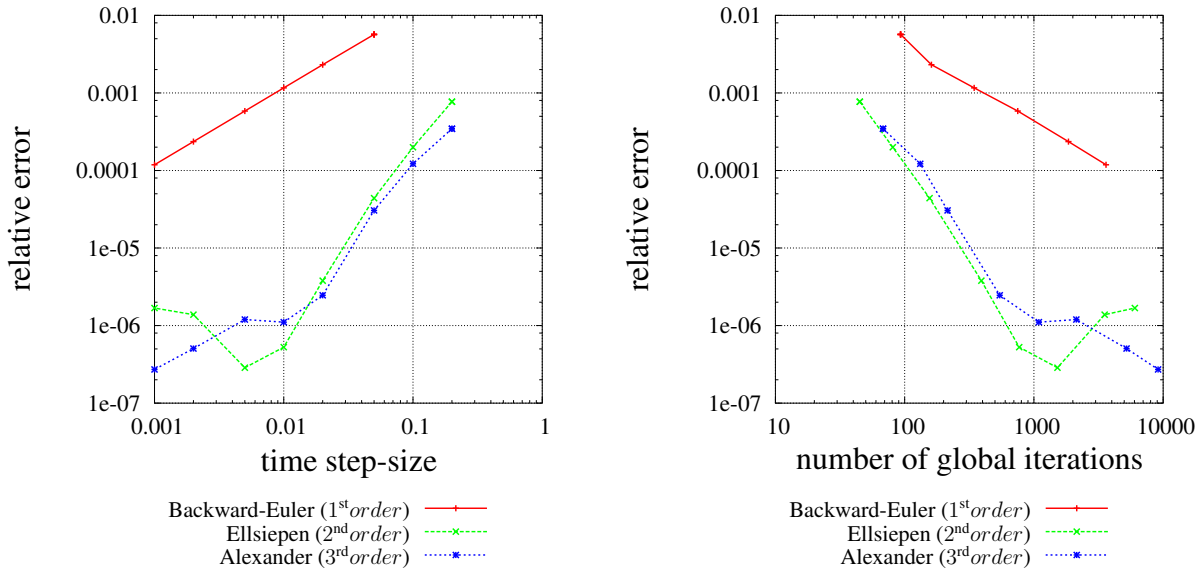

(a) Relative error over time step-size

(b) Rel. error over no. of global Newton iterations

Figure 6.2: Model of elastoplasticity (η=0)

Since the viscoplasticity model introduced in Section 3.4 emerges from the elastoplasticity model introduced in Section 3.3 a small viscosity will not create a significant difference between the results of the elastoplasticity model and the viscoplasticity model and can be considered as a regularization of the elastoplasticity problem. In Fig. 6.3 the influence of the introduced viscosity parameter η on the axial pressure in a die-compaction simulation is depicted. As can be seen there the behavior of the material is not changed significantly for $\eta \leq 1$. The index

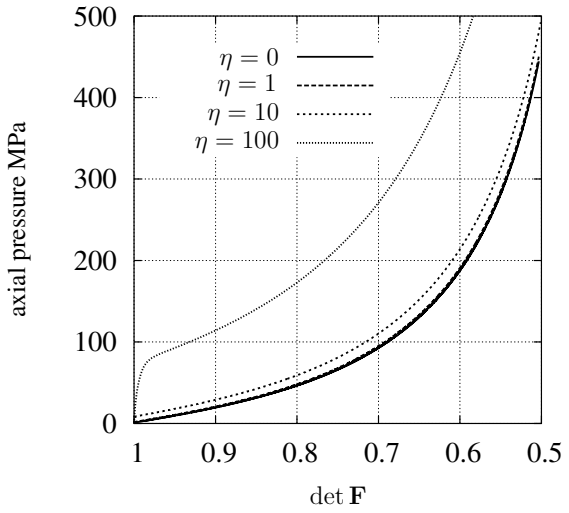

Figure 6.3: Variation of viscosity η

of the resulting DAE-system is in the viscoplasticity case 1 and the equations are more smooth. However, the differential part may be stiff so that the merit of this endeavor is not clear a priori, since order reduction of higher order integration methods may also appear in the case of stiff differential equations. Taking a look at Figure 6.4 one observes that now both the method of Ellsiepen and the method of Alexander do not yield an order much higher than one. However, the accuracy which they reach is significantly better than the accuracy reached by the Backward-Euler method. Accordingly, we do not observe a positive effect of the regularization by choosing a finite viscosity η, although the introduction of the viscosity does not change the calculated results for the pressure needed on the top surface of the structure much. In the case of $\eta = 0.1$ the required pressure is calculated to be about 0.1% higher and for $\eta = 1$ the increase is about 1% (in the studied case for the assumed velocity). In order to compare the different methods also for significant viscosities ($\eta = 1000$) the relative error is again plotted over the step-size in Fig. 6.5(a) and the number of global Newton iterations in Fig. 6.5(b). The plots show that the method of Alexander does now indeed reach approximately 3^{rd} order and the method of Ellsiepen reaches 2^{nd} order. If the accuracy demands are very strict the 3^{rd} order method can save a significant number of iterations in comparison with the 2^{nd} order method. However, for moderate accuracy requirements the 2^{nd} order method seems to be favorable over the other two, since it does not suffer severely from order reduction in any of the studied cases and is surely superior in performance over the simple Backward-Euler method. The order reduction phenomenon is not visible in the case of smooth problems, see HARTMANN [59] or HARTMANN [63].

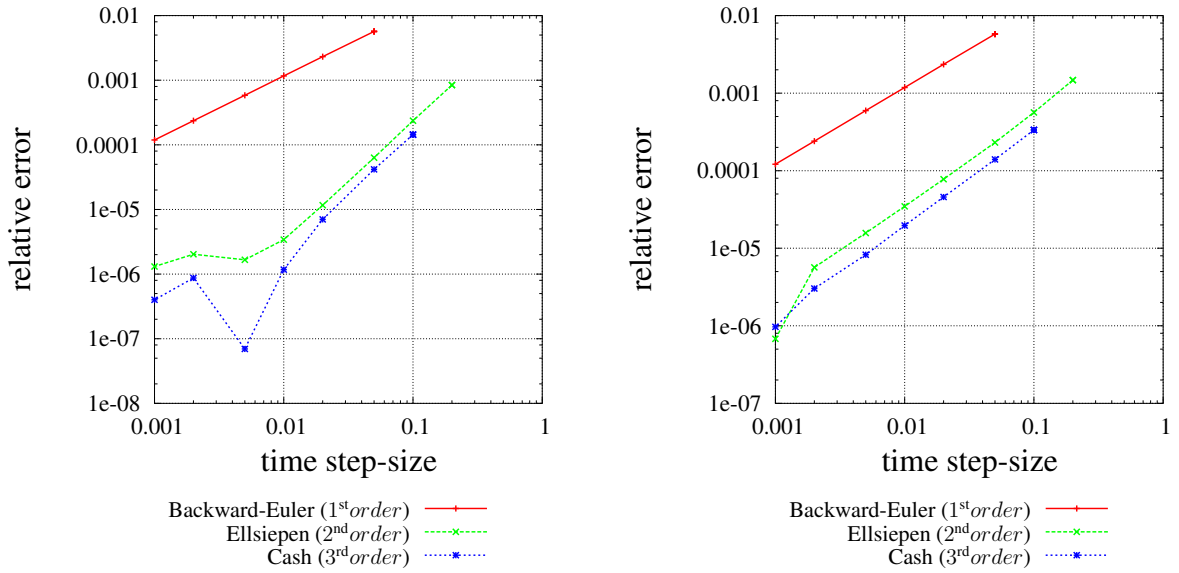

(a) Relative error over time step-size

(b) Rel. error over no. of global Newton iterations

Figure 6.4: Model of viscoplasticity ($\eta = 0.1$, $\eta = 1.0$), to mirror the elastoplasticity model.

6.2 L-shaped profile

In Figure 6.6 the geometry and boundary conditions for the second numerical example are depicted. The two-dimensional L-shaped structure is modeled with a single layer of three-dimensional hexahedral elements. The displacements in z-direction are locked for all nodes. The total initial height of the structure is 12 mm, the displacements at the top are prescribed to go 3 mm down (representing the movement of the rigid top punch u_y). In order to induce an inhomogeneous deformation the prescribed displacements at the bottom of the L-profile at $y = 0$ are assumed to be $0.8 \times (-u_y) = 2.4$ mm up. The computations have been done with two different time-adaptive strategies. The simpler time-adaptive strategy uses the number of global Newton iterations to estimate the current nonlinearity of the equations. And increases or decreases the time step-size of the Backward-Euler integration based on

$$\begin{aligned} \Delta t_{\text{new}} &= \Delta t_{\text{n}} \times \text{fac} \\ \text{with} \quad \text{fac} &= \begin{cases} 0.75 & \text{if } m > 12 \text{ (or if local procedure fails to find solution)} \\ 1.3 & \text{if } m \leq 6 \end{cases} . \end{aligned} \tag{6.1}$$

In the higher order Runge-Kutta methods the step-size control is based on an estimation of the local integration error, see the paragraph on time-adaptivity within Section 5.1.1. The absolute and relative error tolerances $\varepsilon_a = \varepsilon_r = 10^{-4}$ are chosen. The global Newton-iteration of the Multilevel-Newton algorithm requires a value of $\|\Delta \boldsymbol{U}\| \leq \text{tol}_u = 0.01 \times \varepsilon_a$. The stress computation, local nonlinear system, is assumed to be converged if $\|\Delta \mathbf{Q}^{(k)}\| \leq 10^{-9}$. The second order method of ELLSIEPEN [44] uses an embedded first order method and the third order method of CASH [25] uses an embedded second order method for the step-size control. We compare all three methods to a reference solution produced with a fourth order method with embedded third order method for step-size control. For the reference solution the error tolerances $\varepsilon_a = \varepsilon_r = 10^{-6}$ are chosen and the global Newton-iteration of the Multilevel-Newton algorithm requires a value

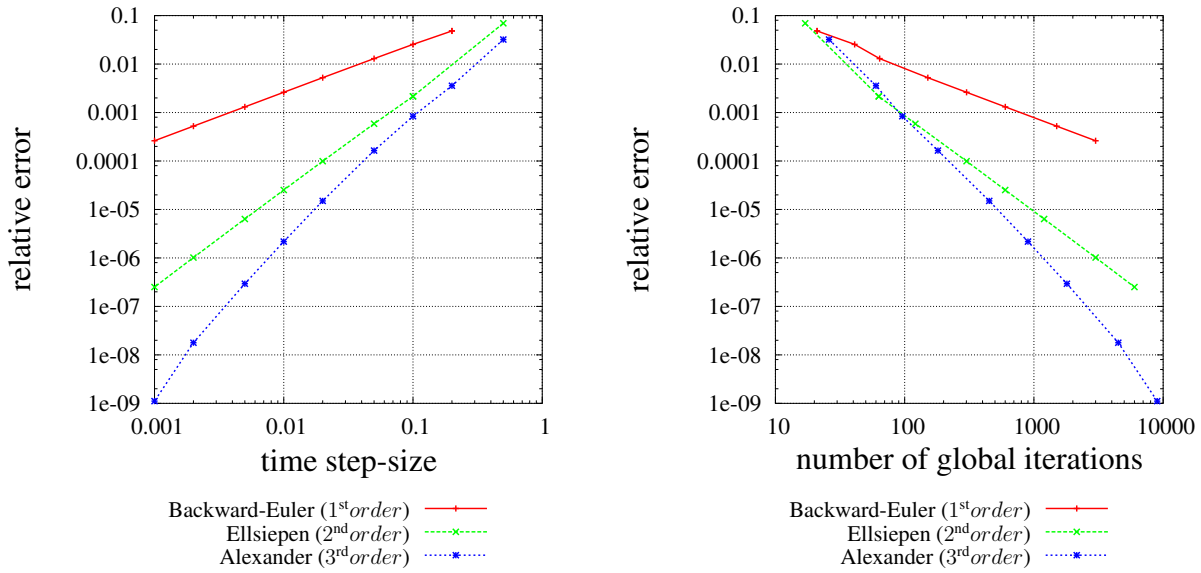

(a) Relative error over time step-size

(b) Rel. error over no. of global Newton iterations

Figure 6.5: Viscoplasticity (η=1000)

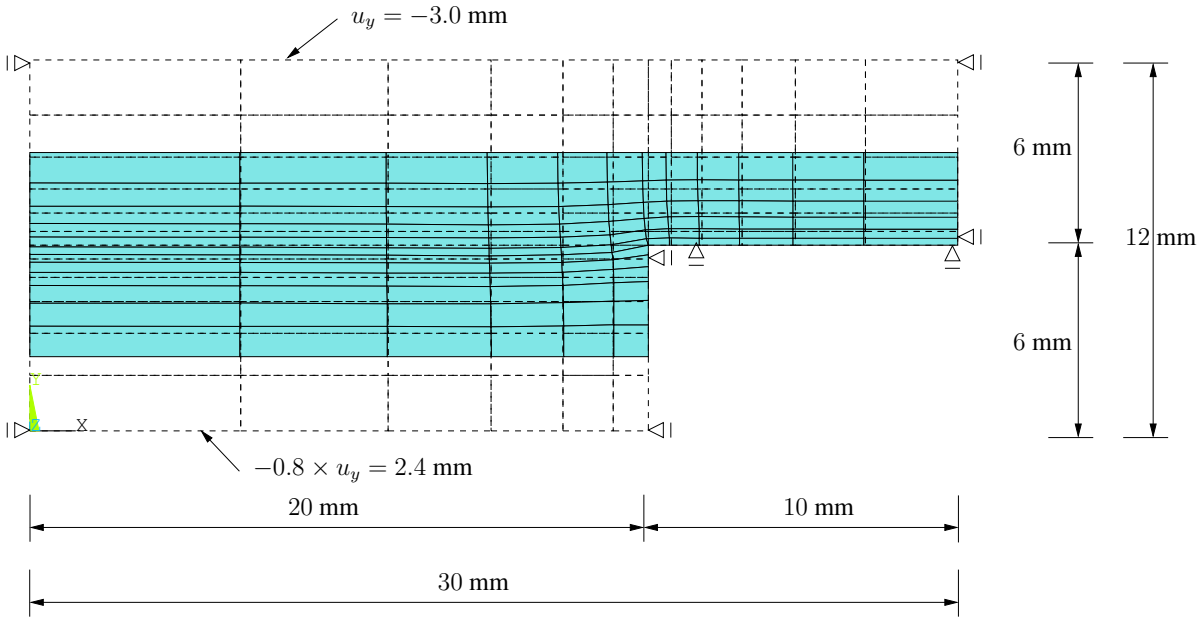

Figure 6.6: Boundary conditions of simple test structure

of $\|\Delta \boldsymbol{U}\| \leq \text{tol}_u = 0.01 \times \varepsilon_a$. The stress computation, local nonlinear system, is assumed to be converged if $\|\Delta \mathbf{Q}^{(k)}\| \leq 10^{-11}$ in the case of the reference solution computation. For the comparison of the spatial distribution of the integration error achieved by the three methods I choose the scalar quantity r_{K} of Eq. (3.77). Since r_{K} depends on $\mathbf{C}_{\text{p}}$, $r_{\text{K}} = \ln(\det \mathbf{C}_{\text{p}})/2$, which results from the time integration of the flow-rule, it appears to be a reasonable quantity for this comparison. In Figure 6.7 the spatial distribution of the error is depicted in contour plots. In every case the integration error is higher in the vicinity of the spatial singularity at the corner of

the L-shaped profile. Therefore, in Figure 6.9 the errors computed for each Gauss-point along the cuts through the L-profile at $x = 19.07\,\text{mm}$, $z = 0.21\,\text{mm}$ and at $y = 7.05\,\text{mm}, z = 0.21\,\text{mm}$, see Figure 6.8, are depicted. The error-controlled step-size control keeps the integration error significantly lower than the Backward-Euler method with step-size control technique (6.1). In every case the error increases close to the spatial singularity but not dramatically. The third order method does not seem to be superior to the second order method, in agreement with the previously observed order reduction phenomenon. Consequently, in the next example only the Backward-Euler method and the second order method of Ellsiepen will be considered.

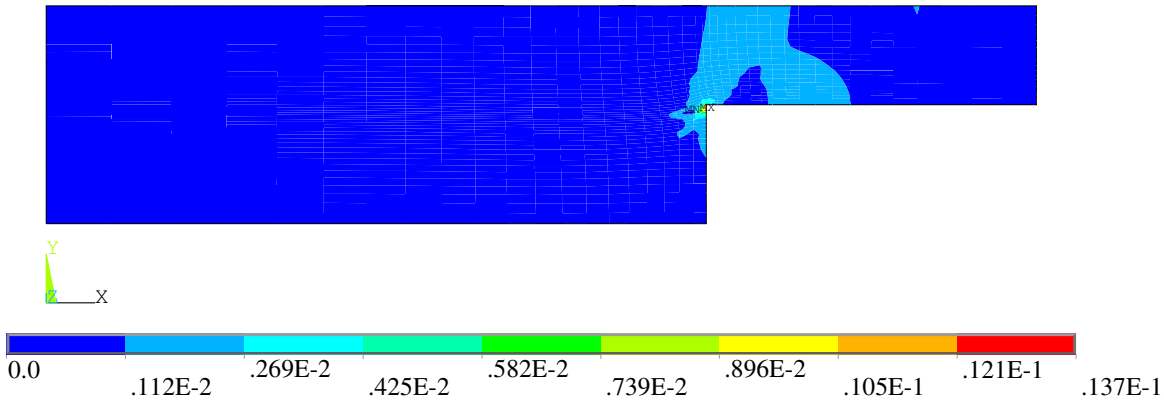

(a) Relative error of r_K contours (Backward-Euler)

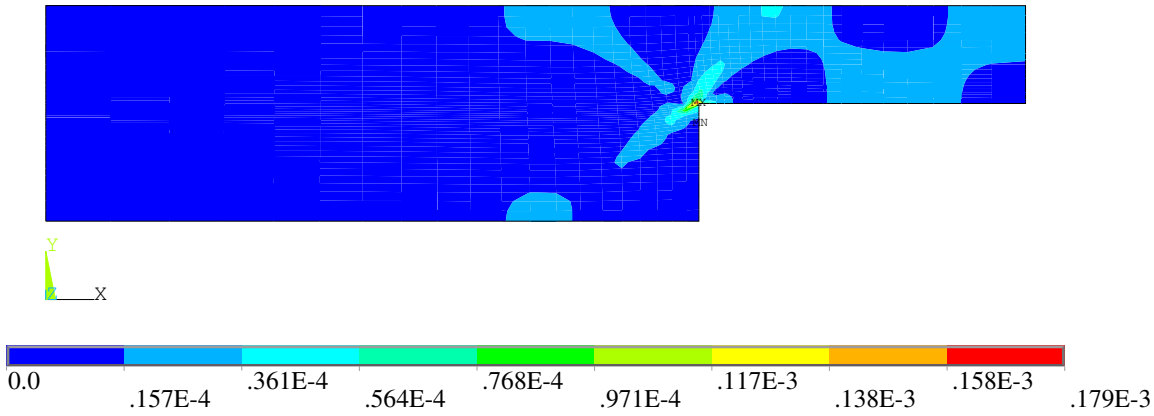

(b) Relative error of r_K contours (Ellsiepen)

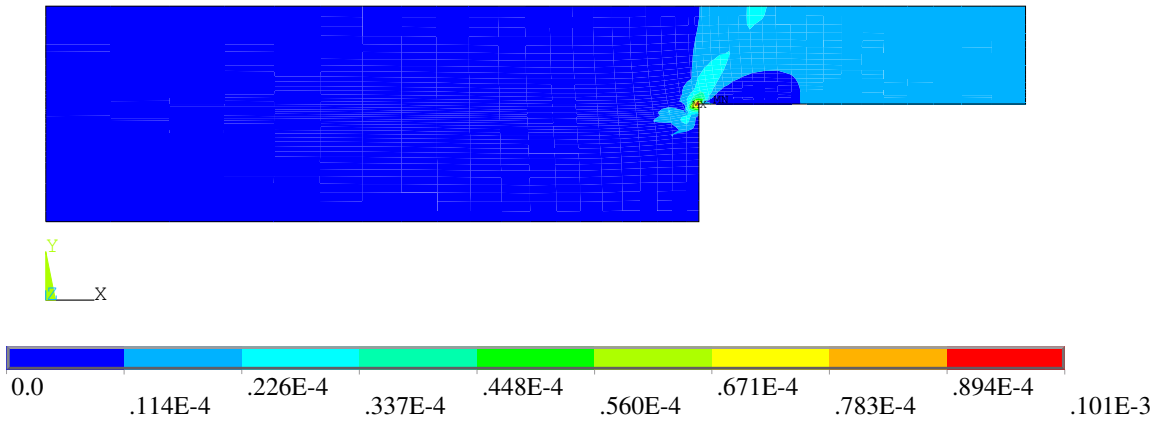

(c) Relative error of r_K contours (Cash)

Figure 6.7: Spatial distribution of relative errors of the quantity r_K for the L-shaped structure.

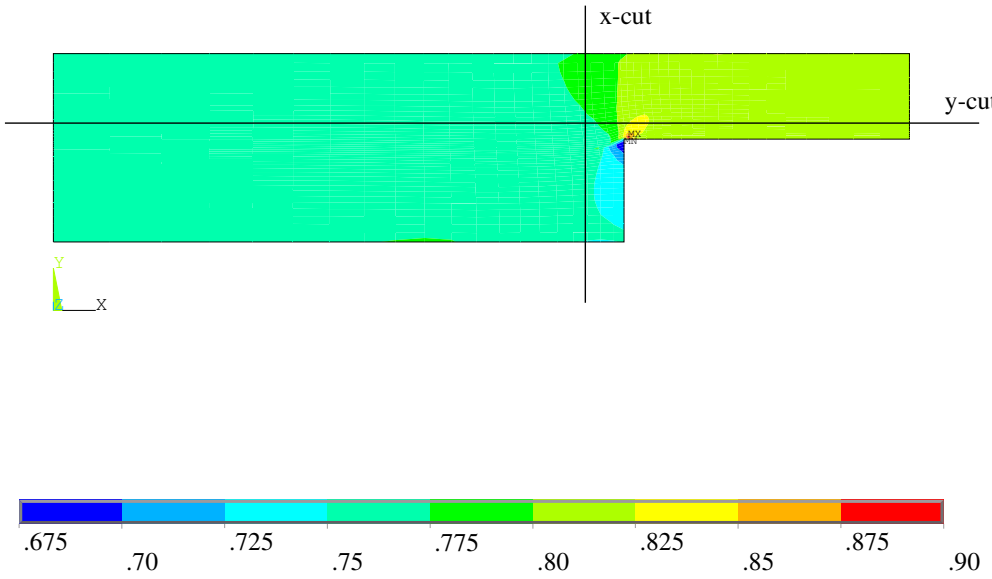

Figure 6.8: The relative density achieved by the compaction process in the L shaped structure (reference solution). The cutlines along which the relative errors are plotted in figure 6.9 are depicted.

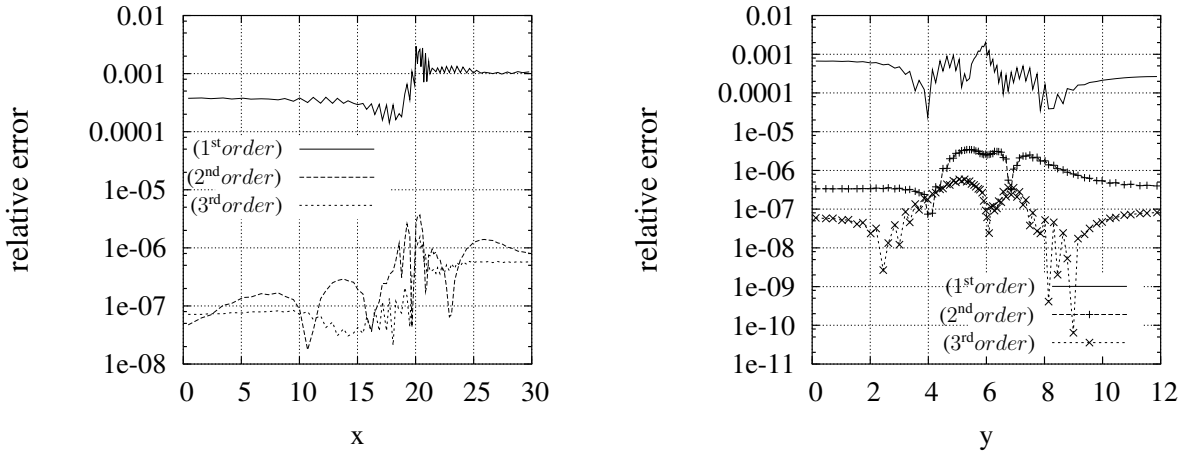

(a) Relative error over x-coordinate of Gauss-point along x-cut

(b) Relative error over y-coordinate of Gauss-point along y-cut

Figure 6.9: Error plotted along cuts vs. the free coordinate, see Figure 6.8 for definition of cuts.

6.3 A flat washer-like problem

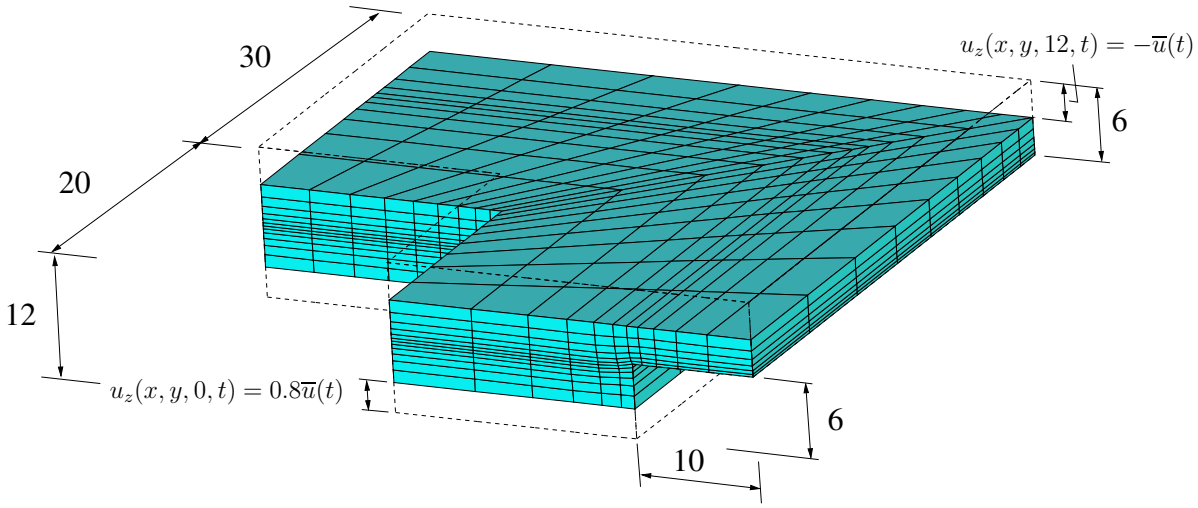

Figure 6.10: Geometry and deformed mesh of 3D-mesh of flat washer like problem (2394 nodes, 1836 eight-noded hexahedral elements)

The third studied geometry is a rectancular flat washer like structure, where only a quarter of the washer is discretized (symmetry), see Figure 6.10. Again the displacements are prescribed at the top and the bottom of the structure. At the bottom with $u_z(x, y, 0, t) = 0.8\overline{u}(t)$ and at the upper surface with $u_z(x, y, 12, t) = -\overline{u}(t)$ with $\overline{u}(t)$ given by[1]

$$\overline{u}(0) = 0\text{mm}, \quad \overline{u}(1) = 3\text{mm}, \quad \overline{u}(2) = 2.98\text{mm}. \tag{6.2}$$

All other surfaces are fixed in out of plane direction, i.e. a rigid behavior of the die is assumed and any influence of friction is neglected as well. The computations are done both for $\eta = 0$ and for $\eta = 1$. In each case a simple Backward-Euler method combined with the load-control of Eq. (6.1) is applied and compared to the error-controlled method of Ellsiepen (2^{nd} order Runge-Kutta) using an embedded first order method for step-size control as described in Section 5.1.1 based on the proposals of ELLSIEPEN [44], DIEBELS ET AL. [38] and ELLSIEPEN AND HARTMANN [45]. The step-size behavior is depicted in Figures 6.11(a) and 6.11(b) for $\eta = 0$ and $\eta = 1$ respectively. In the case of a small viscosity η the Backward-Euler method reaches higher step-sizes since the problems nonlinearity is reduced. The method of Ellsiepen handles both cases with nearly the same step-sizes to ensure that the integration error stays below the specified tolerances. Both algorithms increase the step-size significantly in the region where unloading takes place. There the behavior of the material is (at least in most Gauss-points) elastic leading to a less nonlinear set of equations. The achieved relative density distribution in the flat washer after unloading is depicted in Figure 6.12.

The same geometry has been chosen to demonstrate the increase in numerical efficiency gained by the numerical procedures discussed in Section 5.1.3. Table 6.1 compares the relative computation times needed to compute the washer compaction problem with $\eta = 1$ using again the second order error-controlled method of Ellsiepen and analytical consistent tangent

[1] The prescribed displacement $\overline{u}(t)$ is piecewise linear between the breakpoints at $t = 0, 1, 2$ provided in Eq.(6.2). The final value of the displacement at $t = 2$ is selected in such a manner that the resulting axial load at the end of the process is approximately zero.

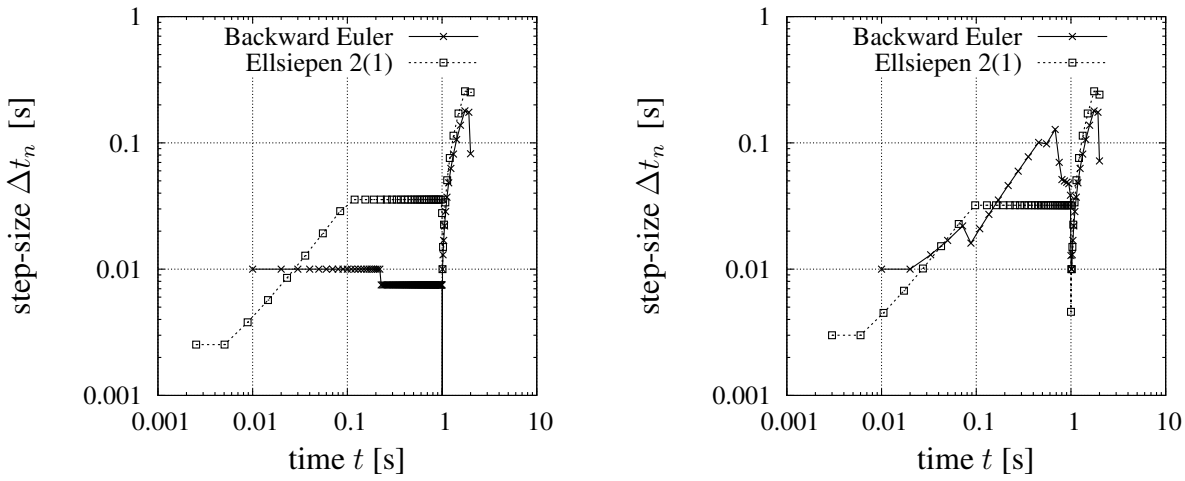

(a) $\eta = 0$ **(b)** $\eta = 1$

Figure 6.11: Step-size behavior of different integration methods

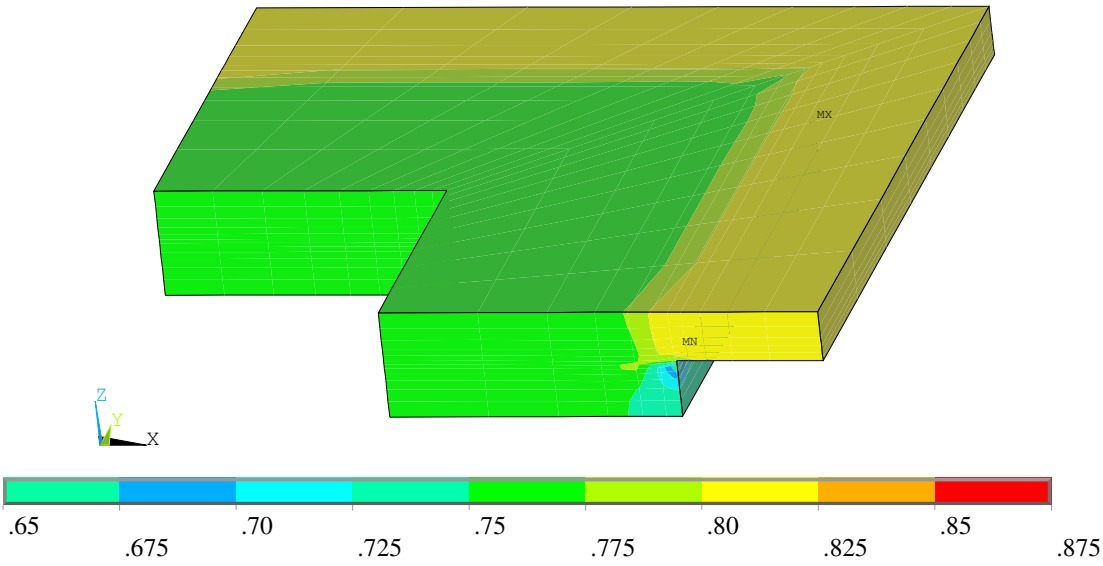

Figure 6.12: Relative density distribution in the flat washer like structure

with the original Newton-method, see Tab. 5.4, to solve the local nonlinear system compared to the Newton-method with damping, see Tab. 5.5 and the fully constrained Newton method from Tab. 5.7. The more stable Newton-algorithm with line-search and constraints leads to significantly reduced computation time since it converges for significantly greater step-sizes.

The fully constrained line-search algorithm, see Table 5.7, which is considered to be the most stable and efficient in most cases, is used for the final study testing the influence of numerical vs. analytical tangents. The reference computation is the compaction of the three-dimensional washer example using the Backward-Euler method with the simple step-size control using fully analytical expressions for the Jacobian of the local iterations as well as for the consistent tangent. One semi-analytical computation is done using a numerical version of the local Jacobian

Table 6.1: Comparison of computation time for different Newton-like algorithms applied to solve the local nonlinear system of equations within the Multilevel-Newton algorithm.

local solution algorithm	relative computation time in %
Newton method (Table 5.4)	100%
damped Newton (Table 5.5)	94%
fully constrained line-search (Table 5.7)	58%

but still an analytical consistent tangent and the other semi-analytical computation is done using an analytical Jacobian on local level but a numerical consistent tangent. Finally, a fully numerical version is computed. The results with respect to computation time are given in Table 6.2 below. The numerical differentiations are computed using forward differences (1^{st} order). The tremendous increase in computation time for the fully numerical version is caused by the fact that the step-size control based on the number global iterations does not incease the step-size, since the algorithm almost never converges within 6 iterations probably, because of the lack of accuracy reached by the two subsequent numerical differentiations.

Table 6.2: Comparison of computation time using analytical and numerical tangents within the local Newton-like iterations and in the Multilevel-Newton algorithm.

computation	relative computation time in %
fully analytical	100%
analytical local Jacobian, numerical consistent tangent	282%
numerical local Jacobian, analytical consistent tangent	110%
fully numerical	5737%

Chapter 7

Conclusions

This thesis presents the development, implementation and application of a constitutive model for metal powders. Following the continuum mechanical principles described in Chapter 2 a constitutive model falling into the class of finite strain elastoplasticity is formulated on the plastic intermediate configuration. Furthermore, the straightforward expansion of the elastoplasticity model to viscoplasticity is proposed and studied with respect to the numerical implications. The heart of the established constitutive model is a new pressure dependent yield function (compressible elastoplasticity). It is demonstrated that the new yield function can reproduce the yield behavior of a metal powder under compressive loads and that it exhibits a number of desirable properties, like uniqueness in principal stress space, shape flexibility[1], smoothness and convexity. Beyond the new yield surface a certain emphasis is placed on a thermo-mechanical motivation of the evolution equations ensuring, together with the associative flow-rule, an a priori thermo-mechanical consistent constitutive model in the sense that the Clausius-Duhem inequality is fulfilled for all processes.

With respect to the material parameter identification uniaxial die-compaction experiments with monotonic loading and with intermediate un- and reloading cycles are analyzed. The experimental setups were developed by the partner group of Prof. Frage, receiving input from our side with respect to the required experimental data for a reasonable parameter identification. Since the experimental data is not exhaustive, a few parameters are chosen beforehand in a reasonable manner. It is demonstrated that the constitutive model is able to represent the available experimental data very well once the material parameters are identified.

Several variants of a stress algorithm for the proposed constitutive model are developed and implemented into the implicit finite elements code TASA-FEM (HARTMANN [62]). Since the application of the classical Newton algorithm to the non-linear system of equations on the local (Gauss-point) level of the Multilevel-Newton algorithm, which is applied at each stage of the utilized DIRK-method to the DAE-system resulting from the space discretization of the principle of virtual displacements, leads to a frequently non-converging stress algorithm, several globalization strategies for the Newton method like damping, line-search and line search with constraints are implemented. The stress algorithm utilizing line search with constraints is shown to be significantly more robust and efficient than the simple Newton algorithm. Since it is realized that a system of differential algebraic equations (DAE-system) emerges for the proposed constitutive model from the space discretization of the principle of virtual displacements using finite elements, the above mentioned DIRK methods become applicable. The differential part of

[1] In BIER AND HARTMANN [19] it has previously been shown that the shape flexibility of the new yield function is appropriate to reproduce the yield behavior of many compressible materials.

the DAE-system stems from the ordinary differential equations of first order (evolution equation, flow-rule) of the constitutive model. Compared to the classical Backward-Euler scheme the applied DIRK methods offer a higher integration order resulting in a higher accuracy of the time integration, while the structure of the classical implicit finite element implementation of the time integration (Backward-Euler) is maintained.

The applicability of the stress algorithm for the proposed constitutive model is demonstrated in some academic example computations. It is observed that an order reduction phenomenon occurs, i.e. the order of the higher order DIRK method can not be reached. This leads to the conclusion that a second order method is showing the best performance.

With respect to the constitutive model presented in this thesis several directions for expansions and generalizations of the model are thinkable. One interesting point could be the inclusion of temperature effects aiming beyond the simulation of compaction processes at ambient temperature like uniaxial die compaction and cold isostatic pressing (CIP) towards *warm compaction* and *hot isostatic pressing (HIP)*. Changes in the same direction would be necessary to allow the simulation of the sintering process usually following the pressing process. Minor changes of the model increasing its complexity but also its range of applicability would be to consider the dependence of the yield function on the third invariant of the stress tensor, a more elaborate elasticity relation or a non-associative flow-rule. On the other hand the increase in model complexity would imply additional material parameters demanding an equally higher experimental effort for their determination. A further direction for the generalization of the constitutive model could be the combination of the elastoplasticity model with a damage model enhancing the possibilities to describe the behavior of powder compacts under non-compressive loading conditions.

With respect to the numerical treatment efficient methods for the time integration are applied, i.e. time integration with embedded error estimation for an error controlled time step-size. Another direction to increase the efficiency could be to consider an adaptive space-integration and a combination of time and space integration adaptivity. Furthermore, the implementation of the constitutive model into a commercial finite element program would offer the possibility to treat more realistic initial boundary value problems. In this respect especially the consideration of friction between the powder and the mould (die) has to be mentioned.

Appendix A

Limit cases of the interpolated yield function

In the following, it is shown how to define the parameters of $f(I_1)$ from Eq. (3.45) in order to approximate the Drucker-Prager yield function, the ellipse, either centered, as proposed by many authors (see, for example, SHIMA AND OYANE [122] or KUHN AND DOWNEY [89]), or shifted along the hydrostatic axis, as suggested by ABOU-CHEDID [3], as well as the von Mises yield function applied in metal plasticity.

Approximating the Drucker-Prager yield function The Drucker-Prager yield function defines a linear function in Fig. 3.8 starting, for example, at the point $(I_1, \sqrt{J_2}) = (I_0, 0)$ and having a negative slope. Since the proposed yield function is represented by the interpolation of the ellipse and the exponential function, use has to be made of the exponential part in order to approximate the linear function in a user-defined region. To this end, the following two steps must be considered. Firstly, since the exponential function $f_2(I_1)$ is utilized for representing the Drucker-Prager line, it is necessary to show when $f_2(I_1)$ is indeed smaller than the ellipse $f_1(I_1)$ for all I_1 in the relevant region $I_{\text{is}} \leq I_1 \leq I_0$, where $I_{\text{is}} = 3\xi + r(3\xi - I_0)$ defines the intersection point in the compression range. It will be shown that this can be guaranteed by choosing r greater than a certain limit value. Secondly, on the basis of the investigation before, it will be investigated under which conditions the deviation of the interpolated function $f(I_1)$ and the Drucker-Prager function are sufficiently small.

First of all, Eqns.(3.42) and (3.43) are reformulated

$$f_1(I_1) = k\sqrt{1 - \frac{(I_1 - 3\xi)^2}{(I_0 - 3\xi)^2}}, \tag{A.1}$$

$$f_2(I_1) = k\left[1 - \left(1 - \sqrt{1 - r^2}\right)^{[(I_1 - I_0)/((3\xi - I_0)(1+r))]}\right] \tag{A.2}$$

and it must be shown that $f_1(I_1) - f_2(I_1) \geq 0$ holds for $I_{\text{is}} \leq I_1 \leq I_0$, which is the interval of the intersections of the two functions at I_0 and I_{is}. In other words,

$$0 \leq \frac{f_1(I_1) - f_2(I_1)}{k} = \underbrace{\sqrt{1 - \frac{(I_1 - 3\xi)^2}{(I_0 - 3\xi)^2}}}_{\gamma_1(I_1)} - 1 + \underbrace{\left(1 - \sqrt{1 - r^2}\right)^{[(I_1 - I_0)/((3\xi - I_0)(1+r))]}}_{\gamma_2(I_1)} \tag{A.3}$$

has to be satisfied, where two functions $\gamma_1(I_1)$ and $\gamma_2(I_1)$ are introduced. This condition is fulfilled for the case

$$\gamma_1(I_1) + \gamma_2(I_1) \geq 1 \qquad \forall\ I_1 \in [I_{\text{is}}, I_0]. \tag{A.4}$$

At the intersection points I_{is} and I_0 the two terms add up exactly to one, $\gamma_1(I_{\text{is}}) + \gamma_2(I_{\text{is}}) = 1$ and $\gamma_1(I_0) + \gamma_2(I_0) = 1$. Since both functions $\gamma_1(I_1)$ and $\gamma_2(I_1)$ increase within the region $I_{\text{is}} \leq I_1 < 3\xi$, condition (A.4) is fulfilled. Thus, we only need to discuss the interval $3\xi \leq I_1 \leq I_0$ where $\gamma_1(I_1)$ decreases. In order to show under which conditions inequality (A.4) is satisfied in this interval, the two functions $\gamma_1(I_1)$ and $\gamma_2(I_1)$ are replaced by two properly chosen linear functions which are below the two functions throughout the interval. Accordingly, it must be proven that for a sufficiently large value of r the sum of these linear functions is greater than 1.

In Fig. A.1 the two terms together with the linear functions $h_1(I_1)$ and $h_2(I_1)$ are plotted. The linear function $h_1(I_1)$ is constructed to be always smaller than $\gamma_1(I_1)$ defined by

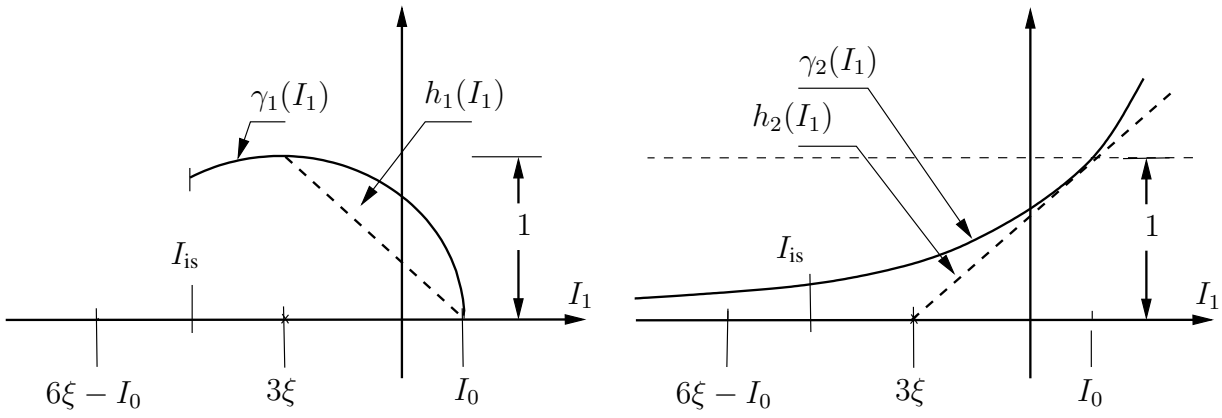

(a) h_1, lower bound for $\gamma_1(I_1)$ **(b)** h_2, lower bound for $\gamma_2(I_1)$

Figure A.1: Graphical representation of the linear functions $h_1(I_1)$ and $h_2(I_1)$ acting as lower bounds for $\gamma_1(I_1)$ and $\gamma_2(I_1)$

$$h_1(I_1) = \frac{1}{3\xi - I_0} I_1 - \frac{I_0}{3\xi - I_0}. \tag{A.5}$$

In the case of the exponential part $\gamma_2(I_1)$, every tangent lies under the function for all values of I_1. In order to make sure that condition (A.4) is satisfied, use is made of the tangent at the point I_0 denoted by

$$h_2(I_1) = \underbrace{\frac{\ln\left(1 - \sqrt{1 - r^2}\right)}{1 + r}}_{=:T(r)} \frac{1}{3\xi - I_0} I_1 + 1 - \frac{\ln\left(1 - \sqrt{1 - r^2}\right)}{1 + r} \frac{I_0}{3\xi - I_0}. \tag{A.6}$$

If the tangent is constructed in such a way that $h_1(I_1) + h_2(I_1) = 1$ holds, which guarantees condition (A.4) as well, then $h_2(3\xi) = 0$ has to be satisfied. Consequently, expression $T(r)$, defined in Eq.(A.6), leads to the non-linear equation

$$\ln\left(1 - \sqrt{1 - r^2}\right) = -(1 + r) \tag{A.7}$$

possessing the solution $r^* \approx 0.602$, i.e. if $r > r^*$ is defined, condition (A.4) is surely satisfied.

So far, it has only been shown that for $r > r^*$ the function $f_2(I_1)$ is the smaller one of the two functions in the interval of interest. This means that there are no further intersection points in this interval. In order to approximate a straight line within the user-defined interval $I^* \leq I_1 \leq I_0$ by means of the exponential function, the relative difference of the tangents' slopes at I_0 and a user-defined hydrostatic pressure I^* should be less than a prescribed tolerance ε

$$\left| \frac{f_2'(I^*) - f_2'(I_0)}{f_2'(I_0)} \right| < \varepsilon \tag{A.8}$$

If a value $r_0 > r^*$ is defined, inequality (A.8) yields the upper limit

$$\xi \leq \frac{I^* - I_0}{3(1+r_0)} \frac{\ln\left(1 - \sqrt{1-r_0^2}\right)}{\ln(1-\varepsilon)} + \frac{I_0}{3} \tag{A.9}$$

of the ellipse' center.

The Drucker-Prager model, $f_{\text{DP}}(I_1) = M\, I_1 + c$, M defines the slope and c is a constant, is chosen to have the derivative of $f_2(I_1)$ at the zero hydrostatic stress state

$$M = f_2'(0) = -A_2 A_3. \tag{A.10}$$

This is done for the convenience of the resulting analytical expressions. If a center ξ_0 is prescribed, satisfying inequality (A.9), the axes ratio of the ellipse is obtained,

$$\alpha = \frac{M^2(1+r_0)^2 \left(1 - \sqrt{1-r_0^2}\right)^{[2I_0/((3\xi_0 - I_0)(1+r_0))]}}{\left(\ln\left(1 - \sqrt{1-r_0^2}\right)\right)^2}, \tag{A.11}$$

where use is made of definitions (3.44). In other words, for given tolerance ε of the slope, the slope of the Drucker-Prager yield function M, the intersection point of a non-negative hydrostatic pressure I_0, the expected range of interest I^* (where the model should reproduce the Drucker-Prager yield function, and a defined $r_0 \geq r^* = 0.602$, the proposed model approximates up to the desired precision the Drucker-Prager model. Additionally, if the parameter c of the interpolation is small enough, the function f comes arbitrarily close to the function f_2.

Retrieving the ellipse yield function The retrieval of the ellipse from the interpolated yield function (3.37), either with $\xi = 0$ (centered ellipse) or for $\xi < 0$ (shifted ellipse), is less laborious. Here, r is sent towards zero so that the exponential function is always larger than the ellipse. Since the ellipse $f_1(I_1)$ does not depend on r, one has only to look at the limit behavior of $f_2(I_1)$ defined in Eq.(A.2). In order to find the limit of $f_2(I_1)$, two cases have to be distinguished. For $I_1 < I_0$ and $I_1 = I_0$ and the condition $3\xi < I_0$, we arrive at

$$I_1 < I_0: \quad \lim_{r \to 0} f_2(I_1) = k, \tag{A.12}$$

$$I_1 = I_0: \quad \lim_{r \to 0} f_2(I_1) = 0. \tag{A.13}$$

In other words, under the condition $r = 0$, the exponential function obtains the values $f_2(I_1) = k$ for all $I_1 < I_0$. Since k is obviously the maximum of $f_1(I_1)$, it has been shown that $f_1(I_1)$ is the smaller one of the two functions and this implies that the difference between f and f_1 is always less than $c \ln 2$, which could be made arbitrarily small by choosing c sufficiently small.

Approximating the von Mises yield function In order to approximate the von Mises yield function, the arguments of the last paragraph are followed, i.e. $r = 0$ is required. Additionally, f_1 is specialized to the case of the centered ellipse, $\xi = 0$. This leads to the cases

$$f_2(I_1) = \begin{cases} k & | \quad I_1 < I_0 \\ 0 & | \quad I_1 = I_0 \end{cases} \tag{A.14}$$

$$f_1(I_1) = \sqrt{k^2 - \alpha(I_1)^2} \qquad \text{with} \qquad k = \sqrt{\alpha I_0^2}. \tag{A.15}$$

The von Mises yield surface is defined by a single parameter which corresponds to k. The basic idea is to utilize an ellipse with a high aspect ratio (small α) which approximates the horizontal line $f(I_1) = k$ with a prescribed tolerance. To this end, the relative difference of f_1 and k is required to be smaller than an arbitrary but fixed value ε for all I_1 within the interval $(-I_\mathrm{f}, +I_\mathrm{f})$. I_f defines the borders of the relevant interval. Thus, the relative difference has to fulfill the condition

$$\frac{k - f_1(I_\mathrm{f})}{k} = 1 - \sqrt{1 - \frac{I_\mathrm{f}^2}{I_0^2}} < \varepsilon \tag{A.16}$$

using Eq.(A.15). In other words, we have to satisfy the condition

$$I_0^2 > \frac{I_\mathrm{f}^2}{1 - (1 - \varepsilon)^2}, \tag{A.17}$$

i.e. I_f and ε have to be prescribed and one obtains the value of I_0 needed.

Appendix B

Proof of convexity

The proof of convexity for the yield function has already been published in BIER AND HARTMANN [19] but is repeated here for the sake of completeness. In order to show convexity of the yield function (3.49), use is made of the Gateaux-derivative

$$\mathsf{D}_{\mathbf{x}} F(\mathbf{x})[\mathbf{H}] = \frac{\mathrm{d}}{\mathrm{d}\lambda} F(\mathbf{x} + \lambda \mathbf{H}) \bigg|_{\lambda=0} . \tag{B.1}$$

Accordingly, the second derivative, or more precisely, the second differential of a scalar function $F(\mathbf{x}) : \mathbb{R}^2 \to \mathbb{R}$ has to be derived. This implies the convexity proof of the composition because $G(g_1(\mathbf{x}), g_2(\mathbf{x}))$ depends on two scalar functions $g_k(\mathbf{x}) : \mathbb{R}^2 \to \mathbb{R}$. In our formulation $\mathbf{x} \in \mathbb{R}^2$ is assembled by $\mathbf{x}^T = \{I_1, \sqrt{J_2}\}$, i.e. $x_1 = I_1$ and $x_2 = \sqrt{J_2}$. The differential (B.1) of $F(\mathbf{x})$ reads

$$\mathsf{D}_{\mathbf{x}} F(\mathbf{x})[\mathbf{H}] = \left\{ \frac{\mathrm{d}G(\mathbf{g}(\mathbf{x}))}{\mathrm{d}\mathbf{g}} \right\}^T \left[\frac{\mathrm{d}\mathbf{g}(\mathbf{x})}{\mathrm{d}\mathbf{x}} \right] \mathbf{H} = \sum_{i=1}^{2} G_{,i} \{ g_{i,\mathbf{x}} \}^T \mathbf{H} \tag{B.2}$$

with

$$G_{,i}(\mathbf{g}(\mathbf{x})) = \frac{\partial G(g_1, g_2)}{\partial g_i} \tag{B.3}$$

and

$$g_{i,\mathbf{x}} = \frac{\mathrm{d}g_i(\mathbf{x})}{\mathrm{d}\mathbf{x}} = \left\{ \begin{array}{c} \dfrac{\partial g_i}{\partial x_1} \\ \dfrac{\partial g_i}{\partial x_2} \end{array} \right\} . \tag{B.4}$$

The second differential

$$\begin{aligned} \mathsf{D}_{\mathbf{x}} \{ \mathsf{D}_{\mathbf{x}} F(\mathbf{x})[\mathbf{H}] \}[\mathbf{H}] &= \mathsf{D}_{\mathbf{x}} \left\{ \sum_{i=1}^{2} G_{,i}(\mathbf{g}(\mathbf{x})) \{ g_{i,\mathbf{x}} \}^T \mathbf{H} \right\} [\mathbf{H}] = \\ &= \sum_{j=1}^{2} \sum_{i=1}^{2} G_{,ij} \left(\{ g_{j,\mathbf{x}} \}^T \mathbf{H} \right) \left(\{ g_{i,\mathbf{x}} \}^T \mathbf{H} \right) + \sum_{i=1}^{2} G_{,i} \left\{ \frac{\mathrm{d}^2 g_i}{\mathrm{d}\mathbf{x}\, \mathrm{d}\mathbf{x}} \mathbf{H} \right\}^T \mathbf{H} = \\ &= \mathbf{H}^T \left[G_{,11}\, g_{1,\mathbf{x}} \{ g_{1,\mathbf{x}} \}^T + 2 G_{,12}\, g_{1,\mathbf{x}} \{ g_{2,\mathbf{x}} \}^T + G_{,22}\, g_{2,\mathbf{x}} \{ g_{2,\mathbf{x}} \}^T \right] \mathbf{H} + \\ &\quad + \mathbf{H}^T \left[G_{,1}\, g_{1,\mathbf{xx}} + G_{,2}\, g_{2,\mathbf{xx}} \right] \mathbf{H} \geq 0 \end{aligned} \tag{B.5}$$

has to be non-negative if the yield function is convex. If the first expression of inequality (B.5) is reordered, (B.5) results in

$$\mathsf{D}_{\mathbf{x}}\left\{\sum_{i=1}^{2} G_{,i}\left(\mathbf{g}(\mathbf{x})\right)\{g_{i,\mathbf{x}}\}^{T}\mathbf{H}\right\}[\mathbf{H}] = \\ = \left\{(\mathbf{H}^{T}g_{1,\mathbf{x}})\,(\mathbf{H}^{T}g_{2,\mathbf{x}})\right\}\begin{bmatrix} G_{,11} & G_{,12} \\ G_{,21} & G_{,22}\end{bmatrix}\begin{Bmatrix}(\mathbf{H}^{T}g_{1,\mathbf{x}}) \\ (\mathbf{H}^{T}g_{2,\mathbf{x}})\end{Bmatrix}+\mathbf{H}^{T}\left[G_{,1}\,g_{1,\mathbf{xx}}+G_{,2}\,g_{2,\mathbf{xx}}\right]\mathbf{H}\geq 0 \tag{B.6}$$

In other words, $F(\mathbf{x})$ is convex if

- $G(\mathbf{g})$ is non-decreasing in each argument ($G_{,1}\geq 0$, $G_{,2}\geq 0$),
- $G(\mathbf{g})$ is convex,
- and, $g_i(\mathbf{x})$, $i=1,2$, are convex.

This proposition is stated by BOYD AND VANDENBERGHE [21], where the proof is left to the reader. In order to complete the proof in view of Eq. (3.49), we have to show the fulfillment of the statements mentioned above.

Monotonicity of $G(g_1,g_2)$ The first condition of a non-decreasing function

$$G(g_1,g_2)=ck\ln\left(\frac{e^{g_1/(ck)}+e^{g_2/(ck)}}{2}\right) \tag{B.7}$$

is apparently given by the first derivatives

$$G_{,1}=\frac{e^{g_1/(ck)}}{e^{g_1/(ck)}+e^{g_2/(ck)}}>0, \qquad G_{,2}=\frac{e^{g_2/(ck)}}{e^{g_1/(ck)}+e^{g_2/(ck)}}>0. \tag{B.8}$$

Convexity of $G(g_1,g_2)$ In order to show the convexity of $G(g_1,g_2)$, the Hessian matrix $G_{,\mathbf{gg}}$ has to be positive semi-definite implying the non-negativity of the diagonal elements $G_{,11}\geq 0$ and $G_{,22}\geq 0$ and the non-negativity of the determinant, $G_{,11}\,G_{,22}-G_{,12}^{2}\geq 0$. The components of the Hessian read:

$$G_{,11}=G_{,22}=-G_{,12}=\frac{e^{(g_1+g_2)/(ck)}}{ck\left(e^{g_1/(ck)}+e^{g_2/(ck)}\right)^{2}}>0 \tag{B.9}$$

The determinant of the Hessian matrix is obviously zero and the diagonal terms are positive for $c>0$ and $k>0$.

Convexity of $g_1(\mathbf{x})$ The convexity of the ellipsoid $g_1(x_1,x_2)$ defined in Eq.(3.46) implies again the coefficients of the Hessian matrix:

$$\frac{\partial^2 g_1}{\partial {x_1}^2}=\frac{x_2^2\alpha}{\left(x_2^2+\alpha(x_1-3\xi)^2\right)^{3/2}} \tag{B.10}$$

$$\frac{\partial^2 g_1}{\partial {x_2}^2}=\frac{\alpha(x_1-3\xi)^2}{\left(x_2^2+\alpha(x_1-3\xi)^2\right)^{3/2}} \tag{B.11}$$

$$\frac{\partial^2 g_1}{\partial x_1\partial x_2}=-\frac{x_2\alpha(x_1-3\xi)}{\left(x_2^2+\alpha(x_1-3\xi)^2\right)^{3/2}} \tag{B.12}$$

Even in this case the determinant of the Hessian is zero, $\det[g_{1,\mathbf{xx}}] = 0$, and the diagonal terms are non-negative for $\alpha > 0$ and $x_2 = \sqrt{J_2} \geq 0$, which is given in view of its physical (geometrical) meaning.

Convexity of $g_2(\mathbf{x})$ A similar behavior stems from the exponential function (3.47) yielding

$$\frac{\partial^2 g_2}{\partial {x_1}^2} = A_2 A_3^2 e^{A_3 x_1} > 0, \qquad \frac{\partial^2 g_2}{\partial {x_2}^2} = \frac{\partial^2 g_2}{\partial x_1 \partial x_2} = 0. \tag{B.13}$$

This leads again to the determinant $\det[g_{2,\mathbf{xx}}] = 0$. In view of the definitions (3.44), $A_2 > 0$ apparently holds.

In conclusion, in the case of a combination of the two convex yield functions g_1 and g_2 the resulting interpolated yield function is also convex.

Appendix C

Study of a specific ODE

In Eq.(3.83) we have an ordinary differential equation of the type

$$\alpha'(s) = \Omega/\alpha(s) - b_D\alpha(s), \quad \text{initial conditions} \quad \alpha(0) = \alpha_0 > 0. \tag{C.1}$$

Although $\Omega > 0$ is in the original expression process-dependent, we assume that Ω is constant (i.e. it is assumed that the resulting ODE behaves similar). s defines the plastic arc-length (see definition (3.72)). The analytical solution of this ODE reads

$$\alpha(s) = \sqrt{\frac{\Omega - (\Omega - b_D\alpha_0^2)e^{-2b_D s}}{\beta_D}}, \tag{C.2}$$

i.e. the equilibrium state of the ODE, $\alpha'(s) = 0$, achieves the value

$$\alpha^* = \lim_{s\to\infty} \alpha(s) = \sqrt{\Omega/b_D}. \tag{C.3}$$

In Fig. C.1 a parameter study is shown for $\alpha_0 = 1$. In other words, for positive initial conditions

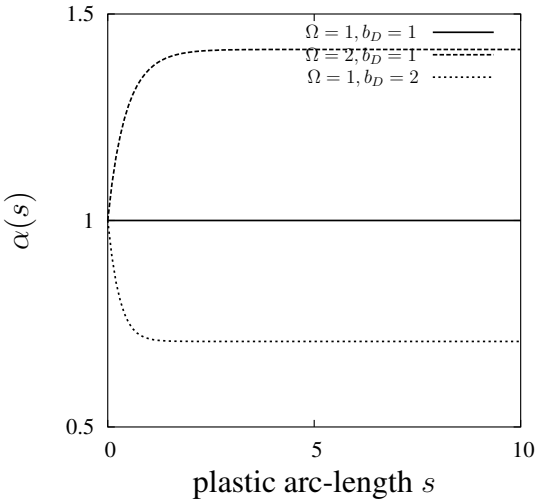

Figure C.1: Study of the ODE in (C.1)

the quantity α can not become negative. This study of the ODE (3.83) has already been published in BIER AND HARTMANN [19] but is repeated here for the sake of completeness.

Appendix D

Analytical consistent tangent

In view of the proposed stress algorithms, which are based on Newton-like procedures on local Gauss-point level, and the related consistent tangent operator various derivatives are necessary. These expressions are summarized in the following. We start with the derivatives denoted term I and term II of the elasticity relation with respect to $\mathbf{C}$ and $\mathbf{C}_\mathrm{p}$ appearing in (5.118) which defines the consistent tangent matrix $\frac{\mathrm{d}\tilde{\mathbf{h}}}{\mathrm{d}\mathbf{C}}$

$$\text{term I} \quad : \quad \frac{\partial \tilde{\mathbf{h}}}{\partial \mathbf{C}} = \frac{1}{2}\Lambda \left[\mathbf{C}^{-1} \otimes \mathbf{C}^{-1}\right] - \left(\frac{1}{2}\Lambda \ln \det(\mathbf{C}_p^{-1}\mathbf{C}) - \mu\right) \left[\mathbf{C}^{-1} \otimes \mathbf{C}^{-1}\right]^{T_{23}} \tag{D.1}$$

$$\text{term II} \quad : \quad \frac{\partial \tilde{\mathbf{h}}}{\partial \mathbf{C}_\mathrm{p}} = -\mu \left[\mathbf{C}_\mathrm{p}^{-1} \otimes \mathbf{C}_\mathrm{p}^{-1}\right]^{T_{23}} - \frac{1}{2}\Lambda \left[\mathbf{C}^{-1} \otimes \mathbf{C}_\mathrm{p}^{-1}\right]. \tag{D.2}$$

The term III in equation (5.118) results from the solution of the linear system of equations (5.122). The functional matrix on the left hand side of equation (5.122) is composed of the partial derivatives of $\mathbf{L}_\mathrm{p}$, L_α and L_F with respect to $\mathbf{C}_\mathrm{p}$, α and ζ where $\mathbf{L}_\mathrm{p}$, L_α and L_F are the Eqns. (5.115)-(5.117) recapped here for the sake of comprehensibility

$$\mathbf{L}_\mathrm{p} = \mathbf{C}_\mathrm{p}^{ni} - \mathbf{C}_\mathrm{p}^{(n)} - \zeta \mathbf{h}_1 \left(\mathbf{C}, \mathbf{C}_\mathrm{p}^{ni}, \alpha^{ni}\right) = \mathbf{0} \tag{D.3}$$

$$L_\alpha = \alpha^{ni} - \alpha^{(n)} - \zeta h_2 \left(\mathbf{C}, \mathbf{C}_\mathrm{p}^{ni}, \alpha^{ni}\right) = 0 \tag{D.4}$$

$$L_F = F^{r_{vp}} - \zeta \sigma_0^{r_{vp}} \frac{\eta}{\Delta t_n a_{ii}} = 0 \tag{D.5}$$

with the abbreviations

$$\mathbf{h}_1 = 2\left[\left\{\left(\frac{\partial F}{\partial \mathrm{I}_1}\right) - \left(\frac{\partial F}{\partial \mathrm{J}_2}\right)\frac{1}{3}\mu \mathrm{tr}\left(\mathbf{C}\mathbf{C}_\mathrm{p}^{-1}\right)\right\}\mathbf{C}_\mathrm{p} + \left\{\left(\frac{\partial F}{\partial \mathrm{J}_2}\right)\mu\right\}\mathbf{C}\right] \tag{D.6}$$

$$h_2 = \left[\frac{c_\mathrm{d}}{\alpha}\left\{\left(\frac{\partial F}{\partial \mathrm{I}_1}\right)(\mathrm{I}_1 - 3\xi) + 2\mathrm{J}_2\left(\frac{\partial F}{\partial \mathrm{J}_2}\right)\right\} - \alpha b_\mathrm{d}\chi\right] \tag{D.7}$$

$$\chi = \sqrt{3\left(\frac{\partial F}{\partial \mathrm{I}_1}\right)^2 + 2\mathrm{J}_2\left(\frac{\partial F}{\partial \mathrm{J}_2}\right)^2}. \tag{D.8}$$

All the derivatives will be given below after recapitulating the yield function and its derivatives with respect to the invariants I_1 and J_2 of the Mandel stress tensor which are expressed as func-

tions of $\mathbf{C}_\mathrm{p}$ and $\mathbf{C}$:

$$\mathrm{I}_1 = \mu \mathrm{tr}\left(\mathbf{C}\mathbf{C}_\mathrm{p}^{-1}\right) + 3\left(\frac{1}{2}\Lambda \ln \det(\mathbf{C}_\mathrm{p}^{-1}\mathbf{C}) - \mu\right) \tag{D.9}$$

$$\mathrm{J}_2 = \frac{1}{2}\mu^2\left(\mathbf{C}\mathbf{C}_\mathrm{p}^{-1}\cdot\mathbf{C}_\mathrm{p}^{-1}\mathbf{C} - \frac{1}{3}\left(\mathrm{tr}\left(\mathbf{C}\mathbf{C}_\mathrm{p}^{-1}\right)\right)^2\right) \tag{D.10}$$

The yield function reads, as specified Eqns. (3.46)-(3.48),

$$F(\mathrm{I}_1, \sqrt{\mathrm{J}_2}) = ck \ln\left(\frac{e^{\frac{g_1(\mathrm{I}_1,\sqrt{\mathrm{J}_2})}{ck}} + e^{\frac{g_2(\mathrm{I}_1,\sqrt{\mathrm{J}_2})}{ck}}}{2}\right) \tag{D.11}$$

with the two partial yield function expressions

$$g_1(\mathrm{I}_1, \sqrt{\mathrm{J}_2}) = \sqrt{\mathrm{J}_2 + \alpha\left(\mathrm{I}_1 - 3\xi\right)^2} - k, \quad g_2(\mathrm{I}_1, \sqrt{\mathrm{J}_2}) = \sqrt{\mathrm{J}_2 + \delta} - k + A_2 e^{A_3 \mathrm{I}_1} \tag{D.12}$$

using furthermore the abbreviations

$$k = \sqrt{\alpha\left(\mathrm{I}_0 - 3\xi\right)^2}, \quad A_2 = \frac{k}{\left(1-\sqrt{1-r^2}\right)^{\left(\frac{\mathrm{I}_0}{3\xi-(rk/\sqrt{\alpha})-\mathrm{I}_0}\right)}}, \quad A_3 = \frac{\ln\left(\frac{k}{A_2}\right)}{\mathrm{I}_0} \tag{D.13}$$

and the hardening variable

$$\xi = -\frac{a_1}{a_2}e^{-a_2 r_\mathrm{K}} + c_\mathrm{K} r_\mathrm{K}, \quad r_\mathrm{K} = \ln\left(\sqrt{\det \mathbf{C}_\mathrm{p}}\right). \tag{D.14}$$

Additionally, the derivatives of the yield function with respect to the first and second invariant I_1 and J_2 are required in Eq. (D.6)-(D.8), these read

$$\frac{\partial F}{\partial \mathrm{I}_1} = w_1\frac{\partial g_1}{\partial \mathrm{I}_1} + w_2\frac{\partial g_2}{\partial \mathrm{I}_1}, \quad \frac{\partial F}{\partial \mathrm{J}_2} = w_1\frac{\partial g_1}{\partial \mathrm{J}_2} + w_2\frac{\partial g_2}{\partial \mathrm{J}_2} \tag{D.15}$$

with

$$w_1 = \frac{e^{\frac{g_1}{ck}}}{e^{\frac{g_1}{ck}} + e^{\frac{g_2}{ck}}}, \quad w_2 = \frac{e^{\frac{g_2}{ck}}}{e^{\frac{g_1}{ck}} + e^{\frac{g_2}{ck}}} \tag{D.16}$$

and

$$\frac{\partial g_1}{\partial \mathrm{I}_1} = \frac{\alpha\left(\mathrm{I}_1 - 3\xi\right)}{\sqrt{\mathrm{J}_2 + \alpha\left(\mathrm{I}_1 - 3\xi\right)^2}}, \qquad \frac{\partial g_1}{\partial \mathrm{J}_2} = \frac{1}{2\sqrt{\mathrm{J}_2 + \alpha\left(\mathrm{I}_1 - 3\xi\right)^2}} \tag{D.17}$$

$$\frac{\partial g_2}{\partial \mathrm{I}_1} = A_2 e^{A_3\mathrm{I}_1} A_3, \qquad \frac{\partial g_2}{\partial \mathrm{J}_2} = \frac{1}{2\sqrt{\mathrm{J}_2 + \delta}}. \tag{D.18}$$

D.1 Derivatives appearing in the functional matrix

The derivatives which appear in the functional matrix of a Newton-like stress algorithm as well as in the coefficient matrix of the linear system (5.122) read:

$$\frac{\partial \mathbf{L}_p}{\partial \mathbf{C}_\mathrm{p}} = \mathbf{1} - \zeta\frac{\partial \mathbf{h}_1}{\partial \mathbf{C}_\mathrm{p}}, \qquad \frac{\partial \mathbf{L}_p}{\partial \alpha} = -\zeta\frac{\partial \mathbf{h}_1}{\partial \alpha}, \qquad \frac{\partial \mathbf{L}_p}{\partial \zeta} = -\mathbf{h}_1 \tag{D.19}$$

$$\frac{\partial L_\alpha}{\partial \mathbf{C}_\mathrm{p}} = -\zeta\left(\frac{\partial h_2}{\partial \mathbf{C}_\mathrm{p}}\right)^T, \qquad \frac{\partial L_\alpha}{\partial \alpha} = 1 - \zeta\frac{\partial h_2}{\partial \alpha}, \qquad \frac{\partial L_\alpha}{\partial \zeta} = -h_2 \tag{D.20}$$

$$\frac{\partial L_F}{\partial \mathbf{C}_\mathrm{p}} = r_{vp}F^{(r_{vp}-1)}\left(\frac{\partial F}{\partial \mathbf{C}_\mathrm{p}}\right)^T, \qquad \frac{\partial L_F}{\partial \alpha} = r_{vp}F^{(r_{vp}-1)}\frac{\partial F}{\partial \alpha}, \qquad \frac{\partial L_F}{\partial \zeta} = -\sigma_0^{r_{vp}}\frac{\eta}{\Delta t a_{ii}} \tag{D.21}$$

D.1.1 Derivatives with respect to $\mathbf{C_p}$

The expressions (D.19)-(D.21) contain derivatives with respect to $\mathbf{C}_\mathrm{p}$, which read

$$\frac{\partial \mathbf{h}_1}{\partial \mathbf{C}_\mathrm{p}} = 2\left(\left[\mathbf{C}_\mathrm{p} \otimes \frac{\partial A}{\partial \mathbf{C}_\mathrm{p}}\right] + A\overset{4}{\mathbf{1}} + \left[\mathbf{C} \otimes \frac{\partial B}{\partial \mathbf{C}_\mathrm{p}}\right]\right), \tag{D.22}$$

$$\frac{\partial h_2}{\partial \mathbf{C}_\mathrm{p}} = \frac{c_\mathrm{d}}{\alpha}\frac{\partial D}{\partial \mathbf{C}_\mathrm{p}} - \alpha b_\mathrm{d}\frac{\partial \chi}{\partial \mathbf{C}_\mathrm{p}}, \tag{D.23}$$

$$\begin{aligned}\frac{\partial F}{\partial \mathbf{C}_\mathrm{p}} = &-3\sqrt{\alpha}c\ln\left(\frac{e^{g_1/(ck)} + e^{g_2/(ck)}}{2}\right)\frac{\partial \xi}{\partial \mathbf{C}_\mathrm{p}} \\ &+ w_1\frac{\partial g_1}{\partial \mathbf{C}_\mathrm{p}} + w_2\frac{\partial g_2}{\partial \mathbf{C}_\mathrm{p}} + w_1\frac{3\sqrt{\alpha}g_1}{k}\frac{\partial \xi}{\partial \mathbf{C}_\mathrm{p}} + w_2\frac{3\sqrt{\alpha}g_2}{k}\frac{\partial \xi}{\partial \mathbf{C}_\mathrm{p}}.\end{aligned} \tag{D.24}$$

Here the abbreviations

$$A = \left\{F_{,\mathrm{I}_1} - F_{,\mathrm{J}_2}\frac{\mu}{3}\mathrm{tr}\,\left(\mathbf{C}\mathbf{C}_\mathrm{p}^{-1}\right)\right\}, \tag{D.25}$$

$$B = \left\{\mu F_{,\mathrm{J}_2}\right\}, \tag{D.26}$$

$$D = \left\{\left(\mathrm{I}_1 - 3\xi\right)F_{,\mathrm{I}_1} + 2\mathrm{J}_2 F_{,\mathrm{J}_2}\right\} \tag{D.27}$$

$$\tag{D.28}$$

are introduced implying the derivatives

$$\frac{\partial A}{\partial \mathbf{C}_\mathrm{p}} = \frac{\partial F_{,\mathrm{I}_1}}{\partial \mathbf{C}_\mathrm{p}} - \frac{\mu}{3}\left[\left(\mathrm{tr}\,\mathbf{C}\mathbf{C}_\mathrm{p}^{-1}\right)\frac{\partial F_{,\mathrm{J}_2}}{\partial \mathbf{C}_\mathrm{p}} + F_{,\mathrm{J}_2}\frac{\partial\left(\mathrm{tr}\,\left(\mathbf{C}\mathbf{C}_\mathrm{p}^{-1}\right)\right)}{\partial \mathbf{C}_\mathrm{p}}\right], \tag{D.29}$$

$$\frac{\partial B}{\partial \mathbf{C}_\mathrm{p}} = \mu\frac{\partial F_{,\mathrm{J}_2}}{\partial \mathbf{C}_\mathrm{p}}, \tag{D.30}$$

$$\frac{\partial D}{\partial \mathbf{C}_\mathrm{p}} = F_{,\mathrm{I}_1}\left(\frac{\partial \mathrm{I}_1}{\partial \mathbf{C}_\mathrm{p}} - 3\frac{\partial \xi}{\partial \mathbf{C}_\mathrm{p}}\right) + \left(\mathrm{I}_1 - 3\xi\right)\frac{\partial F_{,\mathrm{I}_1}}{\partial \mathbf{C}_\mathrm{p}} + 2F_{,\mathrm{J}_2}\frac{\partial \mathrm{J}_2}{\partial \mathbf{C}_\mathrm{p}} + 2\mathrm{J}_2\frac{\partial F_{,\mathrm{J}_2}}{\partial \mathbf{C}_\mathrm{p}}. \tag{D.31}$$

$$\tag{D.32}$$

In the aforementioned derivatives the expressions

$$\frac{\partial\left(\mathrm{tr}\,\mathbf{C}\mathbf{C}_\mathrm{p}^{-1}\right)}{\partial \mathbf{C}_\mathrm{p}} = \frac{\partial}{\partial \mathbf{C}_\mathrm{p}}\left(\mathbf{C}\cdot\mathbf{C}_\mathrm{p}^{-1}\right) = -\mathbf{C}_\mathrm{p}^{-1}\mathbf{C}\mathbf{C}_\mathrm{p}^{-1}, \tag{D.33}$$

$$\frac{\partial \mathbf{C}_\mathrm{p}}{\partial \mathbf{C}_\mathrm{p}} = \overset{4}{\mathbf{1}}, \tag{D.34}$$

$$\frac{\partial \mathrm{I}_1}{\partial \mathbf{C}_\mathrm{p}} = \left(-\mu\mathbf{C}_\mathrm{p}^{-1}\mathbf{C}\mathbf{C}_\mathrm{p}^{-1} - \frac{3}{2}\Lambda\mathbf{C}_\mathrm{p}^{-1}\right), \tag{D.35}$$

$$\frac{\partial \mathrm{J}_2}{\partial \mathbf{C}_\mathrm{p}} = -\mu^2\left(\mathbf{C}_\mathrm{p}^{-1}\mathbf{C}\mathbf{C}_\mathrm{p}^{-1}\mathbf{C}\mathbf{C}_\mathrm{p}^{-1} - \frac{1}{3}\mathrm{tr}\,\left(\mathbf{C}\mathbf{C}_\mathrm{p}^{-1}\right)\mathbf{C}_\mathrm{p}^{-1}\mathbf{C}\mathbf{C}_\mathrm{p}^{-1}\right), \tag{D.36}$$

$$\frac{\partial \xi}{\partial \mathbf{C}_\mathrm{p}} = \frac{\partial \xi}{\partial r_\mathrm{K}}\frac{\partial r_\mathrm{K}}{\partial \mathbf{C}_\mathrm{p}} = \left(a_1 e^{-a_2 r_\mathrm{K}} + c_\mathrm{K}\right)\frac{1}{2}\mathbf{C}_\mathrm{p}^{-1} \tag{D.37}$$

are introduced. In Eqns. (D.22)-(D.23) and (D.29) - (D.31) several derivatives with respect to $\mathbf{C}_\mathrm{p}$ appear. These are in particular

$$\frac{\partial F_{,\mathrm{I}_1}}{\partial \mathbf{C}_\mathrm{p}} = \frac{\partial w_1}{\partial \mathbf{C}_\mathrm{p}} \left(g_{1,\mathrm{I}_1} - g_{2,\mathrm{I}_1}\right) + w_1 \frac{\partial g_{1,\mathrm{I}_1}}{\partial \mathbf{C}_\mathrm{p}} + w_2 \frac{\partial g_{2,\mathrm{I}_1}}{\partial \mathbf{C}_\mathrm{p}}, \tag{D.38}$$

$$\frac{\partial F_{,\mathrm{J}_2}}{\partial \mathbf{C}_\mathrm{p}} = \frac{\partial w_1}{\partial \mathbf{C}_\mathrm{p}} \left(g_{1,\mathrm{J}_2} - g_{2,\mathrm{J}_2}\right) + w_1 \frac{\partial g_{1,\mathrm{J}_2}}{\partial \mathbf{C}_\mathrm{p}} + w_2 \frac{\partial g_{2,\mathrm{J}_2}}{\partial \mathbf{C}_\mathrm{p}}, \tag{D.39}$$

$$\frac{\partial \chi}{\partial \mathbf{C}_\mathrm{p}} = \frac{1}{2} \left(3F_{,\mathrm{I}_1}^2 + 2\mathrm{J}_2 F_{,\mathrm{J}_2}^2\right)^{-1/2} \left[6F_{,\mathrm{I}_1} \frac{\partial F_{,\mathrm{I}_1}}{\partial \mathbf{C}_\mathrm{p}} + 4\mathrm{J}_2 F_{,\mathrm{J}_2} \frac{\partial F_{,\mathrm{J}_2}}{\partial \mathbf{C}_\mathrm{p}} + 2F_{,\mathrm{J}_2}^2 \frac{\partial \mathrm{J}_2}{\partial \mathbf{C}_\mathrm{p}}\right] \tag{D.40}$$

$$\tag{D.41}$$

implying the derivatives:

$$\frac{\partial w_1}{\partial \mathbf{C}_\mathrm{p}} = w_1 w_2 \left[\frac{1}{ck} \left(\frac{\partial g_1}{\partial \mathbf{C}_\mathrm{p}} - \frac{\partial g_2}{\partial \mathbf{C}_\mathrm{p}}\right) - \frac{1}{ck^2} \left(g_1 - g_2\right) \frac{\partial k}{\partial \mathbf{C}_\mathrm{p}}\right], \tag{D.42}$$

$$\frac{\partial w_2}{\partial \mathbf{C}_\mathrm{p}} = -\frac{\partial w_1}{\partial \mathbf{C}_\mathrm{p}} \tag{D.43}$$

$$\tag{D.44}$$

Furthermore, the chain-rule is applied to get

$$\frac{\partial g_{1,\mathrm{I}_1}}{\partial \mathbf{C}_\mathrm{p}} = \frac{\partial g_{1,\mathrm{I}_1}}{\partial \mathrm{I}_1} \frac{\partial \mathrm{I}_1}{\partial \mathbf{C}_\mathrm{p}} + \frac{\partial g_{1,\mathrm{I}_1}}{\partial \mathrm{J}_2} \frac{\partial \mathrm{J}_2}{\partial \mathbf{C}_\mathrm{p}} + \frac{\partial g_{1,\mathrm{I}_1}}{\partial \xi} \frac{\partial \xi}{\partial \mathbf{C}_\mathrm{p}} \tag{D.45}$$

in Eq. (D.38), i.e. the derivative of the ellipsoidal part. The right-hand sides of the summands in (D.45) are already given in Eqns. (D.35)-(D.37), whereas the left-hand sides read:

$$\frac{\partial g_{1,\mathrm{I}_1}}{\partial \mathrm{I}_1} = \frac{\alpha}{\left(\mathrm{J}_2 + \alpha \left(\mathrm{I}_1 - 3\xi\right)^2\right)^{1/2}} - \frac{\alpha^2 (\mathrm{I}_1 - 3\xi)^2}{\left(\mathrm{J}_2 + \alpha \left(\mathrm{I}_1 - 3\xi\right)^2\right)^{3/2}}, \tag{D.46}$$

$$\frac{\partial g_{1,\mathrm{I}_1}}{\partial \mathrm{J}_2} = -\frac{\alpha \left(\mathrm{I}_1 - 3\xi\right)}{2\left(\mathrm{J}_2 + \alpha \left(\mathrm{I}_1 - 3\xi\right)^2\right)^{3/2}}, \tag{D.47}$$

$$\frac{\partial g_{1,\mathrm{I}_1}}{\partial \xi} = -\frac{3\alpha}{\left(\mathrm{J}_2 + \alpha \left(\mathrm{I}_1 - 3\xi\right)^2\right)^{1/2}} + \frac{3\alpha^2 \left(\mathrm{I}_1 - 3\xi\right)^2}{\left(\mathrm{J}_2 + \alpha \left(\mathrm{I}_1 - 3\xi\right)^2\right)^{3/2}}. \tag{D.48}$$

Furthermore, in Eq. (D.38)

$$\frac{\partial g_{2,\mathrm{I}_1}}{\partial \mathbf{C}_\mathrm{p}} = A_2 A_3^2 e^{A_3 \mathrm{I}_1} \frac{\partial \mathrm{I}_1}{\partial \mathbf{C}_\mathrm{p}} + \left[A_3 e^{A_3 \mathrm{I}_1} \frac{\partial A_2}{\partial \xi} + A_2 e^{A_3 \mathrm{I}_1} \frac{\partial A_3}{\partial \xi} + A_2 A_3 \mathrm{I}_1 e^{A_3 \mathrm{I}_1} \frac{\partial A_3}{\partial \xi}\right] \frac{\partial \xi}{\partial \mathbf{C}_\mathrm{p}} \tag{D.49}$$

is required implying the derivatives of the abbreviation A_2 and A_3 defined in Eq. (D.13):

$$\frac{\partial A_2}{\partial \xi} = -\frac{3\left(1 - \sqrt{1 - r^2}\right)^{\frac{\mathrm{I}_0}{(1+r)(\mathrm{I}_0 - 3\xi)}} \sqrt{\alpha} \left((1 + r)\left(\mathrm{I}_0 - 3\xi\right) - \mathrm{I}_0 \ln\left(1 - \sqrt{1 - r^2}\right)\right)}{(1 + r)\left(\mathrm{I}_0 - 3\xi\right)} \tag{D.50}$$

$$\frac{\partial A_3}{\partial \xi} = -\frac{3 \ln\left(1 - \sqrt{1 - r^2}\right)}{(1 + r)\left(3\xi - \mathrm{I}_0\right)^2}. \tag{D.51}$$

Eq. (D.39) necessitates the derivatives

$$\frac{\partial g_{1,\mathrm{J}_2}}{\partial \mathbf{C}_\mathrm{p}} = \left(\mathrm{J}_2 + \alpha\left(\mathrm{I}_1 - 3\xi\right)^2\right)^{-3/2}\left[\frac{3\alpha\left(\mathrm{I}_1 - 3\xi\right)}{2}\frac{\partial \xi}{\partial \mathbf{C}_\mathrm{p}} - \frac{\alpha\left(\mathrm{I}_1 - 3\xi\right)}{2}\frac{\partial \mathrm{I}_1}{\partial \mathbf{C}_\mathrm{p}} - \frac{1}{4}\frac{\partial \mathrm{J}_2}{\partial \mathbf{C}_\mathrm{p}}\right], \tag{D.52}$$

$$\frac{\partial g_{2,\mathrm{J}_2}}{\partial \mathbf{C}_\mathrm{p}} = -\frac{1}{4}\left(\mathrm{J}_2\right)^{-3/2}\frac{\partial \mathrm{J}_2}{\partial \mathbf{C}_\mathrm{p}}. \tag{D.53}$$

Lastly, Eq. (D.42) implies both the derivative

$$\frac{\partial g_1}{\partial \mathbf{C}_\mathrm{p}} = g_{1,\mathrm{I}_1}\frac{\partial \mathrm{I}_1}{\partial \mathbf{C}_\mathrm{p}} + g_{1,\mathrm{J}_2}\frac{\partial \mathrm{J}_2}{\partial \mathbf{C}_\mathrm{p}} + \frac{\partial g_1}{\partial \xi}\frac{\partial \xi}{\partial \mathbf{C}_\mathrm{p}} \tag{D.54}$$

which requires

$$\frac{\partial g_1}{\partial \xi} = -\frac{3\alpha\left(\mathrm{I}_1 - 3\xi\right)}{\sqrt{\mathrm{J}_2 + \alpha\left(\mathrm{I}_1 - 3\xi\right)^2}} + \frac{3\alpha\left(\mathrm{I}_0 - 3\xi\right)}{\sqrt{\alpha\left(\mathrm{I}_0 - 3\xi\right)^2}}, \tag{D.55}$$

and the derivative

$$\frac{\partial g_2}{\partial \mathbf{C}_\mathrm{p}} = g_{2,\mathrm{I}_1}\frac{\partial \mathrm{I}_1}{\partial \mathbf{C}_\mathrm{p}} + g_{2,\mathrm{J}_2}\frac{\partial \mathrm{J}_2}{\partial \mathbf{C}_\mathrm{p}} + \frac{\partial g_2}{\partial k}\frac{\partial k}{\partial \mathbf{C}_\mathrm{p}} + \frac{\partial g_2}{\partial A_2}\frac{\partial A_2}{\partial \mathbf{C}_\mathrm{p}} + \frac{\partial g_2}{\partial A_3}\frac{\partial A_3}{\partial \mathbf{C}_\mathrm{p}} \tag{D.56}$$

with

$$\frac{\partial g_2}{\partial k} = -1, \qquad \frac{\partial g_2}{\partial A_2} = e^{A_3\mathrm{I}_1}, \qquad \frac{\partial g_2}{\partial A_3} = A_2\mathrm{I}_1 e^{A_3\mathrm{I}_1}, \tag{D.57}$$

$$\frac{\partial k}{\partial \mathbf{C}_\mathrm{p}} = -3\sqrt{\alpha}\frac{\partial \xi}{\partial \mathbf{C}_\mathrm{p}}, \qquad \frac{\partial A_2}{\partial \mathbf{C}_\mathrm{p}} = \frac{\partial A_2}{\partial \xi}\frac{\partial \xi}{\partial \mathbf{C}_\mathrm{p}}, \qquad \frac{\partial A_3}{\partial \mathbf{C}_\mathrm{p}} = \frac{\partial A_3}{\partial \xi}\frac{\partial \xi}{\partial \mathbf{C}_\mathrm{p}} \tag{D.58}$$

using the derivatives (D.50) and (D.51).

D.1.2 Derivatives with respect to α

In the functional matrix of (5.118) some derivatives with respect to α are required, see Eqns. (D.19)-(D.21). Here we start with the derivatives of the functions $\mathbf{h}_1$, h_2 and F defined in Eqns.(D.6), (D.7) and (D.11):

$$\frac{\partial \mathbf{h_1}}{\partial \alpha} = 2\left[\left(\frac{\partial F_{,\mathrm{I}_1}}{\partial \alpha} - \frac{\mu}{3}\mathrm{tr}\left(\mathbf{C}\mathbf{C}_\mathrm{p}^{-1}\right)\frac{\partial F_{,\mathrm{J}_2}}{\partial \alpha}\right)\mathbf{C}_\mathrm{p} + \mu\frac{\partial F_{,\mathrm{J}_2}}{\partial \alpha}\mathbf{C}\right] \tag{D.59}$$

$$\frac{\partial h_2}{\partial \alpha} = -\frac{c_\mathrm{D}}{\alpha^2}D + \frac{c_\mathrm{D}}{\alpha}\frac{\partial D}{\partial \alpha} - b_\mathrm{D}\left(\chi + \alpha\frac{\partial \chi}{\partial \alpha}\right) \tag{D.60}$$

$$\frac{\partial F}{\partial \alpha} = c\ln\left(\frac{e^{g_1/(ck)} + e^{g_2/(ck)}}{2}\right)\frac{\partial k}{\partial \alpha} + w_1\frac{\partial g_1}{\partial \alpha} + w_2\frac{\partial g_2}{\partial \alpha} - w_1\frac{g_1}{k}\frac{\partial k}{\partial \alpha} - w_2\frac{g_2}{k}\frac{\partial k}{\partial \alpha} \tag{D.61}$$

In Eq. (D.59) additional derivatives with respect to α occur reading

$$\frac{\partial F_{,\mathrm{I}_1}}{\partial \alpha} = \frac{\partial w_1}{\partial \alpha}\left(g_{1,\mathrm{I}_1} - g_{2,\mathrm{I}_1}\right) + w_1\frac{\partial g_{1,\mathrm{I}_1}}{\partial \alpha} + w_2\frac{\partial g_{2,\mathrm{I}_1}}{\partial \alpha}, \tag{D.62}$$

$$\frac{\partial F_{,\mathrm{J}_2}}{\partial \alpha} = \frac{\partial w_1}{\partial \alpha}\left(g_{1,\mathrm{J}_2} - g_{2,\mathrm{J}_2}\right) + w_1\frac{\partial g_{1,\mathrm{J}_2}}{\partial \alpha} + w_2\frac{\partial g_{2,\mathrm{J}_2}}{\partial \alpha} \tag{D.63}$$

with the further derivatives

$$\frac{\partial w_1}{\partial \alpha} = \frac{w_1 w_2}{ck^2}\left[k\left(\frac{\partial g_1}{\partial \alpha} - \frac{\partial g_2}{\partial \alpha}\right) + \frac{\partial k}{\partial \alpha}\left(g_2 - g_1\right)\right] = -\frac{\partial w_2}{\partial \alpha} \tag{D.64}$$

$$\frac{\partial g_{1,\mathrm{I}_1}}{\partial \alpha} = \frac{\left(\mathrm{I}_1 - 3\xi\right)\sqrt{\mathrm{J}_2 + \alpha\left(\mathrm{I}_1 - 3\xi\right)^2} - \alpha\left(\mathrm{I}_1 - 3\xi\right)^3 \frac{1}{2}\left(\mathrm{J}_2 + \alpha\left(\mathrm{I}_1 - 3\xi\right)^2\right)^{-1/2}}{\mathrm{J}_2 + \alpha\left(\mathrm{I}_1 - 3\xi\right)^2} \tag{D.65}$$

$$\frac{\partial g_{2,\mathrm{I}_1}}{\partial \alpha} = A_3 e^{A_3 \mathrm{I}_1}\frac{\partial A_2}{\partial \alpha} \tag{D.66}$$

$$\frac{\partial g_{1,\mathrm{J}_2}}{\partial \alpha} = -\frac{1}{4}\left(\mathrm{J}_2 + \alpha\left(\mathrm{I}_1 - 3\xi\right)^2\right)^{-3/2}\left(\mathrm{I}_1 - 3\xi\right)^2 \tag{D.67}$$

$$\tag{D.68}$$

exploiting the properties $\partial g_{2,\mathrm{J}_2}/\partial\alpha = 0$ and $\partial A_3/\partial\alpha = 0$. Eqns. (D.64) and (D.66), however, require

$$\frac{\partial g_1}{\partial \alpha} = \frac{1}{2}\left(\mathrm{J}_2 + \alpha\left(\mathrm{I}_1 - 3\xi\right)^2\right)^{-1/2}\left(\mathrm{I}_1 - 3\xi\right)^2 - \frac{\partial k}{\partial \alpha} \tag{D.69}$$

$$\frac{\partial g_2}{\partial \alpha} = -\frac{\partial k}{\partial \alpha} + \frac{\partial A_2}{\partial \alpha}e^{A_3 \mathrm{I}_1} \tag{D.70}$$

$$\frac{\partial A_2}{\partial \alpha} = \frac{\left(\mathrm{I}_0 - 3\xi\right)}{\left(1 - \sqrt{1 - r^2}\right)^{\frac{\mathrm{I}_0}{(1+r)(3\xi - \mathrm{I}_0)}}}\frac{1}{2\sqrt{\alpha}} \tag{D.71}$$

$$\frac{\partial k}{\partial \alpha} = \frac{\left(\mathrm{I}_0 - 3\xi\right)}{2\sqrt{\alpha}} \tag{D.72}$$

$$\tag{D.73}$$

and, finally, Eq. (D.60) contains the derivatives

$$\frac{\partial D}{\partial \alpha} = \left(\mathrm{I}_1 - 3\xi\right)\frac{\partial F_{,\mathrm{I}_1}}{\partial \alpha} + 2\mathrm{J}_2\frac{\partial F_{,\mathrm{J}_2}}{\partial \alpha}, \tag{D.74}$$

$$\frac{\partial \chi}{\partial \alpha} = \left(3F_{,\mathrm{I}_1}^2 + 2\mathrm{J}_2 F_{,\mathrm{J}_2}^2\right)^{-1/2}\left(3F_{,\mathrm{I}_1}\frac{\partial F_{,\mathrm{I}_1}}{\partial \alpha} + 2\mathrm{J}_2 F_{,\mathrm{J}_2}\frac{\partial F_{,\mathrm{J}_2}}{\partial \alpha}\right) \tag{D.75}$$

D.2 Derivatives with respect to $\mathbf{C}$

The derivatives in the right-hand side of Eq. (5.122) read

$$\frac{\partial \mathbf{L}_p}{\partial \mathbf{C}} = -\zeta\frac{\partial \mathbf{h_1}}{\partial \mathbf{C}}, \quad \frac{\partial L_\alpha}{\partial \mathbf{C}} = -\zeta\frac{\partial h_2}{\partial \mathbf{C}}, \quad \frac{\partial L_F}{\partial \mathbf{C}} = r_{vp}F^{r_{vp}-1}\frac{\partial F}{\partial \mathbf{C}}. \tag{D.76}$$

These contain the following derivatives with respect to the right Cauchy-Green tensor $\mathbf{C}$:

$$\begin{aligned}\frac{\partial \mathbf{h}_1}{\partial \mathbf{C}} = 2\Bigg\{&\left[\mathbf{C}_\mathrm{p} \otimes \frac{\partial F_{,\mathrm{I}_1}}{\partial \mathbf{C}}\right] - \frac{1}{3}\mu\mathrm{tr}\left(\mathbf{C}\mathbf{C}_\mathrm{p}^{-1}\right)\left[\mathbf{C}_\mathrm{p} \otimes \frac{\partial F_{,\mathrm{J}_2}}{\partial \mathbf{C}}\right] \\ &-\frac{1}{3}\mu F_{,\mathrm{J}_2}\left[\mathbf{C}_\mathrm{p} \otimes \mathbf{C}_\mathrm{p}^{-1}\right] + \mu\left[\mathbf{C} \otimes \frac{\partial F_{,\mathrm{J}_2}}{\partial \mathbf{C}}\right] + \mu F_{,\mathrm{J}_2}\overset{4}{\mathbf{1}}\Bigg\}\end{aligned} \tag{D.77}$$

$$\frac{\partial h_2}{\partial \mathbf{C}} = \frac{c_\mathrm{D}}{\alpha}\left(F_{,\mathrm{I}_1}\frac{\partial \mathrm{I}_1}{\partial \mathbf{C}} + \left(\mathrm{I}_1 - 3\xi\right)\frac{\partial F_{,\mathrm{I}_1}}{\partial \mathbf{C}} + 2F_{,\mathrm{J}_2}\frac{\partial \mathrm{J}_2}{\partial \mathbf{C}} + 2\mathrm{J}_2\frac{\partial F_{,\mathrm{J}_2}}{\partial \mathbf{C}}\right) - \alpha b_\mathrm{D}\frac{\partial \chi}{\partial \mathbf{C}} \tag{D.78}$$

$$\frac{\partial F}{\partial \mathbf{C}} = w_1\frac{\partial g_1}{\partial \mathbf{C}} + w_2\frac{\partial g_2}{\partial \mathbf{C}} \tag{D.79}$$

$$\tag{D.80}$$

Here, use has been made of

$$\frac{\partial \left(\operatorname{tr} \mathbf{C}\mathbf{C}_{\mathrm{p}}^{-1}\right)}{\partial \mathbf{C}} = \mathbf{C}_{\mathrm{p}}^{-1} \tag{D.81}$$

and the property $(\mathbf{R}\cdot\mathbf{S})\mathbf{T} = [\mathbf{T}\otimes\mathbf{R}]\mathbf{S}$, where $\mathbf{R}$, $\mathbf{S}$ and $\mathbf{T}$ are second order tensors and the dot symbolizes the inner product of two second order tensors. In Eq. (D.77) the derivatives

$$\frac{\partial F_{,\mathrm{I}_1}}{\partial \mathbf{C}} = \frac{\partial w_1}{\partial \mathbf{C}}\left(g_{1,\mathrm{I}_1} - g_{2,\mathrm{I}_1}\right) + w_1\frac{\partial g_{1,\mathrm{I}_1}}{\partial \mathbf{C}} + w_2\frac{\partial g_{2,\mathrm{I}_1}}{\partial \mathbf{C}}, \tag{D.82}$$

$$\frac{\partial F_{,\mathrm{J}_2}}{\partial \mathbf{C}} = \frac{\partial w_1}{\partial \mathbf{C}}\left(g_{1,\mathrm{J}_2} - g_{2,\mathrm{J}_2}\right) + w_1\frac{\partial g_{1,\mathrm{J}_2}}{\partial \mathbf{C}} + w_2\frac{\partial g_{2,\mathrm{J}_2}}{\partial \mathbf{C}} \tag{D.83}$$

with

$$\frac{\partial w_1}{\partial \mathbf{C}} = w_1 w_2\left[\frac{1}{ck}\left(\frac{\partial g_1}{\partial \mathbf{C}} - \frac{\partial g_2}{\partial \mathbf{C}}\right)\right], \tag{D.84}$$

$$\frac{\partial g_{1,\mathrm{I}_1}}{\partial \mathbf{C}} = \frac{\partial g_{1,\mathrm{I}_1}}{\partial \mathrm{I}_1}\frac{\partial \mathrm{I}_1}{\partial \mathbf{C}} + \frac{\partial g_{1,\mathrm{I}_1}}{\partial \mathrm{J}_2}\frac{\partial \mathrm{J}_2}{\partial \mathbf{C}}, \tag{D.85}$$

$$\frac{\partial g_{1,\mathrm{J}_2}}{\partial \mathbf{C}} = \frac{\partial g_{1,\mathrm{J}_2}}{\partial \mathrm{I}_1}\frac{\partial \mathrm{I}_1}{\partial \mathbf{C}} + \frac{\partial g_{1,\mathrm{J}_2}}{\partial \mathrm{J}_2}\frac{\partial \mathrm{J}_2}{\partial \mathbf{C}} \tag{D.86}$$

and

$$\frac{\partial g_{2,\mathrm{I}_1}}{\partial \mathbf{C}} = \frac{\partial g_{2,\mathrm{I}_1}}{\partial \mathrm{I}_1}\frac{\partial \mathrm{I}_1}{\partial \mathbf{C}} + \underbrace{\frac{\partial g_{2,\mathrm{I}_1}}{\partial \mathrm{J}_2}}_{=0}\frac{\partial \mathrm{J}_2}{\partial \mathbf{C}} = \frac{\partial g_{2,\mathrm{I}_1}}{\partial \mathrm{I}_1}\frac{\partial \mathrm{I}_1}{\partial \mathbf{C}}, \tag{D.87}$$

$$\frac{\partial g_{2,\mathrm{J}_2}}{\partial \mathbf{C}} = \underbrace{\frac{\partial g_{2,\mathrm{J}_2}}{\partial \mathrm{I}_1}}_{=0}\frac{\partial \mathrm{I}_1}{\partial \mathbf{C}} + \frac{\partial g_{2,\mathrm{J}_2}}{\partial \mathrm{J}_2}\frac{\partial \mathrm{J}_2}{\partial \mathbf{C}} = \frac{\partial g_{2,\mathrm{J}_2}}{\partial \mathrm{J}_2}\frac{\partial \mathrm{J}_2}{\partial \mathbf{C}} \tag{D.88}$$

are required implying the additional derivatives

$$\frac{\partial g_1}{\partial \mathbf{C}} = g_{1,\mathrm{I}_1}\frac{\partial \mathrm{I}_1}{\partial \mathbf{C}} + g_{1,\mathrm{J}_2}\frac{\partial \mathrm{J}_2}{\partial \mathbf{C}}, \tag{D.89}$$

$$\frac{\partial g_2}{\partial \mathbf{C}} = g_{2,\mathrm{I}_1}\frac{\partial \mathrm{I}_1}{\partial \mathbf{C}} + g_{2,\mathrm{J}_2}\frac{\partial \mathrm{J}_2}{\partial \mathbf{C}} \tag{D.90}$$

with

$$\frac{\partial \mathrm{I}_1}{\partial \mathbf{C}} = \mu\mathbf{C}_{\mathrm{p}}^{-1} + \frac{3}{2}\Lambda\mathbf{C}^{-1}, \tag{D.91}$$

$$\frac{\partial \mathrm{J}_2}{\partial \mathbf{C}} = \mu^2\left(\mathbf{C}_{\mathrm{p}}^{-1}\mathbf{C}\mathbf{C}_{\mathrm{p}}^{-1} - \frac{1}{3}\operatorname{tr}\left(\mathbf{C}\mathbf{C}_{\mathrm{p}}^{-1}\right)\mathbf{C}_{\mathrm{p}}^{-1}\right). \tag{D.92}$$

Finally, Eq. (D.78) needs

$$\frac{\partial \chi}{\partial \mathbf{C}} = \frac{1}{2\chi}\left(6F_{,\mathrm{I}_1}\frac{\partial F_{,\mathrm{I}_1}}{\partial \mathbf{C}} + 4\mathrm{J}_2F_{,\mathrm{J}_2}\frac{\partial F_{,\mathrm{J}_2}}{\partial \mathbf{C}} + 2F_{,\mathrm{J}_2}^2\frac{\partial \mathrm{J}_2}{\partial \mathbf{C}}\right). \tag{D.93}$$

Appendix E

List of publications originating from GIF collaboration

1. HEISSERER, U. & DÜSTER, A. & RANK, E.:
   Follower loads for axisymmetric high order finite elements
   Proceedings in Applied Mathematics and Mechanics 2005, 5, 405-406

2. BIER, W. & HARTMANN, S.:
   A finite strain viscoplasticity model for cold compaction processes of metal powder
   Proceedings in Applied Mathematics and Mechanics, 2005, 5, 263-264

3. BIER, W. & HARTMANN, S.:
   A finite strain constitutive model for metal powder compaction using a unique and convex single surface yield function
   *European Journal of Mechanics, Series A/Solids **25**, 2006, 1009-1030*

4. YOSIBASH, Z. & HARTMANN, S. & HEISSERER, U. & DÜSTER, A. & RANK, E. & SZANTO, M.:
   Axisymmetric pressure boundary loading for finite deformation analysis using p-FEM
   *Computer Methods in Applied Mechanics and Engineering **196**, 2007, 1261-1277*

5. BIER, W. & DARIEL, M.P. & FRAGE, N. & HARTMANN, S. & MICHAILOV, O.:
   Die compaction of copper powder designed for material parameter identification
   *International Journal of Mechanical Sciences **49**, 2007, 766-777*

6. HARTMANN, S. & BIER, W.:
   High-order time integration applied to metal powder plasticity
   *International Journal of Plasticity, **24**(1), 2008, 17–54*

7. HEISSERER, U. & HARTMANN, S. & DÜSTER A. & YOSIBASH, Z.:
   On volumeteric locking-free behavior of p-version finite elements under finite deformations
   currently online available *Communications in Numerical Methods in Engineering 2007*

8. SZANTO, M. & BIER, W. & FRAGE, N. & HARTMANN, S. & YOSIBASH, Z.:
   Experimental based finite element simulation of cold isostatic pressing of metal powders
   currently online available *International Journal of Mechanical Sciences 2008*

9. HEISSERER, U. & HARTMANN, S. & DÜSTER, A. & BIER, W. & YOSIBASH, Z. & RANK, E.:
p-FEM for finite deformation powder compaction
Computer Methods in Applied Mechanics and Engineering, ***197****(6-8), 2008,727–740*

Appendix F

List of symbols

In this Section almost all symbols appearing in the thesis are collected. Only some symbols which appaer only once or in a very small part of the thesis or in the citation of the work of others have been excluded from this collection. The enumeration of the symbols starts with scalar quantities then vector valued quantities after that tensor valued quantities and then matrices and column matrices after that miscellaneous quantities and mathematical operators. In each subsection the symbols are listed in alphabetical order starting with greek letters, then latin letters and finally caligraphic letters.

F.1 Scalar quantities

α, α_0	internal variable and its initial value
β	parameter of Drucker-Prager surface
β	damping or line search parameter
γ	entropy production density
δ	smoothing parameter in yield function
$\varepsilon_r, \varepsilon_a$	realtive and absolute error tolerances
ε	parameter of line search algorithm
ζ	abbreviation in equations after time discretization
η	parameter for expansion of model to viscoplasticity
θ	Haigh-Westergaard coordinate, see also π, ϱ
κ	yield strength (parameter of von Mises yield function)
λ	plastic multiplier
$\tilde{\lambda}$	constitutive function in expansion to viscoplasticity
λ	axial stretch
λ	continuation parameter in embedded Newton algorithm
λ_p	plastic stretch axial
λ_{pq}	plastic stretch radial
λ_0	axial stretch where unloading starts
μ	elasticity parameter
$\overline{\mu}$	mean value of elasticity parameter from experiments
ν	elasticity parameter, Poisson ratio
ν	parameter of line search algorithm
ξ	parameter of new yield surface (centre of ellipsoid)
π	Haigh-Westergaard coordinate, see also θ, ϱ

ϱ	Haigh-Westergaard coordinate, see also π, θ
$\rho(\boldsymbol{x}, t)$	spatial density distribution
$\rho_R(\boldsymbol{X})$	density distribution in reference configuration
ρ_{rel}	relative density
$\rho_{\text{particle material}}$	density of particle material
$\rho_{\text{R,rel}}$	relative density in the reference configuration
σ_0	parameter for expansion of model to viscoplasticity
σ	volume distributed entropy supply to material body
$\sigma_k,\ k = 1, 2, 3$	principal stresses of $\mathbf{T}$
σ_Y	uniaxial yield strength of base material in micromechanical models
σ_Y	uniaxial yield strength of die material
σ_{axial}	axial Cauchy stress measured in die compaction
σ_{radial}	radial Cauchy stress measured in die compaction
τ	time parameter of unit time interval
$\tau_{\text{max}},\ \tau^{(k)}$	(maximum) step size of homotopy Newton method
$\hat{\varphi}(\beta)$	merit function in line search algorithm
$\varphi(\mathbf{Q})$	minimization problem in line search algorithm
$\hat{\psi}$	free energy
$\hat{\psi}_{\text{e}}, \hat{\psi}_{\text{p}}$	elastic, plastic part of free energy
Γ	entropy production within material body
$\Delta d = 2\Delta r$	radial expansion of die
Θ	invariant of stress tensor (alternative to invariant θ)
Λ	elasticity parameter
$\overline{\Lambda}$	mean value of elasticity parameter from experiments
Σ	entropy flux
Σ_m	mean stress (micromechanical model)
Σ_e	deviatoric stress measure (micromechanical model)
$a_{ij},\ b_i,\ c_i$	coefficients of Runge-Kutta method
a_1, a_2	parameters in constitutive equation $\xi(r_K)$
b_D, c_D	parameters in evolution equation for α
c_K	parameters in constitutive equation $\xi(r_K)$
c	interpolation parameter (log-interpolation)
$dV,\ dv$	volume element in reference and in current configuration
e	internal energy density
e_{u}	error norm for nodal displacements
e_{q}	error norm for internal variables
e_{m}	maximum of e_{u} and e_{q}
$f_{\text{min}}, f_{\text{max}}, f_{\text{safety}}$	factors in step size control algorithm
g_1, g_2	parts of reformulated yield function
h, h_0	height of powder in die, initial height of powder
k	abbreviation in new yield surface
$m(\mathcal{B}, t)$	mass of material body $\mathcal{B}$
n	porosity $n = 1 - \rho_{\text{rel}}$
n_{nodes}	number of finite elements nodes
n_{dof}	number of degrees of freedom
n_{u}	number of unknown nodal displacements
n_{p}	number of prescribed nodal displacements

n_i	number of all integration (Gauss) points
n_q	number of internal variables at each Gauss-point
n_Q	number of all internal variables from all Gauss-points
p_Y	macroscopic yield strength
p	hydrostatic pressure $p = -\frac{1}{3} I_1$
p_c	parameter of Cam-clay model (isostatic yield strength)
$p, \hat{p}$	order of Runge-Kutta method
q	deviatoric stress measure $q = \sqrt{3 J_2}$
q_1, q_2	parameters in modified Gurson model
q	heat flux density
$q(h)$	factor between σ_{radial} and Δd as a function of the powder height h
r	volume distributed heat supply
r	parameters of new yield surface
r_{crit}	parameter in Newton algorithm with damping
r_{vp}	parameter for expansion of model to viscoplasticity
r_D, r_K	strain like internal variables
s	entropy density of material body
s	stage of Runge-Kutta method
$\dot{s}$	rate of plastic arc-length
t	time
t_0	start time
u_{axial}	axial displacement of punch
$u_{\text{axial}}^{\text{pow}}$	axial displacement of punch due to powder compaction
$u_{\text{axial}}^{\text{sys}}$	axial displacement of punch due to system compliance
w_j, w_k, w_l	weights of Gauss integration
x^1, x^2, x^3	components of $\boldsymbol{x}$
x_0	intersection point (new yield function)
A_1, A_2, A_3	abbreviations (parameters) of new yield surface
A_c	average contact area between particles (micro-mechanical models)
A, B, C	coefficients in ellipsoidal yield function
B_{axial}	slope of unloading curve (σ_{axial})
B_{radial}	slope of unloading curve (σ_{radial})
D_0, D	(initial) relative density of particle assemblage (micro-mechanical model)
E	internal energy content of material body
E	elasticity parameter, Young's modulus
F_j^i	components of $\mathbf{F}$
$F, \hat{F}$	yield function
F_h	part of yield function defining shape in hydrostatic plane
F_d	part of yield function defining shape in deviatoric plane
$G(g_1, g_2)$	reformulated yield function
H	total entropy exchange of material body with surroundings
H	position of axial expansion sensor
I_1, I_2, I_3	invariants of $\mathbf{T}$
I_1	first invariant of Mandel stress tensor
I_0	parameters of new yield surface, intersection with hydrostatic axis
I_{is}	intersection point of ellipse and exponential part of yield surface
J	determinant of $\mathbf{F}$

J_e	determinant of $\hat{\mathbf{F}}_\mathrm{e}$
J_2, J_3	invariants of the deviator $\mathbf{T}^D$ of $\mathbf{T}$
J_2	second invariant of deviator of Mandels stress tensor
K	kinetic energy content of material body
M	parameter of Cam-clay model (slope)
P_a	power of external forces acting on material body
Q	heat flux into material body
Q_i	component of $\mathbf{Q}$
$\mathsf{Q}_{i,\mathrm{min}}$	constraint for i^{th} component of $\mathbf{Q}$
S	entropy content of material body
T	end time of time interval
T	temperature of material body
T_C	tension cut off parameter of multi surface cap yield function
X^1, X^2, X^3	components of $\boldsymbol{X}$
Y	yield strength cut off parameter of multi surface cap yield function
Z	average number of contacts of individual particle (micro-mechanical model)
$\mathcal{D}_p$	plastic dissipation
$\mathcal{D}_K, \mathcal{D}_D$	parts of plastic dissipation

F.2 Vector valued quantities

$\delta\boldsymbol{u}$	virtual displacements
$\delta\boldsymbol{h}$	virtual spatial displacement gradient
$\delta\boldsymbol{u}$	virtual nodal displacements
$\boldsymbol{\Sigma}$	entropy flux vector
$\boldsymbol{c}(t)$	time dependent translation
$\boldsymbol{dX}$, $\boldsymbol{dx}$	tangent vector of material line in reference and current configuration
$\boldsymbol{dA}$, $\boldsymbol{da}$	surface element in reference configuration, in current configuration
$\boldsymbol{df}$	current force vector
$\vec{e}_r, \vec{e}_\vartheta, \vec{e}_z$	basis vectors of cylindrical coordinate system
$\boldsymbol{g_1}$, $\boldsymbol{g_2}$, $\boldsymbol{g_3}$	basis system of the current configuration
$\boldsymbol{g}$	spatial temperature gradient
$\boldsymbol{k}$	volume distributed external force (ususally gravitational forces)
$\boldsymbol{n}$, $\boldsymbol{n}_R$	surface normal
$\vec{n}_k,\ k = 1, 2, 3$	principal directions of $\mathbf{T}$
$\boldsymbol{q}$, $\boldsymbol{q}_R$	Cauchy heat flux vector, heat flux vector of reference configuration
$\boldsymbol{q}$	internal variables
$\boldsymbol{t}$	Cauchy stress vector
$\boldsymbol{t}_R$	Piola stress vector
$\boldsymbol{u}$	displacement vector
$\boldsymbol{v}(\boldsymbol{x}, t)$	spatial velocity field
$\boldsymbol{x}$	spatial position vector of material point
$\boldsymbol{G_1}$, $\boldsymbol{G_2}$, $\boldsymbol{G_3}$	basis system of the reference configuration
$\boldsymbol{X}$	position of material point in reference configuration

F.3 Second and higher order tensor quantities

$\boldsymbol{\epsilon}$	general strain measure
$\boldsymbol{\epsilon}_{\mathrm{p}}$	general plastic strain measure
$\boldsymbol{\sigma}$	general stress measure
$\hat{\mathbf{\Gamma}}$	strain tensor of plastic intermediate configuration
$\hat{\mathbf{\Gamma}}_e$	elastic part of strain tensor $\hat{\mathbf{\Gamma}}$
$\hat{\mathbf{\Gamma}}_p$	plastic part of strain tensor $\hat{\mathbf{\Gamma}}$
$\mathbf{\Lambda}$	velocity gradient based on $\mathbf{F}_a$
$\mathbf{\Pi}$	transformed strain tensor
$\overset{\triangle}{\mathbf{\Pi}}$	transformed strain rate tensor
$\mathbf{\Sigma}$	transformed stress tensor
$\overset{\triangledown}{\mathbf{\Sigma}}$	transformed stress rate tensor
$\mathbf{a}$	Finger tensor
$\mathbf{b}$	left Cauchy Green tensor
$\mathbf{e}$	Piola tensor
$\tilde{\mathbf{h}}$	elasticity relation
$\mathbf{A}$	Almansi strain tensor
$\mathbf{A}_e$	elastic part of Almansi tensor $\mathbf{A}$
$\mathbf{A}_p$	plastic part of Almansi tensor $\mathbf{A}$
$\mathbf{C}$	right Cauchy Green tensor
$\hat{\mathbf{C}}_e$	elastic right Cauchy Green tensor
$\mathbf{C}_{\mathrm{p}}$	plastic right Cauchy Green tensor
$\mathbf{D}$	strain rate tensor
$\mathbf{D}_p$	symmetric part of plastic velocity gradient, plastic strain rate tensor
$\mathbf{E}$	Green strain tensor
$\mathbf{F}$	deformation gradient
$\hat{\mathbf{F}}_{\mathrm{e}}$	elastic part of $\mathbf{F} = \hat{\mathbf{F}}_{\mathrm{e}}\mathbf{F}_{\mathrm{p}}$
$\mathbf{F}_{\mathrm{p}}$	plastic part of $\mathbf{F} = \hat{\mathbf{F}}_{\mathrm{e}}\mathbf{F}_{\mathrm{p}}$
$\mathbf{F}_a$	part of deformation gradient $\mathbf{F} = (\mathbf{F}\mathbf{F}_a^{-1})\mathbf{F}_a$ (multiplicative decomposition)
$\mathbf{I}$	second order unity tensor
$\mathbf{L}$	spatial velocity gradient
$\mathbf{L}_p$	velocity gradient based on $\mathbf{F}_{\mathrm{p}}$
$\hat{\mathbf{P}}$	Mandel stress tensor
$\mathbf{R}$	orthogonal part of $\mathbf{F} = \mathbf{R}\mathbf{U} = \mathbf{V}\mathbf{R}$
$\mathbf{S}$	weighted Cauchy stress tensor
$\mathbf{T}$	Cauchy stress tensor
$\mathbf{T}_R$	first Piola-Kirchhoff stress tensor
$\tilde{\mathbf{T}}$	second Piola-Kirchhoff stress tensor
$\hat{\mathbf{T}}$	stress tensor of intermediate configuration
$\mathbf{U}$	right stretch tensor
$\mathbf{U}_{\mathrm{e}}$	elastic right stretch tensor
$\mathbf{V}$	left stretch tensor
$\mathbf{W}$	spin or vorticity tensor

F.4 Matrices and column matrices

$\delta, \hat{\delta}$	local integration error
$\boldsymbol{\xi}_{jkl}$	coordinates of Gauss-point j,k,l
$\Delta \boldsymbol{U}$	increment of vector of nodal displacements (from Newton iteration)
$\Delta \mathbf{Q}$	increment of $\mathbf{Q}$ in local iteration
$\Delta \mathbf{C}$	total increment of LVC in homotopy Newton algorithm
$\boldsymbol{\Phi}, \hat{\boldsymbol{\Phi}}$	increment function of Runge-Kutta method
$\boldsymbol{\Psi}(t_n, \boldsymbol{y})$	function to compute local integration error
$\boldsymbol{f}$	vector valued function (explicit ODE)
$\boldsymbol{g}$	algebraic equation system
$\overline{\boldsymbol{p}}(t)$	prescribed external forces
$\boldsymbol{q}_{\text{err}}$	vector of local integration error in internal variables
$\boldsymbol{q}, \boldsymbol{q}_0$	(initial) vector of internal variables
$\mathbf{q}^e_{jkl}$	internal variables of Gauss-point j, k, l in the element e
$\boldsymbol{r}$	right hand side of differential part of equations system
$\tilde{\boldsymbol{r}}$	right-hand side of differential part of DAE-system
$\boldsymbol{u}_{\text{err}}$	vector of local integration error in nodal displacements
$\boldsymbol{u}, \boldsymbol{u}_0$	(initial) vector of nodal displacements
$\boldsymbol{u}^h$	finite elments approximation of displacements
$\boldsymbol{u}_j$	displacement vector of node j
$\boldsymbol{u}_a$	vector of all nodal displacements
$\mathbf{u}^e$	vector of nodal displacements of element e
$\boldsymbol{y}$	vector of unknowns
$\boldsymbol{y}_0$	vector of initial values
$\boldsymbol{y}_n$	vector of unknowns at time t_n
$\boldsymbol{y}_{n+1}$	vector of unknowns at time t_{n+1}
$\boldsymbol{y}_{\text{err}}$	vector of local integration error
$\boldsymbol{A}, \tilde{\boldsymbol{A}}$	coefficient matrix of differential part of DAE-system
$\mathbf{B}^e$	strain displacement matrix of element e
$\mathbf{B}^e_{NL}$	nonlinear part of strain displacement matrix in element e
$\mathbf{C}(\mathbf{U})$	vector representation of right Cauchy Green tensor
$\mathbf{C}^e$	vector representation of right Cauchy-Green tensor
$\boldsymbol{F}$	vector valued function (implicit ODE)
$\mathbf{F}^e_{23}$	matrix representation of push-forward operator
$\boldsymbol{G}$	global nonlinear system of equations
$\boldsymbol{G}_{ni}$	part of nonlinear system resulting from algebraic part of DAE-system in stage ni of Runge-Kutta method
$\mathbf{J}$	jacobian of local nonlinear system
$\mathbf{J}^e$	Jacobian of coordinate transformation to reference element
$\boldsymbol{L}$	local nonlinear system of equations
$\boldsymbol{L}_{ni}$	part of nonlinear system resulting from differential part of DAE-system in stage ni of Runge-Kutta method
$\mathbf{L}$	local system of non-linear equations
$\mathbf{L}^{e(jkl)}_{ni}$	non-linear system at Gauss-point jkl in element e in stage i of n^{th} time step of DIRK-method
$\mathbf{M}^e_{\text{S}}$	matrix in tangent from geometrical non-linearity

$\boldsymbol{N}_a$	matrix of ansatz functions
$\boldsymbol{N}$	matrix of ansatz functions for free nodal displacements
$\overline{\boldsymbol{N}}$	matrix of ansatz functions for prescribed nodal displacements
$\mathbf{N}^e$	matrix of ansatz functions of element e
$\boldsymbol{Q}$	vector of internal variables
$\boldsymbol{Q}_{ni}$	Unknown internal variables in stage ni of Runge-Kutta method
$\mathbf{Q}$	local vector of internal variables
$\mathbf{Q}_{ni}^{e(jkl)}$	internal variables at Gauss-point jkl in element e in stage i of n^{th} time step of DIRK-method
$\boldsymbol{R}_{ni}(\boldsymbol{Y}_{ni})$	resulting nonlinear system in each stage ni of the Runge-Kutta method
$\boldsymbol{S}_{ni}$	start values of stage ni of Runge-Kutta method
$\boldsymbol{S}_{ni}^{\mathrm{q}}$	Internal variables part of $\boldsymbol{S}_{ni}$
$\boldsymbol{U}$	vector of nodal displacements
$\boldsymbol{U}_{ni}$	Unknown nodal displacements in stage ni of Runge-Kutta method
$\mathbf{U}_{ni}^{e(jkl)}$	displacements at Gauss-point jkl in element e in stage i of n^{th} time step of DIRK-method
$\boldsymbol{Y}_{ni}$	stage values of Runge-Kutta method
$\dot{\boldsymbol{Y}}_{ni}$	stage derivatives of Runge-Kutta method
$\boldsymbol{Z}^e, \overline{\boldsymbol{Z}}^e, \boldsymbol{Z}_a^e$	coincidence marices
$\boldsymbol{Z}_q^{e(jkl)}$	coincidence matrix for internal variables

F.5 Miscellaneous

$\varphi^e = \chi^{e-1}$	mapping from reference configuration to reference element
$\varphi(\boldsymbol{x}, t), \varphi_R(\boldsymbol{X}, t)$	production density of physical quantity
$\chi,\ \chi_t,\ \chi_{t_0}$	configuration, current configuration
χ^e	mapping from reference element to reference configuration
$\pi(t, \boldsymbol{u}, \delta\boldsymbol{u}, \boldsymbol{q})$	energy functional (principle of virtual displacements)
Γ	surface of finite elements approximation of material body
$\boldsymbol{\Phi},\ \boldsymbol{\Phi}_R$	flux of physical quantity in current and reference configuration
$\boldsymbol{\Phi}_{t_0}$	motion of material body
$\boldsymbol{\Psi},\ \boldsymbol{\Psi}_R$	physical quantity in current and reference configuration
Ω	volume of finite elements approximation of material body
Ω_{ref}	domain of reference element
$\Omega^e, d\Omega^e$	domain of element e and infinitesimal volume element of element e
$p(\boldsymbol{x}, t), p_R(\boldsymbol{X}, t)$	production density of physical quantity
$\mathcal{B},\ \mathcal{B}_{t_0}\, \mathcal{B}_t$	material body, in initial configuration, in current configuration
$\mathcal{P}$	material point
$\mathcal{K}$	set of configurations
$\mathcal{R}$	reference configuration

F.6 Mathematical operators

$\frac{\partial x}{\partial y}$	partial derivative of x with respect to y
$\frac{\mathrm{d}x}{\mathrm{d}y}$	total derivative of x with respect to y
$f'(x)$	derivative of f with respect to x
Grad	gradient (with respect to material coordinates)
grad	gradient (with respect to spatial coordinates)
Div	divergence (with respect to material coordinates)
div	divergence (with respect to spatial coordinates)
$\dot{\mathbf{A}}$, $\dot{\overline{\text{expr.}}}$	material time derivative of $\mathbf{A}$ or expression expr.
$\overset{\triangle}{\mathbf{A}}$	lower convected Oldroyd rate of $\mathbf{A}$
$\overset{\triangledown}{\mathbf{A}}$	upper convected Oldroyd rate of $\mathbf{A}$
$\det \mathbf{A}$	determinant of $\mathbf{A}$
$\mathbf{A}^T$	transposition of $\mathbf{A}$
$\mathbf{A}^{-1}$	inversion of $\mathbf{A}$
$\mathbf{A}^D$	deviator of $\mathbf{A}$
$\mathrm{tr}\,\mathbf{A} = A_{ii}$	trace of $\mathbf{A}$
$\int_V$, $\int_v$	integral over volume of material body in reference (current) configuration
$\int_A$, $\int_a$	integral over surface of material body in reference (current) configuration
$\ln$	natural logarithm
$\otimes$	dyadic product
$\mathbf{A} \cdot \mathbf{B}$	inner product of two second order tensors
$\|$expr.$\|$	norm of expr.

Bibliography

[1] ABAQUS. *ABAQUS Theory Manual*, v.5.8. edition, 1998.

[2] A.J. Abbo and S.W. Sloan. A smooth hyperbolic approximation to the Mohr-Coulomb yield criterion. *Computers & Structures*, 54:427–441, 1995.

[3] G. V. Abou-Chedid. *Experimental yield surface studies for the compaction of metal powders*. PhD thesis, Massachusetts Institute of Technology, 1993.

[4] A. R. Akisanya, A. C. F. Cocks, and N. A. Fleck. The yield behaviour of metal powder. *International Journal of Mechanical Sciences*, 39(12):1315–1324, 1997.

[5] R. Alexander. Diagonally implicit Runge-Kutta methods for stiff O.D.E.'s. *SIAM Journal on Numerical Analysis*, 14:1006–1021, 1977.

[6] J. Altenbach and H. Altenbach. *Einführung in die Kontinuumsmechanik*. B. G. Teubner, Stuttgart, 1994.

[7] ANSYS INC. *ANSYS Theory Manual*. Canonsburg, release 5.6. edition, 2000.

[8] A. K. Ariffin, M. M. Rahman, N. Muhamad, and J. Sahari. Thermal-mechanical model of warm powder compaction process. *Journal of Materials Processing Technology*, 116: 67–71, 2001.

[9] F. Armero and A. Perez-Foguet. On the formulation of closest-point projection algorithms in elastoplasticity–part I: The variational structure. *International Journal for Numerical Methods in Engineering*, 53:331–374, 2002.

[10] M. Arnold and K. Frischmuth. Solving problems with unilateral constraints by DAE methods. *Mathematics and Computers in Simulation*, 47:47–67, 1998.

[11] E. Arzt. The influence of an increasing particle coordination on the densification of spherical powders. *Acta Metallurgica*, 30:1883–1890, 1982.

[12] U. M. Ascher and L. R. Petzold. *Computer methods for ordinary differential equations and differential-algebraic equations*. Siam, Philadelphia, 1998.

[13] ASM. *ASM Handbook Vol 7: Powder Metal Technologies and Applications*. ASM International, 1998.

[14] M. Aubertin and L. Li. A porosity-dependent inelastic criterion for engineering materials. *International Journal of Plasticity*, 20:2179–2208, 2004.

[15] A. Bakhshiani, A. R. Khoei, and M. Mofid. An endochronic plasticity model for powder compaction processes. *Journal of Materials Processing Technology*, 125-126:138–143, 2002.

[16] A. Bejarano, M. D. Riera, and J. M. Prado. Simulation of the compaction process of a two-level powder metallurgical part. *Journal of Materials Processing Technology*, 143-144:34–40, 2003.

[17] D.P. Bertsekas. *Constrained optimization and Lagrange multiplier methods*. Athena Scientific, 1996.

[18] J. Betten. *Kontinuumsmechanik*. Springer, 2. edition, 2001.

[19] W. Bier and S. Hartmann. A finite strain constitutive model for metal powder compaction using a unique and convex single surface yield function. *European Journal of Mechancics, Series A/Solids*, 25:1009–1030, 2006.

[20] D. Bigoni and A. Piccolroaz. Yield criteria for quasibrittle and frictional materials. *International Journal of Solids and Structures*, 41:2855–2878, 2004.

[21] S. Boyd and L. Vandenberghe. *Convex Optimization*. University Press, 2004.

[22] C. Callari, F. Auricchio, and E. Sacco. A finite-strain cam-clay model in the framework of multiplicative elasto-plasticity. *International Journal of Plasticity*, 14(12):1155–1187, 1998.

[23] P. C. Carnavas. *The effect of particle morphology on metal powder compaction*. PhD thesis, University of Queensland, 1996.

[24] P. C. Carnavas and N. W. Page. Elastic properties of compacted metal powders. *Journal of Materials Science*, 33:4647–4655, 1998.

[25] J. R. Cash. Diagonally implicit Runge-Kutta formulae with error estimates. *Journal of the Institute of Mathematics and its Applications*, 24:293–301, 1979.

[26] J. Cedergren, N. J. Sorensen, and A. Bergmark. Three-dimensional analysis of compaction of metal powder. *Mechanics of Materials*, 34(1):43–59, 2002.

[27] J. Cedergren, N. J. Sorensen, and S. Melin. Numerical investigation of powder compaction of gear wheels. *International Journal of Solids and Structures*, 40:4989–5000, 2003.

[28] W. F. Chen and D. J. Han. *Plasticity for structural engineers*. Springer-Verlag, 1988.

[29] H. Chtourou, A. Gakwaya, and M. Guillot. Modeling of the metal powder compaction process using the cap model.Part II : Numerical implementation and practical applications. *International Journal of Solids and Structures*, 39:1077–1096, 2002.

[30] H. Chtourou, M. Guillot, and A. Gakwaya. Modeling ot the metal powder compaction process using the cap model. Part I. Experimental material characterization and validation. *International Journal of Solids and Structures*, 39:1059 – 1075, 2002.

[31] A. C. F. Cocks. Constitutive modelling of powder compaction and sintering. *Progress in Materials Science*, 46:201–229, 2001.

[32] Y. Corapcioglu and T. Uz. Constitutive equations for plastic deformation of porous material. *Powder Technology*, 21:269–274, 1978.

[33] O. Coube. *Modeling and numerical simulation of powder die compaction with consideration of cracking*. PhD thesis, University Pierre et Marie Curie, Paris, 1998.

[34] O. Coube and H. Riedel. Numerical simulation of metal powder die compaction with special consideration of cracking. *Powder Metallurgy*, 43:123–131, 2000.

[35] R. de Boer and H. T. Dresenkamp. Constitutive equations for concrete in failure state. *Journal of Engineering Mechanics*, 115(8):1591–1608, 1989.

[36] J.E. Dennis and R.B. Schnabel. *Numerical methods for unconstrained optimization and nonlinear equations*. SIAM, 1996.

[37] C. S. Desai. Single surface yield and potential function plasticity models: A review. *Computers & Geotechnics*, 7:319–335, 1989.

[38] S. Diebels, P. Ellsiepen, and W. Ehlers. Error-controlled Runge-Kutta time integration of a viscoplastic hybrid two-phases model. *Technische Mechanik*, 19:19–27, 1999.

[39] F. L. DiMaggio and I. S. Sandler. Material model for granular soils. *Journal of the engineering mechanics division Proceedings of the American Society of Civil Engineers*, pages 935–950, June 1971.

[40] I. Doghri. *Mechanics of deformable solids*. Springer, 2000.

[41] S. M. Doraivelu, H. L. Gegel, J. S. Gunasekera, J. C. Malas, J. T. Morgan, and J. F. Thomas Jr. A new yield function for compressible P/M materials. *International Journal of Mechanical Sciences*, 26(9/10):527–535, 1984.

[42] W. Ehlers. A single-surface yield function for geomaterials. *Archive of Applied Mechanics*, 65:246–259, 1995.

[43] W. Ehlers and P. Ellsiepen. Adaptive Zeitintegration-Verfahren für ein elastisch-viskoplastisches Zweiphasenmodell. *ZAMM Zeitschrift für Angewandte Mathematik und Mechanik*, 78:361–362, 1998.

[44] P. Ellsiepen. *Zeit- und ortsadaptive Verfahren angewandt auf Mehrphasenprobleme poröser Medien*. PhD thesis, Universität Stuttgart, 1999.

[45] P. Ellsiepen and S. Hartmann. Remarks on the interpretation of current non-linear finite element analyses as differential-algebraic equations. *International Journal for Numerical Methods in Engineering*, 51:679–707, 2001.

[46] ESRD. StressCheck is a trademark of Engineering Software Research and Development, Inc., St. Louis, MO, USA. www.esrd.com, 2005.

[47] N. A. Fleck. On the cold compaction of powder. *Journal of the Mechanics and Physics of Solids*, 43(9):1409–1431, 1995.

[48] N. A. Fleck, L. T. Kuhn, and R. M. McMeeking. Yielding of metal powder bonded by isolated contacts. *Journal of the Mechanics and Physics of Solids*, 40(5):1139–1162, 1992.

[49] N. Frage, S. Hartmann, S. Holzer, E. Rank, Z. Yosibash, and M. Dariel. Final report of the project: P-fem for a class of pressure/density dependent plasticity models with application to cold isostatic pressing. Technical report, German-Israeli Foundation for Scientific Research and Development (GIF), 2006.

[50] C. Geindreau, D. Bouvard, and P. Doremus. Constitutive behaviour of metal powder during hot forming. Part I: Experimental investigation with lead powder as a simulation material. *European Journal of Mechanics, A/Solids*, 18:581–596, 1999.

[51] R. M. Govindarajan and N. Aravas. Deformation processing of metal powders: Part I - Cold isostatic pressing. *International Journal of Mechanical Sciences*, 36(4):343–357, 1994.

[52] R. J. Green. A plasticity theory for porous solids. *International Journal of Mechanical Sciences*, 14:215–224, 1972.

[53] R. Greve. *Kontinuumsmechanik*. Springer, 2003.

[54] C. Gu, M. Kim, and L. Anand. Constitutive equations for metal powders: Application to powder forming processes. *International Journal of Plasticity*, 17:147–209, 2001.

[55] A. L. Gurson. Continuum theory of ductile rupture by void nucleation and growth: Part I - yield criteria and flow rules for porous ductile media. *Journal of Engineering Materials and Technology*, 99:2–15, 1977.

[56] H.-A. Häggblad and M. Odenburg. Modelling and simulation of metal powder die pressing with use of explicit time integration. *Modelling and Simulation in Materials Science and Engineering*, 2:893–911, 1994.

[57] E. Hairer, S.P. Norsett, and G. Wanner. *Solving ordinary differential equations I*. Springer series in computational mathematics. Springer, 2nd edition, 1993.

[58] E. Hairer and G. Wanner. *Solving ordinary differential equations II*. Springer series in computational mathematics. Springer, 2nd edition, 1996.

[59] S. Hartmann. Computation in finite strain viscoelasticity: finite elements based on the interpretation as differential-algebraic equations. *Computer Methods in Applied Mechanics and Engineering*, 191(13-14):1439–1470, 2002.

[60] S. Hartmann. *Finite-Elemente Berechnung inelastischer Kontinua. Interpretation als Algebro-Differentialgleichungssysteme*. Habilitation, University of Kassel, Institute of Mechanics, 2003. Report No. 1/2003.

[61] S. Hartmann. A remark on the application of the Newton-Raphson method in non-linear finite element analysis. *Computational Mechanics*, 36:100–116, 2005.

[62] S. Hartmann. TASA-FEM: Ein Finite-Elemente-Programm für raum- und zeitadaptive gekoppelte Strukturberechnungen. Technical report, Institute of Mechanics, University of Kassel, Kassel, Germany, 2006.

[63] S. Hartmann. A thermomechanically consistent constitutive model for polyoxymethylene: experiments, material modeling and computation. *Archive of Applied Mechanics*, 76:349–366, 2006.

[64] S. Hartmann and W. Bier. High-order time integration applied to metal powder plasticity. *International Journal of Plasticity*, 24:17–54, 2008.

[65] S. Hartmann, G. Lührs, and P. Haupt. An efficient stress algorithm with applications in viscoplasticity and plasticity. *International Journal for Numerical Methods in Engineering*, 40:991–1013, 1997.

[66] S. Hartmann, T. Tschöpe, L. Schreiber, and P. Haupt. Large deformations of a carbon black-filled rubber. experiment, optical measurement and parameter identification using finite elements. *European Journal of Mechanics, A/Solids*, 22:309–324, 2003.

[67] P. Haupt. *Continuum Mechanics and Theory of Materials*. Springer Verlag, Berlin, 2000.

[68] P. Haupt, M. Kamlah, and C. Tsakmakis. On the thermodynamics of rate-independent plasticity as an asymptotic limit of viscoplasticity for slow processes. In D. Besdo and E. Stein, editors, *Finite Inelastic Deformations - Theory and Applications*, pages 107–116, Berlin, 1992. IUTAM Symposium Hannover Germany, Springer.

[69] P. Haupt and Ch. Tsakmakis. On the application of dual variables in continuum mechanics. *Continuum Mechanics and Thermodynamics*, 1:165–196, 1989.

[70] P. Haupt and Ch. Tsakmakis. Stress tensors associated with deformation tensors via duality. *Archive of Mechanics*, 48(2):347–384, 1996.

[71] U. Heisserer, S. Hartmann, A. Düster, W. Bier, Z. Yosibash, and E. Rank. p-FEM for finite deformation powder compaction. *Computer Methods in Applied Mechanics and Engineering*, 197:727–740, 2008.

[72] A. S. Helle, K. E. Easterling, and M. F. Ashby. Hot-isostatic pressing diagrams: New developments. *Acta Metallurgica*, 33(12):2163–2174, 1985.

[73] P. R. Heyliger and R. M. McMeeking. Cold plastic compaction of powders by a network model. *Journal of the Mechanics and Physics of Solids*, 49:2031–2054, 2001.

[74] A. Huerta, A. Perez-Foguet, and A. Rodriguez Ferran. Consistent tangent matrices for density-dependent finite plasticity models. *Mechanics of Cohesive-Frictional Materials*, 1:1–30, March 2000.

[75] T.J.R. Hughes. Numerical implementation of constitutive models: rate-independent deviatoric plasticity. In S. Nemat-Nasser, editor, *Theoretical foundation for large-scale computations for non-linear material behavior*. Martinus Nijhoff Publishers, Dordrecht, The Netherlands, 1984.

[76] K. Hutter and K. Jöhnk. *Continuum methods of physical modeling*. Springer Verlag, 2004.

[77] D. Jou, J. Casas-Vasquez, and G. Lebon. *Extended irreversible thermodynamics*. Springer, 2. edition, 1996.

[78] A. R. Khoei, A. Bakhshiani, and M. Mofid. An implicit algorithm for hypoelasto-plastic and hypoelasto-viscoplastic endochronic theory in finite strain isotropic-kinematic-hardening model. *International Journal of Solids and Structures*, 40:3393–3423, 2003.

[79] A. R. Khoei and R. W. Lewis. Finite element simulation for dynamic large elastoplastic deformation in metal powder forming. *Finite Elements in Analysis and Design*, 30:335–352, 1998.

[80] A. R. Khoei and R. W. Lewis. Adaptive finite element remeshing in a large deformation analysis of metal powder forming. *International Journal for Numerical Methods in Engineering*, 45:801–820, 1999.

[81] A. R. Khoei, M. Mofid, and A. Bakhshiani. Modelling of powder compaction process using an endochronic model. *Journal of Materials Processing Technology*, 130-131:175–180, 2002.

[82] A.R. Khoei and A.R. Azami. A single cone-cap plasticity with an isotropic hardening rule for powder materials. *International Journal of Mechanical Sciences*, 47:94–109, 2005.

[83] A.R. Khoei and S. Azizi. Numerical simulation of 3d powder compaction processes using cone-cap plasticity theory. *Materials & Design*, 26:137–147, 2005.

[84] H.G. Kim, O. Gillia, P. Doremus, and D. Bouvard. Near net shape processing of a sintered alumina component: adjustment of pressing parameters through finite element simulation. *International Journal of Mechanical Sciences*, 44:2523–2539, 2002.

[85] K. T. Kim, S. C. Lee, and H. S. Ryu. Densification behavior of aluminum alloy powder mixed with zirconia powder inclusion under cold compaction. *Materials Science and Engineering*, A340:41–48, 2003.

[86] T. Kraft. Determination of the optimum tool geometry of a cutting insert by finite element simulation of compaction and sintering. In *Proceedings of the 2003 International Conference on Powder Metallurgy and Particulate Materials, Part 4*, 2003.

[87] T. Kraft and B. Yazici. Formgenaue pulvertechnologische Zahnräder. *Konstruktion*, pages 13–14, November / Dezember 2006.

[88] G. Kreisselmeier and R. Steinhauser. Systematische Auslegung von Reglern durch Optimierung eines vektoriellen Gütekriteriums. *Regelungstechnik*, 3:76–79, 1979.

[89] H. A. Kuhn and C. L. Downey. Deformation characteristics and plasticity theory of sintered powder materials. *International Journal of Powder Metallurgy*, 7(1):15–25, 1971.

[90] P. V. Lade and M. K. Kim. Single hardening constitutive model for frictional materials, II. yield criterion and plastic work contours. *Computers & Geotechnics*, 6:13–29, 1988.

[91] H. Lämmer and Ch. Tsakmakis. Discussion of coupled elastoplasticity and damage constitutive equations for small and finite deformations. *International Journal of Plasticity*, 16:495–523, 2000.

[92] P. L. Larsson, S. Biwa, and B. Storakers. Analysis of cold and hot isostatic compaction of spherical particles. *Acta Materialia*, 44(9):3655–3666, 1996.

[93] E.H. Lee. Elastic-plastic deformation at finite strains. *Journal of Applied Mechanics*, 36: 1–6, 1969.

[94] E.H. Lee and D.T. Liu. Finite-strain elastic-plastic theory of application to plane wave analysis. *Journal of Applied Physics*, 38:19–27, 1967.

[95] S. C. Lee and K. T. Kim. Densification behavior of aluminum alloy powder under cold compaction. *International Journal of Mechanical Sciences*, 44:1295–1308, 2002.

[96] R. W. Lewis and A. R. Khoei. Numerical modelling of large deformation in metal powder forming. *Computer Methods in Applied Mechanics and Engineering*, 159:291–328, 1998.

[97] R. W. Lewis and A. R. Khoei. A plasticity model for metal powder forming processes. *International Journal of Plasticity*, 17:1659–1692, 2001.

[98] H. Lippmann and R. Iankov. Mathematical modeling of sintering during powder forming processes. *International Journal of Mechanical Sciences*, 39(5):585–596, 1997.

[99] D.G. Luenberger. *Linear and Nonlinear programming*. Addison Wesley, 2 edition, 1989.

[100] G. Lührs, S. Hartmann, and P. Haupt. On the numerical treatment of finite deformations in elastoviscoplasticity. *Computer Methods in Applied Mechanics and Engineering*, 144: 1–21, 1997.

[101] L. Mähler, M. Ekh, and K. Runesson. A class of thermo-hyperelastic-viscoplastic models for porous materials: theory and numerics. *International Journal of Plasticity*, 17:943–969, 2001.

[102] L.E. Malvern. *Introduction to the mechanics of a continuous medium*. Prentice-Hall, 1969.

[103] D. F. Meyer. *Experimentelle Ermittlung und numerische Simulation des mechanischen Verhaltens unterschiedlicher Si_3N_4 Pulver beim Matrizenpressen*. PhD thesis, Uni Karlsruhe, 1994.

[104] N. Ogbonna and N. A. Fleck. Compaction of an array of spherical particles. *Acta Metallurgica et Materialia*, 43(2):603–620, 1995.

[105] J. Oliver, S. Oller, and J. C. Cante. A plasticity model for simulation of industrial powder compaction processes. *International Journal of Solids and Structures*, 33(20-22):3161–3178, 1996.

[106] J. M. Ortega and W. C. Rheinboldt. *Iterative solution of nonlinear equations in several variables*. SIAM, Society for Industrial and Applied Mathematics, Philadelphia, 2000.

[107] A. Perez-Foguet and F. Armero. On the formulation of closest-point projection algorithms in elastoplasticity–part II: Globally convergent schemes. *International Journal for Numerical Methods in Engineering*, 53:331–374, 2002.

[108] A. Perez-Foguet and A. Huerta. Density-dependent finite-strain plasticity. computational issues. In *European Conference on Computational Mechanics*, pages 1–20, 2001.

[109] A. Perez-Foguet, A. Rodriguez-Ferran, and A. Huerta. Consistent tangent matrices for density-dependent finite plasticity models. *Mechanics of Cohesive-Frictional Materials*, 5:1–30, 2000.

[110] A. Perez-Foguet, A. Rodriguez-Ferran, and A. Huerta. Efficient and accurate approach for powder compaction problems. *Computational Mechanics*, 30:220–234, 2003.

[111] P. Perzyna. Fundamental problems in viscoplasticity. *Advances in applied mechanics*, 9: 243–377, 1966.

[112] A. T. Procopio and A. Zavaliangos. Simulation of multi-axial compaction of granular media from loose to high relative densities. *Journal of the Mechanics and Physics of Solids*, 53:1523–1551, 2005.

[113] N.B.G. Rabbat, A.L. Sangiovanni-Vincentelli, and H.Y. Hsieh. A multilivel newton algorithm with macromodeling and latency for the analysis of large-scale nonlinear circuits in the time domain. *Transactions on Circuits and Systems*, 26(9):733–741, 1979.

[114] P. Redanz. Numerical modelling of a cold compation of metal powder. Technical Report 551, Danish Center for Applied Mathematics and Mechanics, 1997.

[115] P. Redanz. Numerical modelling of cold compaction of metal powder. *International Journal of Mechanical Sciences*, 40(11):1175–1189, 1998.

[116] P. Redanz. Numerical modelling of powder compaction of a cup. *International Journal of Mechanical Sciences*, 18:399–413, 1999.

[117] P. Redanz and N. A. Fleck. The compaction of a random distribution of metal cylinders by the discrete element method. *Acta Materialia*, 49:4325–4335, 2001.

[118] A. Rodriguez-Ferran, A. Perez-Foguet, and A. Huerta. Arbitrary Lagrangian-Eulerian (ALE) formulation for hyperelastoplasticity. *International Journal for Numerical Methods in Engineering*, 53:1831–1851, 2002.

[119] K. H. Roscoe and J.B. Burland. *Engineering Plasticity*, chapter On the generalized stress-strain behaviour of 'wet' clay, pages 535–609. Cambridge University Press, 1968.

[120] H. Schwetlick and H. Kretzschmar. *Numerische Verfahren für Naturwissenschaftler und Ingenieure*. Fachbuchverlag, Leipzig, 1991.

[121] A. Shamloo, A.R. Azami, and A.R. Khoei. Modeling of pressure-sensitive materials using a cap plasticity theory in extended finite element method. *Journal of Materials Processing Technology*, 164–165:1248–1257, 2005.

[122] S. Shima and M. Oyane. Plasticity theory for porous metals. *International Journal of Mechanical Sciences*, 18:285–291, 1976.

[123] I. Shridhar and N. A. Fleck. Yield behaviour of cold compacted composite powders. *Acta Materialia*, 48:3341–3352, 2000.

[124] G.A. Shultz, R.B. Schnabel, and R.H. Byrd. A family of trust-region-based algorithms for unconstrained minimization with strong global convergence properties. *SIAM Journal of Numerical Analysis*, 22, 1985.

[125] J.C. Simo and K.S. Pister. Remarks on rate constitutive equations for finite deformation problems: Computational implications. *Computer Methods in Applied Mechanics and Engineering*, 46:201–215, 1984.

[126] P. Spellucci. DONLP2 short users guide. Technical report, Department of Mathematics, TU Darmstadt, 1999.

[127] B. Storakers, N. A. Fleck, and R. M. McMeeking. The viscoplastic compaction of composite powders. *Journal of the Mechanics and Physics of Solids*, 47:785–815, 1999.

[128] X.-K. Sun, S.-J. Chen, J.-Z. Xu, L.-D. Zhen, and K.-T. Kim. Analysis of cold compaction densification behaviour of metal powders. *Materials Science and Engineering A*, 267: 43–49, 1999.

[129] A. Svoboda, L.-E. Lindgren, and A. S. Oddy. The effective stress function algorithm for pressure-dependent plasticity applied to hot isostatic pressing. *International Journal for Numerical Methods in Engineering*, 43:587–606, 1998.

[130] J. Svoboda, H. Riedel, and R. Gaebel. A model for liquid phase sintering. *Acta Metallurgica*, 44(8):3215–3226, 1996.

[131] B. Szabó and I. Babuška. *Finite Element Analysis*. John Wiley & Sons, Inc., New York, 1991.

[132] M. Szanto, W. Bier, N. Frage, S. Hartmann, and Z. Yosibash. Experimental based finite element simulation of cold isostatic pressing of metal powders. *International Journal of Mechanical Sciences*, 2008. currently online available.

[133] W. Törnig and P. Spellucci. *Numerische Mathematik für Ingenieure und Physiker*, volume 1. Springer-Verlag, 2 edition, 1988.

[134] C. Truesdell and W. Noll. *The non-linear field theories of mechanics*. Springer, 3 edition, 2004.

[135] Ch. Tsakmakis. Kinematic hardening rules in finite plasticity. Part I : A constitutive approach. *Continuum Mechanics and Thermodynamics*, 8:215–231, 1996.

[136] T. C. Tszeng and W. T. Wu. A study of the coefficients in yield functions modeling metal powder deformation. *Acta Metallurgica*, 44(9):3543–3552, 1996.

[137] V. Tvergaard. Influence of voids on shear band instabilities under plane strain conditions. *International Journal of Fracture*, 17:389–407, 1981.

[138] V. Tvergaard. On localisation in ductile materials containing spherical voids. *International Journal of Fracture*, 18:237–252, 1982.

[139] T. J. Watson and J. A. Wert. On the development of constitutive relations for metallic powders. *Metallurgical Transactions*, 24A:2071–2081, 1993.

[140] B. Wikman, A. Svoboda, and H. A. Häggblad. A combined material model for numerical simulation of hot isostatic pressing. *Computer Methods in Applied Mechanics and Engineering*, 189:901–913, 2000.

[141] X. J. Xin, P. Jayaraman, G. S. Daehn, and R. H. Wagoner. Investigation of yield surface of monolithic and composite powders by explicit finite element simulation. *International Journal of Mechanical Sciences*, 45:707–723, 2003.